Declaration

The work described in this thesis was carried out in the Department of Chemistry, Crown Street, Liverpool from October 2006 to September 2009 under the supervision of Professor M. J. Rosseinsky. All work is my own unless stated to the contrary and has not been submitted for any other degree at this, or any other, University.

Gary Evans

Abstract

Nanometric Oxides for Functional Materials

PhD thesis, Gary Evans, University of Liverpool

This thesis describes the synthesis and application of complex metal oxide nanoparticles. The work is focussed on three core areas; the synthesis of $CoFe_2O_4$ nanoparticles and their application as CO oxidation catalysts, the controlled assembly of functionalised $CoFe_2O_4$ and $BaTiO_3$ nanoparticles and the preparation and characterisation of magnetoelectric composites from chemically-bonded nanoparticle assemblies.

Chapter 1 gives an introduction to the history of nanotechnology, recent developments in the synthesis of nanoparticles and other areas key to the work described herein.

In Chapter 2 details the synthetic and analytical techniques employed.

Chapter 3 describes the synthesis and characterisation of $CoFe_2O_4$ nanoparticles, and their application as catalysts in the CO oxidation reaction. Nanoparticles were prepared with a range of controlled sizes and were found to be active CO oxidation catalysts. Analysis of their size-dependent activity and stability is performed.

Chapter 4 describes the assembly of $CoFe_2O_4$ and $BaTiO_3$ nanoparticles by direct functionalisation of the nanoparticle surfaces using complementary organic functional molecules. Characterisation of the functionalised nanoparticles and assemblies is performed, and the extensibility of the developed functionalisation and assembly protocol is tested using particles with different sizes and morphologies.

In Chapter 5 the assembled nanoparticles discussed in Chapter 4 are processed into dense ceramics with a view to preparing magnetoelectric composites. The magnetoelectric properties are tested, and optimisation of the ceramics is performed by modification of the starting nanoparticle sizes, composite composition and processing conditions. The composites are tested against control samples prepared by traditional grinding and firing, and characterisation of the ceramics using XRD and electron microscopy provides and insight as to why their magnetoelectric properties differ to those prepared by the traditional technique.

The work contained in this thesis has been published in the following papers: -

G. Evans, I. V. Kozhevnikov, E. F. Kozhevnikova, J. B. Claridge, R. Vaidhyanathan, C. Dickinson, C. D. Wood, A. I. Cooper, M. J. Rosseinsky, "Particle-size Activity Relationship for $CoFe_2O_4$ Nanoparticle CO Oxidation Catalysts," *J. Mater. Chem.* **2008**, 18, 5518.

G. Evans, G. V. Duong, M. J. Ingleson, Z. Xu, J. T. A. Jones, Y. Z. Khimyak, J. B. Claridge, M. J. Rosseinsky, "Chemical Bonding Assembly of Multifunctional Oxide Nanocomposites," *Adv. Funct. Mater.* **2010**, 20, 231.

Acknowledgements

Firstly I would like to thank my primary supervisor Matt Rosseinsky for giving me the opportunity to be a part of his research group for the past 5 years and for his support, encouragement and ideas throughout the course of my PhD. Matt and my secondary supervisor John Claridge have enabled me to improve my research skills to a great extent from when I first entered the group as a final year undergraduate in late 2005 and I have thoroughly enjoyed and value my time in the MJR group.

I thank Vaidhya, Elena, Ivan and Calum for their input to the CO oxidation work, particularly Vaidhya for his help and assistance when I was a new member of the group. Mike Ingleson deserves great thanks for his ideas concerning the nanoparticle functionalisation and assembly work, as does Zhongling Xu for the incredible amount of time and hard work that he dedicated to the microscopy side of my project. I also thank Giap van Duong for his assistance with the magnetoelectric measurements, and Matthew Suchomel for his ideas and assistance concerning the ceramic processing and measurement work presented herein. I'm also appreciative of the input and ideas of Humphrey, Cristina, Upendra and Laurent. Hongjun Niu is thanked for his excellent work in maintaining the group laboratories and instrumentation, as are the technical staff at the University of Liverpool.

My mother Susan, brothers Lewis and Nathan, sisters Lisa and Lesley, nephew Jaden and nieces Jasmine and Amber are all thanked for their much valued support and interest in my work. Finally, I thank all of my friends and colleagues not mentioned thus far, particularly Matt Forster for sharing his good humour and wisdom with me each day.

Nanometric Oxides for Functional Materials

Thesis submitted in accordance with the requirements of the University of Liverpool for the degree of Doctor in Philosophy by:

Gary Evans

August 2010

Table of Contents

Chapter 1 2

1 Introduction

1.1 Early History of Nanoparticles 2

1.2 Recent Developments 3

1.3 $CoFe_2O_4$ 6

1.3.1 Structure and Properties 6

1.3.2 Synthesis 10

1.4 CO Oxidation 11

1.5 $BaTiO_3$ 14

1.5.1 Introduction to Ferroelectrics 14

1.5.2 Structure and Application of $BaTiO_3$ 15

1.5.3 Size-Property Relationship 16

1.5.4 Synthesis 17

1.6 Nanoparticle Functionalisation 18

1.7 Nanoparticle Assembly 20

1.8 Multiferroics and Magnetoelectrics 24

1.8.1 Introduction 24

1.8.2 Bulk Ceramic Magnetoelectric Composites 28

1.8.3 Nanostructured Thin Films 30

1.9 Aims of This Thesis 32

References 32

Chapter 2

2 Synthetic and Experimental Techniques 46

2.1 Introduction 46

2.2 Synthetic Techniques 46

2.2.1 Coprecipitation 46

2.2.2 Solvothermal Reactions 48

2.2.3 Sol-gel Synthesis 50

2.2.4 Solid State Sintering 51

2.3 Experimental Techniques 52

2.3.1 Transmission Electron Microscopy 52

2.3.1.1 Theory 53

2.3.1.2 Sample Preparation 56

2.3.2 Scanning Electron Microscopy 57

2.3.2.1 Theory 57

2.3.2.2 Sample Preparation 59

2.3.3 Energy-Dispersive X-ray Spectroscopy (EDX) 60

2.3.4 Scanning Transmission Electron Microscopy (STEM) 63

2.3.5 X-ray Diffraction (XRD) 63

2.3.5.1 Diffraction Theory 63

2.3.5.2 Powder X-ray Diffraction 69

2.3.5.3 PANalytical X'pert Pro Diffractometer 70

2.3.6 Thermogravimetric Analysis (TGA) 71

2.3.7 Elemental Analysis 72

2.3.8 Inductively Coupled Plasma Atomic Emission Spectroscopy (ICP-AES) 72
2.3.9 Piezoelectric Measurements 74
2.3.10 Infrared Spectroscopy 75
2.3.10.1 Theory 75
2.3.10.2 Fourier Transform Infrared Spectroscopy (FTIR) 77
2.3.11 Raman Spectroscopy 79
2.3.12 Gas Chromatography (GC) and CO Oxidation Catalysis Measurements 81
2.3.13 Nuclear Magnetic Resonance (NMR) 83
2.3.13.1 Theory 83
2.3.13.2 Solid State Nuclear Magnetic Resonance Spectroscopy (SSNMR) 86
2.3.14 SQUID 88
2.3.15 Measurement of the Magnetoelectric (ME) Effect 89
2.3.16 Gas Sorption 91
2.3.17 Ultraviolet and Visible Molecular Absorption Spectroscopy 97
2.3.18 Fluorescence Microscopy 97
References 98
Chapter 3
3 Synthesis and Characterisation of $CoFe_2O_4$ Nanoparticle CO Oxidation Catalysts 103
3.1 Introduction 103

3.2 Experimental 105

3.2.1 Solvothermal Synthesis of Sample C1 105

3.2.1.1 Preparation of Cupferronate Precursors 106

3.2.1.2 Solvothermal Synthesis of $CoFe_2O_4$ 106

3.2.2 Coprecipitation Synthesis of Sample C2 107

3.2.3 Synthesis of Samples C3-C8 108

3.2.4 Synthesis of Samples C9 and C10 109

3.2.5 Synthesis of $NiFe_2O_4$ Nanoparticles 109

3.2.6 Characterisation 110

3.2.6.1 Gas Sorption 110

3.2.6.2 X-ray Diffraction 110

3.2.6.3 Fourier Transform Infrared Spectroscopy 110

3.2.6.4 Thermogravimetric Analysis 111

3.2.6.5 Transmission Electron Microscopy 111

3.2.6.6 Elemental Analysis 111

3.2.6.7 Catalysis Testing 111

3.3 Results and Discussion 112

3.3.1 Synthesis and Characterisation of $CoFe_2O_4$ Nanoparticles 112

3.3.2 CO Oxidation Catalysis Testing 129

3.4 Conclusions 143

References 144

Chapter 4

4 Functionalisation and Assembly of Metal Oxide Nanoparticles 148

4.1 Introduction 148

4.2 Experimental 149

4.2.1 Preparation of 8 nm $BaTiO_3$ (BTO) Nanoparticles 149

4.2.2 Preparation of 50 nm BTO Nanoparticles 149

4.2.3 Preparation of 200 nm BTO Nanoparticles 150

4.2.4 Preparation of BTO Nanowires 150

4.2.5 Preparation of 10 nm $CoFe_2O_4$ (CFO) Nanoparticles 151

4.2.6 Preparation of 12.5 nm CFO Nanoparticles 151

4.2.7 Functionalisation of BTO with 3-Phosphonopropionic Acid 152

4.2.8 Functionalisation of 10 nm Oleic Acid Terminated CFO Nanoparticles 152

4.2.9 Functionalisation of 12.5 nm CFO, 8 nm BTO Nanoparticles with APTMS 153

4.2.10 Electrostatic Assembly of BTO and CFO Nanoparticles (Route **I**) 153

4.2.11 DCCI Assembly of BTO and CFO Nanoparticles (Route **II**) 153

4.2.12 Preparation of BTO-CFO Control Composites (Route **III**) 154

4.2.13 Preparation of BTO-CFO NH_2-NH_2 Control Composite 154

4.2.14 Preparation of BTO-CFO NH_3^+-NH_3^+ Control Composite 154

4.2.15 Transfer of Assemblies from THF to H_2O 154

4.2.16 Functionalisation of CFO with Thymine-1-Acetic Acid 154

4.2.17 Functionalisation BTO with 5'-Adenosine Monophosphate 155

4.2.18 Synthesis of Lucifer Yellow Tagged BTO Nanoparticles 155

4.2.19 Reaction of APTMS Modified BTO with Salicylaldehyde 155

4.2.20 Characterisation 156

4.2.20.1 X-ray Diffraction 156

4.2.20.2 TEM Imaging 156

4.2.20.3 SEM Imaging 156

4.2.20.4 FTIR Spectroscopy 157

4.2.20.5 Elemental Analysis 157

4.2.20.6 ICP-AES Analysis 157

4.2.20.7 Solid-State NMR 157

4.2.20.8 UV-Vis Molecular Absorption Spectroscopy 158

4.2.20.9 Fluorescence Microscopy 158

4.3 Results and Discussion 158

4.3.1 Synthesis and Functionalisation of 8 nm $BaTiO_3$ Nanoparticles 158

4.3.2 Reactions with -CHO and COOMe Terminated Silanes 168

4.3.3 Synthesis and Functionalisation of 12.5 nm $CoFe_2O_4$ 169

Nanoparticles

4.3.4 Assembly of BTO (8 nm) – CFO (12.5 nm) Particles 172

4.3.5 Synthesis and Functionalisation of 10 nm CFO Nanoparticles 174

4.3.6 Synthesis and Functionalisation of 50 nm Cube-like BTO Nanoparticles 178

4.3.7 Preparation of BTO (50 nm) – CFO (12.5 nm) "**a**" Assemblies 183

4.3.8 Functionalisation of 200 nm BTO Particles 190

4.3.9 Preparation of BTO (200 nm) – CFO (12.5 nm) "**b**" Assemblies 195

4.3.10 Further Control Reactions 197

4.3.11 Assembly using Biomolecules 199

4.3.12 Assembly of BTO Nanowires and CFO Nanoparticles 201

4.4 Conclusions 204

References 205

Chapter 5

5 Chemical Bond Assembled Multifunctional Oxide Nanocomposites 209

5.1 Introduction 209

5.2 Experimental 211

5.2.1 Preparation of BTO/CFO Ceramics 211

5.2.2 Processing of BTO/CFO Ceramics 211

5.2.3 Reaction of 200 nm BTO with H_2O_2 211

5.2.4 Synthesis of 50 nm CFO Nanoparticles 212

5.2.5 Characterisation 212

5.2.5.1 X-ray Diffraction 212

5.2.5.2 TEM Imaging 212

5.2.5.3 SEM Imaging 213

5.2.5.4 Piezoelectric Constant Measurements 213

5.2.5.5 Measurement of the Magnetoelectric Coefficient (α_E) 214

5.2.5.6 Fourier Transform Infrared Spectroscopy 214

5.2.5.7 Elemental Analysis 214

5.2.5.8 Thermogravimetric Analysis (TGA) 215

5.2.5.9 Raman Spectroscopy 215

5.2.5.10 SQUID 215

5.3 Results and Discussion 215

5.3.1 Preparation of BTO (50 nm) /CFO (10 nm) '**A**' Ceramic Composites 215

5.3.2 The Piezoelectric Properties of 8, 50 and 200 nm BTO 220

5.3.3 Preparation and Characterisation of BTO (200 nm) /CFO (12.5 nm) '**B**' Ceramic Composites 226

5.3.4 Other Systems 246

5.3.5 Synthesis and Characterisation of a BTO (400 nm) /CFO (12.5 nm) '**C**' Ceramic Composite 247

5.3.6 Hydroxylated BTO (200 nm) /CFO (12.5 nm) '**D**' Ceramic Composites 249

5.3.7 BTO (200 nm) /CFO (50 nm) '**E**' Ceramic Composites 253

5.3.8 BTO (nanowire) /CFO (12.5 nm) '**F**' Ceramic Composites 255

5.4 Conclusions 256

References 258

Chapter 6

Final Conclusions and Future Work 263

6.1 Final Conclusions 263

6.2 Future Work 266

References 268

Chapter 1

Chapter 1

1 Introduction

1.1 Early History of Nanoparticles

The history of nanotechnology dates back centuries. The Lycurgus cup held in the British Museum was made in the late Roman era; it is made of dichroic glass, which changes colour depending on whether light is shining onto it or through it. This property is due to the small amounts of gold and silver nanoparticles dispersed throughout the glass. The stained glass windows produced in the medieval period also made use of gold and silver nanoparticles, while the paints and glazes used by renaissance artists to colour pottery contained small amounts of copper and silver nanoparticles.[1]

Faraday prepared the first metallic nanoparticulate colloids in 1856, and in 1931 Knott and Ruska developed the first electron microscope. The electron microscope was to prove an invaluable tool in the development of nanotechnology and nanoparticle science, enabling the imaging of sub-micrometer structures, which was not possible with light microscopes. Widespread scientific interest in nanometric materials was initiated in 1959 with Richard Feynman's famous lecture entitled 'There is Plenty of Room at the Bottom.' After this, the field of nanotechnology began to develop apace, and a significant breakthrough occurred in 1981 with the development of the scanning tunnelling microscope (STM) by physicists at IBM.

This enabled the imaging and manipulation of individual atoms and the STM, like the electron microscope, has since proved crucial in advancing the field. Another major breakthrough was the discovery of fullerenes in 1985. These carbon-based materials continue to attract a huge amount of interest due to their potential to possess extraordinary strength and hardness, in addition to their electrical properties and chemical and heat resistance.[2, 3]

1.2 Recent Developments

The work detailed in this thesis concerns the synthesis and application of nanoparticles, small objects between 1 and 100 nm in diameter.[4] They have potential technological applications stemming from their unique and often size-dependent properties, which means they can behave considerably differently to the bulk material.[4, 5]

More specifically, the work presented here focuses on the synthesis and application of metal oxide nanoparticles by bottom-up wet chemical approaches.[6-10] Unlike top-down approaches such as nanolithography[11, 12] and milling,[13, 14] where small structures are fabricated from larger ones, bottom-up methods involve the production of complex, large assemblies from smaller building blocks. The synthetic routes employed in this thesis are discussed in Chapter 2, though here we consider generally some recent advances in the fields of nanoparticle synthesis and application. While the discussion here is focussed on metal oxides, a range of materials can be prepared and used as nanoparticles including metals,[15, 16] metal chalcogenides,[17, 18] metal pnictides[19, 20] and polymers,[21, 22] amongst others. Several reviews have been published discussing these materials.[23]

The experimental challenge in the synthesis of nanoparticles lies in the preparation of uniform size and shape objects, which are important characteristics due to the size and shape dependence of, for example, their electrical, optical and magnetic properties.[4] This is perhaps most easily illustrated by the fluorescent emission of quantum dots, which covers the entire visible spectrum as a function of their size.[24] In the field of magnetic data storage, monodisperse nanoparticles are required due to the strong size-dependence of their magnetic properties.[25, 26]

A range of transition metal binary oxides have been prepared as nanoparticles. Sol-gel chemistry has been used to prepare 4 nm monodisperse ZrO_2 nanoparticles from $[Zr(O^iPr)_4]$ and $ZrCl_4$ at 340 °C,[27] while TiO_2 was prepared by a similar route.[28] Monodisperse MnO nanoparticles have been prepared by the thermal decomposition of manganese acetate in the presence of oleic acid at 320 °C.[29] Others include Cu_2O, NiO and ZnO; the latter finds use in the electronics industry, where it is used in liquid crystal displays.[4]

Complex oxides can also be prepared as nanoparticles.[30] For example, $Ni_{0.5}Zn_{0.5}Fe_2O_4$ has been prepared between 9 to 90 nm by the coprecipitation of the corresponding metal nitrates with sodium hydroxide, with a subsequent calcination step. In this instance, the particle size was controlled by the calcination temperature, with sintering performed over a temperature range between 300 and 800 °C. The smaller particles were obtained by sintering at lower temperatures.[31] $Bi_4Ti_3O_{12}$ has been similarly prepared with sizes between 16 and 38 nm when sintering between 500 and 800 °C.[32] The coprecipitation route used to prepare these materials is a flexible approach and a range of other complex oxides including 80 nm $Sm_{1-x}Sr_xFeO_{3-\delta}$,[33] and 10 nm $Ce_{0.8}Y_{0.2}O_{1.9}$[34] have also been prepared in this manner. The sol-gel approach is similarly extendable to the preparation a whole host of complex

metal oxide nanoparticles, and examples include 8 nm oleic acid functionalised $CoAl_2O_4$ prepared by Rangappa et al.[35] (50 nm particles were prepared in the absence of oleic acid) and 35 nm $LaCoO_3$[36] amongst others. The solvothermal approach is also attractive due to the prepared materials not requiring a post-synthesis calcination step, as is often the case with materials prepared by coprecipitation and sol-gel methods. This means the nanoparticle aggregation that can occur during these high-temperature steps is avoided, and a range of ferrites[37, 38] and perovskites[39] have been prepared by the solvothermal method. One issue that affects the chemical synthesis of nanoparticles, and one that must be tackled in order increase their application is the small scale at which these reactions are typically carried out. Continuous flow solvothermal reactors are one way in which this is being addressed, and these have been used to prepare a range of materials including $BaTiO_3$, TiO_2, Fe_3O_4 and $Ce_{1-x}Zr_xO_2$ nanoparticles.[40] The theory behind the synthesis of metal oxide nanoparticles by routes such as coprecipitation and sol-gel is described in more detail in Chapter 2.

Much research is also being performed on the preparation of controlled shape nanomaterials including nanorods, nanowires and nanocubes due to their potential for application as chemical sensors,[41] and nanoscale devices.[42] Nanowires and nanorods are the smallest one dimensional structures capable of transporting electrons and optical excitations.[30] In addition, ferroelectrics including $BaTiO_3$ are being prepared with low dimensionality due to the potential for increasing the storage capacity of ferroelectric random access memory (FeRAM) possibly by a factor of 10,000 when compared to equivalent bulk materials.[43] Examples include $Pb(Zr, Ti)O_3$ nanoparticle films prepared by a modified sol-gel method[44] and

nanowires of $BaTiO_3$ prepared *via* a mixed solvothermal and ion exchange approach.[45]

1.3 $CoFe_2O_4$

1.3.1 Structure and Properties

$CoFe_2O_4$ nanoparticles are one of the materials prepared in the work described in this thesis. It is a transition metal oxide that adopts the inverse spinel structure; the Co^{2+} cation occupies one half of the octahedral coordination sites, with the Fe^{3+} cations occupying the remaining octahedral coordination sites in addition to the tetrahedral coordination sites. This is different to the normal spinel structure (AB_2O_4) were the A^{2+} and B^{3+} cations occupy the tetrahedral and octahedral sites respectively. The crystal structure of $CoFe_2O_4$ is shown in Figure 1.

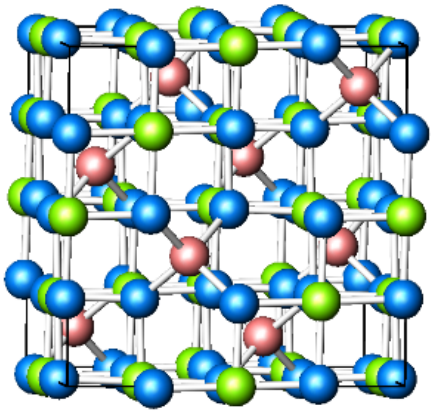

Figure 1. The crystal structure of the inverse spinel, $CoFe_2O_4$. The green atoms represent Co^{2+}, the pink are Fe^{3+} and the blue are O^{2-}.

$CoFe_2O_4$ is a ferrimagnetic oxide that has a net magnetisation of approximately 1 Bohr Magneton per metal ion and a bulk magnetisation of 425 emu cm^{-3} (80.34 emu g^{-1}, 18,850 emu mol^{-1}) at 300 K. It has a lower conductivity than Fe_3O_4, which is also ferrimagnetic, and which has a full complement of octahedral B-site Fe^{2+} ions that can transfer electrons among the Fe^{3+} neighbours in the B sublattice. Its magnetisation is higher than that of $CoFe_2O_4$, with a net magnetisation of $^4/_3$ Bohr Magnetons per metal ion and a magnetisation of 480 emu cm^{-3} (91.60 emu g^{-1}, 21,208 emu mol^{-1}) at 300 K. For comparison, iron has a magnetisation of 1,713 emu cm^{-3} (217.6 emu g^{-1}, 95,683 emu mol^{-1}) and Fe_3C has a magnetisation of 1,082 emu cm^{-3} (140 emu g^{-1}, 25,135 emu mol^{-1}).[46] In most ferrites (spinels were Fe is on the B-site) the electronic interaction in bonding is such that there is little electron orbital momentum (orbital quenching). The main contribution to the magnetic moment is from the electron spins that are not cancelled by antiparallel spins on other sublattices and are free to orient with the applied magnetic field.[47, 48]

The magnetisation behaviour of magnetic nanoparticles including $CoFe_2O_4$ can be markedly different to that of the bulk. In large magnetic particles there is a multidomain structure where regions of uniform magnetisation are separated by domain walls. The formation of the domain walls is a process driven by the balance between the magnetostatic energy (ΔE_{MS}), which increases proportionally with the particle size, and the domain-wall energy (E_{dw}), which increases proportionally with the interfacial area between domains. There is a critical size below which it costs more energy to create a domain wall than it does to support the external magnetostatic energy (stray field) of the single-domain state ($\Delta E_{MS}=E_{dw}$). This critical diameter is typically a few tens of nanometres, though depends on the material. A single-domain particle is uniformly magnetized with all the spins aligned

in the same direction and the magnetisation will be reversed by spin rotation since there are no domain walls to move. This is the reason for the very high coercivity observed in small nanoparticles.[49]

The second important phenomenon that occurs in magnetic nanoparticles is superparamagnetism. The energy barrier $K_{eff}V$ (where K_{eff} is the anisotropy constant and V is the particle volume) separates the two energetically equivalent easy directions of magnetisation. With decreasing particle size, the thermal energy, k_BT (where k_B is the Boltzmann constant and T is the temperature) exceeds the energy barrier $K_{eff}V$ and the magnetisation is easily flipped. In this situation the system behaves like a paramagnet, and instead of atomic magnetic moments there is now a giant (super) moment inside each particle. This system is named a superparamagnet, it has no hysteresis and the data of different temperatures superimpose onto a universal curve of M versus H/T. This is illustrated in Figure 2 below.

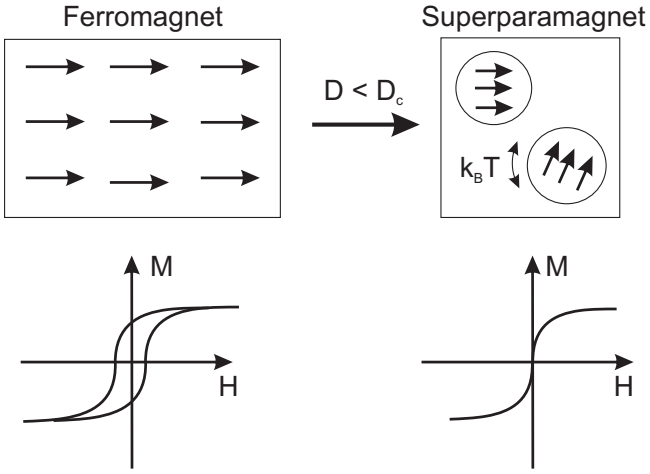

Figure 2. An illustration of the magnetic moments in a ferromagnet (left) and superparamagnet (right), which exists below the critical size D_c. Illustrative M vs. H magnetisation curves are shown for each, note that there is no hysteresis in the magnetisation of a superparamagnet.[49]

The critical size below which $CoFe_2O_4$ is superparamagnetic is around 10 nm.[49-51] This critical size depends on a number of factors including the value of the magnetic saturation, the strength of the crystal anisotropy, surface and domain-wall energy and the shape of the nanoparticles.[52]

The application of an alternating external magnetic field to superparamagnetic nanoparticles leads to the generation of heat from the thermal fluctuations that occur as the spins overcome their blocking energy barrier and flip with the alternating magnetic field. Colloidal suspensions of superparamagnetic $CoFe_2O_4$ nanoparticles are consequently candidate materials for hyperthermia based cancer treatments.[53]

$CoFe_2O_4$ is also finding use in ferrofluids, where small nanoparticles, stabilised by hydrophobic or hydrophilic molecules, are dispersed in organic solvents or water. The colloidal stability of these nanoparticles enables their manipulation by an external magnetic field, without separation of the nanoparticles from the solvent. Ferrofluids have applications in areas ranging from the electronics industry, where they are used to form liquid seals around the spinning drive shafts in hard disks; to medicine, where they are useful as contrast agents in magnetic resonance imaging (MRI).

The magnetostrictive properties of $CoFe_2O_4$ are also of importance. Materials based on the phenomenon of magnetostriction are used for vibration control and ultrasonic generation and detection, and there is scope for their use in automotive and aerospace applications.[53, 55] Magnetostriction, λ, is defined as the contraction or expansion of a magnetic body in the direction of an applied magnetic field.[56] The mechanism of magnetostriction on a macroscopic level can be separated into two processes. The first is the migration of non-180 º domain walls within the material in response to an external magnetic field, and the second is the rotation of the domains. Both of these

mechanisms mean the material can change the domain orientation and this, in turn, causes a dimensional change. It is measured as the % strain, $\lambda = \delta l/l_0$, where l_0 is the length of the material along a given direction in the un-magnetised state, and δl is the resulting strain. λ can be positive or negative, depending on whether the effect is expansive or compressive. The saturation or engineering magnetostriction constant, λ_s, corresponds to the maximum % strain, and usually appears at the saturation field H_s.[57]

$CoFe_2O_4$ has amongst the highest values for magnetostriction for magnetic oxides[58] and due to this, and the properties and applications discussed earlier, much research has been directed towards the controlled synthesis of $CoFe_2O_4$ nanoparticles in order to maximise their utility.

1.3.2 Synthesis

Sun[59] and Xie[60] have demonstrated the synthesis of oleic acid stabilised controlled size ferrites from their $M(acac)_x$ precursors in a high temperature reflux route, with the latter demonstrating the influence of the solvent and reaction temperature on the final particle size (see Figure 3). While their work primarily detailed the synthesis of Fe_3O_4 nanoparticles, these methods enable the preparation of other monodisperse ferrites including $CoFe_2O_4$ and $MnFe_2O_4$.[60] The high reaction temperature required for the Sun route and the passivation of the nanoparticle surface with long chain oleic acid means other routes are often investigated in order to tailor the properties of the nanoparticles for specific applications.

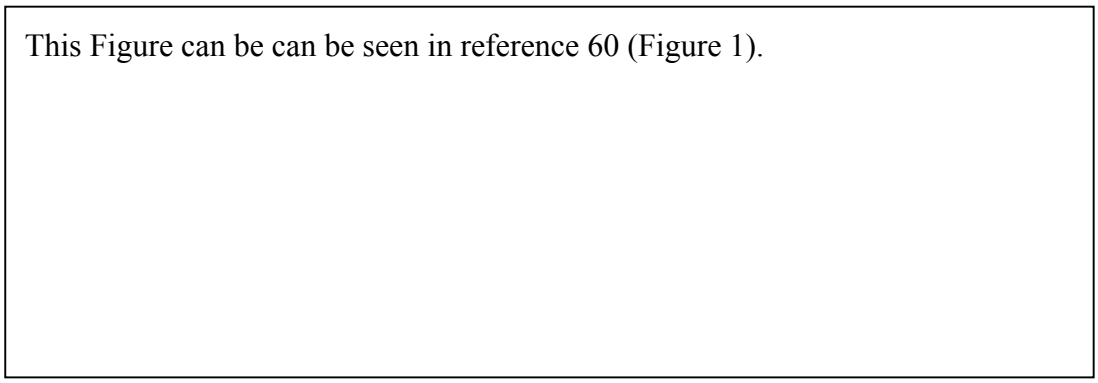

Figure 3. TEM images of oleic acid stabilised $CoFe_2O_4$ nanoparticles prepared by Xie et al.[60] a) 5 nm $CoFe_2O_4$ prepared using 20 mL benzyl ether, b) ~11 nm $CoFe_2O_4$ prepared in 20 mL 1-octadecene, and c) ~14 nm $CoFe_2O_4$ prepared in 10 mL 1-octadecene in the presence of 2 mmol of glucose.

Coprecipitation is a commonly used method for ferrite synthesis as the reactions can be easily scaled to afford gram quantities of nanoparticles at low temperature. Ghosh et al. demonstrated the synthesis of $CoFe_2O_4$ by coprecipitation.[61] This approach involved the aqueous hydrolysis of the metal chloride salts at 80 °C in the presence of the surface stabilising molecules CTAB and *n*-octylamine which act to prevent nanoparticle aggregation and growth. A whole range of other synthetic approaches are used for the synthesis of $CoFe_2O_4$ nanoparticles, and they enable control of the nanoparticle size, morphology, magnetic properties and surface chemistry; these include solvothermal,[38] sol-gel[62] and template[63] based approaches.

1.4 CO Oxidation

Nanoparticles were used as CO oxidation catalysts in the work described in this thesis and they have been used as catalysts in heterogeneous systems since the 19th century.[64] Today, many heterogeneous catalysts contain supported nanoparticles of

the active material in order to optimise their utility, the Cu/ZnO methanol synthesis catalyst is once such example.[65] Nanoparticle catalysts are utilised on a large scale to produce plastics and pharmaceuticals, as well as for environmental applications, such as the removal of NO_x pollutants from vehicle exhausts by noble metal nanoparticle catalysts.[66]

CO oxidation catalysts are much sought after for the removal of CO in vehicle exhaust emissions, respirators and in H_2 rich gas feeds used for fuel cells, amongst other areas.[67-69] CO oxidation is a relatively straightforward reaction; it is irreversible at low temperatures and goes without parallel or secondary reactions, and consequently it is also one of the basic model reactions for heterogeneous catalysts.
CO oxidation over metal oxides is thought to follow the stepwise mechanism first suggested by Mars and van Krevelen in 1954.[70] It occurs in two steps; firstly, CO is oxidised by the surface lattice oxygen atoms in the metal oxide, which leads to the creation of an oxygen vacancy, and this leads to the reduction of the neighbouring metal ions to a lower oxidation state. In the second step the surface metal atoms are re-oxidised by gas phase oxygen. This is illustrated below:

$$CO + O_{cat} \rightarrow CO_{2,ads} + * \quad (1.1)$$

$$CO_{2,ads} \rightarrow CO_2(g) \quad (1.2)$$

$$½O_2 + * \rightarrow O_{cat} \quad (1.3)$$

Where * depicts an oxygen vacancy and O_{cat} is surface lattice oxygen.

As stated, CO oxidation involves the metal ion undergoing changes in oxidation state and so the redox properties of the metal ions are key to the activity of the catalyst.

Transition metal oxides are, consequently, amongst the most studied and active metal oxide CO oxidation catalysts due to their ability to readily change oxidation state.

One presently used CO oxidation catalyst is hopcalite, $CuMn_2O_4$, which was first reported in 1921.[71-73] Hopcalite is an active catalyst at room temperature and at elevated temperatures, though it is known to undergo deactivation under humid conditions.[74] Co_3O_4 is another active metal oxide CO oxidation catalyst. It has also been shown to be active below room temperature[75, 76] in both its supported and unsupported forms though, like hopcalite, it undergoes deactivation in the presence of moisture.

Perhaps the most studied CO oxidation catalysts in recent years have been supported Au nanoparticles. The review by Haruta[77] explored the size and support dependence of the activity of Au nanoparticles in a number of reactions including CO oxidation. Supported Au nanoparticles are highly active CO oxidation catalysts, converting 100% CO to CO_2 below room temperature, though above a critical size of approximately 8 nm Au nanoparticles are inactive.[78, 79] This means they can be prone to deactivation by sintering and are usually considered unsuitable for applications above room temperature. In addition, Au nanoparticles are not active catalysts in the absence of the support, and there has been much investigation into why this is the case, and what the precise role of the support is.[80]

Pirogova et al.[81] demonstrated the potential of ferrites as CO oxidation catalysts. They investigated the temperature dependent activity of materials including bulk $CuFe_2O_4$, $CoFe_2O_4$ and $NiFe_2O_4$, and these showed temperatures of 50% conversion, T_{50}, of 115, 165 and 215 °C respectively. While catalysts with this level of activity would not be suitable for application in respirators they could, for instance, have potential application in catalytic convertors[82] or fuel cells[83, 84] where low temperature

Au nanoparticle catalysts are not suitable due to their deactivation upon sintering.

1.5 $BaTiO_3$

1.5.1 Introduction

Much of the work detailed in this thesis involves nanometric $BaTiO_3$, and what follows is an introduction to its synthesis and properties.

Ferroelectrics were first discovered by Valasek in 1920, though up until 1943 they were thought to be of little practical application due to their water solubility and fragility. That was changed by the discovery of $BaTiO_3$.[85] The structural simplicity of $BaTiO_3$ encouraged theoretical work and its physical properties ultimately helped lead to the creation of the electronic ceramics industry.

Because of the high cost of single crystals, ferroelectric devices were initially limited to bulk ceramics. They found application as piezoelectric transducers, actuators and for pyroelectric detectors. However, there was a change of focus following the integration of ferroelectric thin-films into semiconductor chips,[86] and it was in the form of integrated ferroelectrics that the renaissance of ferroelectric materials occurred.

Ferroelectrics are materials whose intrinsic lattice polarisation P can be reversed through the application of an external electric field E that is greater than the coercive field E_c. They tend to possess a phase-transition, or Curie temperature T_c, above which they are paraelectric. All ferroelectrics are also pyroelectric (though the reverse is not true), and all pyroelectrics are piezoelectric. Ferroelectrics cannot possess a centre of symmetry and most ferroelectric families are not oxides, though these are most studied class because of their robustness and practical applications.[87]

There are, at present, a number of directions for ferroelectrics research. These include studying their synthesis in nanowire and nanotube morphologies, investigating their finite size effects and their use in magnetoelectric composites, as well as researching their application in areas such as in ferroelectric random access memories (FeRAMs).[88]

1.5.2 Structure and Application of $BaTiO_3$

Barium titanate ($BaTiO_3$) is a ferroelectric oxide with the perovskite structure that undergoes a transition from a ferroelectric tetragonal phase to a paraelectric cubic phase upon heating above 130 °C. In the cubic phase, the structure of which is displayed in Figure 4a, titanium atoms are octahedrally coordinated by six oxygen atoms.

This Figure can be seen in reference 89 (Figure 1).

Figure 4. The structure of barium titanate, $BaTiO_3$ in a) the paraelectric cubic form, space group *Pm-3m* and b) the ferroelectric tetragonal form, space group *P4mm*.[89]

Ferroelectricity arises in tetragonal $BaTiO_3$ due to an average relative displacement along the *c*-axis of titanium from its centrosymmetric position in the unit cell, and

consequently the creation of a permanent electric dipole. The tetragonal unit cell is shown in Figure 4b. The elongation of the unit cell along the *c*-axis and the deviation of the *c*/*a* ratio from unity can be used as an indication of the presence of the ferroelectric phase.[90-92] Its ferroelectric properties and high dielectric constant make $BaTiO_3$ useful in an array of applications such as in multilayer ceramic capacitors, gate dielectrics, waveguide modulators, IR detectors, and holographic memory.[93]

1.5.3 Size-Property Relationship

The dielectric and ferroelectric properties of $BaTiO_3$ are known to correlate with size, and the technological trend toward decreasing dimensions means this correlation has been closely examined at the nanoscale,[94, 95] with the ferroelectric phase observed to become unstable at room temperature when particle diameter decreases below a critical size. This critical size is sensitive to a number of parameters including: composition, strain, lattice defects, and surface charge.[96]

Due to the differences in the cell parameters of the tetragonal and cubic phases being small compared to the broadening on the XRD peaks, which occurs as a result of the small particle size, there is likely an overestimation of the critical size from diffraction studies. *Fong et al*. performed work on the perovskite $PbTiO_3$ showed that ferroelectric behaviour persists down to a thickness of only three unit cells,[97] a value significantly less than previously suggested. However, with ferroelectrics being particularly sensitive to surface effects, modelling becomes increasingly complicated as dimensions are reduced. Spanier *et al*. have also found, by theoretical modelling, that certain surface termination of thin films can stabilise polarisation down to a thickness of only several unit cells, and they estimate the critical size for a

$BaTiO_3$ sphere to be 4.2 nm.[96] X-ray diffraction (XRD) studies are consistent with an increasingly cubic structure at smaller particle sizes, not distinguishing between average and local structure,[98] and Raman results have supported the existence of tetragonal symmetry at small dimensions, even when the XRD was unable to detect it.[99]

The dielectric and piezoelectric constants are also strongly size-dependent and vary with the same parameters discussed for the size-structure relationship (composition, lattice defects, surface charge). While the piezoelectric properties tend to diminish with particle size, Wada *et al.*[89] have recently demonstrated the preparation of $BaTiO_3$ particles with very few lattice hydroxyl groups *via* a two-step thermal decomposition method from barium titanyl oxalate. The dielectric constant of the impurity-free $BaTiO_3$ fine particles increases with their decreasing size in the range from 430 to 140 nm but decreases from 140 to 40 nm.

1.5.4 Synthesis

Many strategies have been deployed for the synthesis of well-defined nanometric $BaTiO_3$. Hou *et al*.[100] recently demonstrated the solvothermal synthesis of cube-like $BaTiO_3$ nanoparticles on the order of 50 nm, while Kang *et al.* have demonstrated the synthesis of well-defined nanowires from the ion-exchange reaction between $K_2Ti_4O_9$ nanostructures and barium hydroxide.[45] Finally, Niederberger *et al.* reported a solvothermal preparation of 5 nm particles of $BaTiO_3$ and $SrTiO_3$ from titanium isopropoxide and metallic barium or strontium in benzyl alcohol,[101] with TEM images of these $BaTiO_3$ particles shown in Figure 5 below.

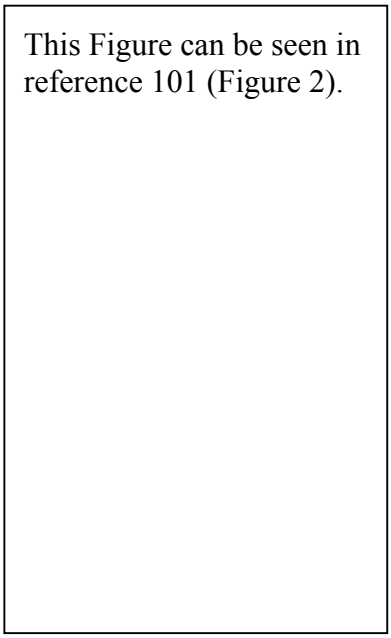

Figure 5. TEM images of 5 nm $BaTiO_3$ nanoparticles prepared by Niederberger *et al*. a) An overview image a showing non-aggregated $BaTiO_3$ nanoparticles; b) selected area electron diffraction (SAED) and c), d) high resolution TEM images of isolated $BaTiO_3$ nanocrystals.[101]

1.6 Nanoparticle Functionalisation

Chemical functionalisation of the external surfaces of nanoparticles enables modification of properties including the charge, functionality, reactivity, stability and dispersibility,[102, 103] and this is explored in some the work described in this thesis. Functionalisation can also be used to provide nanoparticles with magnetic, optical or catalytic properties.[104, 105] The controlled coating of nanoparticles with organised layers is technically challenging due to the possibility of the functionalised nanoparticles agglomerating with one another, thus limiting their utility. There has, however, been considerable progress in recent years in the development of

nanoparticles functionalised with polymers, biomolecules and small organic and inorganic functionalities.

Polymer coated nanoparticles have found application in the manufacture of inks and paints,[105] and in biological applications where they have been used to enhance the biocompatibility of nanoparticles.[106] This type of functionalisation is performed either by polymerisation on the particle surface,[107] or *via* adsorption of polymers to the surface.[108] The former has been illustrated by the preparation of poly(pyrrole) coatings on α-Fe_2O_3 and CeO_2. This was performed by using the oxide surface species to drive the polymerisation of pyrrole on the particle surface, and these functionalised nanoparticles were found to be electrically conductive.[109] An example of the adsorption of polymer layers onto the particle surface is the preparation of polymer-stabilised Ag nanoparticles, where the encapsulation of individual Ag nanoparticles was demonstrated with polystyrene and methacyrlate.[110] The disadvantage of this method is the potential for nanoparticle aggregation inside the polymer matrix.

Particles that are functionalised with biomolecules can be engendered with the ability to target specific cells, antigens or virus molecules. They can also have prolonged circulation in the blood and be used for intercellular drug-delivery.[103] The most common method involves non-covalent binding of the biomolecules to the particle surface, for instance through electrostatic interactions. Bovine serum albumin (BSA) and immunoglobulin G (IgG) have been deposited on polystyrene microspheres by the alternate deposition of the protein and oppositely charged polymer.[111]

Small organic and inorganic molecules can also be used to functionalise nanoparticle surfaces. Generally, these are adhered to the surface of pre-formed nanoparticles by precipitation or surface reactions. Core-shell nanoparticles can be prepared by the

precipitation of tetraethoxysilane (TEOS) on the nanoparticle surface.[112] Surface reactions enable species such as silane molecules to be chemically grafted to metal oxide nanoparticle surfaces *via* the formation of M-O-Si bonds, and this type of functionalisation has been applied to Fe_3O_4 nanoparticles.[113] De Palma *et al*.[114] illustrated the anchoring of a whole host of functional silane molecules to the surface of Fe_3O_4 *via* a ligand exchange reaction, where the electrostatically bound oleic acid functionalities were replaced by chemically bound silane molecules. This enabled modification of the nanoparticles solubility and other properties, with the goal of enhancing the nanoparticles biocompatibility whilst taking advantage of the monodispersity that large stabilising molecules such as oleic acid can provide. Chemical binding of functional molecules to oxide nanoparticle surfaces is not limited to silanes, though these are the most studied materials at present. Kim *et al*.[102] and others[115] have demonstrated the anchoring of phosphonic acid molecules using the same principle, though in this case weaker M-O-P bonds are formed between the functional organic molecules and the nanoparticle surfaces. This has potential application in the preparation of new dielectric materials with high permittivity and dielectric strength, for application in capacitors amongst other areas.[102]

1.7 Nanoparticle Assembly

The assembly of different phases of nanoparticles with one another is discussed in this thesis, and leads to the generation of arrays with combinations of interacting properties.[116-120] For example, binary nanoparticle superlattices (BNSLs) can be prepared from mixtures of nanoparticles that are size-controlled in such a manner

that promotes the formation of structures with, for instance, face centred cubic (fcc) ordering and such chemistry has been applied to the synthesis of Au–αFe_2O_3 and Au–PbSe nanoparticle arrays[121] and structures including Pd, Ag and γ-Fe_2O_3.[122] TEM images of a selection of these structures can be seen in Figure 6.

This Figure can be seen in reference 122 (Figure 1).

Figure 6. TEM images of BNSLs assembled from different nanoparticles, and modelled unit cells of the corresponding three-dimensional structures. The superlattices are assembled from a) 13.4 nm γ-Fe_2O_3 and 5 nm Au; b) 7.6 nm PbSe and 5 nm Au; c) 6.2 nm PbSe and 3.0 nm Pd.[122]

The formation of BNSLs can be driven by a number of forces including purely by entropy;[123] though in some cases, where entropy alone is not thought to be sufficient, Coulomb, van der Waals, charge-dipole and dipole-dipole interactions are thought to play a role.[121]

Chemical functionalisation of the external surfaces of nanoparticles also allows for the assembly of multiple phase arrays and this approach is not particle size limited, as is the case for the BNSLs.[124, 125] Galow *et al*. have demonstrated the assembly of Au–SiO_2 aggregates *via* electrostatic interactions between the functionalised, positively charged SiO_2 nanoparticles and the functionalised, negatively charged

Au.[117] This is illustrated in Scheme 1 below. The authors used an aminosilane to engender the SiO_2 nanoparticles with terminal amine functionalities, while a bi-functional thiol, 11-mercaptodecanoic acid, was used to provide carboxylic acid functionalities on the Au nanoparticle surfaces.

This Scheme can be seen in reference 117 (Scheme 1).

Scheme 1. An illustration of carboxylic acid functionalised Au **1** reacting with amine functionalised SiO_2 **2** to produce, depending on the ratio in which they are mixed, Au-SiO_2 assemblies **3** and **4**.[117]

Bi-functional thiolates are commonly used for the assembly of noble metal nanoparticles. Sendroiu *et al*. demonstrated the assembly of Ag and Au nanoparticles using thiol functionalised nanoparticles and a Co(II) complex,[124] while Mirkin *et al.* assembled Au nanoparticles using complementary strands of DNA, tethered to the nanoparticle surface though thiol linkages.[126]

The assembly of nanostructures is not limited to the spherical nanoparticles. In their

work, Rycenga *et al*.[127] demonstrated the assembly of Ag nanocubes. This was achieved by the selective functionalisation of the cube faces with either hydrophobic or hydrophilic functionalities. This approach enabled the authors to prepare a range of different nanostructures and an extended three-dimensional microstructure, depending on which faces of the nanocubes were functionalised.

The synthesis of metal oxide nanoparticle assemblies is challenging due to the functionalisation chemistry being less well developed than for Au and Ag nanoparticles, for which an array of bi-functional thiolates are commercially available.[128] In one example, a purely complex metal oxide nanoparticle assembly was been demonstrated by Mornet *et al*.[119] They used electrostatic assembly to prepare $BaTiO_3$/PZT – γFe_2O_3 hybrids, a TEM image of which can be seen in Figure 7.

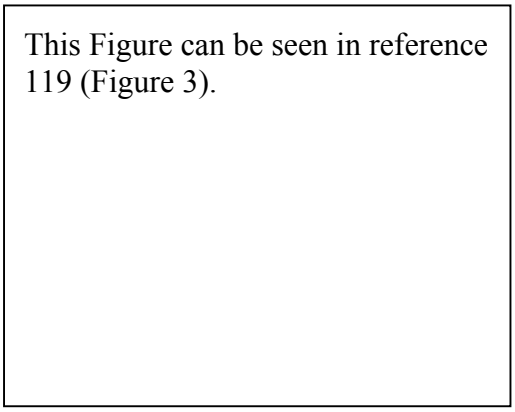

Figure 7. TEM image of a 'nano-raspberry' prepared from $BaTiO_3@SiO_2$ core surrounded by γ-$Fe_2O_3@SiO_2$ nanoparticles.[119]

In this instance the authors used aminosilane functionalised $BaTiO_3@SiO_2$ or $PZT@SiO_2$ nanoparticles and assembled them with γ-$Fe_2O_3@SiO_2$. The partial positive charge on the former interacted with the partial negative charge of the latter

to produce the afore mentioned assemblies.

1.8 Multiferroics and Magnetoelectrics

1.8.1 Introduction

Magnetoelectric composites were prepared in the work described in this thesis, and what follows is an introduction to multiferroics and magnetoelectric materials.

The original definition of a single-phase multiferroic material was one in which two or more of the 'ferroic' properties: ferroelectricity, ferromagnetism and ferroelasticity existed, though this definition has since been expanded to include the possibility of materials possessing ferrotoroidicity. Single-phase materials in which ferromagnetism and ferroelectricity arise independently remain rare. The reason for this was discussed by Hill *et al*., who found that conditions required for the coexistence of ferroelectricity and ferromagnetism in single phase materials are rarely met.[129] Cation off-centring in ferroelectrics (which requires formally empty d-orbitals) and the formation of magnetic moments (which usually requires partially filled d-orbitals)[129, 130] mean that, for ferroelectricity and magnetism to coexist in a single phase, the atoms that move off centre to form the electric dipole must be different to those carrying the magnetic moment. This can only be achieved though a non-d-electron mechanism for magnetism, or though an alternative mechanism for ferroelectricity, with the latter pursued for the synthesis of a new generation of single-phase multiferroics.

Magnetoelectric (ME) coupling describes the influence that an applied magnetic (or electric) field has on the polarisation (or magnetisation) of a material. In ME

materials, it is possible to generate an electric polarisation *via* the application of an external magnetic field, or vice versa. ME coupling may exist whatever the nature of the magnetic and electrical order parameters, and has been observed in paramagnetic ferroelectrics,[131] though the effect does require the phase(s) to be both electrically and magnetically polarisable. The overlap between multiferroic and magnetoelectric materials is illustrated in Figure 8.

This Figure can be seen in reference 132 (Figure 1).

Figure 8. The relationship between multiferroic and magnetoelectric materials. The red intersection represents materials that are multiferroic, while magnetoelectric coupling is an independent phenomenon that can, but need not, arise in any of the materials that are both magnetically and electrically polarisable. In practice, it is likely to arise in all such materials, either directly or *via* strain.[132]

ME coupling may arise directly between the two order parameters, or in materials where the magnetic and electrical order parameters exist in separate but intimately connected phases; which enables strain-mediated indirect ME coupling to occur.[132]

ME materials have potential application in electronic devices such as transducers, magnetic field sensors and in the information storage industry. One target regards their deployment in the development of multiple-state memory devices, where data could be written electrically, and, owing to the coupling of the electric and magnetic parameters, read magnetically. It relies on the reversal of the magnetisation by the application of a magnetic field (or vice versa), which is termed magnetoelectric switching, and this is potentially attractive as it would enable exploitation of the best aspects of ferroelectric random access memory (writing) and magnetic data storage (reading), while avoiding the problems associated with reading FeRAM and generating large local magnetic fields needed to write magnetically. However, there is still work to be done in preparing the magnetoelectric materials that could make a major contribution to the data storage industry, therefore, in the short term, niche applications of magnetoelectric materials are likely to emerge, such as in sensors, microwave devices and transducers.[132]

As previously stated, single-phase multiferroics and magnetoelectrics are rare, however two-phase systems of, for example, ferroelectric and ferromagnetic materials can also possess magnetoelectric properties *via* strain-coupling of the two orders. ME composites were dealt with in detail by Nan *et al*. in their recent review.[133] The advantages of ME composites over their single-phase counterparts include greater design flexibility, and the potential for larger ME coefficients, with the best ME composites possessing ME coefficients several times larger than those observed in single-phase materials.[134]

Much research has been done on ME composites over recent years due to the technologically viable response observed for some of these materials above room temperature. Developed materials include bulk ceramic composites of piezoelectrics

and ferrites,[135, 136] two-phase composites of magnetic alloys and piezoelectrics[137, 138] and nanostructured thin films.[139, 140]

ME composites are generally described in terms of the connectivity of the phases, a concept which was introduced by Newnham *et al.*[141] The connectivity of three of the most common types of bulk ME composite are shown in Figure 9 below. For instance, the connectivity type noted as 0-3 indicates a composite of particles (0) embedded in a matrix of another phase (3).

This Figure can be seen in reference 133 (Figure 1).

Figure 9. Illustration of bulk ME composites with three of the most common connectivity schemes: 0-3 particulate composite (left), 2-2 laminate composite (centre) and 1-3 fibre/rod composite (right).[133]

The magnetoelectric coupling can be measured indirectly by recording changes in the magnetisation at or near the Curie temperature of the ferroelectric material, or changes in the dielectric constant near a magnetic transition temperature. The resulting effects are termed the magnetocapacitance and magnetodielectric response. However, while more challenging, it is much more useful perform direct measurements where, for example, the electrical response to an applied magnetic field, or the magnetic response to an applied electric field is measured. When the

voltage is measured using the former technique, empirical coupling coefficients, termed α_E are obtained and the magnitude of α_E is often used when comparing materials with one another.[133]

1.8.2 Bulk Ceramic Magnetoelectric Composites

What follows is an introduction to bulk ceramic ME composites, and these materials have been prepared with 0-3 and 2-2 type connectivities. The discussion is centred on materials where a piezoelectric phase such as $BaTiO_3$ or PZT is mixed with a ferromagnetic phase, such as $CoFe_2O_4$, as it is these types of materials that are developed and discussed in this thesis.

The original work on the *in situ* formation of the ME ceramic composites was performed at Philips Laboratories,[142-144] were a magnetoelectric coefficient, α_E, of 50 mV cm^{-1} Oe^{-1} was measured for a composite prepared *via* the unidirectional solidification of a eutectic composition of the quinary system Fe–Co–Ti–Ba–O. Subsequent work on a eutectic composition of $BaTiO_3$–$CoFe_2O_4$ prepared by unidirectional solidification lead to an increase of α_E to 130 mV cm^{-1} Oe^{-1}.

Unidirectional solidification requires precise control over composition, and this can be difficult, especially when one of the components is a gas (oxygen). Consequently the majority of research was targeted at the development of ME ceramic composites *via* sintering, which is both an easier and cheaper method for the fabrication of ceramic ME composites of piezoelectrics and ferrites.

In the early 1990s much work was done on the preparation of particulate ceramic composites (materials comprised of piezoelectric and ferromagnetic particles) of BTO or PZT and ferrites *via* the sintering approach. The ME coefficients of these

particulate composite ceramics were considered small at around 1 mV cm^{-1} Oe^{-1} orders of magnitude.[145, 146] However, by controlling the relative amounts of the ferroelectric and ferromagnetic phases, using ferroelectric and ferromagnetic phases with the most favourable properties (such as ferroelectrics with high piezoelectric constants, and ferromagnetic materials with large magnetisations and magnetostriction) and using sintering temperatures and times that optimised the density and phase purity, coefficients of around 10–100 mV cm^{-1} Oe^{-1} were eventually obtained.[147]

The magnitude of α_E was found to be strongly dependent on the sample sintering temperature. Work by Ryu *et al.* demonstrated this,[147] with the authors showing the properties of PZT/$NiFe_2O_4$ composites with respect to sample composition and sintering temperature. A ME coefficient of 115 mV cm^{-1} Oe^{-1} was reported, and the large ME coefficient was attributed to a homogeneous and well-dispersed microstructure, and the large grain size of the matrix PZT phase.

So far, it has proven difficult to match the values of α_E predicted by theoretical calculations with the experimental results. This is thought to be partly due to inter-diffusion between the piezoelectric and ferrite phases during the high-temperature sintering step, which leads to the formation of unwanted phases; and to thermal expansion mismatch between the two phases, which harms the densification process and leads to microcracks forming within the sample during sintering. The low-resistivity ferrite phase also tends to reduce the efficiency of the necessary electrical polarisation of the ferroelectric phase, and leads to leakage of the piezoelectrically stored charge. All of these factors mean it has not been possible to observe the large ME coefficients predicted for materials with a larger than 0.5 mole fraction of ferrite.[133, 147]

Recently, hot pressing[148] and spark plasma sintering[149] (SPS) have been employed to address the inter-diffusion problem. The short time and low temperature required for densification during SPS reduces the chance for unwanted phases to form, and hot-pressed and SPS processed samples have been found to display an increased α_E when compared to the conventionally sintered samples. For example, PZT/$NiFe_2O_4$ composite ceramics with densities of 99% of the theoretical maximum have been prepared using SPS,[149] and these materials have improved ME coefficients (~ 26 mV cm^{-1} Oe^{-1}) when compared analogous ceramics prepared *via* traditional sintering techniques (~ 18 mV cm^{-1} Oe^{-1}).

The leakage problem due to the low resistivity ferrite in the 0-3 and 1-3 type composite ceramics can be eliminated in 2-2 laminate composite ceramics. They are generally prepared by co-firing piezoelectric and ferrite layers at high temperature, with a ME coefficient of 400 mV cm^{-1} Oe^{-1} measured for a PZT/$NiFe_2O_4$ layered composite.[150, 151]

1.8.3 Nanostructured Thin Films

Nanostructured composite thin films of ferroelectric and magnetic oxides have recently been prepared by pulsed laser deposition (PLD),[139] spin coating and sol-gel methods. Nanostructuring enables greater control of the interface between the FE and FM components. It also enables the physical mechanism of the ME coupling effect to be examined at the nanoscale, and could lead to the application of ME materials in microelectronic devices.

Zheng *et al*. used PLD to synthesise composites of $BaTiO_3$ and $CoFe_2O_4$ with the 2-2 and 1-3 connectivities[139] and diagrammatic representations of these can be seen in

Figure 10. In the case of the 1-3 composite, 20-30 nm rods of $CoFe_2O_4$ were embedded into a $BaTiO_3$ matrix. The generation of large ME coefficients is believed to be possible in systems with this type of connectivity, and this was recently demonstrated though switching of the magnetisation on reversal of the ferroelectric polarisation,[152] which was attributed to efficient strain coupling resulting from the large interfacial surface area. However, whilst ME coupling has been observed in these systems *via* microscopy,[153] ME coefficients have not been directly measured because of the leakage resulting from the low resistance ferrite rods penetrating though the film. Consequently, much work remains to be done to exploit the large ME coupling that these systems possess.

This Figure can be seen in reference 139 (Figure 1).

Figure 10. a) Superlattice of a spinel (top) and a perovskite (middle) on a perovskite substrate (bottom). b) Schematic illustration of a multilayer 2-2 structure on a substrate. c) Epitaxial alignment of a spinel (top left) and a perovskite (top right) on a perovskite substrate (bottom). d) Schematic illustration of a self assembled 1-3 nanostructured thin film formed on the substrate.[139]

1.9 Aims of This Thesis

The first aim of this thesis was to prepare controlled size $CoFe_2O_4$ nanoparticles and investigate their activity as CO oxidation catalysts, in the knowledge that $CoFe_2O_4$ had been shown to be a promising catalyst by Pirogova et al.[81] It was thought that a reduction in the nanoparticle size could lead to the enhancement of the catalyst activity, and so a synthetic protocol for the preparation of $CoFe_2O_4$ nanoparticles with a range of controlled sizes was to be developed prior to testing their activity. The second aim was to investigate the formation of functional hybrid nanostructures between metal oxide nanoparticles of the ferromagnetic/superparamagnetic $CoFe_2O_4$ and the ferroelectric $BaTiO_3$, and in doing so, to provide a general approach by which nanoparticle oxides could be functionalised and assembled with one another to form multifunctional nanomaterials. The small amount of literature on the assembly of metal oxide nanoparticles, and the potential applications for mixed metal oxide nanoparticle hybrids drove this aspect of the work. The third aim was to utilise this nanoparticle assembly chemistry to develop magnetoelectric composites of $BaTiO_3$ and $CoFe_2O_4$ nanoparticles. The potential for larger interfaces between the ferroelectric and ferromagnetic phases in these materials than in those prepared *via* the traditional grinding and firing approach could potentially produce larger magnetoelectric effects, and be a step towards the making the widespread use of magnetoelectric materials a reality.

References

1. H-G. Rubahn, *Basics of Nanotechnology, Wiley VCH, Berlin*, **2008**.

2. J. P. Srivastava, *Elements of Solid State Physics, PHI Learning LTD.,* **2006**.

3. Y. Gogotai, *Nanomaterials Handbook, CRC Press,* **2006**.

4. J. Park, J. Joo, S. G. Kwon, Y. Jang, T. Hyeon, *Angew. Chem. Int. Ed.* **2007**, 46, 4630.

5. D. L. Huber, E. L. Venturini, J. E. Martin, P. P. Provencio, R. J. Patel, *J. Magn. Magn. Mater.* **2004**, 278, 311.

6. X. Wang, J. Zhuang, Q. Peng, Y. Li, *Nature* **2005**, 437, 121.

7. F-Y. Cheng, C-H. Su, Y-S. Yang, C-S. Yeh, C-Y. Tsai, C-L. Wu, M-T. Wu, D-B. Sheih, *Biomaterials* **2005**, 26, 729.

8. Y. Xie, C. Yuan, *Appl. Cat. B.* **2003**, 46, 251.

9. H. Herrig, R. Hempelmann, *Mater. Lett.* **1996**, 27, 287.

10. T. J. Daou, G. Pourroy, S. Bégin-Colin, J. M. Grenèche, C. Ulhaq-Bouillet, P. Legaré, P. Bernhardt, C. Leuvrey, G. Rogez, *Chem. Mater.* **2006**, 18, 4399.

11. X-M. Zhao, Y. Xia, G. M. Whitesides, *J. Mater. Chem.* **1997**, 7, 1069.

12. H. Cao, Z. Yu, J. Wang, J. O. Tegenfeldt, R. H. Austin, E. Chen, W. Wu, S. Y. Chou, *Appl. Phys. Lett.* **2002**, 81, 174.

13. A. Zaluska, L. Zaluski, J. O. Ström-Olsen, *J. Alloys Compd.* **1999**, 288, 217.

14. Y. A. Kim, T. Hayashi, Y. Fukai, M. Endo, T. Yanagisawa, M. S. Dresselhaus, *Chem. Phys. Lett.* **2002**, 355, 279.

15. Y. Sun, Y. Xia, *Science* **2002**, 298, 2176.

16. S. H. Joo, S. J. Choi, I. Oh, J. Kwak, Z. Liu, O. Terasaki, R. Ryoo, *Nature* **2001**, 412, 169.

17. J. L. Mohanan, I. U. Arachchige, S. L. Brock, *Science* **2005**, 307, 397.

18. N. L. Pickett, P. O'Brien, *Chem. Rec.* **2001**, 1, 467.

19. K. L. Stamm, J. C. Garno, G. Liu, S. L. Brock, *J. Am. Chem. Soc.* **2003**, 125, 4038.

20. J. F. Janik, *Powder Tech.* **2005**, 152, 118.

21. P. Banerjee, B. M. Mandal, *Macromolecules* **1995**, 28, 3940.

22. M. S. Cho, S. Y. Park, J. I. Huang, H. J. Choi, *Mater. Sci. Engi.* **2004**, 24, 15.

23. C. N. R. Rao, S. R. C. Vivekchand, K. Biswas, A. Govindaraj, *Dalton Trans.* **2007**, 3728.

24. A. L. Rogach, D. V. Talapin, E. V. Shevchenko, A. Kornowski, M. Haase, H. Weller, *Adv. Funct. Mater*. **2002**, 12, 653.

25. T. Hyeon, *Chem. Commun.* **2003**, 8, 927.

26. S. Sun, C. B. Murray, D. Weller, L. Folks and A. Moser, *Science* **2000**, 287, 1989.

27. J. Joo, T. Yu, Y. W. Kim, H. M. Park, F. Wu, J. Z. Zhang, T. Hyeon, *J. Am. Chem. Soc.* **2003**, 125, 6553.

28. T. J. Trentler, T. E. Denler, J. F. Bertone, A. Agrawal, V. L. Colvin, *J. Am. Chem. Soc.* **1999**, 121, 1613.

29. M. Yin, S. O. Brien, *J. Am. Chem. Soc.* **2003**, 125, 10 180.

30. Y. Mao, T-J. Park, S. S. Wong, *Chem. Commun.* **2005**, 46, 5721.

31. A. S. Albuquerque J. D. Ardisson, W. A. Macedo, *J. Appl. Phys.* **2000**, 87, 4352.

32. Y. Du, J. Fang, M. Zhang, J. Hong, Z. Yin Q. Zhang, *Mater. Lett.* **2002**, 57, 802.

33. J. F. Wang, C. B. Ponton, I.R. Harris, *J. Magn. Magn. Mater.* **2002**, 242, 1464.

34. Y. Gu, G-Z. Li, G. Meng, D. Peng, *Mater. Res. Bull.* **2000**, 35, 297.

35. D. Rangappa, T. Naka, A. Kondo, M. Ishii, T. Kobayashi, T. Adschiri, *J. Am. Ceram. Soc.* **2007**, 129, 11061.

36. L. Armaleo, G. Bandoli, D. Barreca, M. Bettinelli, G. Bottaro, A. Caneschi, *Surf. Interface Anal.* **2002**, 34, 112.

37. S. Thimmaiah, M. Rajamathi, N. Singh, P. Bera, F. Meldrum, N. Chandrasekhar, R. Seshadri, *J. Mater. Chem*. **2001**, 11, 3215.

38. U. K. Gautam, M. Ghosh, M. Rajamathi, R. Seshadri, *Pure Appl. Chem.* **2002**, 74, 1643.

39. J. F. Bocquet, K. Chhor, C. Pommier, *Mater. Chem. Phys.* **1999**, 57, 273.

40. B. L. Cushing, V. L. Kolesnichenko, C. J. O'Connor, *Chem. Rev.* **2004**, 104, 3893.

41. K. Ryu, D. Zhang, C. Zhou, *Appl. Phys. Lett.* **2008**, 92, 093111.

42. Y. Xia, P. Yang, Y. Sun, Y. Wu, B. Mayers, B. Gates, Y. Yin, F. Kim, H. Yan, *Adv. Mater.* **2003**, 15, 353.

43. I. I. Naumov, L. Bellaiche, H. Fu, *Nature* **2004**, 432, 737.

44. C. Liu, B. Zou, A. J. Rondinone, Z. J. Zhang, *J. Am. Chem. Soc.* **2001**, 123, 4344.

45. S-O. Kang, B. H. Park, Y-I Kim, *Cryst. Growth Des.* **2008**, 8, 3180.

46. L. J. E. Hofer, E. M. Cohn, *J. Am. Chem. Soc.* **1958**, 81, 1576.

47. C. A. Harper, *Electronic Materials and Processes Handbook, McGraw-Hill Professional* **2003**.

48. A. Chtchelkanova, S. A. Wolf, Y. Idzerda, *Magnetic Interactions and Spin Transport*, *Springer* **2003**.

49. A-H. Lu, E. L. Salabas, F. Schüth, *Angew. Chem. Int. Ed.* **2007**, 46, 1222.

50. C. N. R. Rao, J. Gopalakrishnan, *New Directions in Solid State Chemistry*, *Cambridge University Press*, **1997**, 296.

51. C. Liu, B. S. Zou, A. J. Rondinone, J. Zhang, *J. Am. Chem. Soc.* **2000**, 122, 6263.

52. A. J. Baden Fuller, *Ferrites at Microwave Frequencies, IET* **1987**.

53. J. P. Fortin, C. Wilhelm, J. Servais, C. Menager, J. C. Bacri, F. Gazeau, *J. Am. Chem. Soc.* **2007**, 129, 2628.

54. S. D. Bhame, P. A. Joy, *J. Appl. Phys.* **2006**, 100, 113911.

55. E. Hristoforou, A. Ktena, *J. Magn. Magn. Mater.* **2007**, 316, 372.

56. E. du Tremolet de Lacheisserie, *Magnetostriction: Theory and Applications of Magnetoelasticity, CRC Press, Boca Raton, FL,* **1994**.

57. A.P. Thomas, M.R.J. Gibbs, J.H. Vincent, S.J. Ritchie, *IEEE Trans. Magn*. **1991**, 5247.

58. S. D. Bhame, P. A. Joy, *J. Appl. Phys. D* **2007**, 40, 3263.

59. S. Sun, H. Zeng, D. B. Robinson, S. Rioux, P. M. Rice, S. X. Wang, G. Li, *J. Am. Chem. Soc.* **2003**, 126, 273.

60. J. Xie, S. Peng, N. Brower, N. Pourmand, S. X. Wang, S. Sun, *Pure Appl Chem.* **2006**, 78, 1003.

61. M. Ghosh, G. Lawes, A. Gayen, G. N. Subbana, W. M. Reiff, M. A. Subramanian, A. P. Ramirez, J-P. Zhang, R. Seshadri, *Chem. Mater.* **2004**, 16, 118.

62. G. Ji, S. Tang, B. Xu, B. Gu, Y. Du, *Chem. Phys. Lett.* **2003**, 379, 484.

63. C. Pham-Huu, N. Keller, C. Estournès, G. Ehret, M. J. Ledoux, *Chem. Commun.* **2002**, 17, 1882.

64. J. D. Aitken, R. G. Finke, *J. Mol. Catal. A* **1999**, 145, 1.

65. S. Schur, B. Bems, A. Dessenoy, I. Kassatkine, J. Urban, H. Wilmes, O. Hinrichsen, M. Muhler, R. Schlögl, *Angew. Chem. Int. Ed.* **2003**, 42, 3815.

66. M. Bowker, *Nat. Mater.* **2002**, 1, 205.

67. S. Y. Chin, O. S. Alexeev, M. D. Amiridis, Appl. Catal. A **2005**, 286, 157.

68. G. Avgouropoulos, T. Ioannides, Ch. Papadopoulou, J. Batista, S. Hocevar, H. K. Matralis, *Catal. Today* **2002**, 75, 157.

69. C-H. Tu, A-Q. Wang, M-Y Zheng, T. Zheng, *Appl. Catal. A* **2006**, 297, 40.

70. P. Mars, D. W. van Krevelen, *Chem. Eng. Sci. Spec. Suppl.* **1954,** 41, 3.

71. T. H. Rogers, C. S. Piggot, W. H. Bahlke and J. M. Jennings, *J. Am. Chem. Soc.* **1921**, 43, 1973.

72. H. A. Jones and H. S. Taylor, *J. Phys. Chem.* **1923**, 27, 623.

73. G. J. Hutchings, A. A. Mirzaei, R. W. Joyner, M. R. H. Siddiqui and S. H. Taylor, *Appl. Catal. A Gen*. **1998**, 166, 143.

74. J. W. Saalfrank, W. F. Maier, *C. R. Chemie* **2004**, 7, 483.

75. P. Thormählen, M. Skoglundh, E. Fridell, B. Andersson, *J. Catal.* **1999**, 188, 300.

76. D. A. H. Cunningham, T. Kobayashi, N. Kamijo, M. Haruta, *Catal. Lett.* **1994**, 25, 257.

77. M. Haruta, *Catal. Today* **1997**, 36, 153.

78. C. T. Campbell, *Science* **2004**, 306, 234.

79. M. C. Kung, R. J. Davis and H. H. Kung, *J. Phys. Chem. C.* **2007**, 111, 11767.

80. G. J. Hutchings, *Catal. Today* **2005**, 100, 55.

81. G. N. Pirogova, N. M. Panich, R. I. Korosteleva, Y. V. Voronin, G. E. Kalinina, *Russ. Chem. Bull.* **1996**, 45, 42.

82. Y. Nishihata, J. Mizuki, T. Akao, H. Tanaka, M. Uenishi, M. Kimura, T. Okamoto, N. Hamada, *Nature* **2002**, 418, 164.

83. A. Wang, Y-P. Hsieh, Y-F. Chen, C-Y. Mou, *J. Catal.* **2006**, 237, 197.

84. A. Manasilp, E. Gulari, *Appl. Catal. B* **2002**, 37, 17.

85. A. von Hippel, *U.S. National Defense Research Committee Report 300*, NDRC, Boston, MA, **1944**.

86. J. F. Scott, C. A. Araujo, *Science* **1989,** 246, 1400.

87. D. Damjanovic, *Rep. Prog. Phys.* **1998**, 61, 1267.

88. A. Schilling, D. Byrne, G. Catalan, K. G. Webber, Y. A. Geneko, G. S. Wu, J. F. Scott, J. M. Gregg, *Nano Lett.* **2009**, 9, 3359.

89. M. Yashima, T. Hoshina, D. Ishimura, S. Kobayashi, W. Nakamura, T. Tsurumi, S. Wada, *J. Appl. Phys.* **2005**, 98, 014313.

90. B. Jaffe, W. R. Cook, H. Jaffe, *Piezoelectric Ceramics, Vol 3; Academic Press: New York,* **1971.**

91. M. E. Lines, A. M. Glass, Principles and Applications of Ferroelectrics and Related Materials; Claredon Press: Oxford, **1977**.

92. B. A. Strukov, A. P. Levanyuk, *Ferroelectric Phenomena in Crystals; Springer-Verlag: Berlin,* **1998**.

93. M. B. Smith, K. Page, T. Siegrist, P. L. Redmond, E. C. Walter, R. Seshadri, L. E. Brus, M. L. Steigerwald, *J. Am. Chem. Soc.* **2008**, 130, 6955.

94. V. Buscaglia, M. T. Buscaglia, M. Vivani, L. Mitoseriu, P. Nanni, V. Terfiletti, P. Piaggio, I. Gregora, T. Ostapchuk, J. Pokorny, J. Petzelt, *J. Eur. Ceram. Soc.* **2006**, 26, 2889.

95. J. J. Urban, J. E. Spanier, Y. O. Lian, W. S. Yun, H. Park, *Adv. Mater.* **2003**, 15, 423

96. J. E. Spanier, A. M. Kolpak, J. J. Urban, I. Grinberg, L. Ouyang, W. S. Yun, A. M. Rappe, H. Park, *Nano Lett.* **2006**, 6, 735–739.

97. D. D. Fong, G. B. Stephenson, S. K. Streiffer, J. A. Eastman, O. Auciello, P. H. Fuoss, C. Thompson, *Science* **2004**, 304, 1650.

98. S. Wada, T. Tsurumi, H. Chikamori, T. Noma, T. Suzuki, *J. Cryst. Growth* **2001**, 229, 433.

99. M. El Marssi, F. Le Marrec, I. A. Lukyancuk, M. G. Karkut, *J. Appl. Phys.* **2003**, 94, 3307.

100. B. Hou, Z. J. Li, Y. Xu, D. Wu, Y. H. Sun, *Chem. Lett.* **2005**, 34, 1040.

101. M. Niederberger, G. Gartweitner, N. Pinna, M. Antonietti, *J. Am. Chem. Soc.* **2004**, 126, 9120.

102. P. Kim, S. C. Jones, P. J. Hotchkiss, J. N. Haddock, B. Kippelen, S. R. Marder, J. W. Perry, *Adv. Mater.* **2007**, 19, 1001.

103. F. Caruso, *Adv. Mater.* **2001**, 13, 11.

104. R. Davies, G. A. Schurr, P. Meenan, R. D. Nelson, H. E. Bergna, C. A. S. Brevett, R. H. Goldbaum, *Adv. Mater*. **1998**, 10, 1264.

105. C. H. M. Hofman-Caris, *New J. Chem*. **1994**, 18, 1087.

106. H. Jia, S. Titmuss, *Nanomedicine*, **2009**, 4, 951.

107. S. M. Marinakos, L. C. Brousseau, A. Jones, D. L. Feldheim, *Chem. Mater.* **1998**, 10, 1214.

108. G. Decher, *Science* **1997**, 277, 1232.

109. R. Partch, S. G. Gangolli, E. Matijevic, W. Cai, S. Arajs, *J. Coll. Int. Sci.* **1991**, 144, 27.

110. L. Quaroni, G. Chumanov, *J. Am. Chem. Soc*. **1999**, 121, 10 642.

111. F. Caruso, H. Möhwald, *J. Am. Chem. Soc.* **1999**, 121, 6039.

112. M. Ohmori, E. Matijevic, *J. Coll. Int. Sci.* **1992**, 150, 594.

113. Z. Xu, Q. Liu, J. A. Finch, *Appl. Surf. Sci.* **1997**, 120, 269.

114. R. De Palma, S. Peeters, M. J. Van Bael, H. Van den Rul, K. Bonroy, W. Laureyn, J. Mullens, G. Borghs, G. Maes, *Chem. Mater*. **2007**, 19, 1821.

115. J. Pawsey, K. Yach, L. Reven, *Langmuir* **2002**, 18, 5205.

116. X. Xu, N. L. Rosi, Y. Wang, F. Hou, C. A. Mirkin, *J. Am. Chem. Soc*. **2006**, 128, 9286.

117. T. H. Galow, A. K. Boal, V. M. Rotello, *Adv. Mater*. **2000**, 12, 576.

118. M. Li, S. Mann, *J. Mater. Chem*. **2004**, 14, 2260.

119. S. Mornet, C. Elissalde, O. Bidault, F. Weill, E. Sellier, O. Nguyen, M. Maglione, *Chem. Mater*. **2007**, 19, 987.

120. D. V. Talapin, *ACS Nano* **2008**, 2, 1097.

121. E. V. Shevchenko, D. V. Talapin, C. B. Murray, S. O'Brien, *J. Am. Chem. Soc*. **2006**, 128, 3620.

122. E. V. Shevchenko, D. V. Talapin, N. A. Kotov, S. O'Brien, C. B. Murray, Nature **2006**, 439, 55.

123. M. D. Eldridge, P. A. Madden, D. Frenkel, *Nature*, **1993**, 365, 35.

124. I. E. Sendroiu, D. J. Schiffrin, J. M. Abad, *J. Phys. Chem. C.* **2008**, 112, 10100.

125. D. G. Thompson, R. J. Stokes, R. W. Martin, P. J. Lundahl, K. Faulds, D. Graham, *Small* **2008**, 4, 1054.

126. C. A. Mirkin, R. L. Letsinger, R. C. Mucic, J. J. Storhoff, *Nature* **1996**, 382, 607.

127. M. Rycenga, J. M. McLellan, Y. Xia, *Adv. Mater.* **2008**, 20, 2416.

128. A. Verma, V. M. Rotello, *Chem. Commun*. **2005**, 3, 303.

129. N. A. Hill, *J. Phys. Chem B. Science*, **2000**, 104, 6694.

130. N. A. Spaldin, M. Fiebig, *Science* **2005**, 309, 391

131. B. K. Ponomarev, *Ferroelectrics* **1994**, 161, 43.

132. W. Erenstein, N. D. Mathur, J. F. Scott, *Nature* **2006**, 442, 759.

133. C-W. Nan, M. I. Bichurin, S. Dong, D. Viehland, G. Srinivasan, *J. Appl. Phys.* **2008**, 103, 031101.

134. C. W. Nan, *Phys. Rev. B* **1994**, 50, 6082.

135. M. I. Bichurin, V. M. Petrov, R. V. Petrov, Y. V. Kiliba, F. I. Bukashev, A. Y. Smirnov, D. N. Eliseev, *Ferroelectrics* **2002**, 280, 265.

136. Y. J. Li, X. M. Chen, Y. O. Lin, Y. H. Tang, *J. Eur. Ceram. Soc.* **2006**, 26, 2839.

137. S. X. Dong, J. F. Li, and D. Viehland, *Appl. Phys. Lett.* **2004**, 85, 3534.

138. P. Li, Y. M. Wen, and L. X. Bian, *Appl. Phys. Lett.* **2007**, 90, 022503.

139. H. Zheng, J. Wang, S. E. Lofland, Z. Ma, L. Mohaddes-Ardabili, T. Zhao, L. Salamanca-Riba, S. R. Shinde, S. B. Ogale, F. Bai, D. Viehland, Y. Jia, D. G. Schlom, M. Wuttig, A. Roytburd, and R. Ramesh, *Science* **2004**, 303, 661.

140. R. Ramesh and N. A. Spaldin, *Nat. Mater*. **2007**, 6, 21.

141. R. E. Newnham, D. P. Skinner, L. E. Cross, *Mater. Res. Bull.* **1978**, 13, 525.

142. J. Boomgard, D. R. Terrell, R. A. J. Born, H. F. J. I. Giller, *J. Mater. Sci.* **1974**, 9, 1705.

143. A. M. J. G. Run, D. R. Terrell, J. H. Scholing, *J. Mater. Sci.* **1974**, 9, 1710.

144. J. Boomgard, A. M. J. G. Run, J. Suchtelen, *Ferroelectrics*, **1976**, 295, 1976.

145. G. Harshe, J. P. Dougherty, R. E. Newnham, *Int. J. Appl. Electromagn. Mater.* **1993**, 4, 145.

146. Y. R. Dai, P. Bao, and J. S. Zhu, *J. Appl. Phys*. **2003**, 39, 1209.

147. J. Ryu, A. V. Carazo, K. Uchino, H. E. Kim, *J. Electroceram*, **2001**, 7, 17.

148. G. Srinivasan, C. P. DeVreugd, C. S. Flattery, *Appl. Phys. Lett.* **2004**, 85, 2550.

149. Q. H. Jiang, Z. J. Shen, J. P. Zhou, Z. Shi, C-W. Nan, *J. Eur. Ceram. Soc.* **2007**, 27, 279.

150. G. Srinivasan, E. T. Rasmussen, J. Gallegos, R. Srinivasan, Y. I. Bokhan, V. M. Laletin, *Phys. Rev. B* **2001**, 64, 214408.

151. G. Srinivasan, E. T. Rasmussen, B. J. Levin, R. Hayes, *Phys. Rev. B* **2002**, 65, 134402.

152. F. Zavaliche, H. Zheng, L. Mohaddes-Ardabili, S. Y. Yang, Q. Zhan, P. Shafer, E. Reilly, R. Chopdekar, Y. Jia, P. Wright, D. G. Schlom, Y. Suzuki, and R. Ramesh, *Nano Lett*. **2005**, 5, 1793.

153. F. Zavaliche, T. Zhao, H. Zheng, F. Straub, M. P. Cruz, P.-L. Yang, D. Hao, and R. Ramesh, *Nano Lett*. **2007**, 7, 1586.

Chapter 2

Chapter 2

2 Synthetic and Experimental Techniques

2.1 Introduction

This chapter describes the experimental and synthetic techniques that were employed for in thesis. A greater emphasis is placed on describing the techniques most instrumental to the work, such as electron microscopy and powder X-ray diffraction (XRD).

2.2 Synthetic Techniques

2.2.1 Coprecipitation[1, 2]

Coprecipitation involves the simultaneous precipitation of two or more elements in solution. It can be induced by chemical reduction, oxidation, photoreduction, hydrolysis, or by altering parameters influencing solubility, such as concentration or reaction temperature. The products of these reactions are typically sparingly soluble species formed under high supersaturation conditions, where the chemical potential of a molecule in the crystallised state is less than that of a molecule in solution, in which case nucleation and/or growth of crystallites is possible. Consequently, nucleation is a key step in a precipitation reaction. During nucleation a large number of small particles are formed, however, secondary processes such as agglomeration

and Ostwald ripening (where small particles are consumed by large ones) dramatically affect the final particle size, size-distribution and morphology, as do variables influencing the mixing process, such as the stirring rate and the rate of addition of reagents. Metal oxide nanoparticles can be directly prepared by coprecipitation, or *via* a precursor that then requires further treatment, for instance calcination, though nanoparticle aggregation and growth tends to occur during the calcination process.

Nanoparticles need to be stabilised against thermodynamically favourable aggregation. Typically, this is achieved by steric stabilisation of the nanoparticle surface, for example using the capping group cetyl trimethylammonium bromide (CTAB) (Figure 1) or *via* electrostatic repulsion by anchoring capping groups such as citric acid to the nanoparticle (Figure 2).

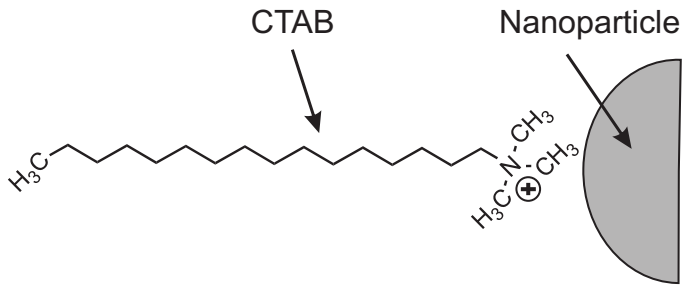

Figure 1. Representation of a CTAB-stabilised nanoparticle.

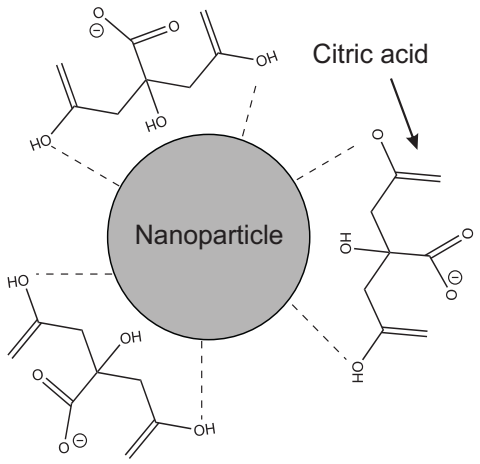

Figure 2. Representation of a citric acid stabilised nanoparticle.

In this work, oxide nanoparticles were precipitated from their metal salts in aqueous solution *via* the addition of sodium hydroxide and in the presence of a stabiliser.

2.2.2 Solvothermal Reactions[1, 3-5]

Solvothermal reactions have been used for the preparation of nanomaterials for the past 20 years.[3] The technique involves performing reactions within closed systems such as autoclaves or bombs (Figure 3). Under these conditions solvents can be brought to temperatures above their boiling point due to the increase in autogenous pressure resulting from heating. Above a certain critical point (374 °C and 218 atm for H_2O) fluids exhibit properties of both a liquid and a gas. The interfaces between solids and these supercritical fluids lack surface tension, and supercritical fluids exhibit high viscosities and easily dissolve chemical compounds that would have very low solubilities under ambient conditions.

Figure 3. A stainless-steel autoclave used for solvothermal reactions. The Teflon reaction vessel shown on the right.

Most solvothermal reactions are carried out in sub-critical conditions where it is still possible to take advantage of the increased solubility and reactivity of metal salts, and to prepare inorganic materials often at substantially lower reaction temperatures than necessary for traditional techniques such as solid-state synthesis. In addition, because the products of solvothermal reactions are usually crystalline, they do not require any high temperature post-annealing treatment. The concentration of the solvent and reagent plays a key role in determining the composition and morphology of the product, as do thermodynamic parameters such as the reaction temperature, pressure and reaction time, and as with coprecipitation it is typically necessary to incorporate surface stabilising molecules. One important distinction is between the terms solvothermal and hydrothermal, solvothermal refers to reactions in non-aqueous solvents, and hydrothermal to reactions in H_2O.

In the work presented here, solvothermal reactions were performed under sub-critical conditions to synthesise metal oxide nanoparticles at low temperature. Parr

Instruments Model 4746 stainless steel autoclaves with a maximum operating temperature of 250 °C and 3,000 psi were used in conjunction with Teflon liners.

2.2.3 Sol-gel Synthesis[1, 6-8]

Sol-gel synthesis is a versatile procedure, widely used for the synthesis of nanoparticles. The process can be thought of as occurring in several steps. Firstly a sol must be prepared, which is a stable solution of a metal alkoxide or a solvated metal precursor. A gel then forms as a result of polycondensation reactions, often promoted by the addition of an acid or base catalyst, forming an oxide or alcohol-bridged network. Ageing of the gel gives a solid mass, and drying removes traces of solvents from the gel. Dehydration of the solid mass is performed at high temperature and during this step surface bound O-H groups are removed from the particle surface.

The gel network structure that is formed by acid or base catalysed hydrolysis of metal alkoxides can be tailored to favour the formation of polymeric chains with extensive crosslinking and branching, or the formation of discrete spherical particles with minimal cross-linking, with the latter being preferred for the preparation of nanoparticles. One example is the preparation of TiO_2 nanoparticles from Titanium(IV) isopropoxide precursors.[1] In this instance, condensation of $Ti(^{i}OPr)_4$ resulted in the formation of 10-20 nm particles, while substitution of one $O^{i}Pr^{-}$ ligand with bidentate acetylacetonate (acac) lead to 5 nm spherical particles being formed. Polymeric chains were formed by condensation of the precursor substituted with two bidentate acac molecules. The nature of the catalyst plays a key role too. Tokumoto et al.[9] prepared ZnO nanoparticles from a zinc acetate-derived precursor and found

the smallest particles were prepared by use of the basic LiOH catalyst, while acetic acid and succinic acid gave larger particles with more impurities. Thus, the size and morphology of the final product strongly depends upon the pH and precursor structure.

Sol-gel chemistry was used in this work to prepare metal oxide nanowires and nanoparticles from their alkoxide precursors.

2.2.4 Solid-state Sintering

The purpose of sintering is to prepare a dense solid. It involves pressing a sample into a pellet using a hydraulic press and die, and firing in a furnace at high temperature (in this work between 500 and 1200 °C). The driving force for densification is the reduction of the surface energy by the transfer of matter from the interior of the grains along the grain boundaries to adjacent pores, which are then filled. The processes of densification and diffusion occur simultaneously and so the duration of the sintering process can also be a key factor. The density of the final sintered pellet also strongly depends upon the density of the initial pressed pellet, and so a cold isostatic press (CIP, Figure 4) was used to press the pellets at 30,000 psi prior to sintering.

In this thesis solid-state sintering reactions were carried out for densification of magnetoelectric ceramics.

Figure 4. Image of the cold isostatic press (CIP) used in pellet preparation. The inset shows the sample holder.

2.3 Experimental Techniques

2.3.1 Transmission Electron Microscopy[10, 11]

The transmission electron microscope (TEM) is a highly sophisticated instrument that has found application across the scientific disciplines. Whilst optical microscopes are restricted in resolution by the wavelength of visible light, the electron microscope is capable of providing both structural and chemical information over a range of length scales as far down as atomic dimensions, due to the wavelength of the electron being much less than 1 Å.

2.3.1.1 Theory

The electron microscope (Figure 5) can use one of three electron sources: a tungsten (W) filament, a W filament with a LaB_6 crystal tip or a field emission gun. The tip is situated inside an uncharged Wehnelt cap held under vacuum and when this is heated electrons are emitted. The electrons are then directed through the positively charged anode, which is typically held at 200 kV.

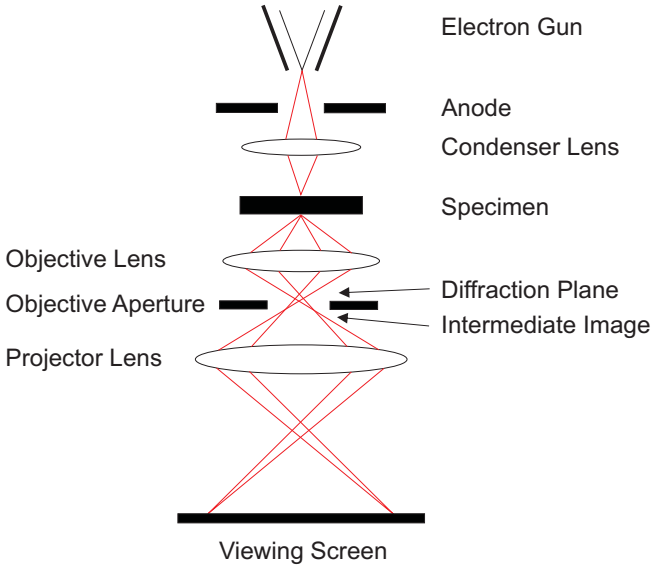

Figure 5. Diagrammatic representation of an electron beam passing down the column of a TEM.

The electrons are accelerated at the anode, and thus have a high kinetic energy and no potential energy. The kinetic energy of an electron (eV) can be calculated as the product of half the mass of the electron (m) multiplied by the square of the velocity (v). De Broglie's equation shows that the momentum of an electron (p) is equal to the product of the mass and velocity, and also Planck's constant (h) divided by the

wavelength (λ), thus the wavelength of the electron can be derived from the kinetic energy. As the accelerating voltage is typically very high (e.g. 200 kV) then the speed of the electrons will be comparable to the speed of light (*c*), and so relativistic corrections are needed. These equations are shown below. Equation 2.1 shows the energy of the electron, 2.2 is De Broglie's equation, 2.3 shows the wavelength of the electron (rearranged from 2.1) and equation 2.4 shows the wavelength taking into account relativistic corrections.[10]

$$eV = \frac{1}{2}mv^2 = \frac{p^2}{2m} = \frac{h^2}{2m\lambda} \tag{2.1}$$

$$p = mv = \frac{h}{\lambda} \tag{2.2}$$

$$\lambda = \frac{h}{\sqrt{2meV}} \tag{2.3}$$

$$\lambda = \frac{h}{\sqrt{2m_0eV_r}} = \frac{h}{\sqrt{2m_0eV_0\left(1+\frac{eV_0}{2m_0C^2}\right)}} \tag{2.4}$$

At 200 kV the wavelength of the electron is 0.00251 nm, which is far smaller than that of visible light (~ 400 nm). Thus, it is possible to achieve a far greater resolution using an electron microscope than with a visible light microscope, making the electron microscope well suited to the characterisation of nanomaterials.

Once accelerated at the anode, the electrons continue moving down the column through a series of lenses and apertures. The condenser lens focuses the beam onto the sample, while the condenser apertures can be used to adjust the image contrast. After passing through the sample, the beam is refocused by the objective lens, which allows for the diffraction plane to be viewed. The objective aperture can be used to

increase sample contrast or to view dark field imaging. Finally the beam passes through the projector lens, which gives the final image on the viewing screen.

High resolution TEM (HRTEM) differs from standard TEM in that it uses either a very large objective aperture (Figure 5) or no aperture at all. Therefore, in contrast to standard TEM where only a fraction of the electrons that have passed through the sample are used to make up the image, a greater proportion of the transmitted electrons are used. The transmitted beam can interfere with one or more diffracted beams and the contrast observed across the image will depend on the relative phases of the various beams. This is often referred to as phase contrast imaging.

Microscope performance is limited by lens defects, the most substantial of which is the unavoidable spherical aberration caused by round electron lenses. This arises due to the difficulty in manufacturing a 100% perfectly curved magnetic lens, and is important in the objective lens as it degrades the image that is viewed in the TEM. Though spherical aberrations also exist in optical microscopes, it is not considered a significant effect due to the limited magnification.

Due to the need for a compromise between small-angle diffraction effects and wide-angle spherical-aberration limits, the resolution of the electron microscope, *d,* can be roughly expressed by an equation of the form:

$$d = AC_s^{1/4}\lambda^{3/4} \tag{2.5}$$

Where C_S is the spherical aberration coefficient of the objective lens, λ is the electron wavelength, and A is a constant with a value ranging from 0.43 to 0.7 depending on the type of imaging (coherent, incoherent, or phase contrast).[10]

Values of *d* typically range from about 3.0 Å down to 1.0 Å as electron energies are increased from 100 to 1250 keV. Modern-day HRTEMs operating at 200 or 300 keV have resolution limits well below 2.0 Å, which is comparable to the spacing between atoms. Individual columns of atoms can thus be resolved in crystalline materials with HRTEM, which enables phase identification to be performed by comparison of the lattice parameters with those obtained from X-ray diffraction. However these columns must first be oriented so that the incident electron beam is aligned along some major crystallographic zone axis of the sample.

2.3.1.2 Sample Preparation

The most common preparation technique is solvent suspension; with volatile solvents such as acetone or ethanol typically used to reduce the time the sample takes to dry. In this work the polarity of the solvent was often an important consideration, so tetrahydrofuran (THF) was used where a non-polar solvent was needed.

The sample preparation involved grinding the sample using a pestle and mortar in order to aid dispersion, then suspending the sample in the solvent at the required dilution and sonicating in an ultrasonic bath to aid the breaking up of large aggregates and help homogenise the sample. A few drops of the solution were then dropped onto a holey carbon film supported on a 3 mm copper grid, a diagram of which is shown in Figure 6. The solvent was then allowed to evaporate, which deposits the sample onto the film.

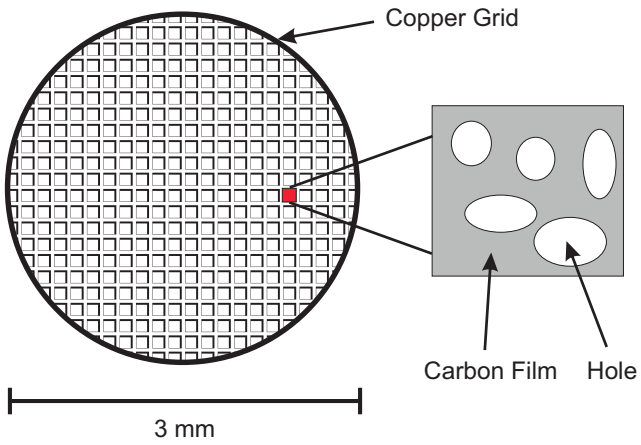

Figure 6. Diagrammatic representation of a copper grid supporting a holey carbon film.

Lower resolution TEM images were recorded using a FEI Tecnai G2 Spirit BioTWIN instrument with a W filament, operating at 100 kV. HRTEM images were recorded on a JEOL 300 kV JEM3010 instrument with a LaB_6 filament. Dr Zhongling Xu at the University of Liverpool performed the TEM imaging.

2.3.2 Scanning Electron Microscopy (SEM)[12]

2.3.2.1 Theory

The scanning electron microscope (SEM) is useful for obtaining three-dimensional topographical data, and for the imaging and analysis of ceramics and other samples that are too thick to be imaged using TEM.

A block diagram of an SEM can be seen in Figure 7. Electrons are emitted down the column, finely focussed into a beam by a series of lenses, and then rastered across

the sample surface. Secondary electrons are emitted when the electrons from the beam interact with the atoms of the sample, ejecting electrons from the inner K-shell. These electrons are detected and give an image of the texture, topography and surface features of a sample. Electrons are also reflected by the sample surface (backscattered) as a result of elastic collisions between the beam and from the inner electron shells of the sample. As heavier elements tend to backscatter more electrons than lighter ones, it is possible to distinguish areas of different composition using a backscattering detector, as there will be a difference in contrast between them. SEM also has a much greater depth of focus than TEM, which gives the images a three-dimensional quality.

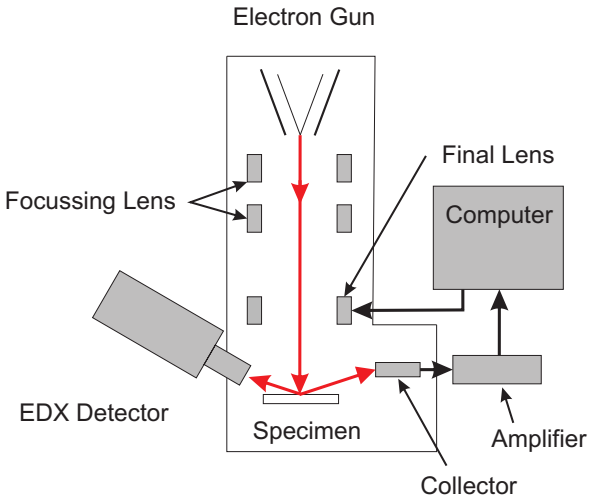

Figure 7. A diagrammatic representation of the inside of an SEM.

Non-conducting samples can experience charging when subjected to the SEM beam. Here, the amount of electrons striking the sample is not equal to the amount of backscattered electrons, leaving the sample with a residual charge. The sample is positively charged if there are more backscattered electrons than incident ones, or

negatively charged if there are more incident electrons than backscattered. Sample charging leads to a loss in the observed structural detail and makes high-quality image collection challenging. The solution is either to operate the SEM at a lower voltage, or to coat the sample with a conducting metal. A compromise is needed however, as topological information can be lost if the coating layer is too thick.

2.3.2.2 Sample Preparation

Ground powders were deposited onto an adhesive carbon tab. The samples were then placed onto a holder, in this case an aluminium holder with an internal screw thread was used.

Pellets were pressed onto the carbon tab for surface structure observations, while for cross-sections it was necessary to break the sample by freeze fracturing. Here, the pellet was cooled using liquid nitrogen (which made the sample more brittle) and with the sample held in a vice, it was broken using a hammer and chisel. Provided it was done correctly, it was possible to obtain flat (up to the micron scale) cross-sectional surfaces in this way. Figure 8 shows SEM images of a pellet surface and of a cross-section prepared using the freeze-fracturing technique.

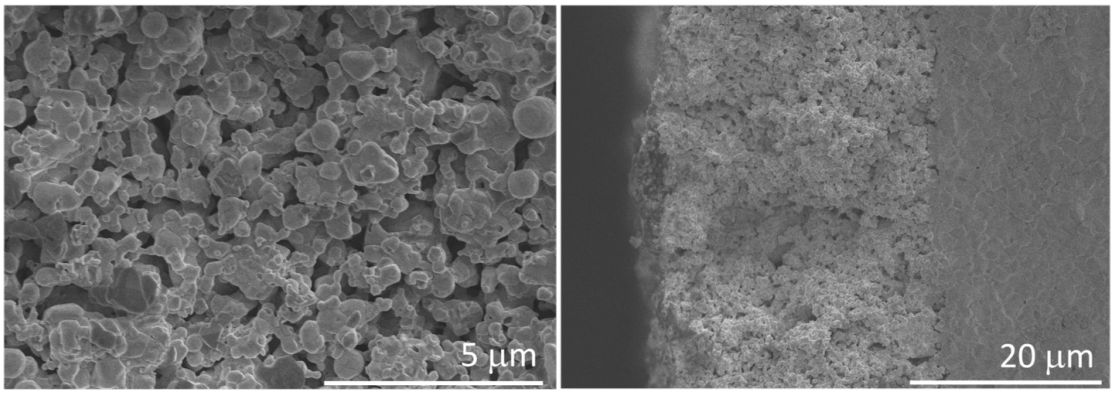

Figure 8. SEM images of (a) the surface of, and (b) a cross-section of a samarium-based solid-oxide fuel cell cathode material.

In this thesis SEM was used for the imaging of powders and ceramic composites. SEM images were recorded using a Hitachi S4800 Type II Cold Field Emission Scanning Electron Microscope. The samples were sputter coated with Au prior to analysis using an Emitech K550X automated sputter coater and were held in place using a M3 aluminium 15 mm cross-section sample holder. The samples were observed using a mix of upper and lower secondary electron detectors operating at acceleration voltages of 3 kV or 25 kV, with working distances of 8.0 mm or 15 mm respectively. The exact operation conditions are noted on each SEM image.

2.3.3 Energy-Dispersive X-ray Spectroscopy (EDX)[13]

Energy-dispersive X-ray spectroscopy (EDX) is useful for identifying the elements present within a sample. It is also possible to obtain element maps to investigate the element distribution over large areas, and to perform line scans to investigate the composition of a sample across an interface. The technique can be utilised on both

TEM and SEM, the latter is best applied to thick samples which cannot be penetrated by the electron beam in the TEM.

The principle behind EDX is as follows. An electron from the electron gun collides with one from the inner shell of an atom in the sample, which causes this electron to be ejected (see Figure 9a). Usually this electron will be from the K-shell, and its removal enables an electron from a higher energy level to drop into its place at the lower energy level, leading to the emission of an X-ray. This X-rays energy will be equal to the energy difference between the two energy levels, and as this energy level difference is atom-specific, the energy of the emitted X-rays can be used to identify the element present. For most elements the emitted X-ray is a K_{α}, i.e. an X-ray emitted as a result of an electron moving from the L-shell to the K-shell. K_{β} describes an electron going from the M-shell to the K-shell, whilst L_{α}, which is also commonly observed and results from an electron moving from the M-shell to the L-shell (see Figure 9b).

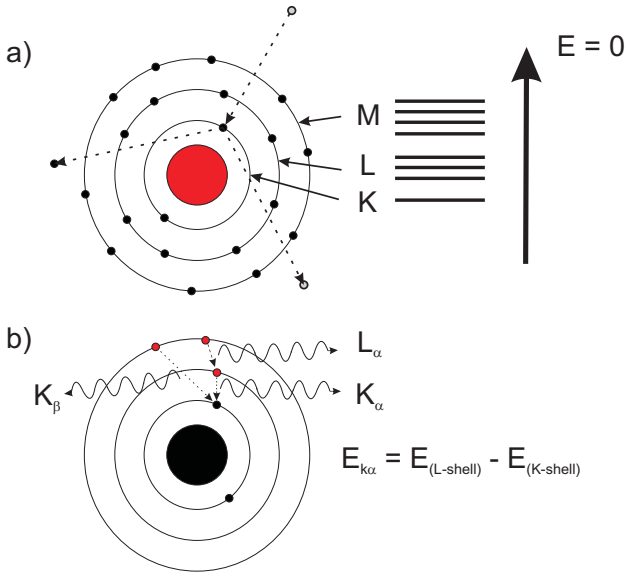

Figure 9. a) Diagram of a bombarding electron knocking out a K-shell electron b) electrons moving into the K-shell from higher shells, emitting X-rays in the process.

Absorption of low energy X-rays emitted from light elements can be a problem with EDX, and can limit the ability to accurately quantify elements with an atomic number less than 11. This can be addressed in a number of ways including through the use of thin samples, positioning of the EDX detector close to the sample and through software processing corrections. The absorption correction is an iterative procedure, initially assuming a starting composition based on uncorrected X-ray intensities. The absorption of different energy X-rays en route to the detector is then accounted for using a Beer–Lambert-type expression, which gives a new composition and this is used to perform a further absorption correction. This procedure is repeated until the change in composition falls below a preset level of accuracy. Through careful measurement and analysis, modern EDX instruments can elements down to 0.1 atom percent, to an accuracy of roughly 5%.

EDX was employed in order to derive compositional information, utilising both point scans for quantitative data on small areas and elemental mapping to assess sample homogeneity. EDX on the TEM was performed using an EDAX detecting unit PV9757/32 ME (model 204(B), active area = 30 mm^2). For the SEM, the operation conditions for EDX and imaging are different as X-ray emission requires operating voltages greater than the 3 kV used for imaging (lower operating voltages are useful as a way to reduce sample charging as discussed earlier), the optimal working distance (the distance between the aperture and the sample) also varies. EDX analysis using the SEM was performed with an Oxford Instruments 7200 EDX detector with 25 kV operating acceleration voltage and 15 mm working distance. Dr Zhongling Xu at the University of Liverpool performed the TEM EDX measurements.

2.3.4 Scanning Transmission Electron Microscopy (STEM)[14]

The scanning transmission electron microscope (STEM) is differentiated from TEM as a probe (with atomic level thickness) is scanned over the sample. The technique has the ability to generate local maps of the chemical composition and electronic structure at atomic resolution in complex and unknown samples. When mapping compositions using the STEM, it is possible to attain resolutions greater than those using EDX, with magnifications of times 10^6 possible. One advantage STEM has over SEM is that the images are not formed using lenses and so defects in imaging lenses (which cause the aberrations described earlier) are not present in STEM images. This is beneficial when dealing with particularly thick specimens, though the process of recording a STEM image is much slower than TEM imaging.

STEM was used in this thesis in order to determine the composition of nanoparticle composites at the nanometre scale. The images were collected by Dr. Z. Xu using a VG HB601 UX STEM operating at 100 kV equipped with an Oxford Instruments INCA TEM 300 EDS system.

2.3.5 X-ray Diffraction (XRD)[15, 16]

2.3.5.1 Diffraction Theory

As the wavelengths of X-rays are typically of the same order of magnitude as the interatomic distances in solids, they are suitable for use in diffraction studies. The majority of inorganic solids are crystalline with a regular, repeating structure that results in diffraction of X-rays. Diffraction occurs when the oscillating electric field of the X-ray interacts with the electron cloud of the atom. The induced oscillating

dipole can be viewed as the source of the diffracted X-ray beam. The resulting observation is scattering of the X-rays by the electron cloud of the atom without a change in wavelength. The positions of the reflections provide information on the size, shape and orientation of the unit cells with the intensities being a result of the positions and identities of the atoms. Thus, the resulting diffraction pattern is characteristic of the structure and composition of the material and comparison of the diffraction pattern with known phases can provide insight into the nature of the material.

It was von Laue who originally put forward the idea that X-rays are diffracted when passing through a crystal due to the similarity between the X-ray wavelength and the lattice spacing.[17] von Laue thought of crystals as three-dimensional networks consisting of rows of atoms and based his analysis of X-ray diffraction on the idea that a crystal behaved as a three-dimensional diffraction grating.

For this treatment a crystal containing only one type of atom is considered, with the atoms regarded as scattering centres situated at the lattice points. The atoms are spaced in three-dimensions at a, b and c along the axes *x*, *y* and *z* respectively. The condition for constructive interference of the waves along the *x*-axis is reduced to a consideration of the path differences between the diffracted beams from adjacent atoms (see Figure 10). For constructive interference the path difference must be a whole number of wavelengths, hence:

$$\left(\mathrm{AB}-\mathrm{CD}\right) = a\left(\cos\alpha_n - \cos\alpha_0\right) = n_x\lambda \tag{2.6}$$

Where α_n and α_0 are the angles between the incident and diffracted beams to the *x*-axis respectively, n_x is an integer and λ is the wavelength.[15]

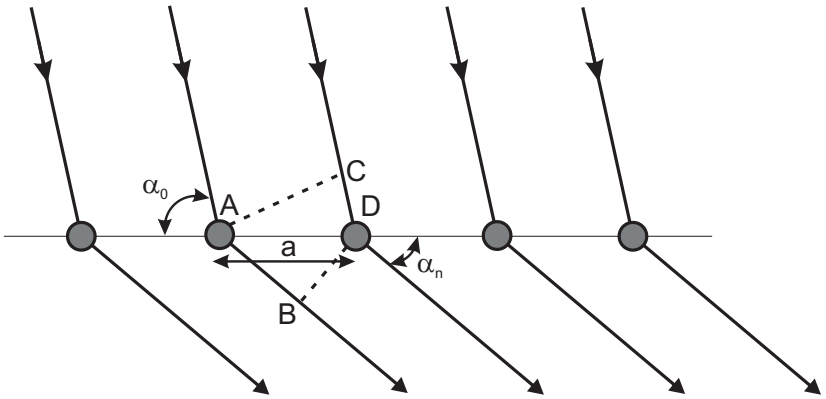

Figure 10. von Laue diffraction from a lattice row along the *x*-axis. The incident and diffracted beams are at angles α_0 and α_n to the row of atoms. The path difference between the incident and diffracted beams is AB-CD.

The same analysis can be performed along the *y* and *z*-axes giving the second and third Laue equations:

$$b\left(\cos\beta_n - \cos\beta_0\right) = n_y\lambda \tag{2.7}$$

$$c\left(\cos\gamma_n - \cos\gamma_0\right) = n_z\lambda \tag{2.8}$$

Where the angles β_n, β_0, γ_n, γ_0 and the integers n_y and n_z are defined as for the *x*-axis variables.[15] For constructive interference to occur from all three atom rows, the Laue equation for each axis must be satisfied simultaneously. Hence, each diffracted beam is identified by three integers (n_x, n_y and n_z). These represent the order of diffraction

from each row of atoms and are more commonly known as the *h*, *k* and *l* Laue indices of the reflecting planes from the Bragg analysis of diffraction.

The scheme shown in Figure 10 only shows the diffracted beam at angle α_n below the atom row. However if this angle was above the atom row, or at any out of plane angle to the paper, as long as the angle to the atom row is α_n then the conditions for constructive interference are still met. Therefore all diffracted beams of the same order construct a cone centred on the atom row with a semi-apex angle α_n, see Figure 11. The same situation occurs along the other two axes and a diffracted beam only occurs where the cones from each axis intersect.

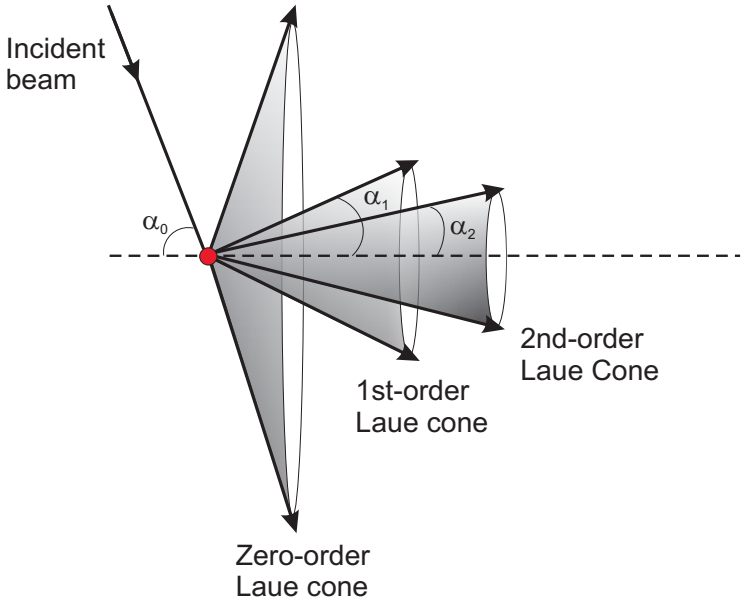

Figure 11. Three Laue cones representing the diffracted beams from a row of atoms along the *x*-axis.

This analysis suffered from the disadvantage that in order for the diffraction angle to be calculated; six angles, three lattice spacings and three integers needed to be determined. Bragg envisaged diffraction as the reflection of the incident beam from planes of atoms[18] as depicted in Figure 12. This significantly simplifies the problem, and whilst it is not correct in a physical sense, it is correct in a geometric sense. Based on Figure 12 Bragg's law can be derived,[16] with the path difference between beams scattered from adjacent lattice planes separated by d_{hkl} given by:

$$\left(\mathrm{AB}+\mathrm{BC}\right)=\left(d_{hkl}\sin\theta+d_{hkl}\sin\theta\right)=2d_{hkl}\sin\theta \tag{2.9}$$

Hence for constructive interference:

$$n\lambda=2d_{hkl}\sin\theta \tag{2.10}$$

Where n is an integer. AB = BC in Figure 12 as the positions of the atoms are the same in each plane. However where they are different (AB ≠ BC), the sum AB + BC remains the same and so Bragg's law is still valid. The result of this means that the positions of the atoms do not matter, only the spacing d_{hkl} needs to be considered. In addition, Bragg's law is two-dimensional as opposed to von Laue's treatment, and so this further simplifies the solution.

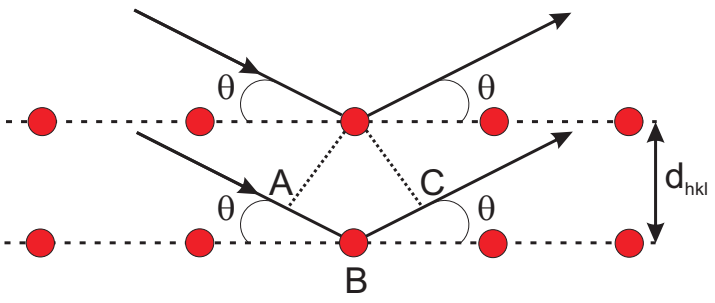

Figure 12. Schematic diagram of diffraction as envisioned by Bragg.

Fast-moving electrons that are emitted from a tungsten filament produce X-rays by two mechanisms. In laboratory X-ray diffractometers the electrons produced by the W filament bombard a metal anode target (often copper, chromium, molybdenum or in the work presented here, cobalt) and are accelerated at a high voltage from a cathode. The high-speed electrons decelerate in the vicinity of the nucleus as they pass through the strong electric field; this quantum process decreases the energy of the electron and an X-ray photon is produced. These X-rays occur over a continuous range of wavelengths and are called Bremsstrahlung radiation. Higher energy X-rays are also emitted at discrete frequencies as a result of the emitted electrons colliding with the inner shell of the anode materials atoms causing expulsion of an electron (as described in section 2.3.3). When the vacancy is filled with a higher energy electron, X-rays are emitted, see Figure 9 for an illustration of this process. The emitted X-rays are typically the $K_{\alpha 1}$ X-rays which have a wavelength of 0.1788965 nm when a cobalt anode is used, though a particular wavelength can be selected though the use of filters and monochromators. Both transmission and reflection diffraction can be carried out, though reflection was exclusively used in this work. A schematic of a reflection diffractometer is shown in Figure 13 below.

Particle size can also be calculated from the XRD pattern using the Debye-Scherrer equation (2.11).[15]

$$D = \frac{k\lambda}{\beta \cos\theta} \qquad (2.11)$$

Where D is the particle size in Angstroms, λ is the wavelength of the radiation in Angstroms (1.788965 Å for Co $K_{\alpha 1}$ radiation), β is the full-with at half-maximum of

the diffraction peak in radians, θ is the angle of reflection in degrees and k is the shape factor, which is typically 0.9.

This formula gives a volume average measure of the particle size, as opposed to measurement by TEM where a number average is obtained. The major advantages of using the XRD particle size instead of that determined by TEM is that it is a bulk measurement, measuring the entire sample rather than a few particles as in TEM, and so the results are less skewed by anomalously large or small particles.

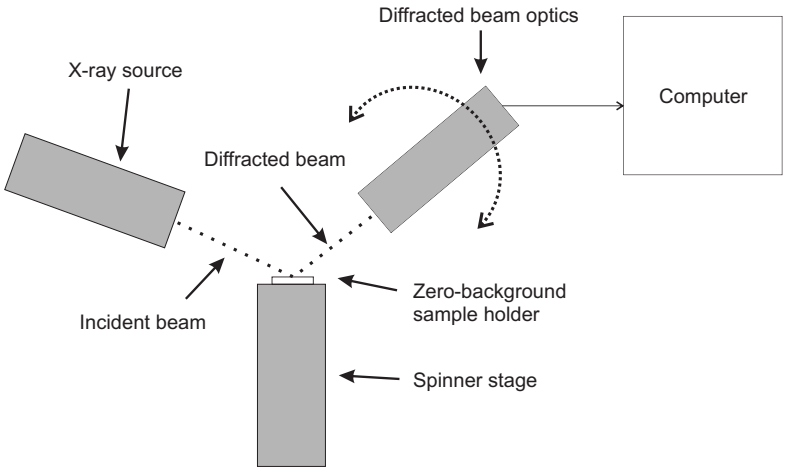

Figure 13. Diagrammatic representation of a reflection powder X-ray diffractometer.

2.3.5.2 Powder X-ray Diffraction

The random orientation of crystallites in a powdered sample means it scatters the X-ray beam in all possible directions according to Bragg's law. This results in the three-dimensions of a crystal being reduced into a one-dimensional powder diffraction profile, as there is a cone of diffracted intensity for each lattice plane. The reduction in dimensionality leads in an overlap of otherwise crystallograpically

distinct lattice planes and thus there is an irretrievable loss of information in powder X-ray diffraction compared to single crystal studies.

2.3.5.3 PANalytical X'pert Pro Diffractometer

The Panalytical X'pert Pro diffractometer was exclusively used for the collection of powder X-ray diffraction data in this thesis. The diffractometer has a sealed ceramic X-ray tube where a cobalt target is housed operating at current of 40 mA and a voltage of 40 kV. An iron filter removes K_{β} radiation. The detector is based on real time multiple step (RTMS) technology, this offers direct detection of diffracted X-rays.

Samples were prepared by grinding a small amount of powder and placing it onto a zero background holder, which is a silicon crystal of dimensions 32 mm in diameter and 2 mm thickness, cut to ensure it has no diffraction peaks in the operating angle range of the diffractometer. A volatile solvent, typically acetone or ethanol, was then dropped onto the holder using a pipette, with gentle agitation used to help disperse the sample over the holder. Any excess was then wiped off from around the outside of the holder. The samples were rotated during data collection to minimise preferred orientation effects and the adjustable beam mask, anti-scatter and diffracted anti-scatter slits were adjusted to 15 mm, 4 ° and 13 mm respectively, with an illuminated length of 15 mm. Data collections were performed over the desired scan range with a 10 - 90 ° 2θ scan taking approximately 2 hours.

XRD was used in this thesis in order to identify the phases present in metal oxide nanoparticle samples, and to determine the particle size using the Scherrer equation.

2.3.6 Thermogravimetric Analysis (TGA)[17]

Thermogravimetric analysis (TGA) is used to provide information about the thermal stability and composition of a compound. It is performed by monitoring the change in mass of a sample as it is heated or held isothermally.

The instrument consists of a heating furnace, a balance (which is typically housed outside of the furnace to maintain good mass sensitivity) and inlets through which gases can be passed. For instance, O_2 or air can be used for oxidising samples, H_2 for reducing or N_2 to provide an inert atmosphere. Typically a sample is heated at a known rate under the gas of choice whilst the weight and temperature of the sample are simultaneously monitored. Instruments can have either a horizontal or vertical relationship between the balance and the furnace, the former reducing buoyancy effects that occur as the sample is heated, which result in thermal drift at high temperature. The TGA normally has an operating range between room temperature and 1000 °C, though this can be higher depending on the exact specification. The samples are held in high-temperature inert sample holders; generally ceramics such as alumina or metals such as platinum are used. Samples of approximately 2 mg or greater can analyzed, with the instrument sensitive to a change in mass of more than 5 μg.

TGA was used in this thesis to determine the composition of surface-functionalised nanoparticles and to determine the labiality of surface-bound capping. Analysis was performed using a Seiko SII-TG/DTA 6300 thermal analyser under a flow of N_2 or O_2.

2.3.7 Elemental Analysis[17]

Elemental analysis is used for the determination of the carbon, hydrogen and nitrogen content of combustible materials. The process involves the complete and instantaneous oxidation of a sample by flash combustion, which converts the organic and inorganic substances into their combustion products (CO_2, H_2O and NO_x). The gases then pass into a reduction furnace, which is a quartz tube containing metallic copper. The reduction furnace removes excess oxygen and any species that are not C, H or N-combustion products, whilst also reducing nitric oxides to N_2 gas. The gases are then carried by helium into a chromatographic column where they are separated and detected by a thermal conductivity detector (TCD). An output signal is given that is proportional to the amount of each gas present, thus this is a quantitative technique.

In this thesis elemental analysis was used to determine the extent of loading of functional molecules and capping groups on the surfaces of nanoparticles *via* the analysis of the C, H and, if applicable, N content. Steven Apter at the University of Liverpool performed this technique using a Thermo Flash EA 1112 Series CHNS instrument.

2.3.8 Inductively Coupled Plasma Atomic Emission Spectroscopy (ICP-AES)[17, 18]

Inductively coupled plasma atomic emission spectroscopy (ICP-AES) works on the principle that excited electrons emit electromagnetic radiation in narrow, well-defined wavelengths as they return to ground state. It is a highly sensitive technique used for determining the concentration of trace metals and several non-metals. One

major advantage ICP has over EDX is that it is a bulk technique, enabling the average composition of the entire sample to be derived.

The ICP plasma torch (Figure 14) consists of 3 concentric quartz glass tubes, with the inner tube containing the sample aerosol and Ar support gas, and the outer tube carrying Ar gas used flow that is used to cool the tubes. A radio frequency (RF) generator typically operating at 1-5 kW at 27 or 41 MHz produces an oscillating current in an induction coil that is wrapped around the tubes, in turn creating an oscillating magnetic field. The RF power supply maintains the plasma, which is ignited by a Tesla coil. The plasma is between 5000-8000 K and is a highly efficient atomisation source; meaning every molecule should be dissociated provided the correct conditions are used.

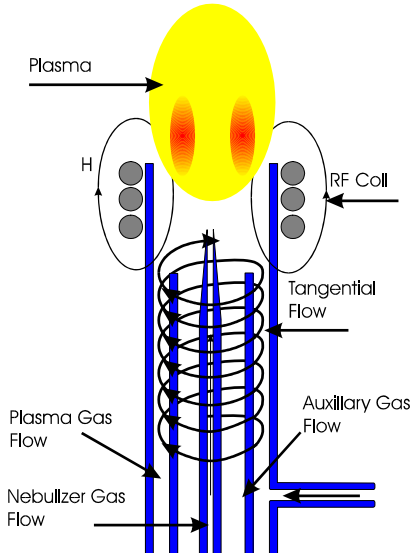

Figure 14. Schematic of the ICP Torch.[18]

As the excited species leave the high temperature region, the absorbed energy is released as UV and visible photons. Transfer lenses are then used to focus the emitted light onto a diffraction grating where it is separated into its component

radiation in the optical spectrometer. The light intensity is then measured with a photomultiplier tube at the specific wavelength for each element line involved. The intensity of the emitted radiation at any given wavelength is proportional to the concentration of that element in the sample, and so quantitative analysis is possible by comparing the measured intensities to standards with a known composition.

ICP-AES was used in this thesis for determination of the loading of functionalities on nanoparticle surfaces. The samples for ICP-AES need to be in aqueous solution; therefore it was necessary to digest samples prior to analysis. Typically HCl or a HF/HNO_3 mixture was used to digest the few mg of sample necessary for analysis. This analysis was performed by Steven Apter at the University of Liverpool, using an ICP AES Spectro Ciros CCD instrument.

2.3.9 Piezoelectric Measurements[19]

Piezoelectric testing involves the determination of both the charge produced by and the capacitance of a piezoelectric material when a compressive force is applied to it. The piezoelectric coefficient is calculated using the equation below:

$$d_{33} = \frac{D_{\max}}{X_{\max}} \tag{2.12}$$

Where the piezoelectric constant, d_{33} in CN^{-1} (coulombs per newton), is the induced charge per unit force applied in the same direction, $D_{\max}$ in units of C is the amplitude of the piezoelectric charge and $X_{\max}$ in units of N is the amplitude of the alternating driving pressure. The measurement requires the material to be dense enough for the compressive force to be efficiently translated through the sample and

so sintered, dense pellets were used, with the sample surfaces coated in a conductive silver paint to enable the charge to be measured.

d_{33} measurements were performed in order to quantify the piezoelectric response of both magnetoelectric ceramics and ferroelectric nanoparticles. These measurements were performed on a Piezotest Piezometer System PM300 at a frequency of 110 Hz with a dynamic force of 0.25 N.

2.3.10 Infrared Spectroscopy[17]

2.3.10.1 Theory

Infrared spectroscopy (IR) is a non-destructive technique that can be used to identify organic and inorganic molecules. IR is based on the absorption of infrared radiation of different frequencies, which causes excitation of the vibrational state of a molecule. This absorption requires the frequency of the photon to be the same as that of the specific vibration of the molecule and for the change in vibrational state to result in a change in dipole moment of the molecule.

The major types of molecular vibrations, stretching and bending, are illustrated in Figure 15. As rotational motion typically accompanies vibrational motion, absorption bands rather than sharp peaks are usually observed in an IR spectrum. Each atom can be considered to have 3 degrees of freedom (along the *x*, *y* and *z* axes) and so, in a polyatomic molecule with *n* atoms, there are 3*n* degrees of freedom. These are reduced to 3*n* - 6 true, fundamental vibrations for non-linear molecules and *3n* – 5 for linear molecules due to some motions describing translation and rotation of the molecule.

In practice, the number of observed absorption bands is not equal to $3n$ - 6 (or $3n$ - 5) as some bands are not IR active, whilst other bands mask each other if they occur at the same frequency. Additional bands are also generated by the appearance of overtones (integral multiples of fundamental absorption frequencies), by combinations of fundamental frequencies, differences of fundamental frequencies, coupling interactions between fundamental frequencies and coupling interactions between fundamental vibrations and overtones or combination bands. While the intensity of overtone, difference and combination bands is less than that of the fundamental bands, the combination of all these factors leads to a unique IR spectrum being obtained for each compound.

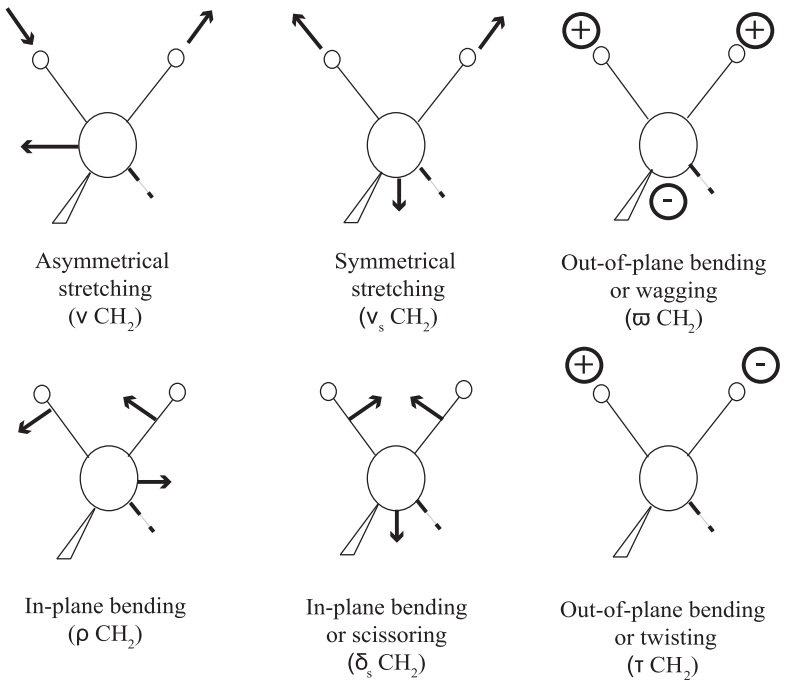

Figure 15. Major vibrational modes for a non-linear group, CH_2. (+ indicates motion out of the plane of the page, - indicates motion into the plane of the page).

An infrared spectrum can typically be broken down into three parts. Firstly the functional group region (4000 to 1300 cm^{-1}) is where strong absorption bands occur, usually from stretching vibrations between hydrogen and other small elements up to a mass of 19; such as ν(O-H) (~ 2800-3000 cm^{-1}), ν(C-H) (2700-2900 cm^{-1}) and ν(C=O) stretching (1550-1850 cm^{-1}). The narrow frequency range over which functional molecules absorb IR radiation mean that this region enables the identification of functional groups within a molecule based on comparison with the literature.

The fingerprint region (1300-910 cm^{-1}) includes contributions from complex interacting vibrations that are generally specific to each individual molecule, thus enabling the identification of the structure of a molecule through comparison with known compounds and their IR spectra. The absence of absorptions in the aromatic region (910-650 cm^{-1}) can generally rule out aromatic character in a compound, though some non-aromatic molecules such as amides and amines also have absorptions in this region.

2.3.10.2 Fourier Transform Infrared Spectroscopy (FTIR)

Fourier transform infrared spectrometers provide enhanced speed and sensitivity when compared with traditional dispersive instruments, they examine all frequencies simultaneously. An illustration of a FTIR spectrometer is shown in Figure 16. The instrument is composed of a radiation source, interferometer and a detector. The interferometer produces interference signals containing infrared spectral information, generated after passing through a sample. It divides radiant beams, generating an optical path difference between them and then recombines them to produce repetitive

interference signals, measured as a function of optical path difference by the detector. Fourier transformation converts the interferogram (a time domain spectrum displaying intensity versus time within the mirror scan) into the familiar intensity versus frequency spectrum. It is possible to perform FTIR analysis on thick or highly absorbing solid materials using attenuated total reflectance (ATR).

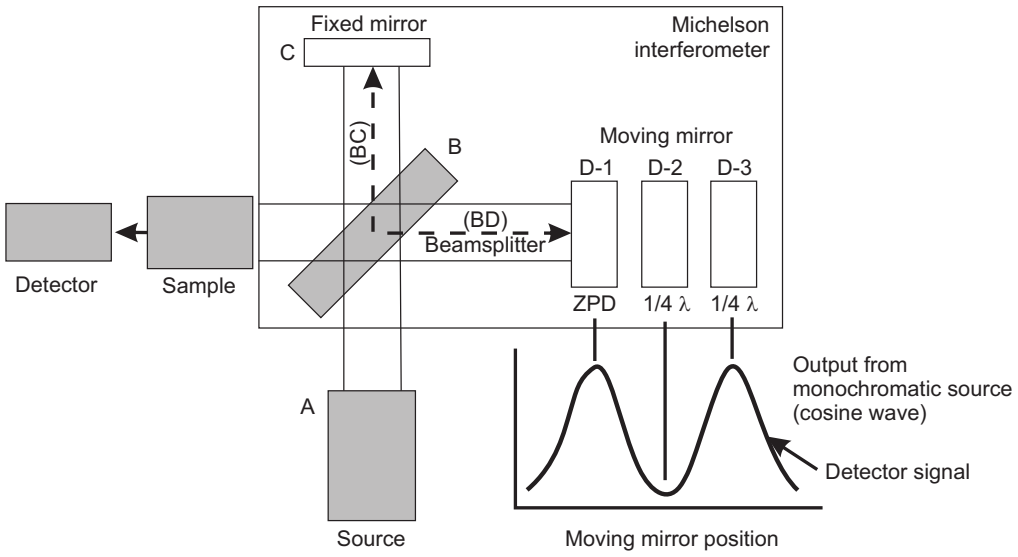

Figure 16. Simplified schematic of an FTIR spectrometer.

ATR spectra resemble conventional IR spectra however the relative intensities of the bands are different. ATR can be obtained using dispersive or FT instruments, with FTIR spectrometers enabling higher quality data to be obtained in this energy-limited situation.

FTIR spectroscopy was used in this thesis to identify organic molecules anchored to the surfaces of metal oxide nanoparticles. A Nicolet Nexus instrument was used to

acquire the spectra along with a Jasco FTIR-4200 spectrometer equipped with an ATR attachment.

2.3.11 Raman Spectroscopy[17]

Raman spectroscopy probes molecular vibrations *via* the scattering of incident photons, which have a much larger energy than the vibrational transition energy of the molecule. Most high-energy photons are scattered by the sample without change, termed Rayleigh scattering, however some photons are scattered and possess less energy after the interaction. It is these photons give rise to so-called Raman-Stokes lines, while scattered photons with a higher energy than the incident photons are termed anti-Stokes photons. The difference in the energies between the incident and scattered photons corresponds to the vibrational transitions, thus the molecules are being promoted to an excited vibrational state, as in IR spectroscopy.

The information obtained from Raman spectroscopy can be quite different to that obtained from IR. The selection rules are different for Raman; a change in polarisability is required (how easily the electron cloud can be distorted by an external electric field), rather than a change in dipole moment. Thus, even homonuclear, diatomic molecules such as H_2 or X_2 (where X is a halogen) are Raman active. Yet as with IR spectroscopy, Raman scattering information is presented as intensity versus wavelength shift in cm^{-1}, with the same vibrational transitions being excited by both methods. Consequently the group frequencies from IR tables can be used to obtain structural information from the Raman spectroscopy, though not all IR-active modes are also Raman-active and *vice versa*. For instance, in

centrosymmetric molecules the totally symmetric vibration is IR-inactive but Raman-active.

In Raman spectroscopy there are $3n$ - 6 fundamental vibrations for non-linear molecules and $3n$ - 5 for linear molecules but as in the case of IR, some modes are not active and degeneracies can occur. Raman spectra are typically simpler than their IR counterparts due to overtones, combination and difference bands being rare.

Raman spectroscopy is useful for identifying vibration modes (phonons) in solids. This means structural changes that are induced by external factors, such as changing pressure or temperature can be explored using Raman spectroscopy.[20] For instance, the ferroelectric barium titanate can adopt a number of structures including a ferroelectric tetragonal form, and a paraelectric cubic form. As the former is Raman active, and the latter Raman inactive it is possible to determine which phase is present though Raman spectroscopy. This is especially useful for nanoparticulate samples where line broadening means powder XRD analysis can be inconclusive and may fail to pick up the pick splitting characteristic of the tetragonal phase. In samples where both the tetragonal and cubic phases are present, the position and nature of the bands in the Raman spectrum can provide information as to the relative amounts of these phases present. Kolen'ko et al.[21] prepared barium titanate using a solvothermal approach, and obtained samples with particle sizes ranging from 5 to 37 nm. Using Raman spectroscopy, and drawing comparisons with a bulk tetragonal $BaTiO_3$ standard, the authors were able to determine that below 17 nm the nanoparticles were locally distorted cubic phase $BaTiO_3$, while at and above 17 nm they were primarily tetragonal phase. The positions, intensities and symmetries of the peaks were all considered during the data analysis.

In this thesis, Raman spectroscopy was used to probe the molecular vibrations of functionalised piezoelectric nanoparticles. The Raman spectra were recorded on JY LabRam-HR Spectrometer operated in backscattering geometry by using 514.5 radiation and a sample area of 500 μm diameter, with a typical acquisition of 20 × 7 seconds. The calibration was performed by referencing the spectrometer to the 520.07 cm^{-1} line of silicon.

2.3.12 Gas Chromatography (GC)[17] and CO Oxidation Catalysis Measurements

Gas chromatography (GC) performs the dynamic separation and identification of all types of volatile organic compounds and several inorganic gases. It enables the quantitative and qualitative determination of the nature of compounds in mixtures and can be automated for the analysis of solid, liquid and gas-phase samples.

GC involves the partitioning of gaseous solutes between an inert gas mobile phase and a stationary liquid or solid phase. The instrument is composed of four major parts: the injection port, the column, the detector and the data acquisition system. GC requires the use of a carrier gas to carry the sample through the system, with helium most commonly used. The column is used for the separation of the components in the sample mixture, with the stationary phase chosen in order to optimise the separation of the components in the gaseous mixture. Packed and capillary columns are available, though the latter is more popular due to its ability to perform high-quality separation.

The choice of detector depends upon the type of separations being performed. Thermal conductivity detectors (TCD) can detect any type of gas provided it is

different to the carrier gas, while flame ionisation detectors (FID) are particularly useful for the analysis of organics and require the use of hydrogen or air to support the combustion of the organics.

The TCD works by sensing changes in the thermal conductivity of the column effluent and compares it to the reference flow of carrier gas. Since most compounds have a thermal conductivity much less than that of the common carrier gases (helium or hydrogen), when an analyte elutes from the column the effluent thermal conductivity is reduced and this produces a detectable signal. The TCD consists of an electrically heated filament in a temperature-controlled cell. The TCD is routinely used for the analysis of gases such as CO_2, H_2 and O_2, and unlike the FID it is not limited to the analysis of hydrocarbons.

Gas chromatography was used in this thesis to measure the temperature dependent oxidation of carbon monoxide in the presence of a catalyst and oxygen gas. The setup is shown in Figure 17.

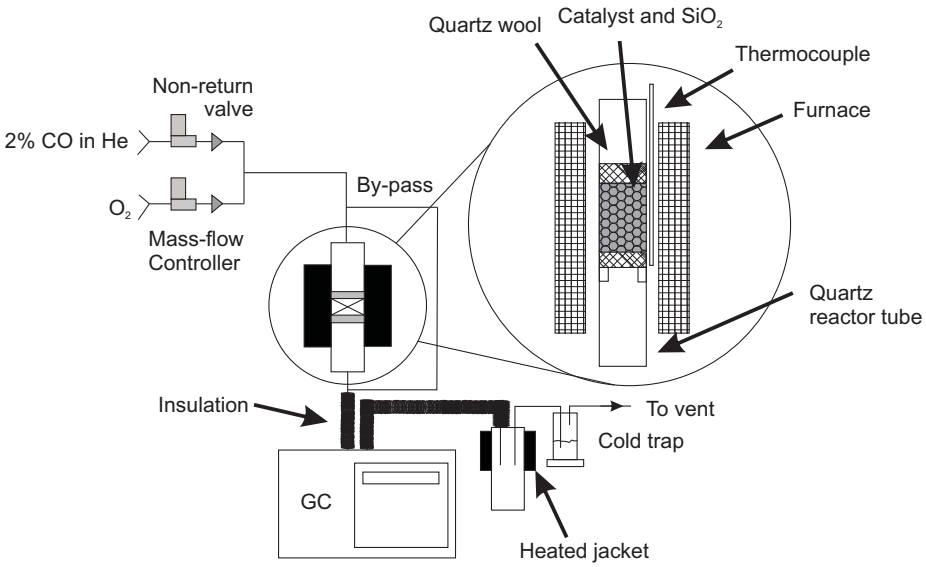

Figure 17. Schematic of the setup used to evaluate temperature-dependent CO oxidation activity.

CO oxidation was carried out in a Pyrex glass continuous flow microreactor (9 mm i.d.) with an online Varian 3800 gas chromatograph equipped with a TCD. A gas mixture of 2% CO at 25 ml min^{-1} and O_2 at 5 ml min^{-1} was used, with He used as the carrier gas. 0.02 g catalyst samples were diluted with 0.18 g of SiO_2 for testing. The reactor was initially held at room temperature and the gases were flowed through the by-pass. The CO level was monitored for a period of 30 minutes before the by-pass was closed, and the CO levels were monitored for a further 30 minutes and found to be the same as when flowing though the by-pass. The temperature of the furnace was then increased in 10 to 20 °C temperature jumps and the CO levels were measured after 30 min time on stream at each temperature, which enabled the reactor to stabilise after heating. CO conversion was taken as being a reduction in the level of CO measured by GC, as compared to the level measured when flowing the gases though the by-pass. The samples were not subjected to pre-treatment prior to measurement.

2.3.13 Nuclear Magnetic Resonance (NMR)[17]

2.3.13.1 Theory

Nuclear magnetic resonance (NMR) enables the identification and proof of structure of chemical compounds. The application of NMR to solution systems has yielded a wealth of structural information derived from chemical shifts, couplings and integrated intensities of spectral resonances.

Magnetically active nuclei possess a property called spin, they also have a magnetic moment and angular momentum and the ratio between these two properties is known

as the magnetogyric ratio. When a nucleus is placed in an external magnetic field, B_0, Zeeman splitting and nuclear precession can be observed. Zeeman splitting results in the creation of $2I + 1$ magnetic energy states (Figure 18); where I is the spin quantum number. Nuclei with an atomic mass and number that are even ($I = 0$) cannot produce an NMR signal, but for spin ½ nuclei such as ^{1}H, ^{31}P, ^{15}N and ^{13}C, Zeeman splitting results in the existence of two energy levels and the difference in energy is proportional to the strength of the external magnetic field, B_0. Nuclear precession is the motion of a spinning body whose axis of rotation is constantly changing orientation. The spinning axis describes a cone around the external magnetic field axis (Figure 19). The precessional frequency for any nucleus is equal to the strength of B_0 multiplied by the magnetogyric ratio.

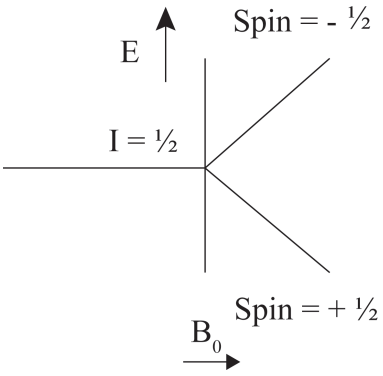

Figure 18. The nuclear Zeeman splitting for spin ½ nuclei.

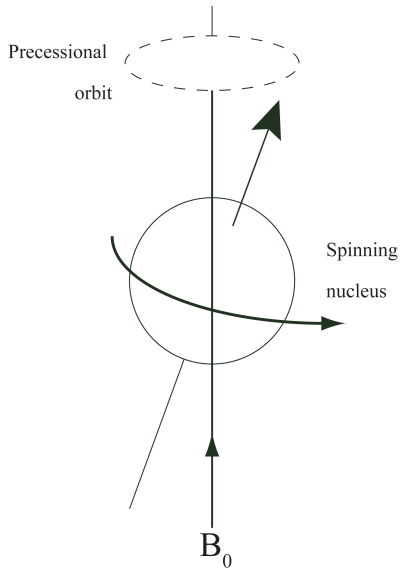

Figure 19. Nuclear precession in a magnetic field B_0.

In the magnetic field B_0 the precessing nucleus may have its magnetic moment aligned with the field (the low-energy state) or against the field (the high-energy state). At room temperature there is only a small excess of nuclei in the low-energy state (about 1 part in 10^5) and consequently NMR is a measurement with relatively low sensitivity.

NMR spectroscopy provides information about the structure of a compound due to effects known as chemical shift and spin-spin coupling. The chemical shift in an NMR spectrum arises as a consequence of the local environment of the nuclei; circulating electrons in nearby atoms produce magnetic fields that can either oppose or reinforce the external magnetic field. When the local magnetic field opposes the external field the nucleus is described as being shielded. A shielded nucleus experiences lower effective field strength and therefore resonates at a lower frequency. The opposite is true when the local magnetic field reinforces the external field. Consequently each type of nucleus can have a slightly different resonant

frequency depending on its environment, and this difference is called the chemical shift. It is defined as the difference in resonant frequency of a nucleus in a particular environment relative to a reference nucleus, divided by the spectrometer frequency. Therefore, upon comparison with the many tables of chemical shifts for specific nuclei available in the literature, it is possible to ascertain information about the local environment of a nucleus.

The magnetic field of a nucleus also exerts an effect on neighbouring nuclei called spin-spin coupling. This is transmitted though bonds *via* bonding electrons and results in the splitting of the NMR lines into $2nI+1$ lines, where n is the number of neighbouring nuclei and I is the spin quantum number. The coupling constant J is independent of the external magnetic field strength, and its magnitude can give information about the stereochemical relationship between nuclei, with the number of splittings giving information about the number of neighbouring nuclei. Coupling can occur through more than one bond, though it becomes weaker the further apart the nuclei are.

2.3.13.2 Solid State Nuclear Magnetic Resonance (SSNMR)

The application of NMR to solid systems has historically proven challenging as dipole-dipole interactions are not averaged to zero in the solid state, and so there is significant line broadening resulting in most of the structural information being lost.

The nuclear spins in the solid state can interact with one another in a number of ways depending on the orientation of the nuclear spin vector to the magnetic field. These interactions can be separated into five components: the Zeeman, chemical shift,

dipolar, electron spin and quadrupolar interactions. The second and third components are generally the biggest contributing factors to spectral broadening. The chemical shift interaction adjusts the resonance position due to magnetic field modification by surrounding electrons, which, in solids, can be anisotropic thus leading to broadening. Dipolar interactions between equal and unequal nuclear spins, which are only significant between adjacent nuclei, split the resonance by an amount dependent upon the two spins orientation with respect to the magnetic field. It is therefore a huge problem in the solid state as all orientations are present. The quadrupolar interaction occurs for nuclei with a non-integral spin above ½, which experience non-spherically symmetric electric fields proportional to the field strength and the quadrupolar coupling constant. The electron-spin interaction is very small and can usually be ignored. Finally, the Zeeman interaction is that which determines the observational frequency and aligns the nucleus to the applied field.

The technique of magic angle spinning (MAS) has been developed for use in solid state NMR spectroscopy in order to reduce the problem of spectral broadening. The sample is spun mechanically around an axis inclined at an angle θ to the magnetic field axis, at a frequency comparable with the frequency spread of the chemical shift anisotropy. Both the dipolar and chemical shift anisotropy are dependent on a orientation term proportional to $(3\cos^2 \theta\text{-}1)$, and thus can be reduced to zero by setting the value of θ to 54.73°. Spinning rates are of the order of several kHz, with slower rates leading to non-averaging of the dipolar interactions resulting in spinning side bands.

MAS-NMR spectroscopy was used in this thesis for probing the binding sites of organic molecules anchored to the surface of inorganic nanoparticles. Spectra were recorded at 9.4T on a Bruker DSX400 spectrometer equipped with a 4mm ^{1}H/X/Y

triple resonance probehead. Samples were spun in zirconia rotors using dry N_2 bearing gas. The $^{31}P\{^1H\}$ solid-state NMR spectra were acquired at 400.16 MHz for ^1H and 161.98 MHz for ^{31}P at an MAS rate of 10.0 kHz. A ^{31}P $\pi/3$ pulse length was 2.6 μs and the recycle delay was 90 s. Two Phase Pulse Modulation (TPPM) decoupling was used during acquisition. The ^{31}P chemical shifts are quoted in ppm with respect to 85% wt. H_3PO_4 solution. Data processing was performed using Bruker Topspin 1.3 software. Dr. James T. A. Jones at the University of Liverpool performed the MAS-NMR experiments.

2.3.14 SQUID[22]

The principle of magnetic induction is used to generate a magnetic moment in the SQUID. A superconducting magnet is charged to generate a static field, which then induces a magnetic moment in the sample being measured. A superconducting detection coil comprised of a set of three coils, located in the sample chamber, couples inductively with the sample. The sample is moved through the coils and an electric current is induced, which produces an oscillation in the magnetic flux. The SQUID measures a change in voltage, which is proportional to the magnetic moment of the sample. The temperature is then changed and the detection process repeated.

A Quantum Design MPMS-XL Superconducting Quantum Interference Device (SQUID) magnetometer was used to test the magnetic properties of the prepared materials by measuring the magnetism as a function of temperature and magnetic field, to produce a DC magnetisation curve. For the measurement, 50 mg of sample was placed in a gelatine capsule, which was then placed in a straw and attached to

the probe before placing in the SQUID. Dr. Giap van Duong at the University of Liverpool performed these measurements.

2.3.15 Measurement of the Magnetoelectric (ME) Effect[23, 24]

There are three direct methods for measuring the magnetoelectric effect, these are the static, quasi-static and dynamic methods. In the static and quasi-static methods, the charge produced by poling and measuring tends to accumulate at the grain boundaries and moves towards the electrode during the measurement, and this can lead to inaccurate results. The set up for measurement of the ME effect by the dynamic method is shown in Figure 20.

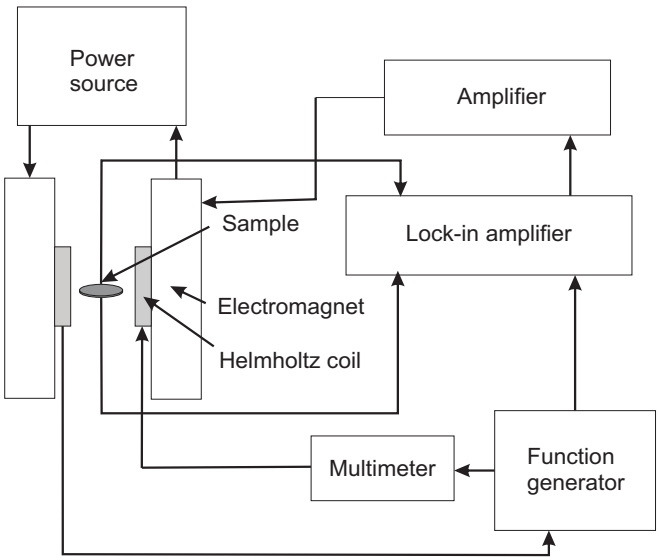

Figure 20. Schematic of the setup for measuring the magnetoelectric effect *via* the dynamic method.

The principle of this technique is to measure the value of a small AC ME voltage (V_{out}) that appears across the sample when applying a small AC magnetic field, instead of measuring the ME charge or voltage as in the static method. The bias AC magnetic field prevents charges moving towards the electrodes since a suitable signal with an appropriate frequency is used where the polarity of the signal changes with time.

The ME coefficient α_E was measured employing the lock-in technique in which a small AC magnetic field (0.25 Oe, calculated from the driving current that was measured using a Maplin Precision Gold M-5010 EC multimeter) produced by a Helmholtz coil of 28 turns each with 50 mm diameter and powered by a function generator (Wavetek) and an amplifier (Prosound 1600), is superimposed onto the DC bias field (up to 10 kOe) which is generated by an electromagnet (LakeShore, Model EM4-HVA) and a programmable DC power source (LakeShore Model 642 Electromagnet Power Supply). The ME response was measured using a lock-in amplifier (Signal Recovery, Model 5210). The samples were placed perpendicular to the field and thus the ME coefficient measured is a longitudinal one. All measurements were carried out at RT. Data acquisition was performed by altering the current produced by the DC power source between 0 A and 60 A at 5 A intervals, noting the ME signal and phase at each point.

As the magnitude of the magnetoelectric effect depends upon the AC magnetic field strength and the thickness of the sample, the measured potentials must be normalised to allow for comparison between samples. The magnetoelectric coefficient, α_E, is given by the equation:

$$\alpha_E = \frac{V_{out}}{h_0 d} \tag{2.13}$$

Where V_{out} is the measured potential in mV, h_0 is the strength of the AC magnetic field in Oe and d is the effective thickness of the piezoelectric phase in the sample in cm.[23] Variation of the DC magnetic bias field enables the ME effect to be investigated at different points, and by changing the frequency of the AC field, it is possible to study the response of the sample under different time scales. As the ME signal measured by this method has a well-defined frequency (determined by the driving current) and is measured by a lock-in amplifier, the noise of the signal is dramatically reduced when compared to other methods, and the issue of charge accumulation is avoided.

In this work the dynamic method was used to measure the magnitude and evolution of the ME effect of a series of magnetoelectric samples prepared by different methods.

2.3.16 Gas Sorption[25, 26]

Gas sorption occurs as solid surfaces have a tendency to attract surrounding gas molecules. It refers to the process by which solids simultaneously absorb gas molecules inside, and adsorb gas molecules onto the surface. By monitoring the gas sorption process it is possible to obtain useful information about the solid, such as the surface area and pore size.

In order to perform these measurements it is necessary to ensure the solid sample is free of moisture and other contaminants, such as oils. Therefore a degassing step is

carried out prior to analysis, which typically involves heating the sample under vacuum, or in the flow of a dry, inert gas. The sample is then brought to a constant temperature, usually by cooling in a liquid N_2-filled dewar and small amounts of the adsorbate gas (often dry N_2 gas) are admitted into the sample chamber, which is normally a glass tube. Adsorption of the gas to the sample quickly takes place, with the strength of the interaction between the adsorbate and the sample determining whether the adsorption process is physical (weak) or chemical (strong) in nature. Physisorption arises due to weak, long-range van der Waals interactions between the adsorbate and the surface, while chemisorption occurs when the adsorbate forms a chemical bond with the surface.

The energetics of adsorption depends upon the extent to which the available surface is covered with adsorbate molecules. This is because the adsorbates can interact with each other when they lie upon the surface, and in general they would be expected to repel each other. The fractional coverage of a surface is defined by the quantity:

$$\theta = \frac{\text{Number of occupied adsorption sites}}{\text{Total number of adsorption sites}} \tag{2.14}$$

At any temperature, the adsorbate and the surface come to a dynamic equilibrium where the chemical potentials of the free adsorbate and the surface bound adsorbate are equal. The chemical potential of the free adsorbate depends on the pressure of the gas, and the chemical potential of the bound adsorbate depends on the coverage. Thus the coverage at a given temperature is a function of the applied adsorbate pressure. The variation of θ with pressure, p, at a given temperature, T, is called an adsorption isotherm. The different types of isotherms are shown in Figure 21 below.

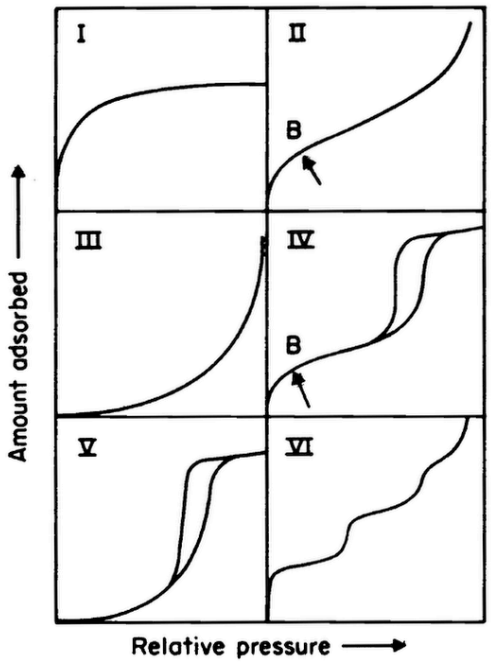

Figure 21. Types of physisorption isotherms.[27]

The simplest isotherm, the Type I or Langmuir[25] isotherm, is useful for considering adsorption at low coverage, though at high adsorbate pressures and high coverage it fails to predict experimental results. It is typical for microporous materials which have small external surfaces (e.g. activated carbons and zeolites), and the limiting uptake is governed by the accessible micropore volume rather than by the internal surface area. The Langmuir treatment does not take into account the possibility of the initial overlayer of adsorbate acting as a substrate surface itself, allowing for multilayer coverage. This possibility was considered by Brunauer, Emmett and Teller.[26]

The reversible Type II or BET isotherm is obtained for a non-porous or macroporous absorbent. The Type II isotherm represents unrestricted monolayer-multilayer

absorption. Point B (Figure 21) is often considered to be the point at which multilayer absorption begins.

The BET isotherm is found to adequately describe physisorption at intermediate coverage (θ = 0.8 - 2.0), but fails to represent observations at low or high coverage. The BET isotherm is, however, reasonably valid around θ = 1.0 and this is useful in characterising the area of the absorbent. If one can determine experimentally the number of moles of adsorbate required to give θ = 1.0 (i.e. a monolayer), one can determine the specific area of the adsorbent, SA:

$$SA = \frac{\text{Surface area of adsorbent}}{\text{Mass of adsorbent}} \tag{2.15}$$

Practically, θ is not directly measured, but instead, the number of moles adsorbed is measured as a function of equilibrium pressure. Algebraic rearrangement of the BET isotherm to produce a linear equation is usually applied to experimental data:

$$\frac{z}{n\,(1-z)} = \frac{1}{n_{mono}\,c} + \left(\frac{(c-1)}{n_{mono}\,c}\right) z \tag{2.16}$$

Where z is the relative pressure (p/p^o), n is the number of moles adsorbed, n_{mono} is the number of moles adsorbed in a monolayer and c is a constant representing the relative strengths of adsorption to the surface and condensation of the pure adsorbate.[26]

This implies that over the range where the BET isotherm is valid a plot of $z/n(1-z)$ vs. z will be linear. The slope and intercept of this line allows the determination of n_{mono} and c respectively. The specific area of the sample is therefore simply:

$$SA = \frac{N_A n_{mono} \sigma}{m} \tag{2.17}$$

Where N_A is Avogadro's number; σ is molecular area of the adsorbate (e.g. 15.8 Å^2 for N_2) and m is the mass of the sample.[26]

Other types of isotherms shown in Figure 21 include Type IV isotherms. They have a characteristic hysteresis loop, which results from capillary condensation taking place in mesopores, and the limiting uptake over a range of high p/p^o. The initial part of the isotherm is the same as that for Type II, though the Type IV isotherm is typically observed with mesoporous absorbents.

Types III, V and VI are observed much less frequently. Type III does not exhibit a point B as for Type II. For these isotherms adsorbate-adsorbate interactions play an important role. Type V is related to Type III in that the adsorbate-adsorbent interaction is weak, and is found with certain porous adsorbents. Type VI represents stepwise multilayer adsorption on a uniform non-porous surface. The sharpness of the steps depends on the system and the temperature.

Gas Sportion is also a useful for determining the size, distribution and volume of the pores in a sample. Generally, the porosity of a sample is described by one of the following terms: non-porous, microporous (pores < 2 nm in diameter), mesoporous (pores between 2 – 50 nm) and macroporous (pores > 50 nm in diameter). The pore volume can be calculated from the amount of gas adsorbed onto the solid surface using the adsorption and desorption isotherm. According to the Barrett, Joyner and Halenda (BJH) theory, the volume of pores with diameters ranging from 1.7 to 300 nm in size can be given.[28] BJH theory also enables the calculation of the pore diameter, D_p using the following equation:

$$D_p = D_k + 2 \times t \tag{2.18}$$

D_k is given by the Kelvin equation below:

$$D_k = -\frac{4 \times V_0 \times \sigma \times \cos\phi}{R \times T \times \ln\frac{p}{p^o}} \tag{2.19}$$

The layer thickness t can be determined using Halsey's relationship:

$$t = 0.354 \times \left(\frac{-5.00}{\ln\frac{p}{p^o}} \right)^{0.333} \tag{2.20}$$

Where D_p is the pore diameter, t is the adsorbed layer thickness, D_k is the inner pore (Kelvin) diameter filled with condensate, V_0 is the gas molecular volume, σ is the surface tension, ϕ is the contact angle of liquid nitrogen in the pores, R is the gas constant, T is the temperature in Kelvin and p/p^o is the relative pressure.[28]

Plotting the pore diameter against the relative pressure enables an assessment of the pore size distribution. For nanomaterials, the pore diameter can be a measure of the size of the interstitial voids between the particles if it found that the pore diameter is larger than the size of a particle.[29, 30]

In this thesis gas sorption was used to obtain BET surface areas and pore sizes of metal oxide nanoparticles. A Micrometrics ASAP 2000 nitrogen adsorption analyser was used and samples were outgassed for 3 h at 250 °C under vacuum. Full BET adsorption and desorption isotherms were collected for each sample (53 points of data).

2.3.17 Ultraviolet and Visible Molecular Absorption Spectrometry[17]

Ultraviolet and visible molecular absorption spectroscopy (UV/Vis) is a quantitative technique that relies on the absorption of UV (λ = 200-400 nm) or visible light (λ = 400-800 nm) photons. The absorption of the photon of light excites electronic transitions within the sample, with the most common transitions involving pi systems and non-bonding electrons (e.g. $\pi \rightarrow \pi^*$ or $n \rightarrow \pi^*$). UV/Vis spectroscopy is useful for the qualitative identification of molecular species, often achieved by comparing the spectrum of the unknown compound with reference spectra. In addition, UV/Vis spectrophotometers are sensitive enough to enable the quantitative determination of the concentration of reactive species in multicomponent systems.

UV/Vis measurements reported in this thesis were carried in order to investigate the nature of organic molecules bound to nanoparticle surfaces and were performed on a Perkin Elmer 650 S Spectrophotometer.

2.3.18 Fluorescence Microscopy[31]

The fluorescence microscope is used to study materials using the properties of fluorescence and phosphorescence. Typically, the material to be studied is labelled with a fluorophore and illuminated at a specific wavelength that excites electronic transitions within the fluorophore, which then emits light of a longer wavelength as the excited electrons relax down to the lower energy state. The required wavelength required for excitation is achieved by the use of filters, which can be interchanged to obtain other wavelengths.

In this thesis Lucifer yellow was used as the fluorophore and was bound to the surface of functionalised nanoparticles and excited with 425 nm radiation, with emission occurring at 532 nm (the green part of the visible spectrum). The measurements were carried out in order to confirm the presence of organic molecules on nanoparticle surfaces. The measurements were carried out by Miss Cristina Olariu at the University of Liverpool, on a Leica DMiL inverted microscope using a DFC 350F camera.

References

1. B. L. Cushing, V. L. Kolesnichenko and C. J. O'Connor, *Chem. Rev*. **2004**, 104, 3893-3946.

2. J. A. Dirksen and T. A. Ring, *Chem. Eng. Sci.* **1991**, 46, 2389-2427.

3. G. Demazeau, *J. Mater. Sci.* **2008**, 43, 2104-2114.

4. M. Yoshimura and K. Byrappa, *J. Mater. Sci.* **2008**, 43, 2085-2103.

5. K. Byrappa, *J. Ceram. Soc. Jpn*. **2009**, 117, 236-244.

6. J. Livage, M. Henry and C. Sanchez, *Prog. Solid State Chem.* **1988**, 18, 259-341.

7. S. Laurent, D. Forge, M. Port, A. Roch, C. Robic, L. V. Elst and R. N. Muller, *Chem. Rev.* **2008**, 108, 2064-2110.

8. G. Gartweitner and M. Niederberger, *J. Am. Ceram. Soc.* **2006**, 89, 1801-1806.

9. M. S. Tokumoto, S. H. Pulcinelli, C. V. Santilli, V. Briois, *J. Phys. Chem. B* **2003**, 107, 568.

10. D. B. Williams and C. B. Carter, *Transmission Electron Microscopy*; Plenum Press, **1996**.

11. D. J. Smith, *Characterisation of Nanomaterials Using Transmission Electron Microscopy*, *Nanocharacterisation*; RSC Publishing, **2007**.

12. P. J. Goodhew, J. Humphreys, R. Beanland, *Electron Microscopy and Analysis*; Taylor & Francis, **2001**.

13. R. Brydson, *Electron Energy Loss Spectroscopy and Energy Dispersive X-ray Analysis*, *Nanocharacterisation*; RSC Publishing, **2007**.

14. A. R. Lupini, S. N. Rashkeev, M. Varela, A. Y. Borisevich, M. P. Oxley, K. van Benthem, Y. Peng, N. de Jonge, G. M. Veith, S. T. Pantelides, M. F. Chisholm and S. J. Pennycook, *Scanning Transmission Electron Microscopy*, *Nanocharacterisation*; RSC Publishing, **2007**.

15. C. Hammond, *The Basics of Crystallography and Diffraction*; Oxford University Press, **1997**.

16. W. L. Bragg, *Proceedings of the Cambridge Philosophical Society*, **1912**, 17, 43-57.

17. F. Settle, *Handbook of Instrumental Techniques for Analytical Chemistry*; Prentice Hall, **1997**.

18. T. J. Manning and W. R. Grow, *Inductively Coupled Plasma – Atomic Emission Spectroscopy*, Springer-Verlag, **1997**.

19. D. Damjanovic, *Rep. Prog. Phys.* **1998**, 61, 1267.

20. J. G. Solé, L. E. Bausá, D. Jaque, *An Introduction to the Optical Spectroscopy of Inorganic Solids;* Wiley, **2005**.

21. Y. V. Kolen'ko, K. A. Kovnir, I. S. Neir, T. Taniguchi, T. Ishigaki, T. Watanabe, N. Sakamoto, M. Yoshimura, *J. Phys. Chem. C* **2007**, 111, 7306.

22. J. Clarke, A. I. Braginski, *The SQUID Handbook: Applications of SQUIDs and SQUID Systems*

23. G. V. Duong, R. Groessinger, M. Schoenhart and D. Bueno-Basques, *J. Magn. Magn. Mater.* **2007**, 316, 390-393.

24. M. M. Kumar, A. Srinivas, S. V. Suryanarayana, G. S. Kumar and T. Bhimasankaram, *Bull. Mater. Sci*, **1998**, 21, 251-255.

25. I. Langmuir, *J. Am. Chem. Soc.* **1918**, 40, 1361-1403.

26. S. Brunauer, P. H. Emmett and E. Teller, *J. Am. Chem. Soc.* **1938**, 60, 309-319.

27. K. S. W. Sing, D. H. Everett, R. A. W. Haul, L. Moscou, R. A. Pierotti, J. Rouquérol, T. Siemieniewska, *Pure Appl. Chem.* **1985**, 57, 603.

28. M. Hasznos-Nezdei, J. Kovács, S. Kováts, A. B. Shahroodi, P. Szabó-Révész, *Powder Technol.* **2006**, 167, 104.

29. J. Rouquerol, D. Avnir, C. W. Fairbridge, D. H. Everett, J. H. Haynes, N. Pernicone, J. D. F. Ramsay, K. S. W. Sing and K. K. Unger, *Pure Appl. Chem*. **1994**, 66, 1739.

30. R. G. Avery and J. D. F. Ramsay, *J. Coll. Int. Sci*. **1973**, 42, 597.

31. J. R. Lakowicz, *Topics in Fluorescence Microscopy*; Kluwer Academic Publishers, **1992**.

Chapter 3

Chapter 3

3 Synthesis and Characterisation of $CoFe_2O_4$ Nanoparticle CO Oxidation Catalysts

3.1 Introduction

The synthesis of metal oxide nanoparticles has attracted interest due to the unique and size dependent properties these materials can possess. This size dependence has been found to cover the electronic, optical, thermal, mechanical, magnetic and chemical properties.[1] Semiconductor quantum dots have, for instance, been found to display remarkable luminescence, non-linear optical properties and quantum confinement effects as the particle size decreases,[2, 3] whilst nanoparticles of magnetic materials are known to have markedly different field-dependent magnetisation behaviour when contrasted with the bulk.[4] Wet chemical approaches to the synthesis of nanoparticles enable considerable control over particle size and morphology, and include solvothermal,[5,6] coprecipitation,[7,8] reverse micelle,[9,10] sol-gel,[11,12] and template-based[13,14] methods.

Nanoparticles have, for many years, been of interest as catalysts.[15] Heterogeneous catalysts often contain supported nanoparticles of the active material in order to optimise utilisation, an example of which is the Cu/ZnO methanol synthesis catalyst.[16] The application of nanoparticle catalysts to heterogeneous systems dates

back to the 19th century and today they are utilised on a large scale to produce plastics and pharmaceuticals. There are also environmental applications, such as in the removal of NO_x pollutants from vehicle exhausts by noble metal nanoparticle catalysts.[17]

Catalysis of CO oxidation is another important reaction where nanoparticles have found use. CO oxidation catalysts that are stable and exhibit a high activity at room temperature and below have applications for CO removal in respirators, vehicle exhaust emissions and in H_2 rich gas feeds used for fuel cells, amongst others.[18-20] Presently used CO oxidation catalysts include hopcalite, $CuMn_2O_4$, which was first reported in 1921.[21-23] Though active at room temperature, hopcalite also remains effective at elevated temperatures, though it is known to undergo deactivation under humid conditions. Supported Au nanoparticles are amongst the most active CO oxidation catalysts, displaying 100% conversion of CO to CO_2 under ambient conditions, although they can be more expensive than transition metal oxide catalysts and are only active below 8 nm in size.[24, 25] They can also be prone to deactivation and poisoning.[26-28] In other applications, such as in incinerators, low temperature conversion is not required due to the high operating temperatures of these systems, and so thermal stability and resistance to deactivation are more important considerations in this case.

In this chapter $CoFe_2O_4$ nanoparticles are prepared *via* wet chemical approaches with a range of controlled particle sizes. These nanoparticles are tested for activity and stability as CO oxidation catalysts and the relationship between the nanoparticle size and catalytic activity is established. Oxides containing transition metals are candidates as catalysts for CO oxidation due to the mechanism the reaction follows, which was first described by Mars and van Krevelen.[29] The process involves both the

oxidation and reduction of the active metal centre, and consequently due to their favourable redox properties, transition metal oxides are good candidates for CO oxidation catalysis. Scalable and cheap routes to quantities of metal oxide nanoparticles with a range of controlled sizes are also developed, with characterisation performed using a range of techniques, including XRD, TEM and TGA. Although the importance of surface area is widely acknowledged in heterogeneous catalysis, the study of non-supported single particle catalysts allows the direct identification of the features of a specific particle that control activity. The catalysis of the CO oxidation reaction by metal oxides is dealt with in more detail in the introductory chapter, Chapter 1.

3.2 Experimental

$CoFe_2O_4$ nanoparticles were prepared using solvothermal and coprecipitation techniques in order to obtain samples with range of controlled sizes for CO oxidation catalysis studies. High-temperature sintering of smaller size samples was also performed to prepare nanoparticles of larger sizes. Samples are denoted C*n* where *n* is the sample number.

3.2.1 Solvothermal Synthesis of Sample C1

Sample C1 was prepared by the solvothermal route detailed by Gautam et al.[30] for the synthesis of MFe_2O_4 nanoparticles (M = Fe, Co or Zn) and was carried out as follows:

3.2.1.1 Preparation of Cupferronate Precursors

Iron (III) cupferronate and cobalt (II) cupferronate were prepared as precursors to $CoFe_2O_4$. For $Fe(cupferron)_3$, 6.5g of ferric alum (0.0135 mol, $FeNH_4(SO_4)_2.12H_2O$) was dissolved in 150 ml of H_2O and 125 mL of concentrated HCl was added. The solution was cooled in an ice bath and a 125 mL aqueous solution containing 6.27g of cupferron (0.0404 mol), also cooled in an ice bath, was added with vigorous stirring using a magnetic stirrer bar at 1000 rpm. The brown precipitate was collected *via* suction filtration using a Büchner flask and funnel, and was then washed with dilute HCl followed by 5M NH_3 in order to remove excess cupferron. The crude product was recrystallised from hexane giving 0.38 g of $Fe(cupferron)_3$ (0.8136 mmol, 5.41% yield). Microanalysis: 46.23% C, 3.19% H, 17.77% N (expected: 46.28% C, 3.21% H, 18% N).

For $Co(cupferron)_2$, 5 g $CoCl_2.6H_2O$ (0.0210 mol) was dissolved in 100 ml H_2O and the solution was cooled with an ice bath. A solution of 6.51 g cupferron (0.0420 mol) in 130.2 ml of H_2O, also cooled in an ice bath, was then added. The resulting pink precipitate was collected by suction filtration using a Büchner flask and funnel and was recrystallised from methanol. 1.6 g of product was obtained (2.5428 mmol, 20.61% yield). Microanalysis: 42.28% C, 4.41% H, 14.6% N (expected: 43.27% C, 3% H, 16.82% N).

3.2.1.2 Solvothermal Synthesis of $CoFe_2O_4$

The decomposition of the metal cupferronate complexes was performed solvothermally as the precursor complexes were only sparingly soluble at room

temperature. Fe(cupferron)$_3$ (0.19 g, 0.4068 mmol) and Co(cupferron)$_2$ (0.068 g, 0.203 mmol) were mixed in 7 mL of toluene and 0.8 g of *n*-dodecylamine was added. The mixture was then poured into a 23 mL capacity sealed autoclave (30% filling) and was then heated in an oven preheated to 230 °C for 1 hour. The autoclave was quenched to room temperature by removal from the oven and 2-propanol was added to the resulting solution in order to increase the polarity of the solvent and cause the hydrophobic *n*-dodecylamine-capped particles to precipitate. The solution was then decanted and the black coloured product was washed repeatedly with 2-propanol and dried at 40 °C overnight. 0.012 g of $CoFe_2O_4$ was obtained (25.2% yield).

3.2.2 Coprecipitation Synthesis of Sample C2

Sample C2 was prepared according to the route detailed by Ghosh et al.[31] A solution was made consisting of 10 ml of 0.1 M $CoCl_2.6H_2O$ in H_2O and 10 mL of 0.2 M $FeCl_3.6H_2O$ in H_2O. This was heated to 70 °C and 50 mL of a 0.3 M solution of hexadecyltrimethylammonium bromide (CTAB) in H_2O was added and the heating was continued. 3 M NaOH at 70 °C was then added to pH 12 under magnetic stirring at 1000 rpm and the reaction was left for 1 hour. The solution was then allowed to cool and the liquid was decanted by magnetic assistance. This involved placing a NdFeB magnet beneath the reaction vessel until the solution appeared clear and the nanoparticles had collected at the bottom, whereupon the liquid was decanted off and the magnet removed. The product was washed repeatedly with H_2O using this decanting process, and then dried at 40 °C for 24 hours.

3.2.3 Synthesis of Samples C3-C8

Samples C3-C8 were prepared *via* coprecipitation using oxalic acid (ox) and ethylenediamine (en) or triethanolamine (TEA) as stabilising groups. The procedure is outlined as follows for sample C3:

Oxalic acid (6.0 mmol) and ethylenediamine (3.0 mmol) were mixed and dissolved in 5 ml H_2O with magnetic stirring at 1000 rpm. This solution was added to another solution consisting of 10 ml of 0.1 M $CoCl_2.6H_2O$ in H_2O and 10 mL of 0.2 M $FeCl_3.6H_2O$ in H_2O at 70 °C (the ratio of ox to Co^{2+} was therefore 6:1). Upon addition of the oxalic acid-ethylenediamine (ox-en) mixture an orange coloured precipitate formed, indicating the formation of M $(oxalate)_n$ (M = Co, Fe) complexes. Addition of approximately 3 ml of concentrated HCl removed the precipitated metal oxalates, leaving the pH of the solution at 1. A 3 M NaOH solution at 70 °C was then added dropwise, with magnetic stirring at 1000 rpm, until pH 12 was reached. The reaction was left stirring at 70 °C for 1 hour and the black-coloured product was collected by magnetically-assisted decanting of the liquid. The product washed several times with H_2O and dried at 40 °C for 24 hours.

Samples C4-C8 were prepared using the same procedure as detailed for sample C3, however the composition of the capping groups was different for each sample. For sample C4, 3.0 mmol of ox and 3.0 mmol of en were used so that the ratio of ox to en was 1:1, and the ox to Co^{2+} ratio was 3:1. For sample C5, 12.0 mmol of ox and 6.0 mmol of en were used, meaning a 2:1 ratio of ox to en and a ox to Co^{2+} ratio of 12:1, twice that of C3. For sample C6, 9.0 mmol of ox and 3.0 mmol of triethanolamine were used, giving a ox to Co^{2+} ratio of 9:1, whilst 6.0 mmol of ox were used for sample C7 with no other capping group, giving a 6:1 ratio of ox to

Co^{2+}. Finally, 3.0 mmol of en were used for sample C8, with no other capping group, giving a Co^{2+} to en ratio of 3 to 1.

3.2.4 Synthesis of Samples C9 and C10

Samples C9 and C10 were prepared by heating 100 mg of sample C6 in an alumina crucible at 600 °C and 700 °C respectively for 2 hours in air. In both cases the heating rate was 5 °C min^{-1} and the cooling rate 10 °C min^{-1}.

3.2.5 Synthesis of $NiFe_2O_4$ Nanoparticles

$NiFe_2O_4$ nanoparticles were prepared according to the route reported by Yener et al.[10] Two solutions were prepared, the first consisted of 21.79 g (0.0490 mol) of docusate sodium (AOT), 22.05 mL (0.1340 mol) of isooctane and 50 mL of NH_4OH solution (28-30% NH_3 basis). The second consisted of 21.79 g (0.0490 mol) of AOT, 22.05 mL (0.1340 mol) of isooctane, 3.38 g (8.40 mmol) of $Fe(NO_3)_3.9H_2O$ in 10 mL H_2O and 1.28 g (4.4 mmol) of $Ni(NO_3)_2.6H_2O$ in 10 mL H_2O. The solutions were mixed at room temperature, which formed an orange/brown microemulsion, which was stirred over 48 hours. The microemulsion was then washed 4 times with methanol, which was decanted after each wash, and the solid material was dried at 85 °C overnight. Calcination was then carried out at 300 °C for 6 hours which gave the ferromagnetic product.

3.2.6 Characterisation

3.2.6.1 Gas Sorption

Surface area measurements were carried out using the BET method on a Micrometrics ASAP 2000 nitrogen adsorption analyser. Samples were outgassed for 3 h at 250 °C under vacuum. Full BET adsorption and desorption isotherms were collected for each sample (53 points of data).

3.2.6.2 X-ray Diffraction

XRD was carried out on a PANalytical X'pert system using Co $K_{\alpha 1}$ radiation. The samples were ground and deposited onto a zero-background Si sample holder and acetone was dropped on, with agitation performed to distribute the sample across the surface of the holder. Once the acetone had evaporated, the holder was mounted onto the spinner stage and data was collected using a 15 mm beam mask, 4 ° incident beam slit and 13 mm diffracted beam slit. Data collection was performed over the angle range 30 – 60 ° 2θ.

3.2.6.3 Fourier-Transform Infrared Spectroscopy

FTIR was carried out on a Nicolet Nexus instrument. 4 mg of sample was ground with spectroscopic grade KBr (400 mg) and scanned 256 times at 2 cm^{-1} resolution. Pure KBr was used for determining the background and analysis was performed using the Omnic E.S.P software.

3.2.6.4 Thermogravimetric Analysis

TGA was performed using a Seiko SII-TG/DTA 6300 thermal analyser under a flow of N_2. The samples were heated at a rate of 5 °C min^{-1}, held for 30 minutes at the target temperature and cooled at 10 °C min^{-1}`.

3.2.6.5 Transmission Electron Microscopy

TEM was carried out on a Jeol JEM-2011 electron microscope operated at 200 kV. The powder specimen for TEM examination was ground, suspended in acetone and deposited on a copper specimen grid supported by a holey carbon film. TEM images were recorded with a Gatan 794 CCD camera at magnifications of 600,000 to 1,000,000.

3.2.6.6 Elemental Analysis

Microanalysis was performed on a Thermo Flash EA 1112 Series C, H, N and S analyser.

3.2.6.7 Catalysis Testing

The CO oxidation reactions were carried out in a Pyrex glass continuous flow microreactor (9 mm i.d.) with an online Varian 3800 gas chromatograph equipped with a TCD. A gas mixture of 2% CO in He at 25 ml min^{-1} and O_2 at 5 ml min^{-1} was used, and 0.02 g catalyst samples were diluted with 0.18 g of SiO_2 for testing. A typical run involved flowing the gases through the by-pass for 30 minutes to

determine the composition of the gas mixture, then opening the inlet to the reactor, which was initially held at room temperature. The composition of the gas mixture was observed to be equal in both cases. The temperature-dependent CO conversion was measured after allowing the catalyst to stabilise at each temperature for 30 minutes on stream, with the temperature jumps ranging from 20 °C to 10 °C. The latter was performed once conversion was first observed to occur. The catalysts were not subjected to pre-treatment prior to the measurement. All chemicals were used as received from Sigma-Aldrich Inc

3.3 Results and discussion

3.3.1 Synthesis and Characterisation of $CoFe_2O_4$ Nanoparticles

Nanoparticle samples with a range of controlled sizes were prepared in order to study their behaviour as CO oxidation catalysts. The first sample, C1, was prepared solvothermally in toluene in the presence of *n*-dodecylamine.[30] X-ray diffraction (XRD) was used to confirm the phase-purity of the sample and the particle size was calculated by applying the Scherrer equation (3.1) to all reflections in the angle range 35-60 ° 2θ. For sample C1, the particle size was determined to be 6.1 nm.

$$D = \frac{k\,\lambda}{\beta \cos\theta} \tag{3.1}$$

Where D is the particle diameter in nanometres, k is the structure factor (0.9 for these samples), λ is the wavelength of the radiation (17.88965 nm Co $K_{\alpha 1}$), β is the full width half-maximum of the XRD reflection in radians and θ is the angle of reflection in degrees.

A coprecipitation route using the capping agent CTAB[28] was used to prepare sample C2. The X-ray diffraction (XRD) pattern for this sample can be seen in Figure 1, and the Scherrer equation gave a particle size of 12.9 nm for this sample.

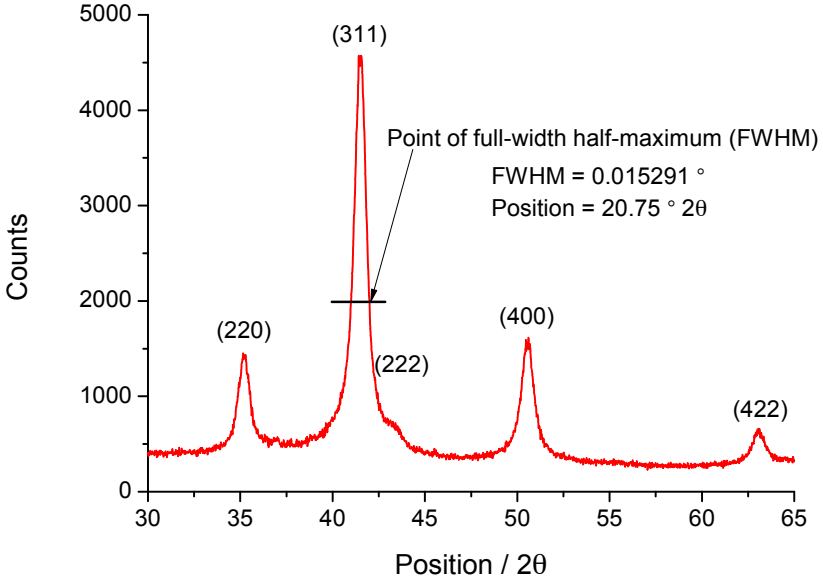

Figure 1. X-ray diffraction pattern of sample C2, CTAB stabilised $CoFe_2O_4$ nanoparticles. The expected reflections for $CoFe_2O_4$ over this angle range are marked.

The coprecipitation route was chosen for the preparation of further samples as it enabled the synthesis of large amounts of material more quickly and under milder conditions than the solvothermal route. Yields of around 12 mg were typically obtained for the solvothermal reactions at 220 °C in contrast to yields of 500 mg for the coprecipitation synthesis which was carried out at 80 °C. Hence, further size control of $CoFe_2O_4$ nanoparticles was explored through variation of the capping group using the coprecipitation synthetic procedure.

Sample C3 was prepared using the same procedure as sample C2, with some modifications. Instead of using CTAB as a capping group, two candidate surface stabilising groups: oxalic acid (ox) and ethylenediamine (en) were used, which are shown in Figure 2.

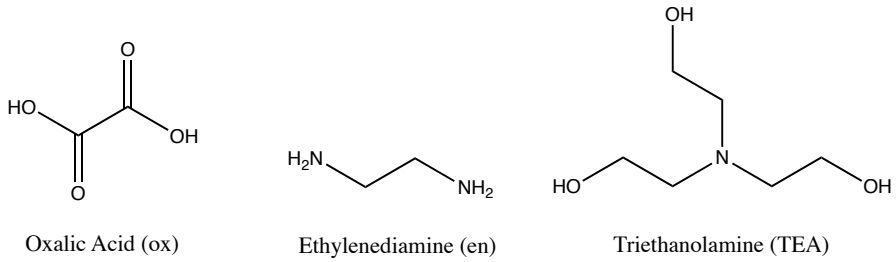

Oxalic Acid (ox) Ethylenediamine (en) Triethanolamine (TEA)

Figure 2. Oxalic acid (ox), ethylenediamine (en) and triethanolamine (TEA), the stabilising groups used for samples C3-C8.

The idea was that formation of a hydrogen-bonding array between these molecules on an oxide nanoparticle surface would arrest the particle growth and enable the stabilisation of particle size. Although this hydrogen-bonding array did not operate in practice, this combination of capping groups and the resulting synthetic protocol did reproducibly produce controlled size spinel nanoparticles.

The XRD pattern for sample C3 is shown in Figure 3. The XRD particle size for this sample was determined to be 8.2 nm. By modifying the ratio of ox to en, substituting en for triethanolamine (TEA) and changing the ratio of the capping group concentration to that of the Co^{2+} salt, it was possible to further tune the particle size.

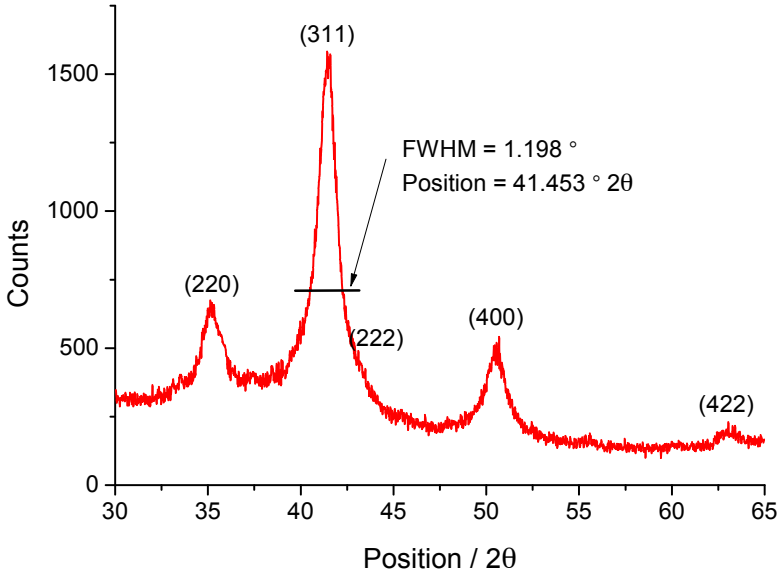

Figure 3. X-ray diffraction pattern for sample C3, 8.2 nm $CoFe_2O_4$ nanoparticles prepared using oxalic acid and ethylenediamine capping groups at a molar ratio of 2:1.

Sample C4, prepared with an ox to en ratio of 1:1 and an ox to Co^{2+} ratio of 3:1 afforded 7.8 nm particles, while sample C5, prepared with an ox to en ratio of 2:1 and an ox to Co^{2+} ratio of 12:1 (twice that of sample C3) afforded 7.6 nm particles. The use of triethanolamine (TEA) in place of en at a 3:1 ox to TEA ratio, and a 9:1 ox to Co^{2+} ratio permitted the synthesis of 5.8 nm $CoFe_2O_4$ (sample C6) using the same procedure. Sample C7 prepared with oxalic acid only, at a 6:1 ratio to Co^{2+} had a particle size of 12 nm, while sample C8 prepared with ethylenediamine only, at a 3:1 ratio to Co^{2+} afforded 10.4 nm $CoFe_2O_4$.

Increases in particle size were observed after heating samples of C6 in an alumina crucible at 600 (sample C9) and 700 °C (sample C10) for 2 hours. Sample C9 had an

XRD particle size of 15 nm, while sample C10 had an XRD particle size of 30 nm. All samples were phase-pure by XRD, with Figure 4 demonstrating the XRD peak sharpening across a range of samples with increasing particle size.

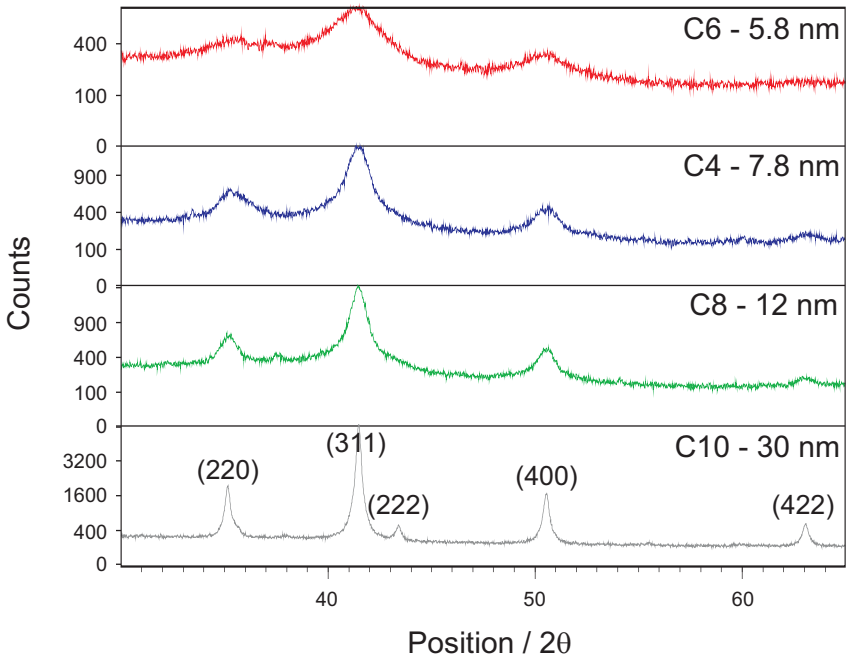

Figure 4. X-ray diffraction patterns for a range of $CoFe_2O_4$ nanoparticle samples with increasing particle size. The (222) reflection is less visible in samples with smaller particle sizes due to its low intensity and overlap with the nearby, intense (311) reflection.

A summary of the samples particle sizes and synthesis conditions is displayed in Table 1. BET surface areas (calculated and experimental) for selected samples are also presented.

Sample Name	Particle diameter /nm	Preparation route	Capping group(s)	Theoretical surface area / $m^2 g^{-1}$	Experimental surface area / $m^2 g^{-1}$
C1	6.1	Solvothermal	*n*-dodecylamine	186	-
C2	12	Coprecipitation	CTAB	94	37
C3	8.2	Coprecipitation	ox-en 2:1	138	-
C4	7.8	Coprecipitation	ox-en 1:1	145	57
C5	7.6	Coprecipitation	ox-en 2 x 2:1	149	85
C6	5.8	Coprecipitation	ox-TEA 3:1	195	104
C7	12	Coprecipitation	Ox	94	-
C8	10.4	Coprecipitation	En	109	-
C9	15	C6 @ 600 °C	None	75	24
C10	30	C6 @ 700 °C	None	37	15

Table 1. A tabulated summary of the sample preparation conditions, X-ray diffraction particle sizes and BET surface areas for $CoFe_2O_4$ nanoparticles.

HRTEM images of samples C6 and C3 in Figures 5 and 6 show the particles are spherical in shape. This data also shows the Scherrer equation provides a good estimate of the particle size of these samples. For example, the XRD-derived particle size is 5.8 nm for sample C6 and 8.2 nm for C3, whilst the TEM yields a value of 4 ± 3 nm for C6 and 8 ± 3 nm for C3. The closer agreement in the case of sample C3 may be related to a more even particle size distribution, shown in Figure 7, and the difference in the numbers can be accounted for by considering the types of measurement used: the XRD evaluation of the particle size is a volume average measure which takes into account the entire sample, whilst the TEM evaluation provides a number average and this can be more easily skewed by particularly small

or large particles. The absence of large stabilising groups on the nanoparticle surfaces of samples C3-C10 leads to particle aggregation on the TEM grids, producing experimental uncertainty in assessing the true size distribution, which contributes to the large standard deviations observed in the TEM assessments of particle size. However, the TEM measurements indicate that the Scherrer equation is measuring actual particle sizes rather than smaller domains within larger particles, due to the good agreement between the XRD and TEM-derived sizes.

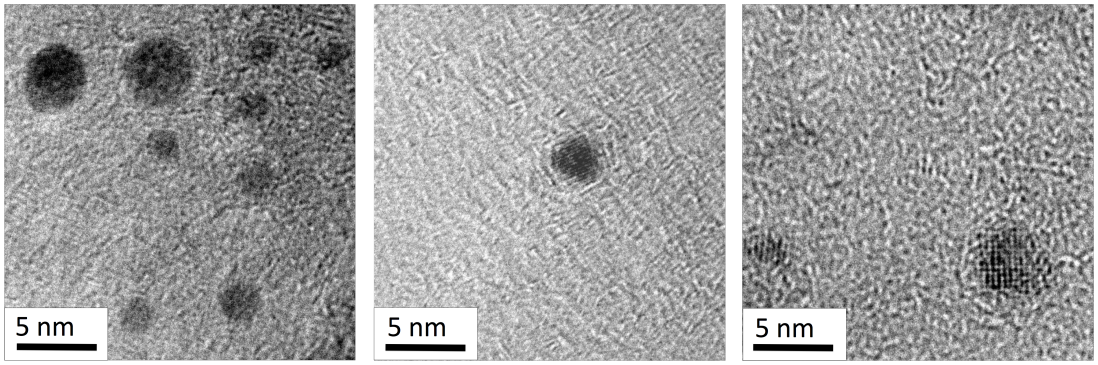

Figure 5. High-resolution transmission electron microscopy images of sample C6, 5.8 nm XRD-size $CoFe_2O_4$ nanoparticles prepared with ox-TEA (3:1) capping group.

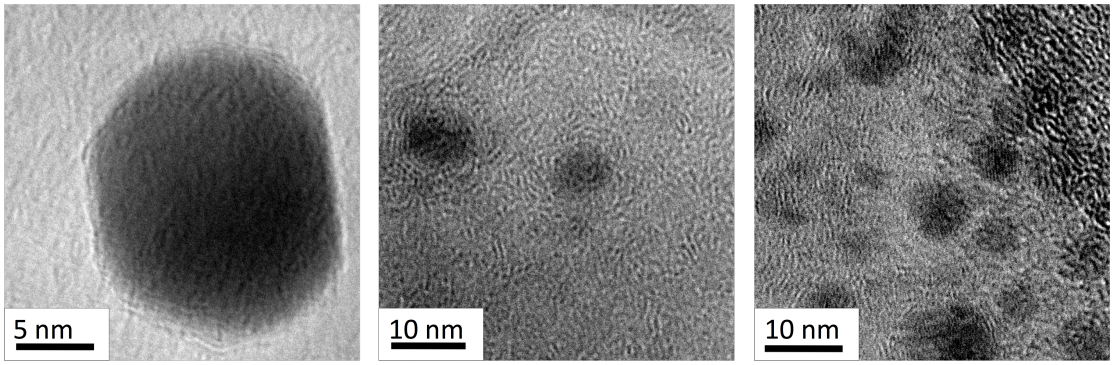

Figure 6. High-resolution transmission electron microscopy images of sample C3, 8.2 nm XRD-size $CoFe_2O_4$ nanoparticles prepared with ox-en (2:1) capping group.

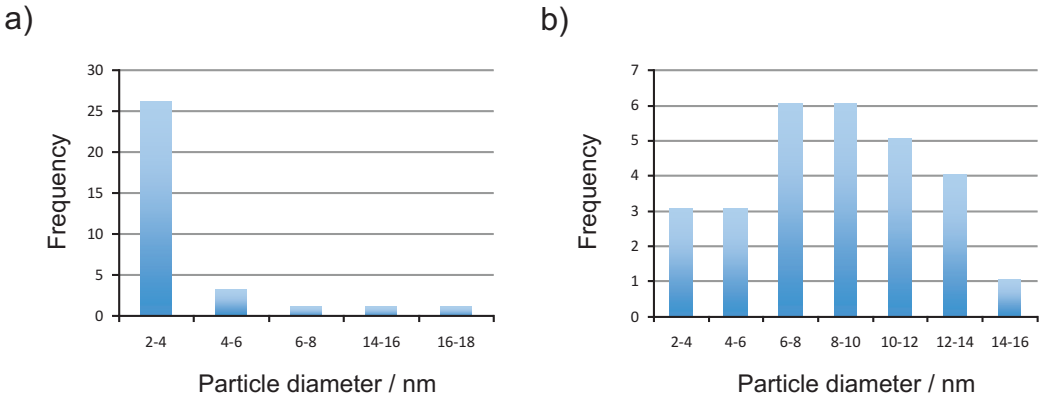

Figure 7. Histograms showing the TEM particle size distributions for $CoFe_2O_4$ samples C6 (a) and C3 (b).

BJH desorption pore sizes are presented in Figure 8 for samples C2, C4, C9 and C10. This measurement acts as a bulk probe of the sample, and the even distribution of the BJH desorption pore sizes suggests that the samples are all non porous. This is supported by the N_2 adsorption isotherms, which show Type IV character (see Figure 9a and b for samples C2 and C10 respectively). There is also a correlation between the pore diameter and particle size (Figure 10), further supporting the TEM and X-ray evidence that the particle size is systematically varied across the sample set. The measured pore diameters are thought to arise from the interstitial voids between the particles, which become larger with increasing particle size; this is typical behaviour for non-porous solids where the particles are sufficiently closely packed.[32, 33]

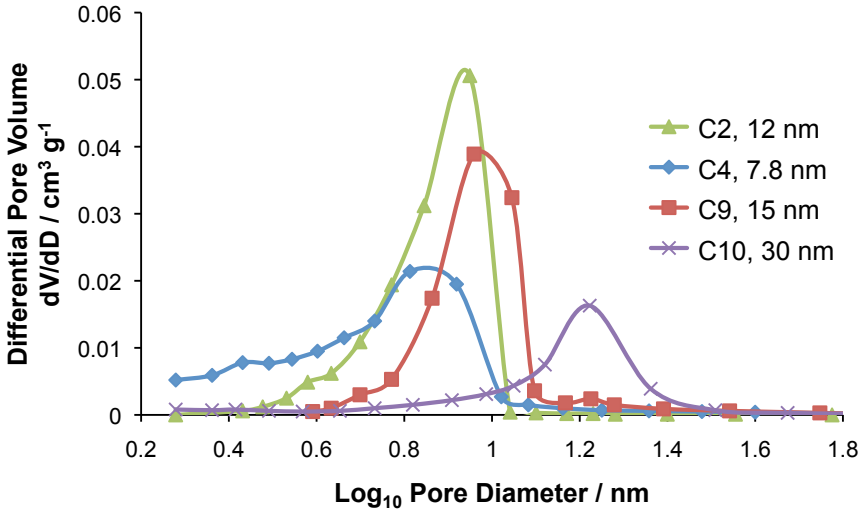

Figure 8. BJH desorption *dV/dD* pore size distribution for selected $CoFe_2O_4$ nanoparticle samples.

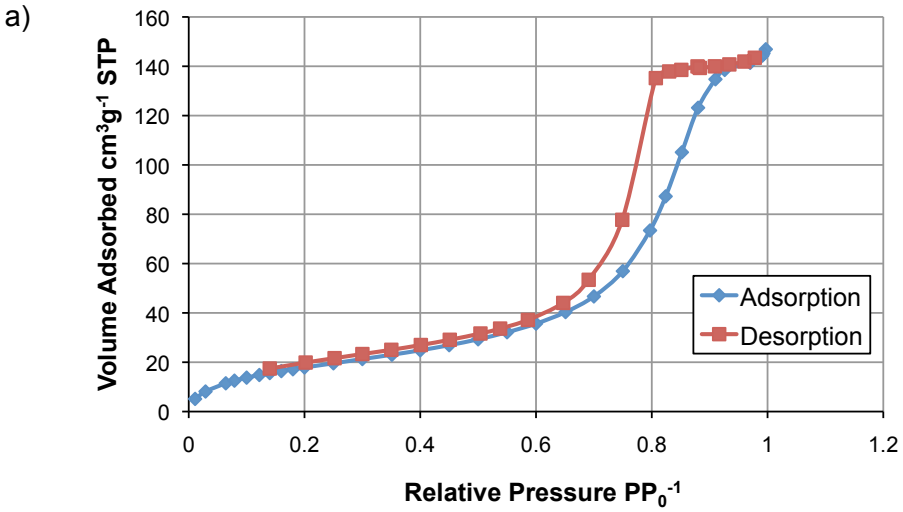

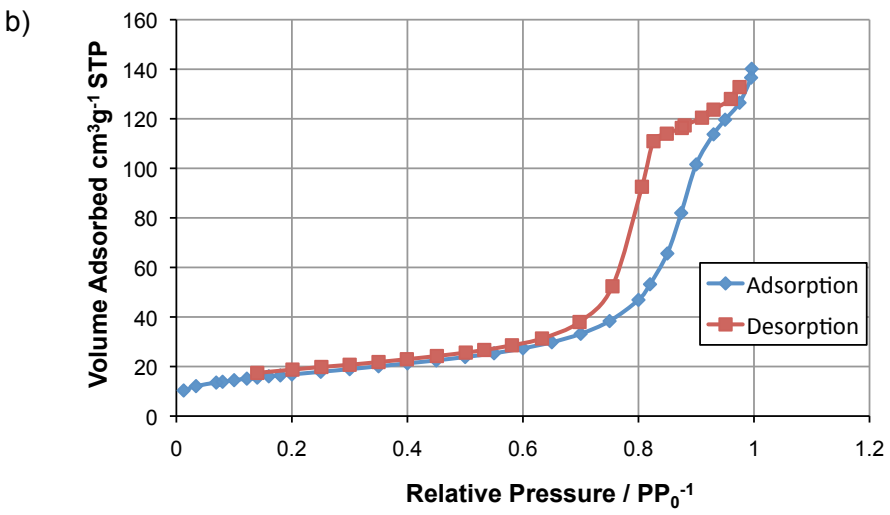

Figure 9. Nitrogen adsorption isotherms for $CoFe_2O_4$ nanoparticle samples C2 (a) and C10 (b). Both samples display Type IV behaviour.

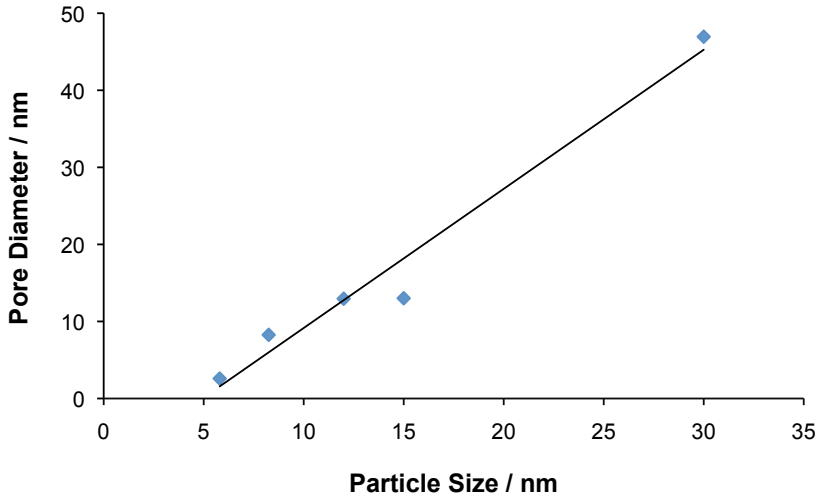

Figure 10. A graph of pore diameter versus X-ray diffraction particle size for samples C2, C4, C6, C9 and C10.

Experimental and theoretical BET surface areas are displayed in Table 1. Theoretical surface areas were calculated as follows. Considering the surface area of a nanoparticle, SA_{NP}, of radius r:

$$SA_{NP} = 4\pi r^2 \tag{3.2}$$

The volume of the nanoparticle V_{NP} with radius r:

$$V_{NP} = \frac{4}{3}\pi r^3 \tag{3.3}$$

The mass of the nanoparticle with m_{NP} with a density ρ:

$$m_{NP} = \rho V_{NP} \tag{3.4}$$

The number of nanoparticles per gram, N, is therefore:

$$N = \frac{1}{m_{NP}} \tag{3.5}$$

So the theoretical surface area per gram of $CoFe_2O_4$, SA, is:

$$SA = SA_{NP} N \tag{3.6}$$

Where SA_{NP} is the surface area of a nanoparticle in m^2 with a radius r in metres, V_{NP} is the volume of a nanoparticle in m^3 with a radius r in metres, m_{NP} is the mass of a nanoparticle in grams, ρ is the theoretical density of $CoFe_2O_4$ *in* gm^{-3}, N is the number of nanoparticles per gram and SA is the surface area in m^2g^{-1}.

As expected, these data show the surface area per gram of sample increasing with decreasing particle size. A plot of the surface area versus particle size is shown in Figure 11 below. The data follows a $1/r^2$ relationship, as one would expect for

spherical particles. The differences in the experimental and theoretical surface areas (e.g. 195 m^2 g^{-1} theoretical versus 104 m^2 g^{-1} experimental for sample C6) likely arise due to the particle size distributions within the sample (the calculation for the theoretical surface area assumes the particles are perfect spheres of a uniform XRD-derived particle size, whilst the TEM shows there is some size-distribution present). Aggregation of the nanoparticles is also likely to occur under the BET pre-treatment conditions where the particles are heated at 250 °C under vacuum for 3 hours.

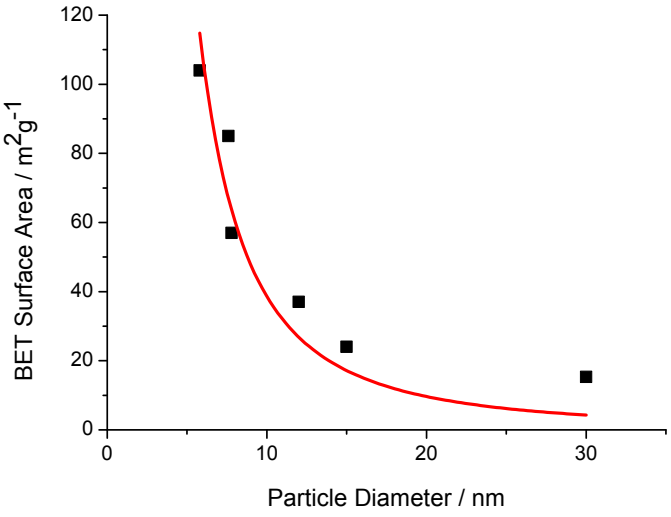

Figure 11. Experimental BET surface area versus the X-ray diffraction-derived particle diameter for samples C2, C4, C5, C6, C9 and C10. The data is fitted to the function $y = Ax^{-2}$ where A is 3862 ± 316.

Considering the nature of the nanoparticles surfaces, the CHN microanalysis data in Table 2 shows an absence of nitrogen in samples C3-C6 where mixed ox-en or ox-TEA capping groups were used. As both en and TEA are nitrogen-containing ligands, one would expect to observe nitrogen in the microanalysis of these samples

if these ligands were present on the surfaces of the nanoparticles. The conclusion can therefore be drawn that the originally envisaged hydrogen bonded assemblies of the two stabilising groups are not present on the surfaces of the particles.

Sample	C / %	H / %	N / %	Formula	Per NP	Per Ion
C1	14.21	3.76	1.20	$CoFe_2O_4(dodecylamine)_{0.36}$	583	0.88
C2	7.44	1.79	0	$CoFe_2O_4(CTAB)_{0.20}$	2408	0.94
C3	0.77	1.02	0	$CoFe_2O_4(ox)_{0.10}$	393	0.33
C4	0.78	1.04	0	$CoFe_2O_4(ox)_{0.11}$	371	0.36
C5	1.24	1.21	0	$CoFe_2O_4(ox)_{0.17}$	531	0.52
C6	2.53	1.69	0	$CoFe_2O_4(ox)_{0.34}$	473	0.79
C7	0.31	0.92	0	$CoFe_2O_4(ox)_{0.04}$	492	0.19
C8	1.99	1.53	1.22	$CoFe_2O_4(en)_{0.12}$	961	0.50

Table 2. Elemental analysis and compositional formulae for samples C1-C8. 'Per NP' refers to the number of capping group molecules calculated per $CoFe_2O_4$ nanoparticle based on microanalysis data and XRD particle sizes. 'Per Ion' is a measure of the coverage of the capping group molecules on the particle surface and refers to the number of capping group molecules per surface M^{2+} ion.

The presence of carbon and hydrogen and the absence of nitrogen in the microanalysis data of samples C3-C6 suggests that only the more strongly chelating oxalic acid groups are binding to the metal oxide surface: under the basic conditions where the nanoparticles are precipitated, the oxalic acid molecules will be de-protonated and the charged O^- ligands would be expected to bind to Co^{2+} and Fe^{3+}

more strongly than the neutral N. The amines do, however, appear to perform a significant role in controlling the particle size. For instance, sample C7, prepared in the absence of an amine but with oxalic acid, had an average particle size of 12 nm, roughly double that found when oxalic acid was used in conjunction with triethanolamine (sample C6, 5.8 nm). The amines may be controlling the precipitation process from solution and influencing the particle nucleation by coordination to the transition metal cations.

The compositional formulae $CoFe_2O_4(ligand)_x$ for samples C1-C8 were calculated as follows for sample C3. Considering the weight fraction of oxalic acid in a theoretical mixture of oxalic acid and $CoFe_2O_4$ at a 1:1 molar ratio:

$$\frac{MW_{ox}}{MW_{ox} + MW_{CoFe_2O_4}} = \frac{90.03}{(90.03 + 234.63)} = 0.28 \tag{3.7}$$

And the weight percentage of carbon in oxalic acid:

$$\frac{MW_C}{MW_{ox}} = \frac{(12 \times 2)}{90.03} = 26.68\% \tag{3.8}$$

Then the weight percentage of carbon in a theoretical mixture of oxalic acid/$CoFe_2O_4$ at a 1:1 molar ratio is:

$$26.68\% \times 0.28 = 7.40\% \tag{3.9}$$

So the fraction of oxalic acid per $CoFe_2O_4$ in sample C3 is:

$$\frac{C\%_{Expt}}{C\%_{Theor}} = \frac{0.77}{7.40} = 0.10 \tag{3.10}$$

Where MW refers to the molecular weight and C% refers to the percentage of carbon in the theoretical 1:1 mixture ($C\%_{Theor}$) and the measured C% in the sample ($C\%_{Expt}$).

Therefore the compositional formula is $CoFe_2O_4(ox)_{0.1}$ for sample C3. The excess of hydrogen observed in the microanalysis data likely results from adsorbed surface H_2O species. Using these formulae and considering the XRD-derived particle sizes, it is possible to approximate the number of capping groups per nanoparticle. An example calculation is presented for sample C3. Considering the volume of an individual spherical nanoparticle, V_{NP}, of diameter 8.2 nm:

$$V_{NP} = \frac{4}{3}\pi r^3 = \frac{4}{3}\pi(4.1\times10^{-9})^3 = 2.89\times10^{-25} m^3 \quad (3.11)$$

The mass of this nanoparticle m_{NP} is:

$$m_{NP} = \rho V = 5.3\times10^{6}\times2.89\times10^{-25} = 1.53\times10^{-18} g \quad (3.12)$$

And the mass of $CoFe_2O_4$, $m_{CoFe_2O_4}$ is:

$$m_{CoFe_2O_4} = \frac{MW_{CoFe_2O_4}}{N_A} = 3.90\times10^{-22} g \quad (3.13)$$

Then the number of $CoFe_2O_4$ units per nanoparticle is:

$$N_{CoFe_2O_4} = \frac{m_{NP}}{m_{CoFe_2O_4}} = \frac{1.53\times10^{-18}}{3.90\times10^{-22}} = 3931 \text{ units of } CoFe_2O_4 \text{ per nanoparticle} \quad (3.14)$$

And so the number of capping groups per nanoparticle is:

$$N_{CG} = N_{CoFe_2O_4}\times0.10 = 393.1 \quad (3.15)$$

Where r is the radius of the nanoparticle in metres, ρ is the theoretical density of $CoFe_2O_4$ in gm^{-3}, m_{NP} is the mass of a nanoparticle of a radius r in grams, $m_{CoFe_2O_4}$ is the mass of one $CoFe_2O_4$ unit in grams, N_A is Avogadro's number, $N_{CoFe_2O_4}$ is the number of $CoFe_2O_4$ units per nanoparticle and N_{CG} is the number of capping groups

per nanoparticle. The number 0.10 in equation 3.15 is the amount of oxalic acid per $CoFe_2O_4$ as calculated in equation 3.10.

From this, it is possible to determine the number of capping group molecules per surface M^{2+} ion, i.e. the coverage of the capping group. Figure 12 illustrates the principle behind this part of the calculation.

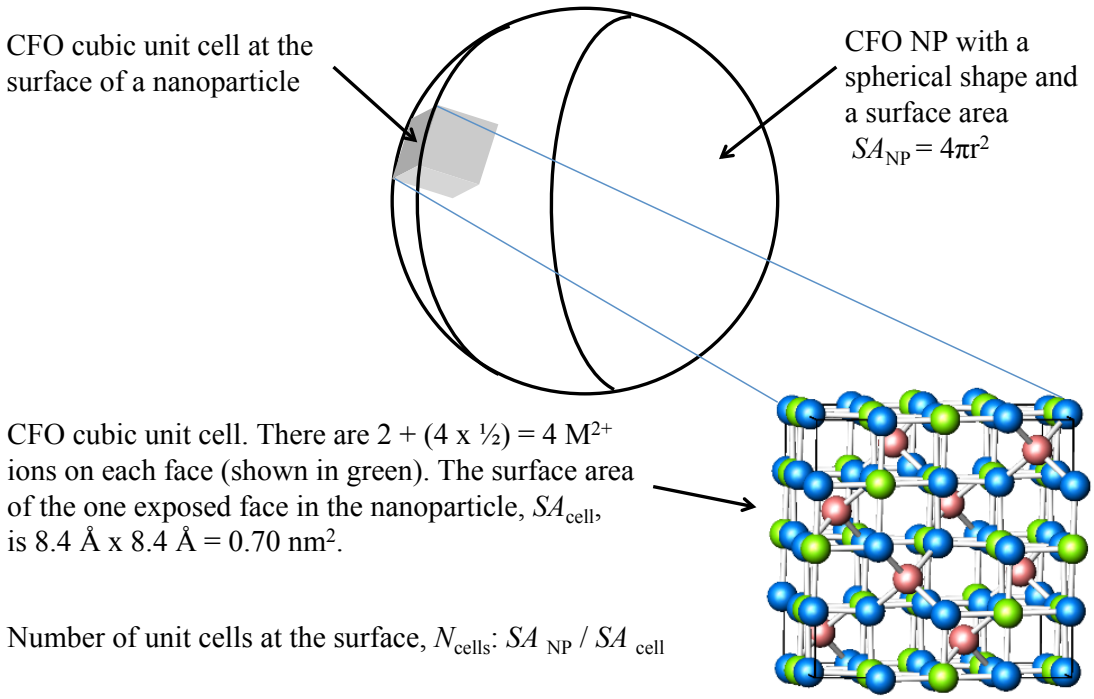

Figure 12. Illustration of a $CoFe_2O_4$ unit cell on the surface of a spherical nanoparticle. The labelling used for calculating the coverages of the capping group molecules on the nanoparticle surfaces, per M^{2+} ion is shown. This figure was prepared by Dr. Laurent Bouffier at the University of Liverpool.

Considering the surface area of a nanoparticle, SA_{NP}:

$$SA_{NP} = 4\pi r^2 = 4\pi(4.1)^2 = 211.42 \text{ nm}^2 \quad (3.16)$$

The area of one face of the $CoFe_2O_4$ unit cell, SA_{cell}, is:

$$SA_{cell} = d^2 = 0.84^2 = 0.70 \text{ nm}^2 \quad (3.17)$$

Then the number unit cells on the surface of the nanoparticle, N_{cells}, is:

$$N_{cells} = \frac{SA_{NP}}{SA_{cell}} = \frac{211.24}{0.70} = 299.97 \text{ cells} \quad (3.18)$$

Considering there are 4 M^{2+}/Co^{2+} units on each face of the unit cell, the number of surface M^{2+} units per nanoparticle, $N_{M^{2+}}$, is:

$$N_{M^{2+}} = N_{cells} \times 4 = 299.97 \times 4 = 1199.89 \text{ surface } Co^{2+} \text{ per NP} \quad (3.19)$$

So the number of capping groups per surface M^{2+}, $N_{CGM^{2+}}$, is:

$$N_{CGM^{2+}} = \frac{N_{CG}}{N_{M^{2+}}} = \frac{393.15}{1199.89} = 0.3277 \text{ capping groups per surface } M^{2+} \quad (3.20)$$

Where SA_{NP} is the surface area of a nanoparticle in nm^2, r is the nanoparticle radius in nm, SA_{cell} is the surface area of one face of the unit cell in nm^2, d is the length of one side of the $CoFe_2O_4$ cubic unit cell in nm, N_{cells} is the number of unit cells on the surface of a nanoparticle, $N_{M^{2+}}$ is the number of M^{2+} ions on the surface of the nanoparticle and $N_{CGM^{2+}}$ is the number of capping groups per surface M^{2+}.

Considering the number of capping groups per M^{2+} is lower than 1 for all samples (see Table 2), then the conclusion can be drawn that single layers, rather than multi-layers, of the surface-stabilising capping groups are present on the nanoparticle surfaces. It is likely that any multi-layers that do form during the precipitation reactions for samples C3-C8 are removed during the washing of the samples with H_2O.

3.3.2 CO Oxidation Catalysis Testing

Each sample was evaluated for CO oxidation activity. The tests involved measuring the temperature dependent conversion of CO to CO_2 up to 100% conversion (this was taken as the point where CO was no longer detectable by GC), whereupon the reactor was cooled and the test was repeated from room temperature in order to establish the reproducibility of the measurements and determine the stability of the catalysts to prolonged CO exposure and high temperatures. The temperature dependent conversion of CO to CO_2 by sample C1 over 4 runs of testing is shown in Figure 12. 'light-off' refers to the temperature at which that catalyst begins conversion, whilst T_{50}, the temperature of 50% conversion, is referred to when comparing the activity of the catalysts.

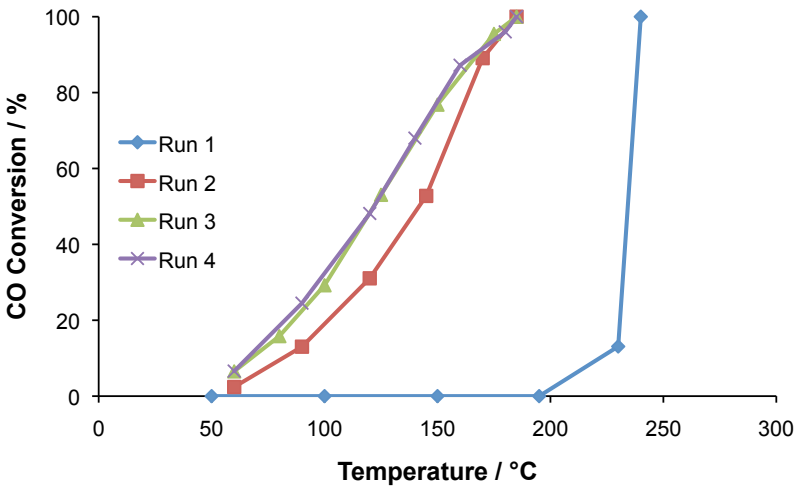

Figure 13. A graph showing the temperature dependent conversion of CO to CO_2 by sample C1, 6.1 nm *n*-dodecylamine capped $CoFe_2O_4$ nanoparticles over 4 runs of testing.

Figure 13 shows that the conversion of CO to CO_2 follows a reproducible pattern from the third run of testing onwards. The discrepancies that are observed between the first, second and third runs can be attributed to the activation of the catalysts, which occurs *in-situ* by the decomposition and desorption of the capping groups. This is further illustrated for sample C2 in Figure 14 below.

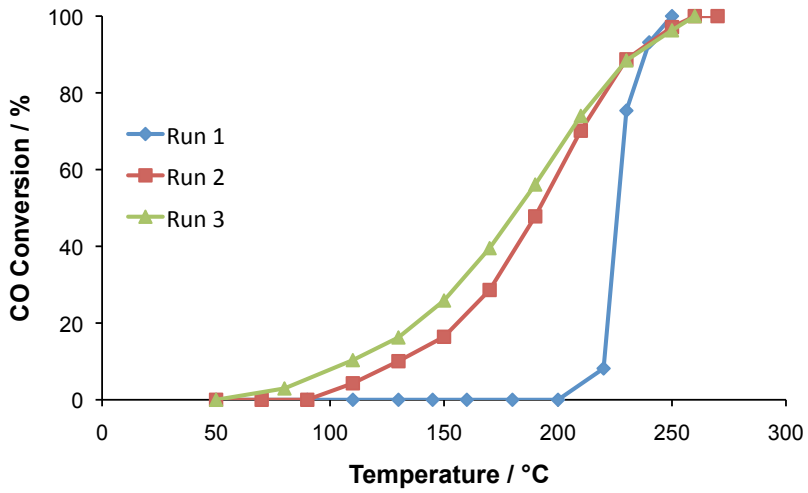

Figure 14. A graph showing the temperature dependent conversion of CO to CO_2 by sample C2, 12 nm CTAB capped $CoFe_2O_4$ nanoparticles over 3 runs of testing.

In this case, the initial activation of the catalyst is observed between 200-220 °C on the first run of testing. This correlates with the TGA results in Figure 15 which show the major weight loss of 13.66% occurring in this region, and with the literature where the decomposition and desorption of nanoparticle surface-bound CTAB molecules is observed in this temperature range.[34] Furthermore, CHN of post-catalysis samples shows a large decrease in organic content, supporting the hypothesis that the capping groups are removed during catalysis testing (Table 3).

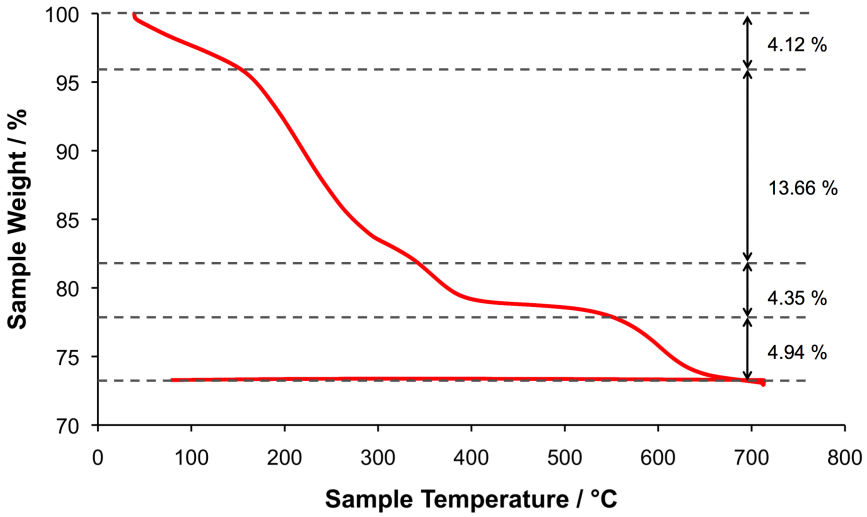

Figure 15. Thermogravimetric analysis of sample C2, the 12 nm CTAB-capped $CoFe_2O_4$ nanoparticles.

Sample	Pre-catalysis			Post-catalysis		
	C / %	H / %	N / %	C / %	H / %	N / %
C1	14.21	3.76	1.20	0.42	0.24	0
C2	7.44	1.79	0	0.55	0.13	0
C3	0.77	1.02	0	0.16	0.47	0
C4	0.78	1.04	0	0.19	0.44	0
C5	1.24	1.21	0	0.66	0.56	0
C6	2.53	1.69	0	0.57	0.70	0
C7	0.31	0.92	0	0	0.31	0
C8	1.99	1.53	1.22	0.43	0.33	0

Table 3. Microanalysis data for the $CoFe_2O_4$ CO oxidation catalysts**,** performed both before and after the catalyst testing reactions.

The TGA measurement also enables the calculation of the number of capping groups per nanoparticle using the formula shown below:[35]

$$N = \frac{\omega N_A \rho \frac{4}{3} \pi r^3 \times 10^{-23}}{MW} \tag{3.21}$$

Where N is the number of capping groups per nanoparticle, ω is the percentage weight loss in the TGA due to capping group loss (22.95%), N_A is Avogadro's number, ρ is the density of the nanoparticle (5.35 g/cm^3), r is the radius of the nanoparticle in nm and MW is the molecular weight of the capping group (364.45).

Taking the weight loss of the organics to be the 22.95% loss between approximately 160 and 700 °C (with the loss below 160 °C considered to be the loss of H_2O), then the number of capping groups per nanoparticle from the TGA is 1767, compared to 2408 calculated from microanalysis. Considering the assumptions made in both the TGA and microanalysis-based calculations of the number of capping groups (such as the assumptions on uniformity of particle size and particle shape), the numbers can be considered to be in good agreement with one another.

For samples C3-C8 the coverage of the stabilising groups was shown to be lower than for the long-chain *n*-dodecylamine and CTAB-capped particles, samples C1 and C2 (Table 2). For instance, the number of capping group molecules per surface Co^{2+} for sample C2 was 0.94, whilst this number varied between 0.33-0.79 for samples C3-C8, where the ox, en and TEA capping groups were used. This incomplete coverage of the particle surface means the samples do not display such a dramatic jump in activation during the first run of testing, but instead show a steady increase in activity as the capping groups are removed at high temperatures, demonstrated for sample C6 in Figure 16. This is likely to be because some of the $CoFe_2O_4$ surface is

accessible for catalysis in samples C3-C8 prior to capping group removal, due to the lower capping group coverage.

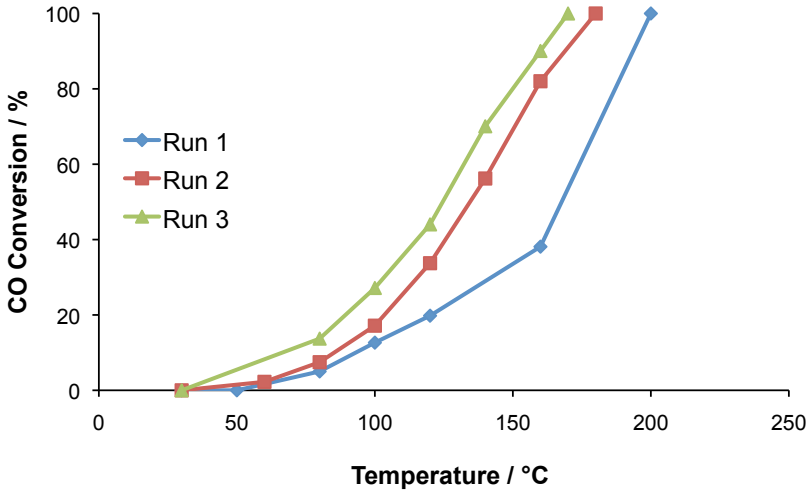

Figure 16. A graph showing the temperature dependent conversion of CO to CO_2 by sample C6, 5.8 nm $CoFe_2O_4$ nanoparticles capped with the oxalic acid and triethanolamine capping groups, over 3 runs of testing.

TGA for sample C3 is presented in Figure 17. This profile is typical for the $CoFe_2O_4$ nanoparticles prepared with the ox, en and TEA capping groups (samples C3-C7). The data shows a steady weight loss between room temperature and 220 °C, likely due to the removal of both physisorbed and H-bonded H_2O. At around 220 °C an inflection in the TGA profile is observed. This is likely indicating the loss of the oxalic acid capping groups, and this temperature is close to the decomposition temperature of oxalic acid (189.5 °C), though it is difficult to determine the exact temperature at which the loss of organic molecules begins due to the overlap with the H_2O loss region. Applying equation 3.21 to these TGA results enables an estimation of the number of oxalic acid capping groups per nanoparticle. Taking the 3.63%

weight loss that occurs from 220 °C to be the loss of the organic capping groups; the number of capping groups per nanoparticle is 361. As for sample C2, considering the approximations made, this is in good agreement with the 393 capping groups per nanoparticle calculated from microanalysis (Table 2).

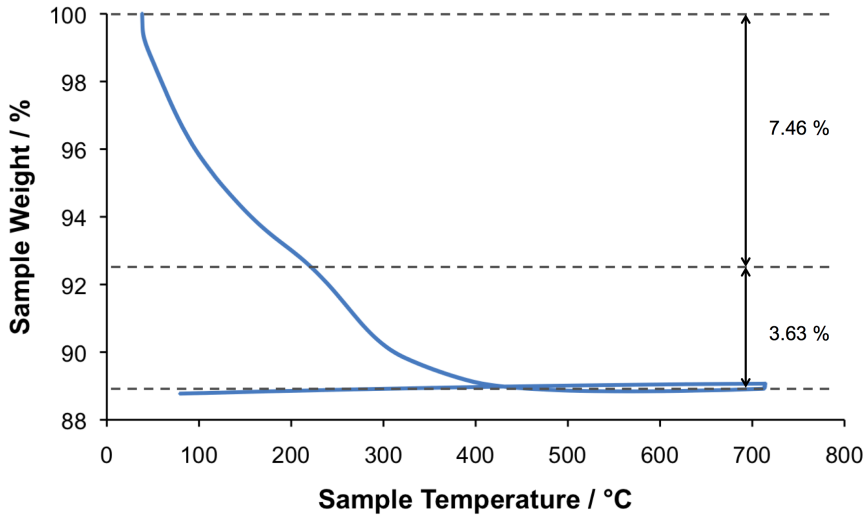

Figure 17. Thermogravimetric analysis of sample C3, $CoFe_2O_4$ nanoparticles prepared with the oxalic acid and ethylenediamine capping groups a 2:1 ratio.

Fourier transform infrared spectroscopy (FTIR) was also used to characterise the nature of the nanoparticle surface. For samples C1 and C2, where long-chain capping groups were used with high carbon contents, the FTIR clearly shows the presence of ν(C-H) stretching bands, shown in Figure 18 for sample C2 (2913 and 2846 cm^{-1}). The peak at 1481 cm^{-1} is indicative of ν(CH_2) bending vibrations, while both this peak and those due to ν(C-H) stretching disappear post-catalysis, supporting the theory that the capping groups are lost *in-situ* during testing.

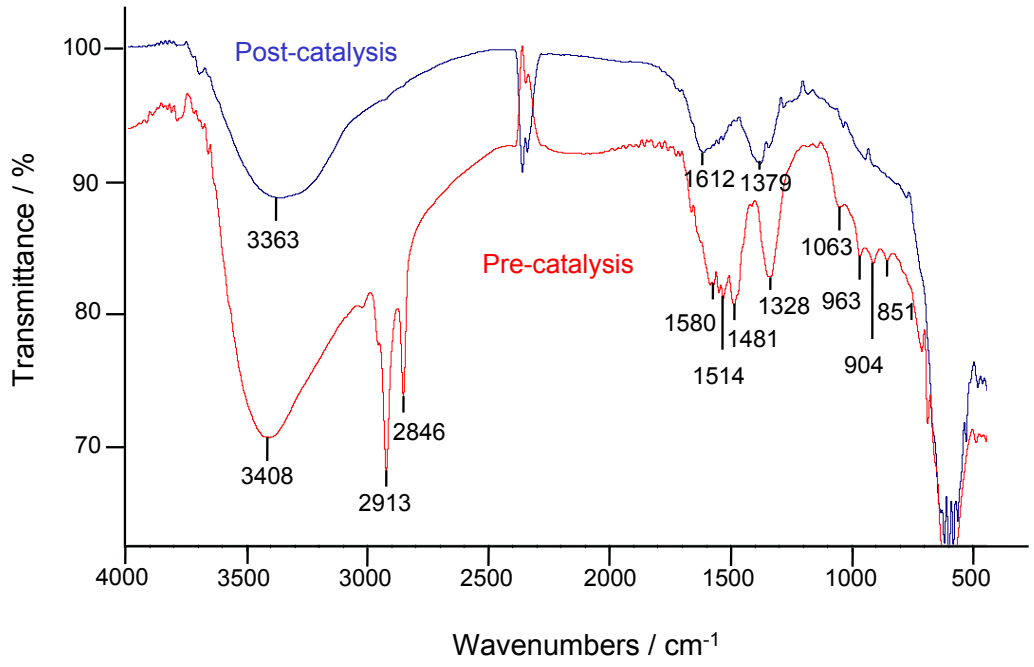

Figure 18. FTIR spectrum for sample C2, CTAB capped $CoFe_2O_4$ nanoparticles. A 1% mixture of the samples in dried KBr was used for each of the spectra.

Figure 19 shows the FTIR spectrum of sample C4, pre and post-catalysis. The appearance of this spectrum is typical for samples C3-C7 where oxalic acid is the capping group. Due to the lower coverage of the capping groups in these samples (see Table 2), and the fact that the molecular weight of oxalic acid (90.03) is much lower than CTAB (364.45), the characteristic stretching and bending frequencies are much less intense. The most intense frequencies for oxalic acid are the ν(O-H) stretching at 3400 cm^{-1}, ν(C=O) stretching at 1680 cm^{-1} and ν(C-O) stretching at 1260 cm^{-1}. These frequencies are comparable to the absorptions at 3400, 1513 and 1328 cm^{-1} in Figure 19, which diminish in intensity post-catalysis. This indicates removal of the oxalic acid capping groups *in-situ* during the catalysis testing. The peaks at around 2350 cm^{-1} in both Figures 18 and 19 are due to the presence of CO_2.

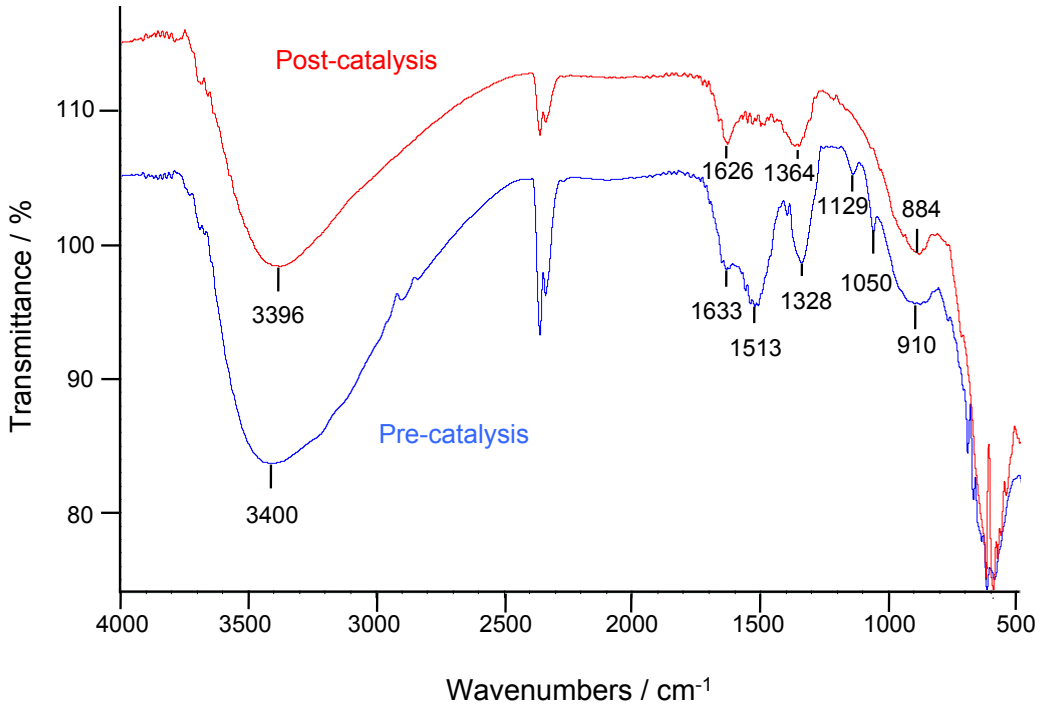

Figure 19. FTIR spectrum for sample C4, $CoFe_2O_4$ nanoparticles prepared with the oxalic acid and ethylenediamine capping groups at a 1:1 ratio. This spectrum is representative of those obtained for samples C3, C5 and C6. A 1% mixture of the samples in dried KBr was used for each of the spectra.

The CO oxidation catalysis results also showed that sample C1 (6.1 nm) has a temperature of 50% conversion of CO to CO_2, T_{50}, at 123 °C. In comparison, sample C2 (12 nm) proved less active with a T_{50} of 183 °C whilst sample C3 (8.2 nm) had a T_{50} of 133 °C, intermediate between that of samples C1 and C2. A T_{50} of 125 °C was recorded for sample C6 (5.8 nm), which also had the smallest XRD-derived particle size, whilst the highest T_{50} (262 °C), was recorded for the largest XRD-derived particle size sample, C10 (30 nm). The T_{50} was some 137 °C higher for sample C10 than for sample C6. The T_{50} of 125 °C for sample C6 compares well with the T_{50} of 160 °C that was reported in a previous study of $CoFe_2O_4$ as a CO oxidation

catalyst.[36] The temperature dependent conversion of CO to CO_2 is shown for all samples is shown in Figure 20.

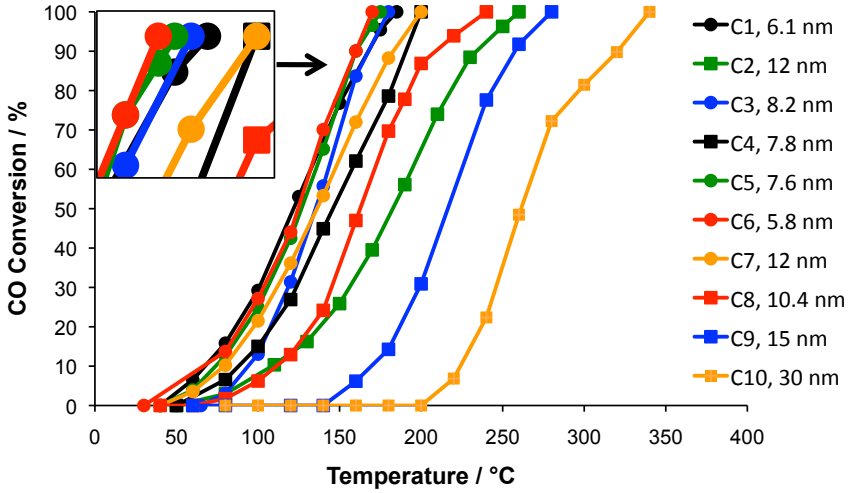

Figure 20. Graphs of conversion of CO to CO_2 versus temperature for $CoFe_2O_4$ catalysts, each on the third run of testing. Each data point was taken after 30 minutes time on stream. The inset is an expansion of the graph for the most active samples, which are closely matched in terms of activity. It is intended to be an aid to the eye and helps show the activity of the samples at 100% conversion decreasing in the order C6 > C5 > C3 > C1 > C7 ≈ C4.

XRD data on the post-catalysis samples confirmed the all samples were thermally stable under the test conditions, with no significant changes in particle size or crystal structure observed. This is illustrated for sample C4 in Figure 21. In this instance the pre-catalysis XRD particle size was 7.8 nm, while the post-catalysis size was 8.0 nm. It should be noted that the maximum temperature the samples were subjected to was the temperature at which 100% conversion of CO to CO_2 was observed, which

ranged from 170 °C for sample C6 to 360 °C for C10. The samples were held at these temperatures for 30 minutes in order to allow the reactor to stabilise and to take measurements, before cooling.

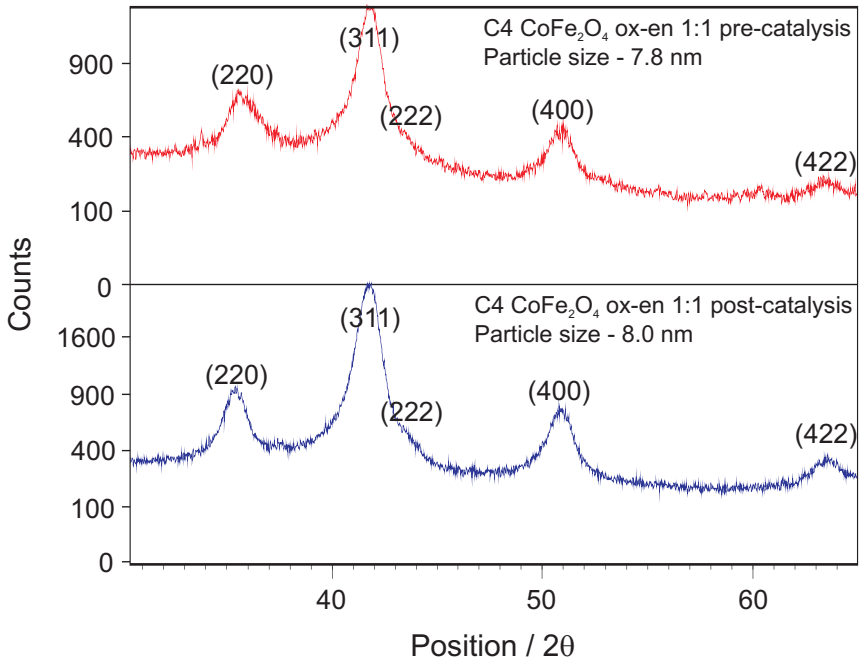

Figure 21. A comparison of X-ray diffraction patterns for sample C4 pre and post-catalysis, shown in red and blue respectively.

Sample C6 (5.8 nm) was tested for stability of catalytic performance over time, and the data can be seen in Figure 22. The test involved holding the reactor at two temperatures (100 and 140 °C) for a period of two hours, over which time the catalyst was periodically tested for activity every 8 minutes. The catalyst exhibited a sufficiently stable performance over this 2 hour period with the conversion of CO to CO_2 dropping by 5.8% from 29% at 100 °C and by 8.2% from 71% at 140 °C. This

level of stability compares well with supported Au[37] and Au-Ag[38] nanoparticles reported in the literature.

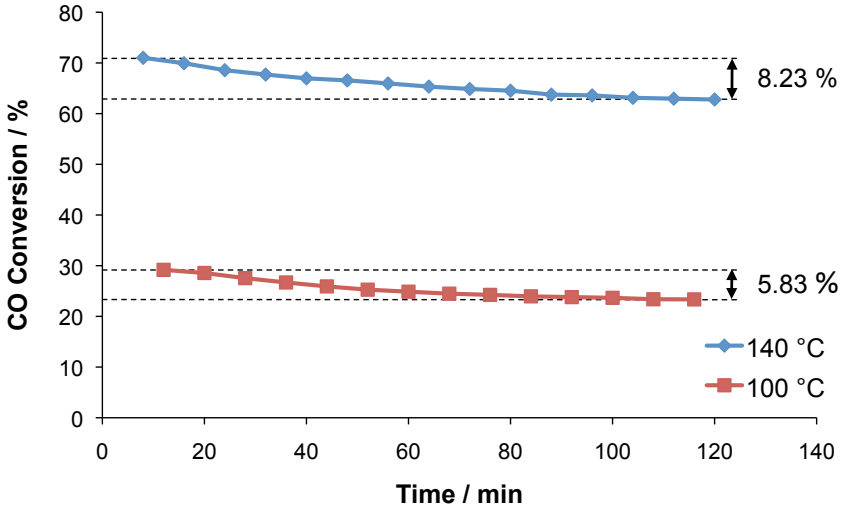

Figure 22. A graph showing the conversion of CO to CO_2 versus time on stream for sample C6 at 100 °C and 140 °C, which are the red and blue lines respectively.

Considering the temperature of 50% conversion (T_{50}) for each sample, the relationship between T_{50} and the XRD-derived particle size can be plotted as shown in Figure 23. Here it can be seen that there is a quasi-linear relationship between the particle size and T_{50} over the studied range of sizes.

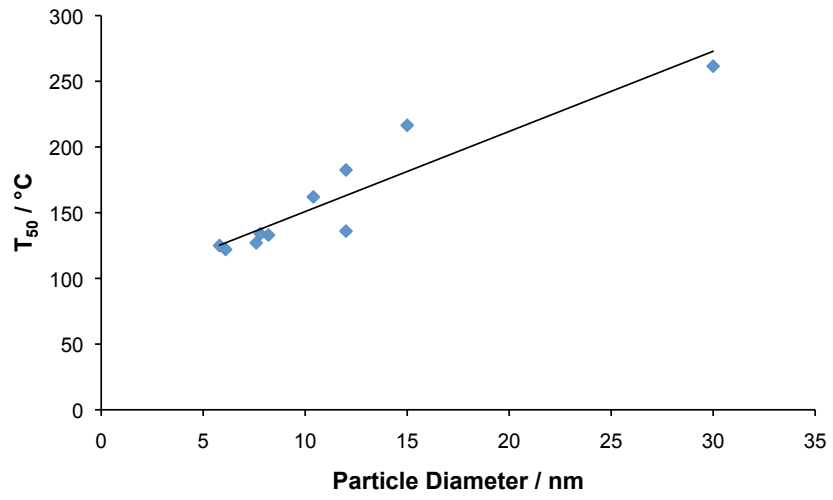

Figure 23. A graph of the temperature of fifty percent conversion, T_{50}, versus particle diameter for $CoFe_2O_4$ nanoparticle catalysts.

In addition, the activity correlations are similar whether the measured BET surface area is used, or the surface area is estimated for each sample using the particle size (see Figures 24 and 25).

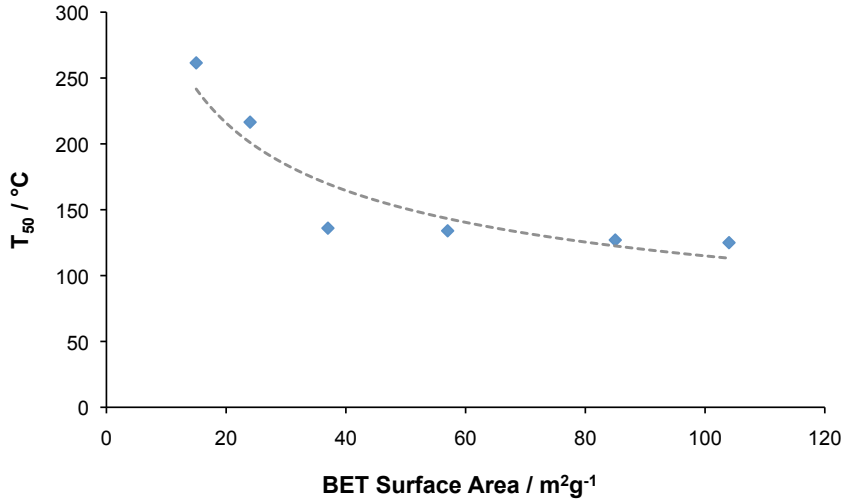

Figure 24. A graph of T_{50} versus BET surface area for samples C2, C4, C5, C6, C9 and C10. The line is intended to be a guide to the eye.

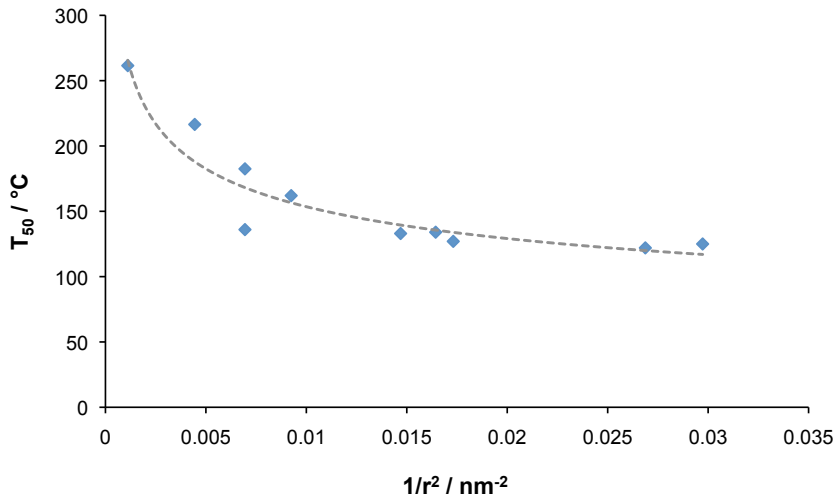

Figure 25. A graph of T_{50} versus $1/r^2$ for samples C1-10. The line is intended to be a guide to the eye.

This relationship between the XRD particle size and activity presented in Figure 23 enables the prediction of the CO oxidation activity for $CoFe_2O_4$ nanoparticles based solely upon the XRD-derived particle size, an analysis that can be performed rapidly at room temperature. In turn, this enables a comparison to be made between the CO oxidation activities of different ferrites.

For instance, $NiFe_2O_4$ nanoparticles prepared *via* the microemulsion method[10] were found to have an XRD size of 4.4 nm, (Figure 26) and a T_{50} of 295 °C. At this XRD size, $CoFe_2O_4$ would be expected to have a T_{50} of 117 °C (considering the equation of the straight line in Figure 23 is: $y = 6.1052x + 90.355$), suggesting $CoFe_2O_4$ is more active as a CO oxidation catalyst. This prediction is supported by the observations of Pirogova et al,[36] where $CoFe_2O_4$ was found to be more active than $NiFe_2O_4$, though the particle sizes were not normalised in that work.

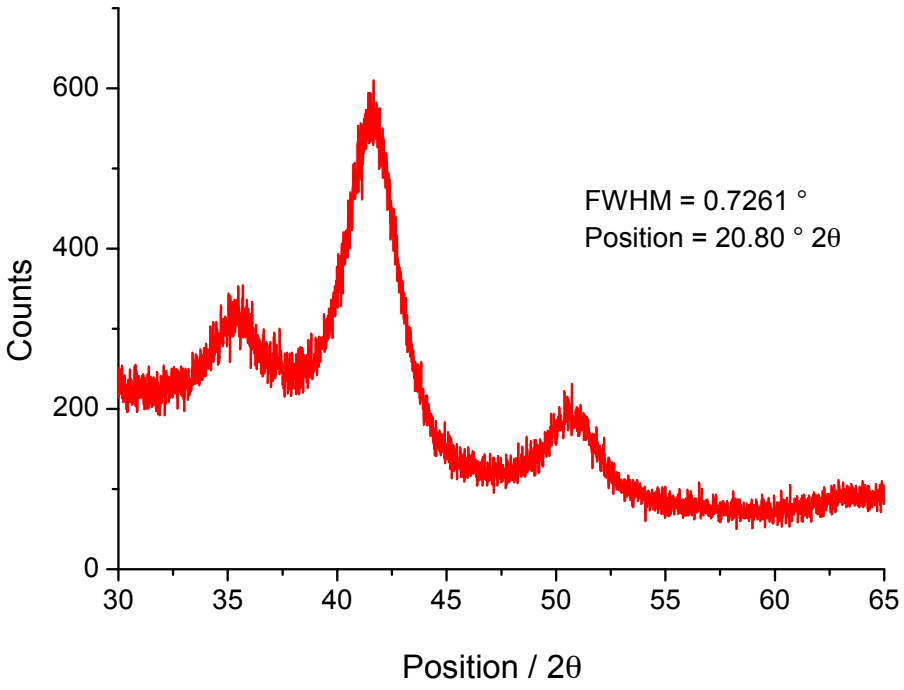

Figure 26. X-ray diffraction pattern of $NiFe_2O_4$ nanoparticles prepared by the microemulsion method. The particle size was determined to be 4.4 nm by use of the Scherrer equation.

It is probable that the mechanism of CO oxidation over $CoFe_2O_4$ follows that described by Mars and van Krevelen for CO oxidation over metal oxides[29] (see Chapter 1, Section 1.4). The most active catalyst had a T_{50} of 125 °C and this compares well with the $CoFe_2O_4$ catalyst reported elsewhere, where a T_{50} of 160 °C was observed.[36] These catalysts do not match the activity of sub-8 nm supported Au nanoparticles which can be active below room temperature, though Au nanoparticles lose their activity when larger than 8 nm in diameter. This can be problematic in high temperature reactions as Au nanoparticles tend to grow in size at high temperatures due to Ostwald ripening.[39]

3.4 Conclusions

The size-activity relationship for the CO oxidation reaction has been mapped out for a model CO oxidation catalyst, where the surface area is systematically controlled *via* the particle size rather than through other mechanisms such as support effects. Particle size has been shown to have a significant effect upon the activity of the catalyst when the unsupported particle dimensions are reduced to the nanometre range and the results also demonstrate that $CoFe_2O_4$ nanoparticles are active CO oxidation catalysts under relatively mild conditions with 100% conversion at 185 °C. The measured activities compare favourably with those previously reported for $CoFe_2O_4$[36] and although they do not match supported Au nanoparticle catalysts for activity, the $CoFe_2O_4$ nanoparticles do display a good degree of thermal and chemical stability under the test reaction conditions. Coprecipitation has also been proven to be a rapid route to large quantities of the catalyst, with the ox-en and ox-triethanolamine capping/complexing agents having a pronounced effect on the particle size in a simple one step water-based process. The oxalate capping group can also be readily removed in an activation step during catalysis, thus removing the need for a high temperature pre-treatment step which could result in particle aggregation or growth prior to testing. Deposition or impregnation of the $CoFe_2O_4$ nanoparticles onto a suitable support could enhance their activity further, and it is possible that the control of activity through the particle size without support effects could be applied to more active catalysts such as Cu-Mn-O containing hopcalites and Co_3O_4[40] in order to further enhance their activities.

References

1. B. Cushing, L. V. Kolesnichenko and C. J. O'Connor, *Chem. Rev.* **2004**, 104, 3893.
2. M. S. Neo, N. Venkatram, G. S. Li, W. S. Chin and J Wei, *J. Phys. Chem. C.* **2009**, 113, 19055.
3. M. A. Tagliente, M. Massaro, G. Mattei, P. Mazzoldi, V. Bello and G. Pellegrini, *J. Appl. Phys*. **2008**, 104, 093505.
4. D. L. Huber, E. L. Venturini, J. E. Martin, P. P. Provencio and R. J. Patel, *J. Magn. Magn. Mater.* **2004**, 278, 311.
5. M. Niederberger, N. Pinna, J. Polleux and M. Antonietti, *Angew. Chem. Int. Ed.* **2004**, 43, 2270.
6. N. Pinna, G. Garnweitner, M. Antonietti and M. Niederberger, *J. Am. Chem. Soc*. **2005**, 127, 5608.
7. Q. Chen, A. J. Rondinone, B. C. Chakoumakos and Z. J. Zhang, *J. Magn. Magn. Mater.* **1999**, 194, 1.
8. D-H. Chen and Y-Y. Chen, *J. Coll. Int. Sci***. 2001**, 235, 9.
9. N. Moumen and M. P. Pileni, *Chem. Mater.* **1996**, 8, 1128.
10. D. O. Yener and H. Giesche, *J. Am. Ceram. Soc.* **2001**, 84, 1987.
11. C-H. Han, S-D. Han, J. Gwak and S. P. Khatkar, *Mater. Lett*. **2007**, 61, 1701.
12. H. H. Hamdeh, K. Barghout, J. C. Ho, R. J. Willey, M. J. O'Shea and J. Chaudhuri, *J. Magn. Magn. Mater*. **2000**, 212, 112.
13. S. R. Ahmed and P. Kofinas, *Macromolecules* **2002**, 35, 3338.
14. D. K. Yi, S. S. Lee, G. C. Papaefthymiou and J. Y. Ying, *Chem. Mater*. **2006**, 18, 614.
15. J. D. Aiken and R. G. Finke, *J. Mol. Catal. A* **1999**, 145, 1.

16. M. Schur, B. Bems, A. Dassenoy, I. Kassatkine, J. Urban, H. Wilmes, O. Hinrichsen, M. Muhler and R. Schlögl, *Angew. Chem. Int. Ed*. **2003**, 42, 3815.
17. M. Bowker, *Nature Mater.* **2002**, 1, 205.
18. S. Y. Chin, O. S. Alexeev and M. D. Amiridis, *Appl. Catal. A* **2005**, 286, 157.
19. G. Avgouropoulos, T. Ioannides, Ch. Papadopoulou, J. Batista, S. Hocevar and H.K. Matralis, *Catal. Today* **2002**, 75, 157.
20. C.-H. Tu, A.-Q. Wang, M.-Y. Zheng, X.-D. Wang and T. Zhang, *Appl. Catal. A* **2006**, 297, 40.
21. T. H. Rogers, C. S. Piggot, W. H. Bahlke and J. M. Jennings, *J. Am. Chem. Soc.* **1921**, 43, 1973.
22. H. A. Jones and H. S. Taylor, *J. Phys. Chem.* **1923**, 27, 623.
23. G. J. Hutchings, A. A. Mirzaei, R. W. Joyner, M. R. H. Siddiqui and S. H. Taylor, *Appl. Catal. A Gen*. **1998**, 166, 143.
24. C. T. Campbell, *Science* **2004**, 306, 234.
25. M. C. Kung, R. J. Davis and H. H. Kung, *J. Phys. Chem. C.* **2007**, 111, 11767.
26. M. Haruta, N. Yamada, T. Kobayashi and S. Iijima, *J. Catal.* **1989**, 115, 301.
27. M. Haruta, *Gold Bull.* **2004**, 37, 27.
28. G. J. Hutchings, *Catal. Today* **2005**, 100, 55.
29. P. Mars and D. W. van Krevelen, *Chem. Eng. Sci.* **1954**, 3(Spec. Suppl.), 41.
30. U. K. Gautam, M. Ghosh, M. Rajamathi and R. Seshadri, *Pure Appl. Chem.* **2002**, 74, 1643.
31. M. Ghosh, G. Lawes, A. Gayen, G. N. Subbanna, W. M. Reiff, M. A. Subramanian, A. P. Ramirez, J.-P. Zhang and R. Seshadri, *Chem. Mater.* **2004**, 16, 118.

32. J. Rouquerol, D. Avnir, C. W. Fairbridge, D. H. Everett, J. H. Haynes, N. Pernicone, J. D. F. Ramsay, K. S. W. Sing and K. K. Unger, *Pure Appl. Chem*. **1994**, 66, 1739.

33. R. G. Avery and J. D. F. Ramsay, *J. Coll. Int. Sci*. **1973**, 42, 597.

34. Z. Sui, X. Chen, L. Wang, Y. Chai, C. Yang and J. Zhao, *Chem. Lett*. **2005**, 34, 100.

35. R. De Palma, S. Peeters, M. J. Van Bael, H. V. den Rul, K. Bonroy, W. Laureyn, J. Mullens, G. Borghs and G. Maes, *Chem. Mater.* **2007,** 19, 1821.

36. G. N. Pirogova, N. M. Panich, R. I. Korosteleva, Yu. V. Voronin and G. E. Kalinina, *Russ. Chem. Bull*. **1996**, 45, 42.

37. D. Wang, Z. Ma, S. Dai, J. Liu, Z. Nie, M-H. Engelhard, Q. Hou, C. Wang and R. Kou, *J. Phys. Chem. C*. **2008**, 112, 13499.

38. J-H. Liu, A-Q. Wang, Y-S. Chi, H-P. Lin and C-Y. Mou, *J. Phys. Chem. B*. **2005**, 109, 40.

39. K. Yu, Z. Wu, Q. Zhao, B. Li and Y. Xie, *J. Phys. Chem. C*. **2008**, 111, 2244.

40. D. A. H. Cunningham, T. Kobayashi, N. Kamijo and M. Haruta, *Catal. Lett*. **1994**, 25, 257.

Chapter 4

Chapter 4

4 Functionalisation and Assembly of Metal Oxide Nanoparticles

4.1 Introduction

Nanostructuring of bulk inorganic materials has focused on single phases and control of the associated properties.[1-5] However, by assembling different phases of nanoparticles with one another, it is possible to prepare arrays with combinations of interacting properties.[6-9] For example, binary nanoparticle superlattices (BNSLs) can be prepared from mixtures of nanoparticles that are size-controlled in such a manner that promotes the formation of structures with face centred cubic (f.c.c.) ordering, for instance, and such chemistry has been applied to the synthesis of Au-αFe_2O_3 and Au-PbSe nanoparticle arrays, amongst others.[10, 11] Chemical functionalisation of the external surfaces of nanoparticles also allows for the assembly of multiple phase arrays and this approach is not particle size limited as in the case of the BNSLs.[12, 13] Galow et al. have demonstrated the assembly of Au-SiO_2 aggregates *via* electrostatic interactions between the functionalised, positively charged SiO_2 nanoparticles and the functionalised, negatively charged Au.[7]

In this chapter, a chemical functionalisation and bonding approach to predictably assemble oxide nanoparticles with distinct properties (ferroelectricity and ferromagnetism) is developed. Oxide nanoparticles are a particularly interesting class of materials; they possess properties covering many aspects of materials science, and they find application in areas ranging from in electroceramics, catalysis and energy

storage and conversion, amongst others.[14-16] The assembly of oxide nanoparticles is challenging as the functionalisation chemistry is less well developed than for semiconductor and Au nanoparticles, with the latter aided by the propensity of Au to form bonds with thiol (-SH) groups, and the range of bi-functional thiolates that are commercially available.[17] After assembling the ferroelectric (FE) and ferromagnetic (FM) nanoparticles, we also detail the processing of these arrays into multifunctional composites, with magnetoelectricity the target property in this proof-of-principle work. The preparation of magnetoelectric ceramics from the assembled ferroelectric and ferromagnetic nanoparticles is discussed in detail in Chapter 5.

4.2 Experimental

4.2.1 Preparation of 8 nm $BaTiO_3$ (BTO) Nanoparticles

4.73 mmol $Ba(OH)_2.8H_2O$ was dissolved in 20 mL 2-methoxyethanol by magnetic stirring for 1 hour. A solution of 4.3 mmol titanium(IV) tetraisopropoxide in EtOH (10 mL) was then added dropwise under continuous stirring. 7 mL of the mixture was transferred into a 23 mL capacity Teflon liner (30% filling), and then sealed inside an autoclave, before being heated at 240 °C for 6 hours. The product was collected by centrifugation, washed with H_2O and dried overnight at 80 °C. To remove the $BaCO_3$ admixture from the as-synthesised product, the powder was sonicated in a 20 mL 1% v/v aqueous acetic acid solution for 10 minutes, before being washed with H_2O and dried overnight at 80 °C. This route is as-described by Kolen'ko et al.[18]

4.2.2 Preparation of 50 nm BTO Nanoparticles

9.1 mmol of $TiCl_4$ was added dropwise to 20 ml of EtOH, a second solution of 14.6

mmol of $Ba(OH)_2.8H_2O$ in 20 mL 2-methoxyethanol was also prepared. The Ti^{4+} containing solution was then added dropwise to the Ba^{2+} solution, with magnetic stirring, and a white slurry was formed. This was stirred for a further 10 minutes before 40 mL H_2O was added which lead to a clear solution forming. 125 mmol NaOH was then added and the slurry was reformed, with the solution then stirred for a further 10 minutes, transferred into an autoclave and heated at 240 °C for 24 hours. The 23 mL capacity Teflon liners were each filled to 30% capacity. Following the reaction, the product was collected by centrifugation, dried overnight at 80 °C, then treated with AcOOH as described for 8 nm BTO above. This route, aside from the AcOOH treatment, is as described by Hou et al.[19]

4.2.3 Preparation of 200 nm BTO Particles

Used as received from Inframat Advanced Materials LLC.

4.2.4 Preparation of BTO Nanowires

BTO nanowires were prepared *via* a potassium tetratitanate ($K_2Ti_4O_9$) nanowire precursor, which was prepared as follows: 50 mmol of potassium methoxide was dispersed in 10 mL of EtOH, and 50 mmol of titanium ethoxide was added. The hydrolysis and condensation reactions were controlled by the addition of 20 mL of H_2O and approximately 3.5 mL of conc. HCl, to adjust the pH of the solution to 7. The sol solution was prepared by stirring at 40 °C for 2 h and was then left for 100 h under ambient conditions for aging. The obtained wet gel was then dried over 48 h at 100 °C. After drying, the xerogel was heated at 850 °C for 4 h to crystallize the $K_2Ti_4O_9$ nanostructures with a heating and cooling rate of 5 °C min^{-1}. The precrystallized K_2O phase was rinsed out with hot H_2O several times, and the

surface-rinsed $K_2Ti_4O_9$ nanostructures were dried overnight in the drying oven at 80 °C.

The BTO nanowires were then prepared *via* an ion exchange reaction as follows: The $K_2Ti_4O_9$ nanostructures were dispersed in 40 mL H_2O and mixed with a 0.3 M in 50 mL aqueous solution of barium hydroxide octahydrate ($Ba(OH)_2 \cdot 8H_2O$). The ion exchange reaction was carried out in an autoclave at 90 °C for 42 h (with 80% filling of the 23 mL capacity Teflon liner). The autoclave was quenched with flowing water following the reaction, and the final product was rinsed with H_2O several times at 90 °C. The BTO nanowires were then washed with AcOOH as described for the BTO nanoparticles. This route is as described by Kang et al.[20]

4.2.5 Preparation of 10 nm $CoFe_2O_4$ (CFO) Nanoparticles

Under flow of N_2, a solution was prepared consisting of: 1 mmol $Co(acac)_2$, 2 mmol $Fe(acac)_3$, 10 mmol 1, 2-hexadecane diol, 6 mmol oleic acid and 6 mmol oleylamine in 20 mL 1-octadecene. Under a blanket of N_2, the solution was magnetically stirred and heated to 200 °C for 2 hours, and then refluxed at 310 °C for 1 hour. The solution was then allowed to cool to RT, 40 mL EtOH was added, and the black precipitated material was separated by centrifugation and then added to hexane to achieve a concentration of 10 mg mL^{-1}. 0.05 mL oleic acid and 0.05 mL oleylamine also added were then added to the nanoparticle solution. This route is as described by Xie et al.[21]

4.2.6 Preparation of 12.5 nm CFO Nanoparticles

$Co(NO_3)_2.6H_2O$ (0.0426 mol) and $Fe(NO_3)_3.9H_2O$ (0.0852 mol) were dissolved in deionised H_2O (250 mL) in a 1 L beaker with magnetic stirring at 1500 rpm. The

solution was heated to 70 °C and NaOH (250 mL of a 2.05 M solution), also at 70 °C, was added. The solution was continuously stirred at 1500 rpm during the addition of NaOH, with the stirring speed slowed to 1000 rpm 10 min after the NaOH addition. The solution was left for a total of 1 h at 70 °C before being repeatedly washed with deionised H_2O until the pH of the solution was 7. The particles were then dried overnight at 80 °C.

4.2.7 Functionalisation of BTO with 3-Phosphonopropionic Acid

50 or 200 nm BTO particles, or BTO nanowires (500 mg) were dispersed by ultrasonication in a 95:5 (v/v) ethanol/H_2O mixture. To this suspension, 3-phosphonopropionic acid (0.2mmol) dissolved in the ethanol/H_2O solvent (1 mL) was added. The mixture was ultrasonicated for 10 min before being heated at 80 °C for 2 h. The nanoparticles were separated by centrifugation and washed with excess ethanol by ultrasonicating the solution at 40 °C for 1 h. The washing process was performed a total of 3 times. The nanoparticles were then dried at 80 °C overnight under vacuum. The route is adapted from that described by Kim et al.[22]

4.2.8 Functionalisation of 10 nm Oleic Acid Terminated CFO Nanoparticles

0.45 mL 3-aminopropyl trimethoxysilane (APTMS) was added to 1.8 mL of the CFO in hexane solution (prepared at a 10 mg mL^{-1} concentration) along with 90 mL hexane. 0.2 ml of conc. AcOOH was then added and the mixture was magnetically stirred for 72 h, during which time the nanoparticles precipitated. The black-brown precipitate was separated using a magnet, with the particles were washed three times with hexane to remove all excess silanes. In order to deprotonate the NH_3^+ terminal functional group and remove the oleate counterion, 10 mg of the particles were

added to 10 mL H_2O, raised to pH 8 with NaOH, whereupon they dissolved. The solution was sonicated for 5 minutes and the particles re-precipitated. Hexane was added to remove any residual oleic acid, before being separated, and the precipitated nanoparticles were collected with a magnet. The nanoparticles were then dried overnight at 40 °C. The ligand exchange reaction was preformed as described by De Palma et al.[23]

4.2.9 Functionalisation of 12.5nm CFO, 8 nm BTO Nanoparticles with APTMS.

CFO or BTO nanoparticles (250 mg) were dried at 100 °C overnight under vacuum. Then, under Ar flow, APTMS (approximately 5 mL) was added to excess. The reaction vessel was sealed under Ar and magnetically stirred at 1000 rpm at 80 °C for 48 h. The particles were retrieved *via* centrifugation and washed 3 times with THF/MeOH (3:1), then dried overnight in air at 80 °C.

4.2.10 Electrostatic Assembly of BTO and CFO Nanoparticles (Route **I***)*

The desired quantities of nanoparticles (e.g., 250 mg of BTO and 250 mg of CFO for the 1:1 composite) were dispersed in THF (25 mL) by ultrasonication for 10 min. The solutions were then mixed together and stirred overnight under ambient conditions. The particles were then collected by centrifugation at 2000 rpm and dried at 80 °C for 2 h.

4.2.11 DCCI Assembly of BTO and CFO Nanoparticles (Route **II***)*

As described above for route **I**, however following overnight stirring, DCCI (15 mg) was added to the reaction mixture which was then heated at 60 °C for a period of 4 h. The reaction mixture was then centrifuged, washed with THF and centrifuged again

to ensure removal of excess DCCI. The product was then dried at 80 °C for 2 h.

4.2.12 Preparation of BTO–CFO Control Composites (Route **III***)*

Prepared as described above for route **I** however unfunctionalised BTO and CFO particles were used instead.

4.2.13 Preparation of BTO-CFO NH_2-NH_2 Control Composite

Prepared as described above for route **I** however 50 nm BTO nanoparticles were directly functionalised with APTMS as for 8 nm BTO and reacted with APTMS functionalised 10 nm CFO.

4.2.14 Preparation of BTO-CFO NH_3^+-NH_3^+ Control Composite

Prepared as described above for the NH_2-NH_2 control reaction, however the particles were separately dispersed in an aqueous solution of acetic acid at pH 4 prior to mixing.

4.2.15 Transfer of Assemblies from THF to H_2O

Assemblies were transferred to H_2O *via* collection of the composite through centrifugation (1000 rpm) and addition of H_2O. The assemblies were always retained post-centrifugation if re-dispersed in THF.

4.2.16 Functionalisation of CFO with Thymine-1-Acetic Acid

N-hydroxysuccinimide (NHS, 0.087 mmol) was added to a mixture of *N*-(3-Dimethylaminopropyl)-*N*′-ethylcarbodiimide hydrochloride (EDC, 0.087 mmol) and thymine-1-acetic acid (0.027 mmol) in 5 mL H_2O with stirring. 4.5 mg 10 nm

APTMS-functionalised CFO nanoparticles were then added, and the reaction was left stirring overnight at RT. The particles were then collected by centrifugation and washed with H_2O before being dried overnight at 40 °C.

4.2.17 Functionalisation of BTO with 5'-Adenosine Monophosphate

20 mg of 50 nm BTO were dispersed in 50 mL DMF by sonication for 10 minutes. 0.2 mmol 5'-Adenosine Monophosphate (5'-AMP) was added to this suspension and the mixture was sonicated for a further 10 minutes before being heated to 80 °C for 2 hours. The particles were collected by centrifugation, washed with hot DMF and then dried at 80 °C overnight under vacuum.

4.2.18 Synthesis of Lucifer Yellow-Tagged BTO Nanoparticles

5 mg 3-phosphonopropionic acid functionalised 200 nm BTO particles were suspended by sonication in 500 μL potassium phosphate buffer solution (pH = 5.5). 500 μL EDC solution (0.057%) was added and sonication was carried out for 10 minutes. Lucifer yellow solution (500 μL, 50% v/v aqueous solution) then was added and the reaction was left overnight at room temperature with gentle rotation. The nanoparticles were collected and by centrifugation and washed with in a buffer of pH 7.5 containing 10 mmol Tris base, 0.15 M NaCl (0.1% (w/v) BSA, 1 mM EDTA and 0.1% sodium azide). This experiment was performed by Miss Cristina Olariu at the University of Liverpool.

4.2.19 Reaction of APTMS Modified BTO with Salicylaldehyde

20 mg of 8 nm BTO nanoparticles were dispersed in 6 mL EtOH and 0.076 mmol of salicylaldehyde was added. The mixture was magnetically stirred and heated to 85

°C for 2 hours. The product was collected by centrifugation and washed 3 times with EtOH, then dried overnight at 80 °C.

4.2.20 Characterisation

4.2.20.1 X-ray Diffraction

X-ray diffraction data were collected on a Panalytical X-Pert diffractometer with an X-Celerator detector and Co $K_{\alpha 1}$ radiation and using variable divergence slits with an illuminated length of 15mm.

4.2.20.2 TEM Imaging

The lower resolution TEM images were recorded using a FEI Tecnai G2 Spirit BioTWIN instrument with a W filament, operating at 100 kV. HRTEM were taken on a Jeol 300 kV JEM3010 instrument with a LaB_6 filament and EDS maps were collected using a VG HB601 UX STEM operating at 100 kV equipped with an Oxford Instruments INCA TEM 300 EDS system. All TEM samples were prepared by sonicating the powder (of as-prepared samples or pre-grinded ceramics) in the appropriate solvent (THF or H_2O), and then dropping the suspended powder onto a holey copper grid covered with holey carbon film. Dr Zhongling Xu at the University of Liverpool performed the TEM imaging.

4.2.20.3 SEM Imaging

SEM images were recorded using a Hitachi S4800 Type II cold field emission scanning electron microscope. The samples were sputter coated with Au prior to analysis using an Emitech K550X automated sputter coater and were held in place using a M3 aluminium 15 mm cross-section sample holder. The samples were

observed using a mix of upper and lower secondary electron detectors operating at an acceleration voltage of 3 kV, with working distance of 8.0 mm.

4.2.20.4 FTIR Spectroscopy

FTIR spectra were recorded using a Nicolet Nexus Instrument with the samples prepared by mixing the loose powder with KBr prior to measurement.

4.2.20.5 Elemental Analysis

Microanalysis was performed on a Thermo Flash EA 1112 Series C, H, N and S analyser.

4.2.20.6 ICP-AES Analysis

An HF/HNO_3 mixture was used to digest the few milligrams of sample necessary for analysis. This analysis was performed by Steven Apter at the University of Liverpool, using an ICP AES Spectro Ciros CCD instrument.

4.2.20.7 Solid-State NMR

Solid-state NMR spectra were recorded at 9.4 T on a Bruker DSX400 spectrometer equipped with a 4mm 1H/X/Y triple resonance probehead. Samples were spun in zirconia rotors using dry N_2-bearing gas. The $^{31}P\{^1H\}$ solid-state NMR spectra were acquired at 400.16 MHz for ^1H and 161.98 MHz for ^{31}P at an MAS rate of 10.0 kHz. A ^{31}P $\pi/3$ pulse length was 2.6 ms and the recycle delay was 90 s. Two-phase pulse modulation (TPPM) decoupling was used during acquisition. The ^{31}P chemical shifts are quoted in ppm with respect to 85 wt% H_3PO_4 solution. Data processing was performed using Bruker Topspin 1.3 software. Solid state NMR spectra were

acquired by Dr James T. A. Jones at the University of Liverpool

4.2.20.8 UV-Vis Molecular Absorption Spectoscopy

UV/Vis measurements were performed on a Perkin Elmer 650 S Spectrophotometer.

4.2.20.9 Fluorescence Microscopy

Fluorescence microscopy images were recorded on a Leica DMiL inverted microscope with a DFC 350F camera at a magnification of x50 using a green light filter. Miss Cristina Olariu performed the fluorescence microscopy imaging at the University of Liverpool.

4.3 Results and Discussion

4.3.1 Synthesis and Functionalisation of 8 nm $BaTiO_3$ Nanoparticles

The ferroelectric material barium titanate, $BaTiO_3$ (BTO) was one of the two components in the proposed metal oxide nanoparticle assemblies. The aim was to synthesise nanoparticles of BTO and the ferromagnetic cobalt ferrite, $CoFe_2O_4$ (CFO), and then engender the nanoparticles with complementary functionalities that would promote their assembly in solution. Initial experiments involved the synthesis of 8 nm cubic-phase BTO *via* the solvothermal route described by Kolen'ko et al.[18] XRD (Figure 1) shows the nanoparticles are phase pure with the Scherrer equation used to calculate the 8 nm particle size.

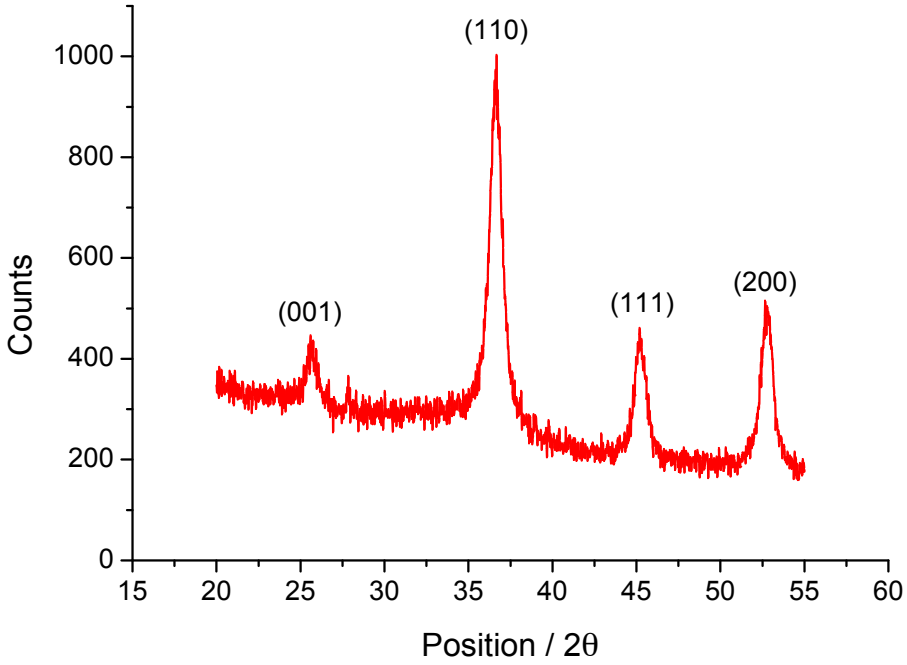

Figure 1. X-ray diffraction pattern of solvothermally-prepared 8 nm XRD-size $BaTiO_3$ nanoparticles.

The 8 nm BTO particles were functionalised with (3-aminopropyl)trimethoxysilane (APTMS) *via* a direct reaction between the BTO nanoparticles and the neat silane under an inert argon atmosphere over 48 hours. This idea was to use the acidic surface M-O-H species that are known to be present on the metal oxide surface,[24] and bind the silane to the nanoparticle surface through M-O-Si bonds *via* a condensation reaction that eliminates methanol. This is illustrated in Scheme 1. Nanoparticle functionalisation using silanes is common for Fe_3O_4 nanoparticles in biomedical applications, for example,[25, 26] and it was used by Galow et al.[7] for the assembly of Au-SiO_2 aggregates.

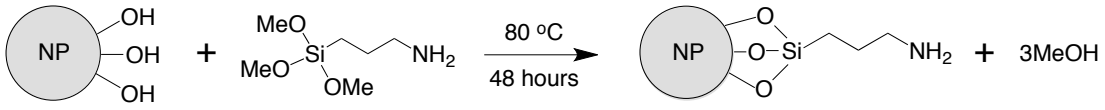

Scheme 1. An illustration of the anchoring of an aminosilane molecule to the surface of a $BaTiO_3$ nanoparticle.

The functionalisation procedure involved an initial overnight drying of the nanoparticles at 100 °C under vacuum, with the nanoparticles then heated at 80 °C in the presence of neat silane under an inert argon atmosphere. These steps were taken to exclude water from the system, which can lead to the self-condensation of the aminosilane molecules and the formation of insoluble polymers.

Several techniques were used to characterise the functionalised nanoparticles following washing and drying. Firstly, microanalysis data was obtained and this showed nitrogen was present in the post-functionalisation sample (C = 2.94%, H = 0.77%, N = 0.71%), which was in contrast to the pre-functionalisation sample (C = 0.79%, H = 0.42%, N = 0%). This data enabled the estimation of the coverage of the APTMS molecules on the nanoparticle surface. Using the equations 3.2 to 3.6 that are presented in Chapter 3, the theoretical surface area of the 8 nm BTO nanoparticles can be calculated to be 128 m^2g^{-1}. From the microanalysis data, it is possible to calculate the compositional formula of $BaTiO_3(APTMS)_{0.21}$ using the equations 3.7 to 3.10. By use of equations 3.11 to 3.15, the number of APTMS molecules per $BaTiO_3$ nanoparticle can be approximated to be 851, and equations 3.16 to 3.20 enable the calculation of the number of APTMS molecules per surface metal Ba^{2+}/Ti^{4+} ion, which was determined to be 0.68.

STEM was used to confirm that the APTMS molecules were present on the surface of the nanoparticle, rather than being self-condensed aminosilane polymers mixed

with BTO nanoparticles. The STEM maps presented in Figure 2 show the Si signal on the surface of the nanoparticles, suggesting they were functionalised with the aminosilane. This correlated with TEM imaging of the functionalised nanoparticles, which did not show any amorphous material that could be self-polymerised silane molecules.

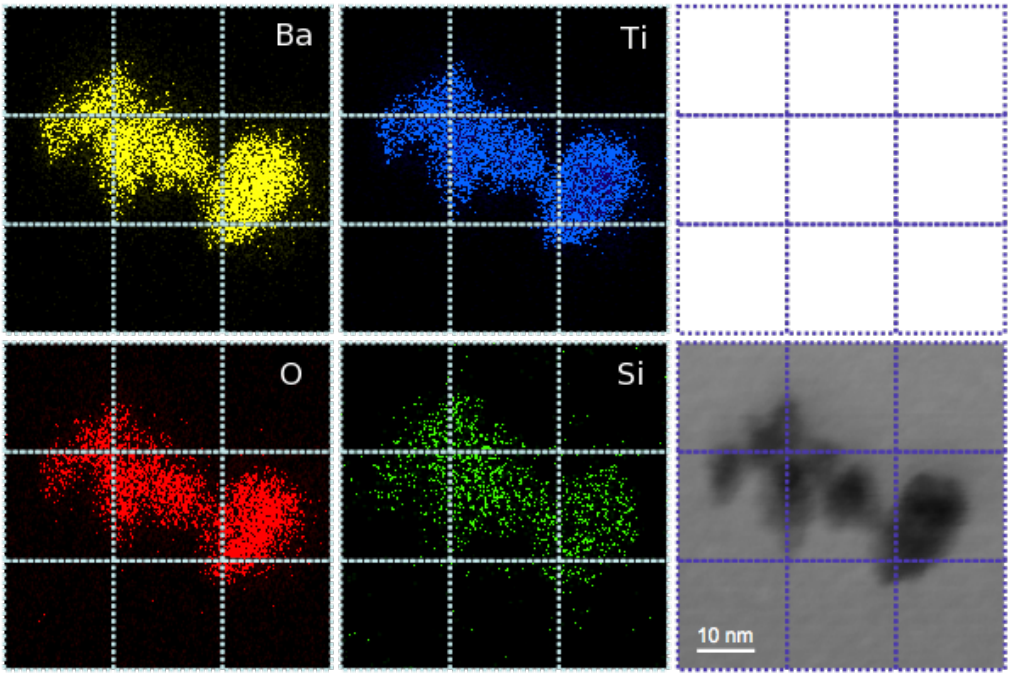

Figure 2. Scanning transmission electron microscopy images of 3-aminopropyl trimethoxysilane-functionalised $BaTiO_3$ nanoparticles.

Furthermore, EDX analysis showed that 2.26% Si was present in the sample, which is close to the 1.42% Si that you would expect based on the microanalysis nitrogen content of 0.71%. The difference in the numbers can be accounted for by considering that microanalysis is a bulk measurement of the entire sample, whilst EDX can be influenced by local variations in elemental concentration.

Determining the orientation of the APTMS molecule on the nanoparticle surface was important, as the NH_2 groups would only be available for reaction with the

functionalised CFO nanoparticles if the silane was bound through M-O-Si bonds.

^{29}Si solid-state NMR (MAS-NMR) was performed on the functionalised particles to probe the binding to the nanoparticle surface and the NMR spectrum can be seen in Figure 3.

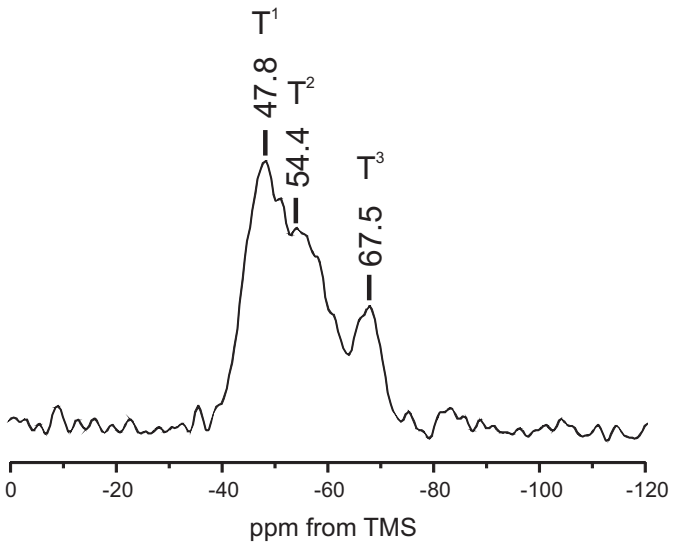

Figure 3. ^{29}Si solid state nuclear magnetic resonance spectrum of APTMS-functionalised 8 nm $BaTiO_3$ nanoparticles.

The presence of three peaks in the MAS-NMR spectrum suggests that the APTMS molecule is bound to the particle surface *via* M-O-Si bonds, and that the silane has three different modes of binding to the particle surface. If the aminosilane was bound to the particle surface *via* the nitrogen atoms, or if it was unbound, then one would expect to see a single resonance at -42.2 ppm in the ^{29}Si NMR, and this is not observed.[27]

A ^{15}N MAS-NMR spectrum of the 8 nm APTMS functionalised BTO nanoparticles can be seen in Figure 4. The spectrum shows just one peak, and its position is consistent with that expected for the free APTMS amine group.[27] This supports the ^{29}Si NMR data in suggesting that the aminosilane is bound through M-O-Si bonds

rather than *via* weak interactions between surface metal ions and nitrogen. The binding modes of the aminosilanes to the BTO nanoparticle surface are illustrated in Scheme 2.

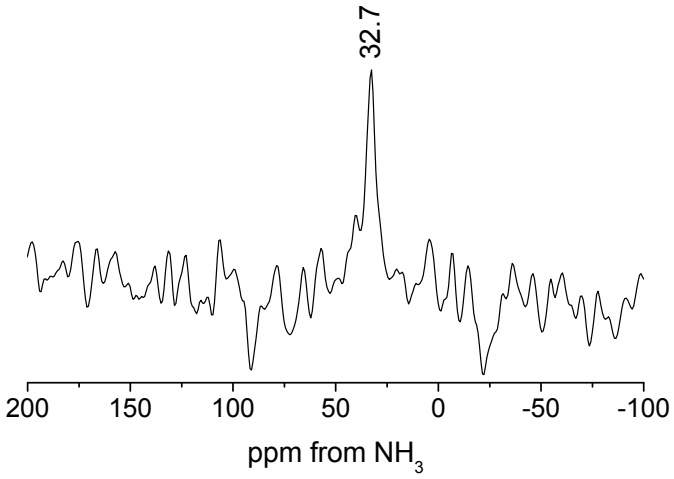

Figure 4. ^{15}N solid state nuclear magnetic resonance spectrum of APTMS functionalised 8 nm BTO nanoparticles.

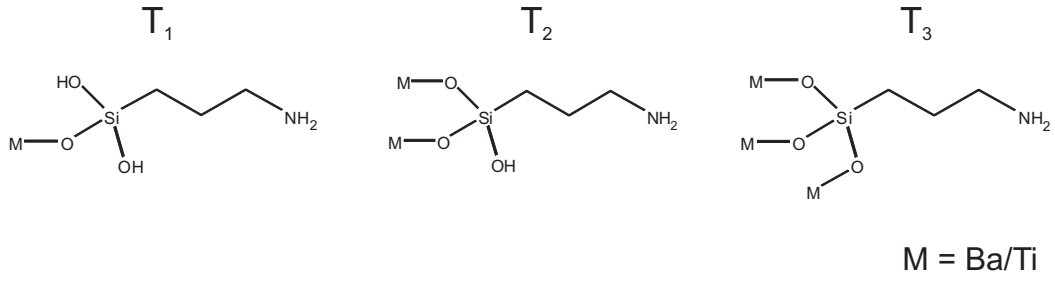

Scheme 2. An illustration of the binding modes of the APTMS molecule to the $BaTiO_3$ nanoparticle surface.

Furthermore, ^{13}C NMR was carried out to ensure the APTMS molecule was intact on the particle surface. The ^{13}C MAS-NMR spectrum can be seen in Figure 5.

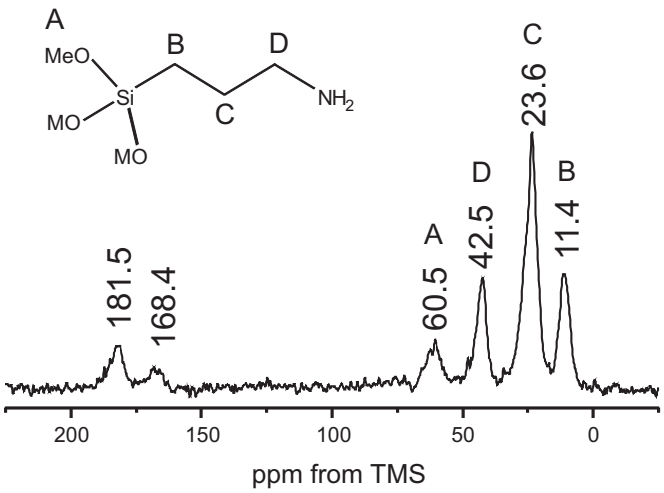

Figure 5. ^{13}C solid state NMR of APTMS-functionalised 8 nm $BaTiO_3$ nanoparticles.

The ^{13}C MAS-NMR spectrum shows all of the APTMS resonances in the range 11.4-60.5 ppm. They are shifted from those of the free aminosilane which occur at 50.8 (A), 6.5 (B), 28.0 (C), 45.3 ppm (D).[27] The resonances at 168.4 and 181.5 ppm are likely due to a small amount of $BaCO_3$ impurity remaining in the sample after washing with AcOOH, which is supported by the 0.79 carbon detected by microanalysis in the unfunctionalised sample.

In summary, the solid state NMR data showed that the aminosilane is was anchored to the nanoparticle surface *via* M-O-Si bonds with 3 different modes of binding, that the NH_2 groups remained free for reaction post-functionalisation and that the aminosilane molecules were stable under the functionalisation conditions of 80 °C for 48 hours under Ar.

In order to test the reactivity of the aminosilane functionalised nanoparticles, a test reaction was carried out with salicylaldehyde. This reaction was chosen as it results in the formation of an imines (Scheme 3), and these groups tend to have electronic transitions in the UV/Vis region; thus enabling a straightforward, qualitative assessment of the reactions success.

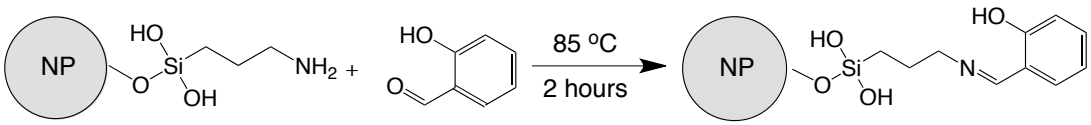

Scheme 3. A reaction scheme for the reaction between amine terminated $BaTiO_3$ nanoparticles and salicylaldehyde.

The product from the reaction was yellow in colour, while the BTO nanoparticle starting material was white. This observation suggested that the reaction had worked and that the salicylaldehyde molecules were bound to the BTO nanoparticle *via* imines bonds. This was supported by the UV/Vis molecular absorption spectra (Figure 6) where an additional absorption was observed at 412 nm.

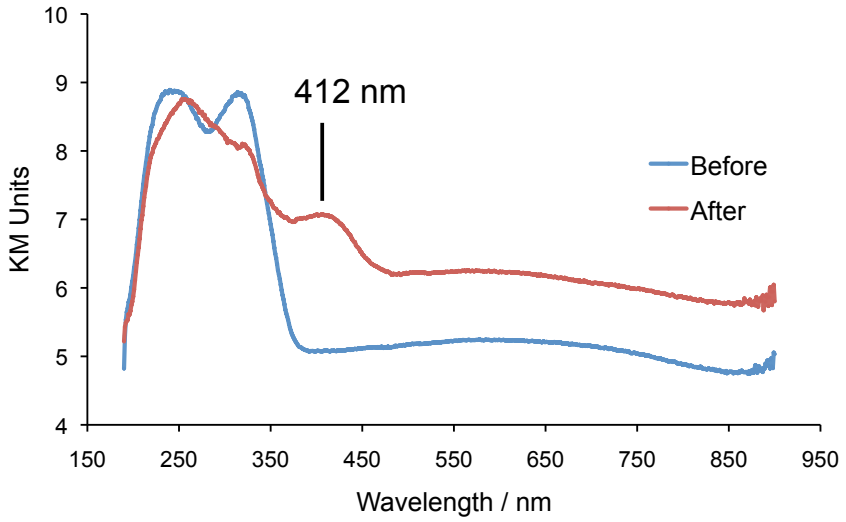

Figure 6. UV/Vis molecular absorption spectrum of salicylaldehyde-reacted APTMS-functionalised 8 nm $BaTiO_3$ nanoparticles (red), and the APTMS functionalised particles before the reaction with salicylaldehyde (blue).

Elemental analysis of the product from the salicylaldehyde reaction showed an increase in carbon and hydrogen content, and a decrease in nitrogen content post-reaction (the reduction in nitrogen content is expected as salicylaldehyde contains no nitrogen). The percentage of amine terminal groups that reacted with salicylaldehyde can be calculated based on the carbon content of the microanalysis results:

Considering the microanalysis data of the APTMS-functionalised 8 nm BTO particles (C = 2.94%, H = 0.77%, N = 0.71%).

The mass of carbon in 1g of material: $1 \times \frac{2.94}{100} = 29.4$ mg

Number of mols of carbon in 29.4 mg: $\frac{29.4}{12} = 2.45$ mmol carbon

Number of functional groups for 2.45 mmol of carbon = $\frac{2.45}{3} = 0.82$ mmol

(where 3 is the number of carbons in each APTMS molecule).

Applying the same calculations to the material after the salicylaldehyde reaction, using the microanalysis data; C = 4.76%, H = 0.92%, N = 0.23%:

The mass of carbon in 1g of material = 47.6 mg

Number of mols of carbon in 47.6 mg = $\frac{47.6}{12}$ = 3.97 mmol carbon

Assigning '*x*' to be the amount of unreacted amine functional groups and '*y*' to be the amount of reacted groups, and considering there are 3 carbon atoms in the unreacted amine functional groups and 10 in the salicylaldehyde-reacted functional groups:

A: $3x + 10y = 3.97$ mmol carbon, post saliycylaldehyde reaction

B: $x + y = 0.82$ as the total number of bound groups should be the same before and after the salicylaldehyde reaction.

Solving the simultaneous equations:

A: $3x + 10y = 3.97$

B: $3x + 3y = 2.46$

A – B: $7y = 1.51$

Therefore: $y = 0.22$ mmol, which is the number of reacted functional groups

Thus the percentage of reacted groups is:

$$\frac{\text{Number of salicylaldehyde reacted groups}}{\text{Total number of groups}} = \frac{0.22}{0.82} \times 100 = 26.83\%$$

This data shows the nanoparticles were reactive towards salicylaldehyde, though the reaction did not go to completion. This is likely due to steric hindrance preventing salicylaldehyde reacting with all of the available amine groups, and the slower kinetics of the reaction between the solid nanoparticles and liquid salicylaldehyde, performing the reaction at a higher temperature and over a longer period of time would likely increase the percentage of reacted APTMS sites.

4.3.2 Reactions with –CHO and COOMe Terminated Silanes

Functionalisation reactions were performed with a range of other silanes to assess their reactivity towards the metal oxide surface. Initially the goal was to form a silane-mediated assembly between BTO and CFO, however due to the lack of availability of a carboxylic acid-terminated silane (this molecule would spontaneously self-polymerise) a number of other molecules were investigated.

Functionalisation experiments were performed with -COOMe and -CHO terminated silanes according to the route developed for APTMS functionalisation. The -COOMe terminated silane could be hydrolysed into a carboxylic acid, which could interact with the amine terminated nanoparticles *via* acid base interactions; while the -CHO terminated silane could directly react with the amine terminated particles to form an imine. Microanalysis data suggested these reactions were not successful, with no significant increases in carbon or hydrogen content post-reaction. Furthermore, the FTIR did not show the absorption bands of either the ester or aldehyde functional groups, such as the strong C=O stretching bands.

The extent of functionalisation and reactivity of a silane molecule towards the

surface is complicated and is known to depend on a number of factors including the nature of the terminal functional group, silane concentration, reaction temperature and nature of the anchoring group amongst other parameters.[31] In the relatively mild conditions that were utilised for the functionalisation experiments described herein, these silane molecules were not found to bind to the nanoparticle surface, though at higher reaction temperatures, for instance, and by modifying other reaction parameters functionalisation may be possible.

4.3.3 Synthesis and Functionalisation of 12.5 nm $CoFe_2O_4$ Nanoparticles

Cobalt ferrite, $CoFe_2O_4$ (CFO), was the second component in the proposed assembly reactions. It is a ferromagnetic material and initial experiments involved the coprecipitation synthesis of CFO nanoparticles without external surface capping groups, in order to facilitate the binding of functional molecules to the OH species on the nanoparticle surface. The XRD diffraction pattern in Figure 7 shows coprecipitated sample is phase pure, while TEM images of the sample are shown in Figure 8, with a histogram of the particle size distribution shown in Figure 9.

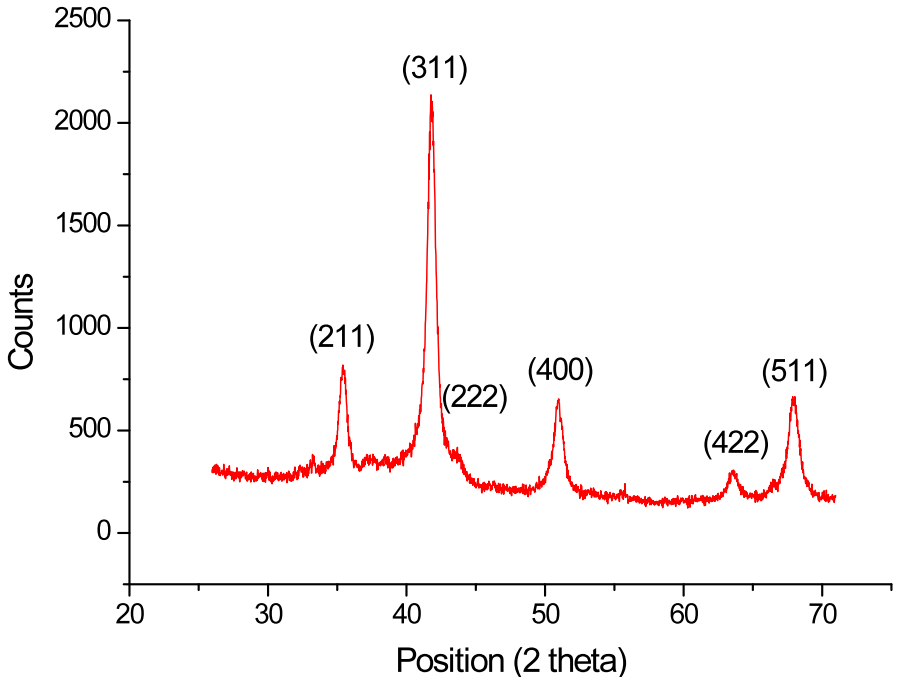

Figure 7. X-ray diffraction pattern of 12.5 nm $CoFe_2O_4$ nanoparticles prepared *via* the coprecipitation route, without external surface capping groups.

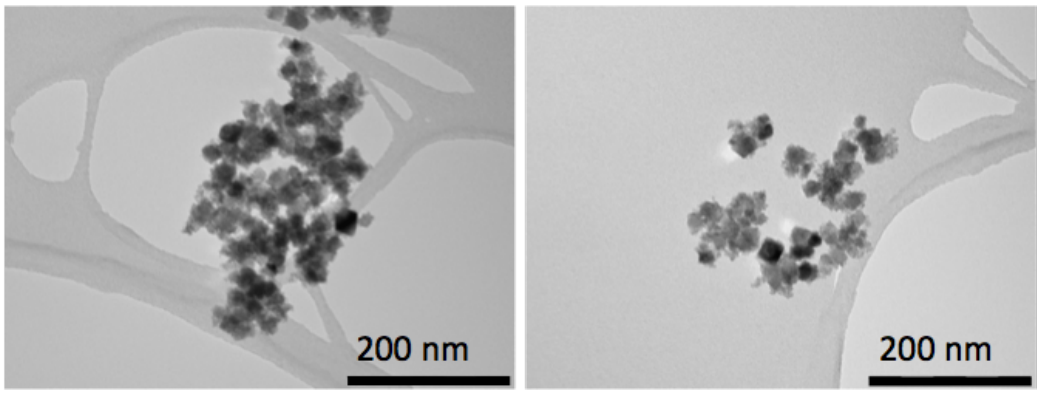

Figure 8. Transmission electron microscopy images of 12.5 nm $CoFe_2O_4$ nanoparticles prepared *via* the coprecipitation route, without external surface capping groups.

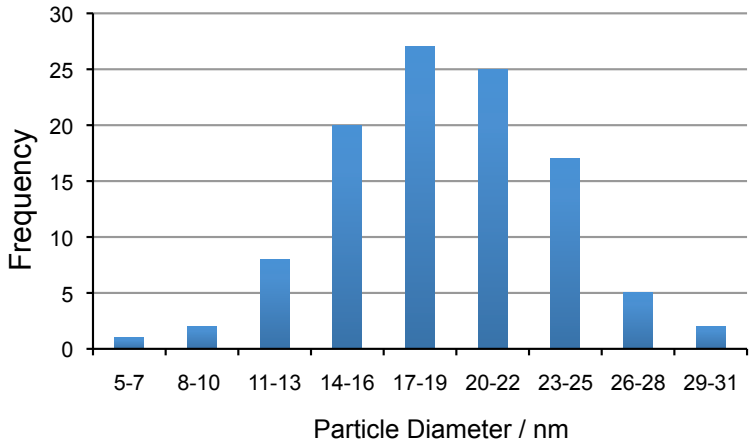

Figure 9. Histogram of the particle size distribution determined from TEM for 12.5 nm X-ray diffraction-size $CoFe_2O_4$ nanoparticles.

From the XRD, a particle size of 12.5 nm was calculated, which matches reasonably well with the TEM size of 19 ± 5 nm. This suggests that the particles consist of single domains, though there is a particle size distribution within the sample. The lack of capping groups on the nanoparticles is responsible for the size distribution, as the nucleated nanoparticles coalesce following their precipitation from solution,[28] this also likely leads to their irregular shape as observed in the TEM.

Due to the difficulty in binding other complementary silanes to the surface of BTO, 3-phosphonopropionic acid was chosen as the candidate molecule for anchoring to the CFO nanoparticle surface. This carboxylic acid-terminated phosphonic acid is widely available, and has previously been shown to bind to Fe_3O_4 nanoparticle surfaces.[29]

The idea was to graft the phosphonic acid molecules to the nanoparticle though a condensation reaction between the nanoparticle surface OH groups and the OH groups bound to the phosphorus atom. Following the functionalisation reaction, the nanoparticles were characterised with elemental analysis and inductively coupled

plasma atomic absorption spectroscopy (ICP-AES); the latter showed there was 2.11% phosphorous present in the sample, which enabled a coverage of 1.30 phosphonic acid molecules per surface M^{2+} ion to be calculated. This indicates there is multilayer coverage of the phosphonic acid on the CFO surface, likely due to intermolecular hydrogen bonding between the carboxylic acid groups.

FTIR spectroscopy (Figure 10) further suggested that the reactions had been successful with the absorption at 1026 cm^{-1} assigned to P-O vibrations, which matches assignments made for a similar system in the literature.[30]

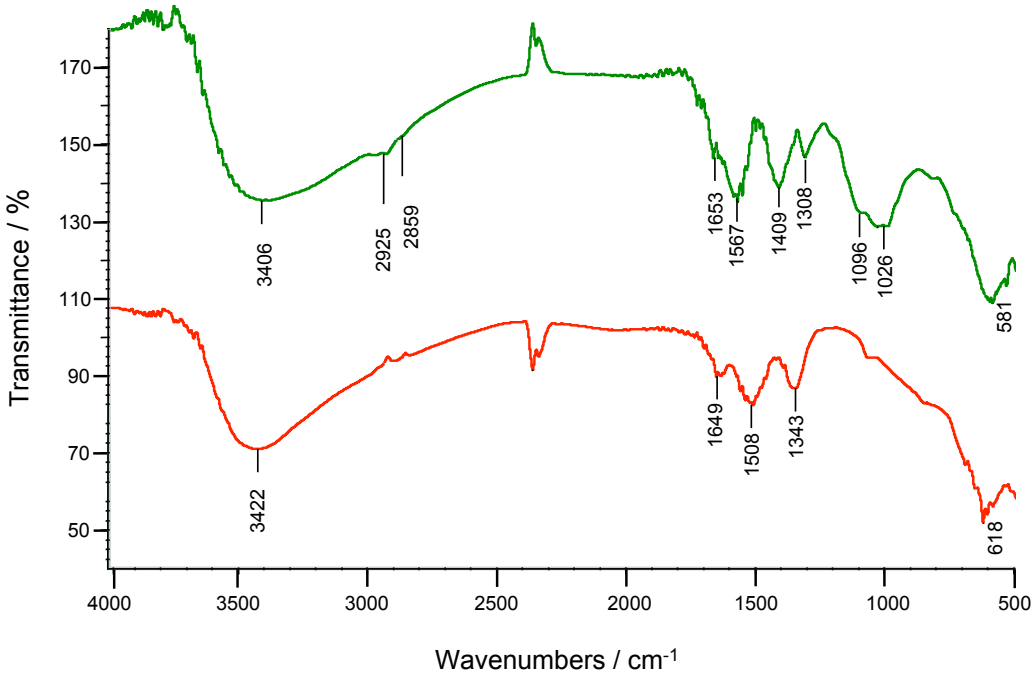

Figure 10. FTIR spectrum of 3-phosphonopropionic acid-functionalised $CoFe_2O_4$ nanoparticles.

4.3.4 Assembly of BTO (8 nm) – CFO (12.5 nm) Particles

Synthesis of the first generation of BTO-CFO nanoparticle assemblies was performed between the functionalised 8 nm BTO and 12.5 nm CFO nanoparticles *via*

the overnight mechanical stirring of the dispersed particles at room temperature in THF, the idea being that assemblies of BTO and CFO would be formed *via* electrostatic attraction between the amine-terminated BTO and the carboxylic acid-terminated CFO.

TEM images of the product from this reaction (Figure 11) proved inconclusive, and this was attributed to the similar sizes of the BTO (8 nm) and CFO (12.5 nm) particles making them difficult to distinguish from one another when considering the resolution limits of the instrument and the particle size distributions that were observed in the TEM.

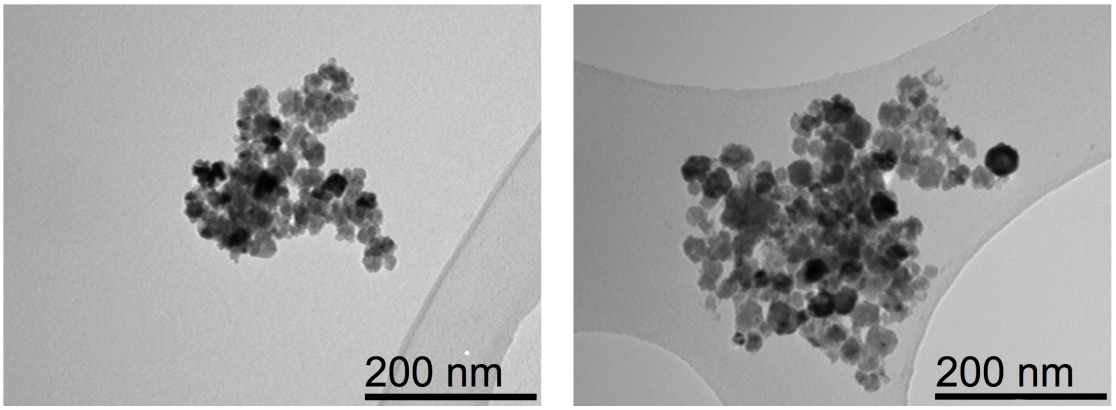

Figure 11. TEM images of the product from the assembly reactions between 8 nm amine-terminated $BaTiO_3$ and 12.5 nm carboxylic acid-terminated $CoFe_2O_4$.

Consequently it was necessary to identify a new set of BTO and CFO nanoparticles, with more distinct sizes and shapes to one another, and with a smaller size distribution. This would enable the identification of each phase *via* TEM imaging. Additionally, these new sets of particles needed to be readily functionalisable, and so well dispersed, small size distribution nanoparticles with inert surfaces (e.g. CTAB capped nanoparticles) would not be suitable.

4.3.5 Synthesis and Functionalisation of 10 nm CFO Nanoparticles

In order to obtain smaller size distribution CFO particles, the nanoparticle synthesis followed by ligand exchange route described by De Palma et al[23] was employed for the preparation of CFO nanoparticles. This route was considered appealing due to the fact that it involves, in the first step, the synthesis of well dispersed, oleic acid stabilised nanoparticles that have a small size distribution. The oleic acid sterically stabilises the nanoparticles preventing agglomeration and acts as a hydrophobic shell that enables dispersion of the nanoparticles in non-polar solvents such as hexane. An XRD pattern of the 10 nm CFO nanoparticles can be seen in Figure 12 and TEM images of the oleic acid stabilised particles can be seen in Figure 13, with a histogram of the TEM particle size distribution shown in Figure 14. The data shows the XRD and TEM particle sizes are closely matched (10 nm XRD size versus 8 ± 2 nm TEM size), with the particle size distribution smaller than for the 12.5 nm CFO nanoparticles (19 ± 5 nm).

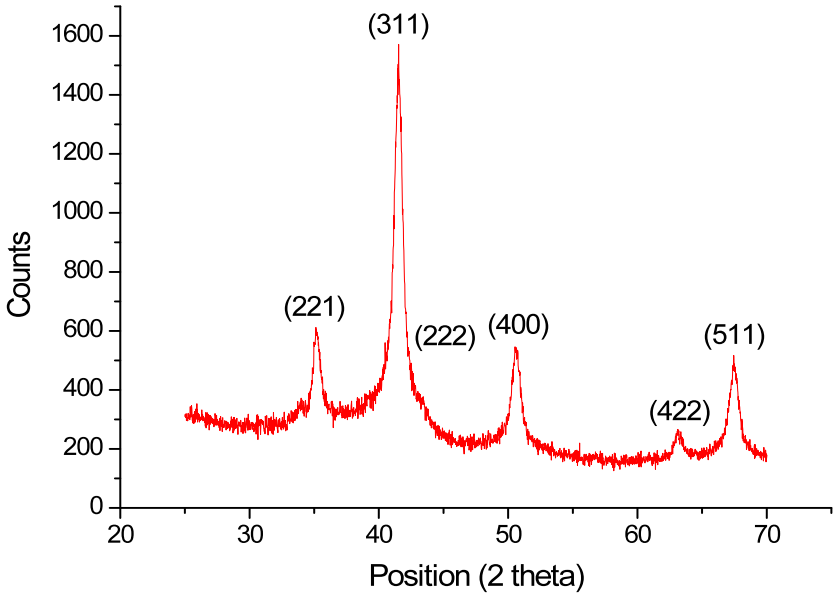

Figure 12. X-ray diffraction pattern of oleic acid stabilised 10 nm $CoFe_2O_4$ nanoparticles.

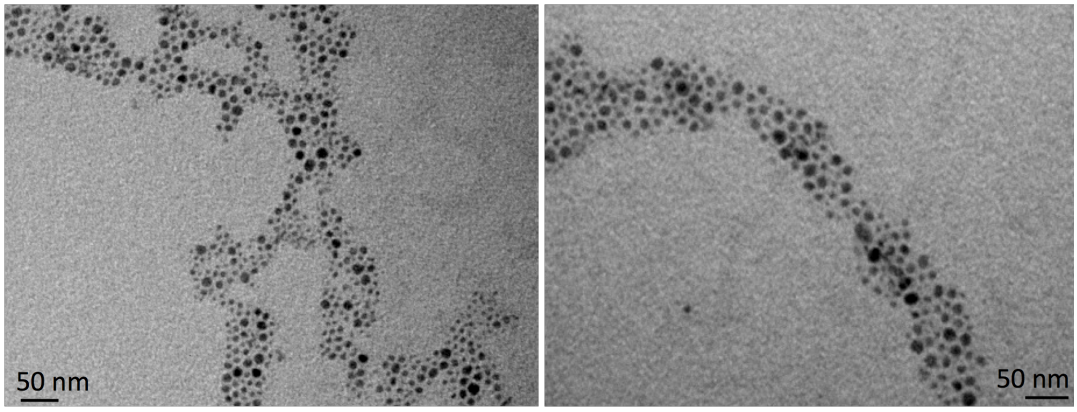

Figure 13. Transmission electron microscopy images of the oleic acid stabilised $CoFe_2O_4$ nanoparticles prepared by the Xie et al method.[21]

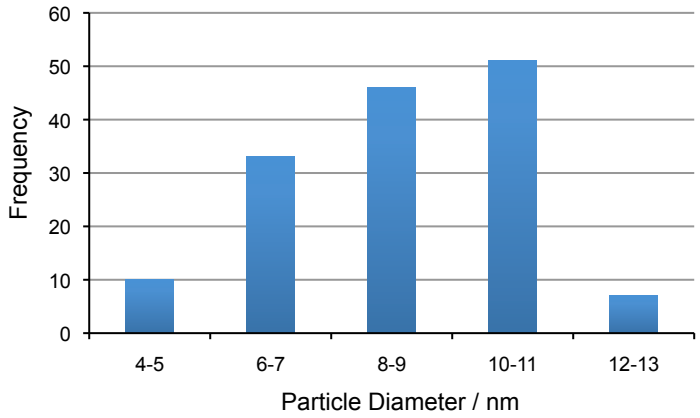

Figure 14. Histogram of the particle size distribution determined by transmission electron microscopy for 10 nm X-ray diffraction-size $CoFe_2O_4$ nanoparticles.

The nanoparticles were given terminal amine functional groups in the second step, a ligand exchange reaction between the oleic acid, which is bound to the CFO nanoparticle surface though electrostatic interactions, and APTMS. The ligand exchange reaction is catalysed by acetic acid, with the oleic acid molecules replaced by APTMS over the course of the reaction. This results in an increase in the nanoparticles hydrophilicity, leading to the nanoparticles dropping out of the hexane solvent in which they were previously colloidally stable (see Scheme 4).

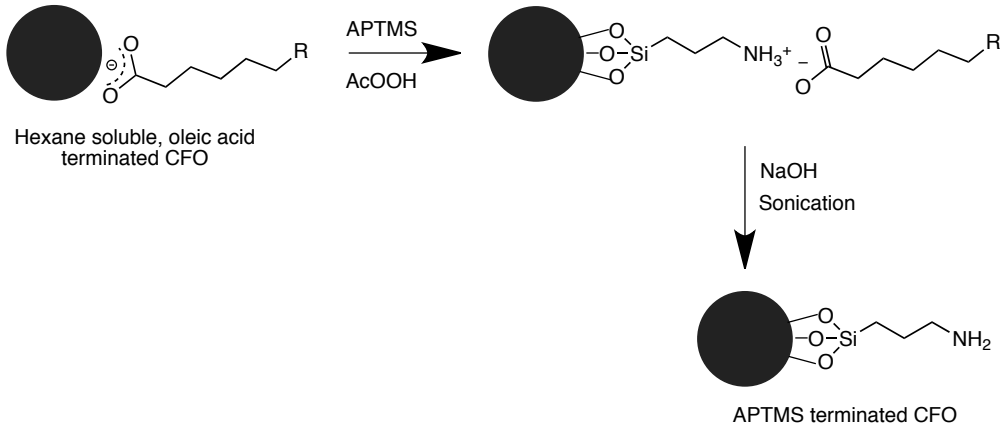

Scheme 4. Schematic of the $CoFe_2O_4$ oleic acid to APTMS ligand exchange reaction.

At this point the particles did not disperse well in water due to the oleate counterion coordinating to the NH_3^+ groups; these were present due to the protonation of the APTMS amine group by the acetic acid catalyst. The removal of the oleate counterion was performed by dispersing the nanoparticles, by sonication, in a mildly alkaline NaOH solution of pH 8. This results in the deprotonation of the NH_3^+ group and the oleate counterion was extracted into hexane, with the NH_2 terminated CFO nanoparticles then collected with a magnet from the aqueous phase.

XRD of these particles showed they were phase-pure whilst TEM (Figure 15) showed the particles had retained their size and had not agglomerated with one another following functionalisation.

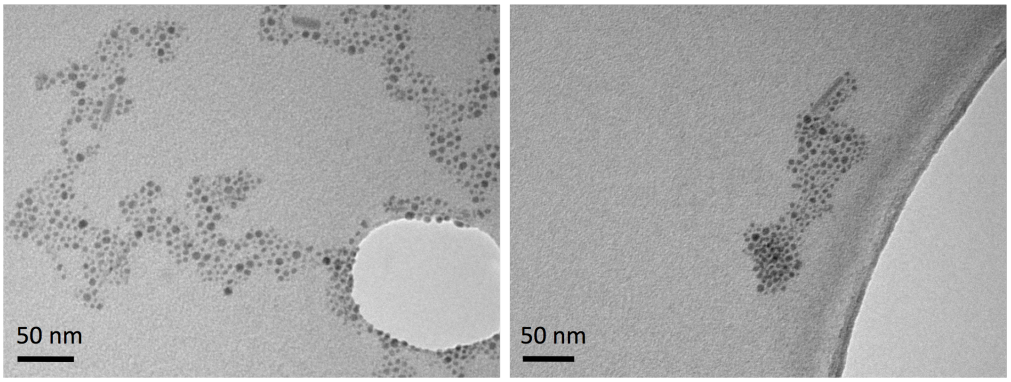

Figure 15. Transmission electron microscopy images of the APTMS-functionalised 10 nm $CoFe_2O_4$ nanoparticles.

The APTMS functionalised 10 nm CFO nanoparticles were characterised using microanalysis. The results showed C = 2.02%, H = 0.67%, N = 0.31%, from which a surface coverage of 0.33 APTMS molecules per surface Co^{2+} ion was calculated. Considering APTMS was previously shown to bind in monodentate, bidentate and tridentate modes to the BTO nanoparticle surface (see Figure 3), this data suggests that the coverage of APTMS on the CFO surface is not complete. Further evidence for the successful binding of the aminosilane came from FTIR (see Figure 16). Post-functionalisation, the FTIR spectrum (the green line in Figure 16) showed the presence of a band at 1060 cm^{-1}, which matches that expected for ν(M-O-Si) stretching.[23] Additionally there are bands observed in the ν(C-H) regions of the FTIR spectrum,[23] further confirming the successful binding of the aminosilane to the $CoFe_2O_4$ nanoparticle surface.

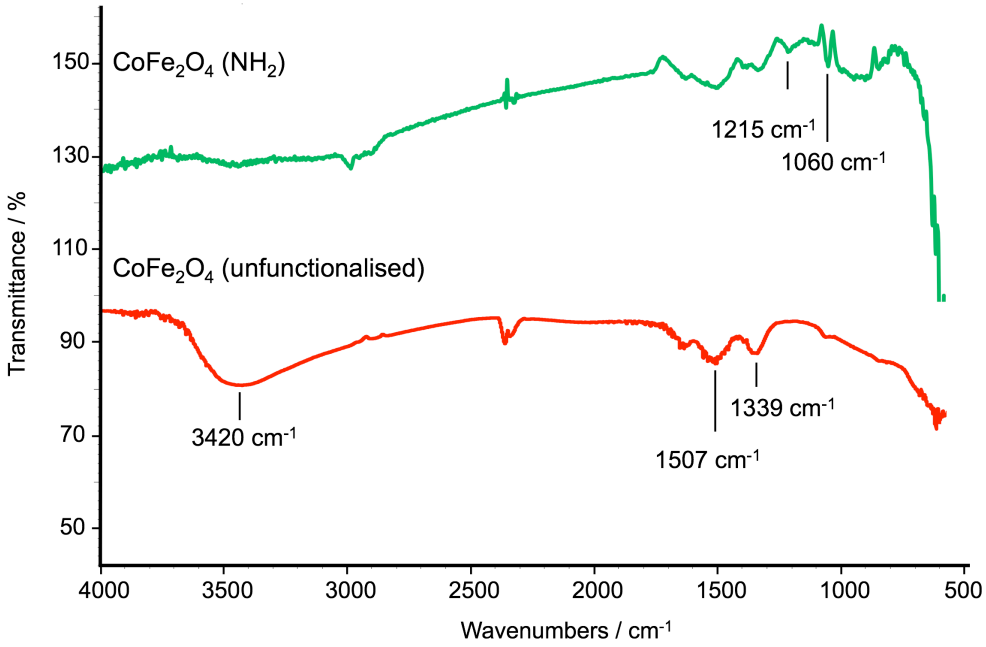

Figure 16. FTIR spectrum of APTMS functionalised 10 nm $CoFe_2O_4$ nanoparticles, with unfunctionalised $CoFe_2O_4$ shown for comparison.

4.3.6 Synthesis and Functionalisation of 50 nm Cube-like BTO Nanoparticles

50 nm cube-like $BaTiO_3$ nanoparticles were prepared *via* the solvothermal method described by Hou et al.[19] The synthesis involved the reaction between $Ba(OH)_2.8H_2O$ and $TiCl_4$ under solvothermal conditions, followed by treatment with dilute AcOOH, in order to remove the unwanted $BaCO_3$ impurity that forms due to its high stability and the presence of CO_2 in the water. XRD of the 50 nm BTO particles pre and post-AcOOH treatment can be seen in Figure 17 and TEM images of the post-AcOOH treatment BTO nanoparticles can be seen in Figure 18.

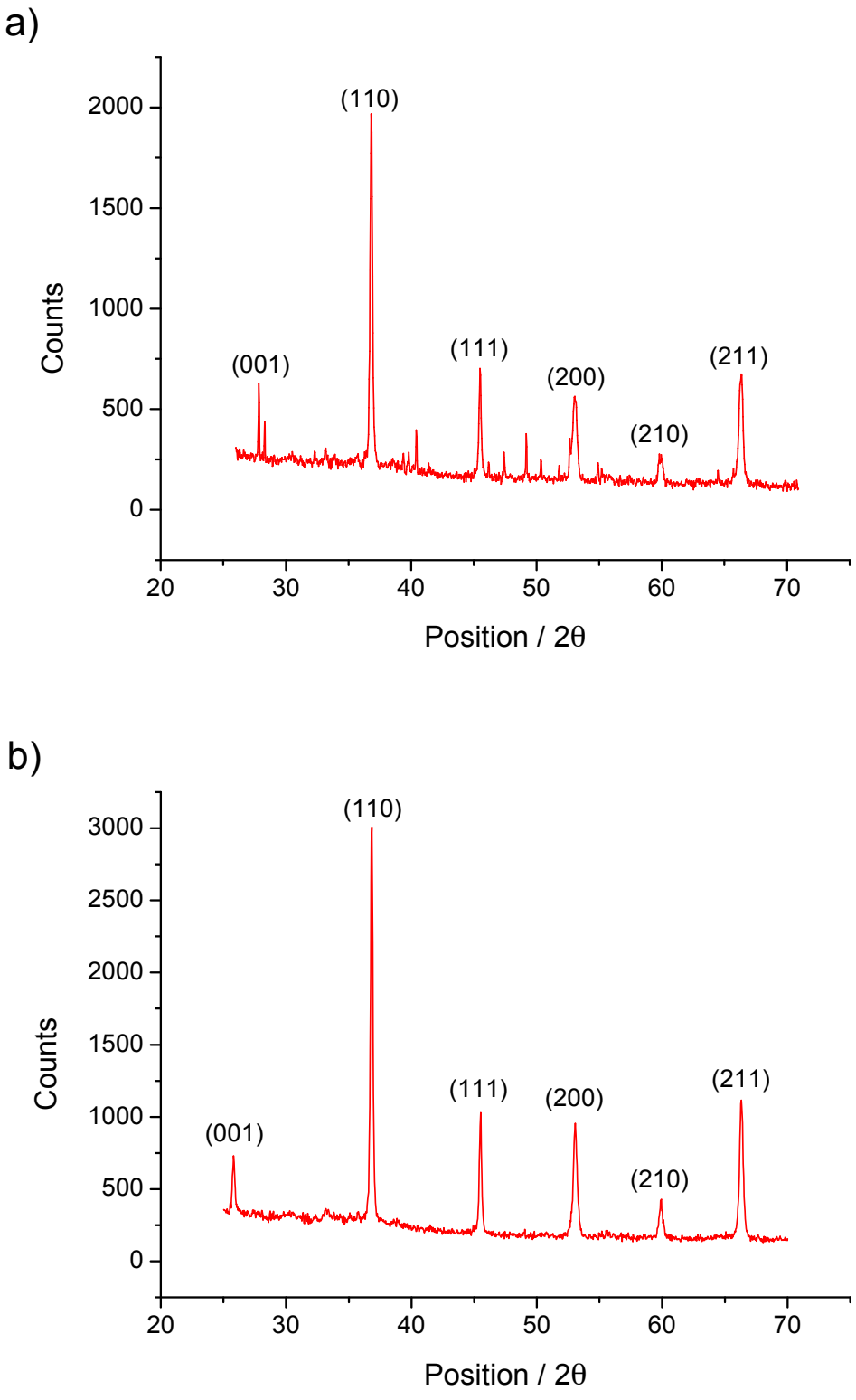

Figure 17. X-ray diffraction patterns of 50 nm cube-like $BaTiO_3$ nanoparticles prepared *via* the solvothermal route a) before AcOOH treatment and b) after AcOOH treatment. The unmarked peaks in a) are the $BaCO_3$ impurity phase.

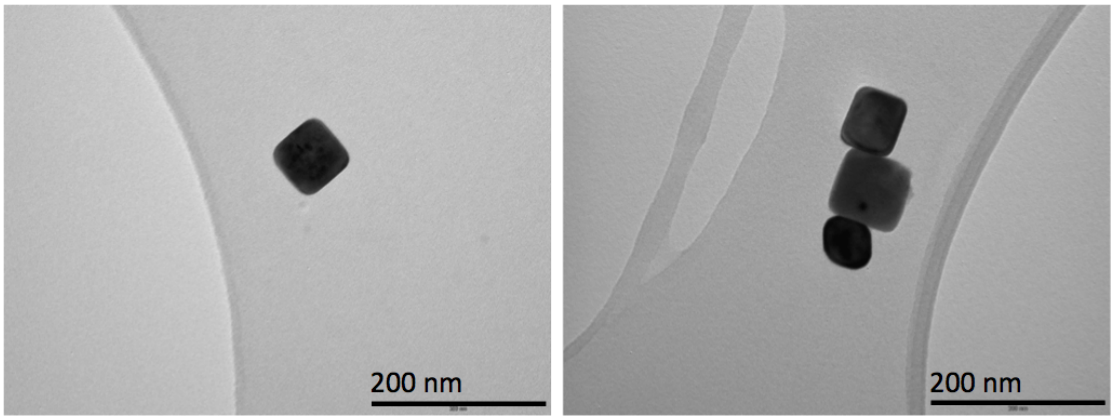

Figure 18. Transmission electron microscopy images of 50 nm cube-like $BaTiO_3$ nanoparticles prepared by the solvothermal route.

Comparing the XRD size (50 nm) with the TEM size (75 ± 17 nm) suggests the particles do not consist of multiple domains. The histogram in Figure 19 shows there is a size distribution present, but there is no overlap between the 50 nm BTO and 10 nm CFO particle sizes.

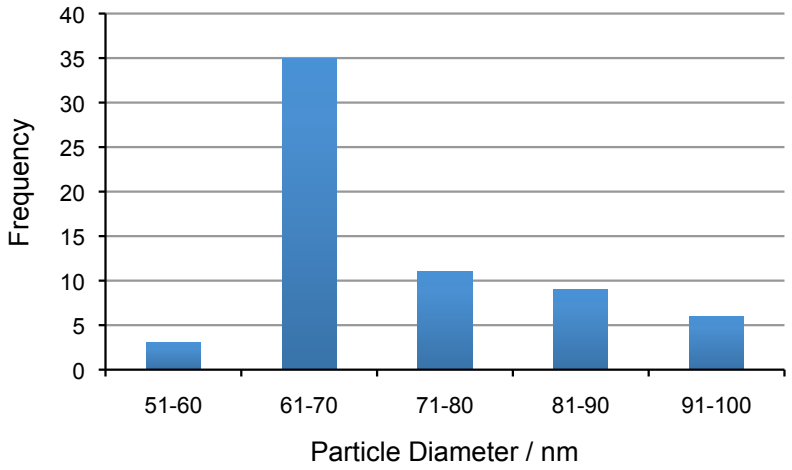

Figure 19. Histogram of the TEM particle size distribution for 50 nm XRD-size $BaTiO_3$ nanocubes.

As the CFO nanoparticles were necessarily functionalised with the aminosilane, the BTO particles were functionalised with 3-phosphonopropionic acid in order to engender them with a terminal COOH functionality. As with the aminosilane functionalisation, the binding of the phosphonic acid is a condensation reaction where the P-OH functional group of the phosphonic acid reacts with the acidic M-OH sites on the BTO nanoparticle surface, leading to binding of the molecule *via* M-O-P bonds and the elimination of a molecule of water (see Scheme 5).

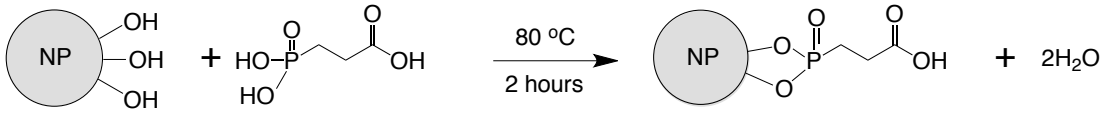

Scheme 5. Illustration of the anchoring of 3-phosphonopropionic acid to the surface of $BaTiO_3$.

Microanalysis performed on the 50 nm BTO particles suggested the functionalisation reactions had been successful with an increased carbon and hydrogen content observed post reaction (before functionalisation: C = 0.14%, H = 0.17%; after functionalisation: C = 0.53%, H = 0.32%), from which a coverage of 0.84 3-phosphonopropionic acid molecules per surface metal ion was calculated.

FTIR analysis (Figure 20) supported the microanalysis data with the C=O stretch of the protonated carboxylic acid observed at 1685 cm^{-1} and the P=O stretch present at 1040 cm^{-1}.[30]

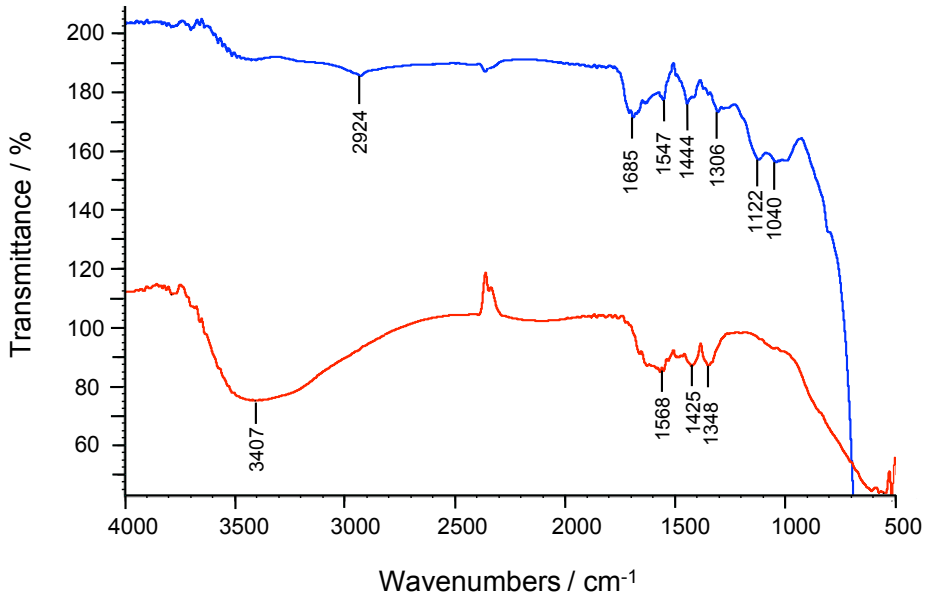

Figure 20. FTIR spectrum of 3-phosphonopropionic acid functionalised 50 nm $BaTiO_3$ nanoparticles.

^{31}P MAS-NMR (Figure 21) showed a resonance at 25 ppm, typical for a phosphonic acid bound to the surface of a nanoparticle *via* M-O-P binding.[30] The free phosphonic acid peak occurs at 34.1 ppm and is not observed in these samples, whilst the minor peak at 4.6 ppm indicates a small amount of bulk metal phosphate may be present, as was found following the binding of phosphonic acids to ZrO_2 nanoparticle surfaces.[30]

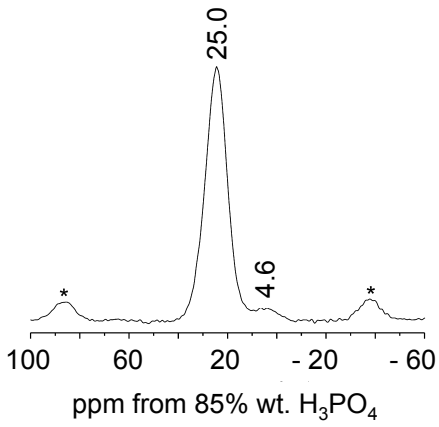

Figure 21. ^{31}P MAS-NMR of 3-phosphonopropionic acid functionalised 50 nm $BaTiO_3$ nanoparticles. The spinning side bands are marked with asterisks.

*4.3.7 Preparation of BTO (50 nm) - CFO (10 nm) "**a**" Assemblies*

The functionalised particles therefore have terminal carboxylic acid (on BTO) and amine (on CFO) functional groups, and were reacted with one another with the aim of controlling aggregation to give an alternating array of FE and FM particles, using two distinct approaches **I** (electrostatic assembly) and **II (**DCCI-coupled assembly). A control using unfunctionalised particles (**III**) was also performed as shown in Scheme 6.

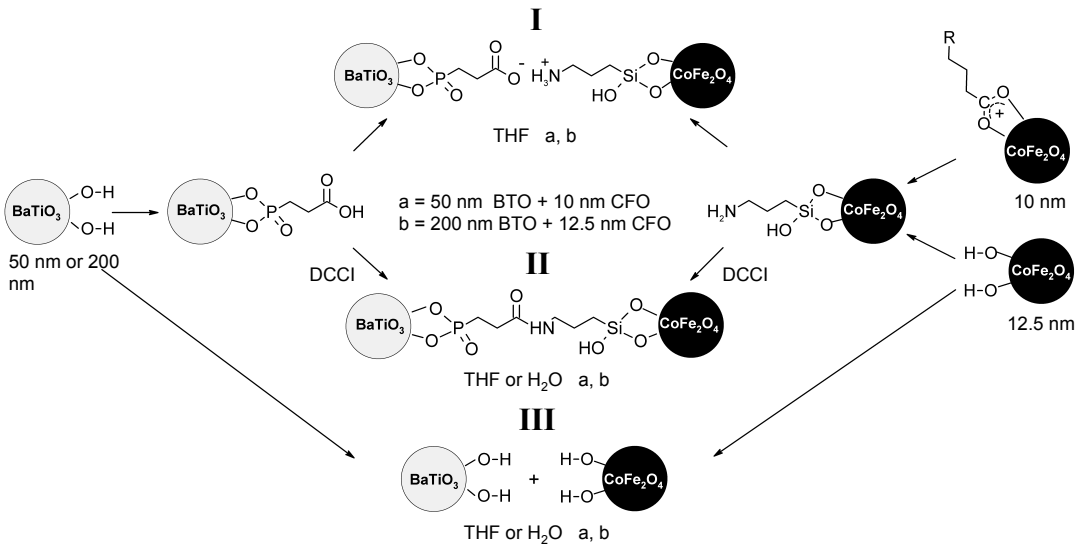

Scheme 6. The nanoparticle functionalisation and assembly procedures utilised in the study. **I** shows the electrostatic assembly of BTO and CFO in THF, **II** shows the DCCI coupled assembly of BTO and CFO in THF by covalent amide bond formation and **III** shows the control reaction performed with unfunctionalised particles in THF. **a** and **b** refer to reactions carried out with (a) 50 nm BTO, 10 nm CFO and (b) 200 nm BTO, 12.5 nm CFO. The as-drawn BTO-CFO products exist as nanoparticle suspensions in solution in the noted solvent(s).

Route **I** (Scheme 6) involved mechanically stirring the functionalised BTO and CFO nanoparticles at RT overnight in THF. TEM images of the product **Ia** (specific samples made using different sized particles are specified by the letter, **a** refers to the use of 50 nm BTO and 10 nm CFO particles to distinguish from a second set prepared and discussed later), prepared at a 1:1 molar ratio of BTO to CFO show the larger, central BTO particles are decorated by the smaller CFO particles (Figure 22). The aggregation of the nanoparticles in **I** is driven by electrostatics with an acid-base interaction between the carboxylic acid-terminated BTO and the amine terminated CFO, similar to that described by Galow et al. for SiO_2-Au aggregates.[7] Increasing the solvent polarity by transferring the nanoparticles into water leads to the **Ia** BTO-CFO aggregates breaking down, as evidenced by TEM (Figure 23). This behaviour confirmed there was only a weak, reversible interaction between the nanoparticles when route **I** was used, which is unfavourable when trying to control the dispersion of one phase in another.

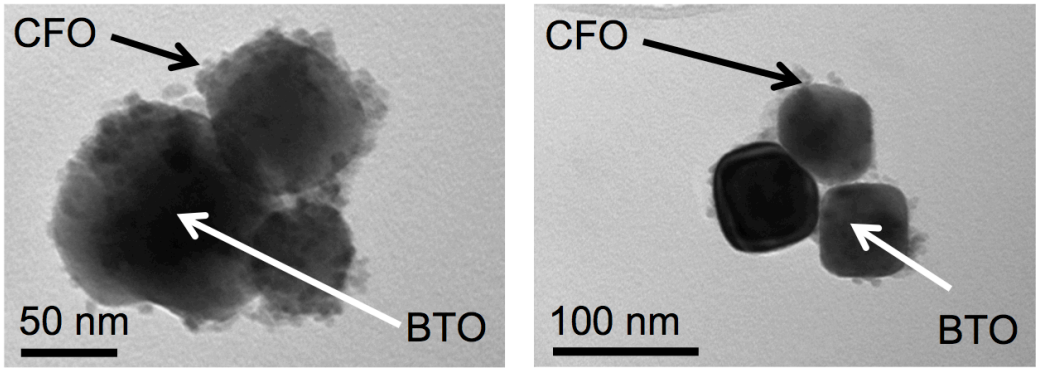

Figure 22. Transmission electron microscopy images of the $BaTiO_3$-$CoFe_2O_4$ **Ia** electrostatic assemblies in tetrahydrofuran.

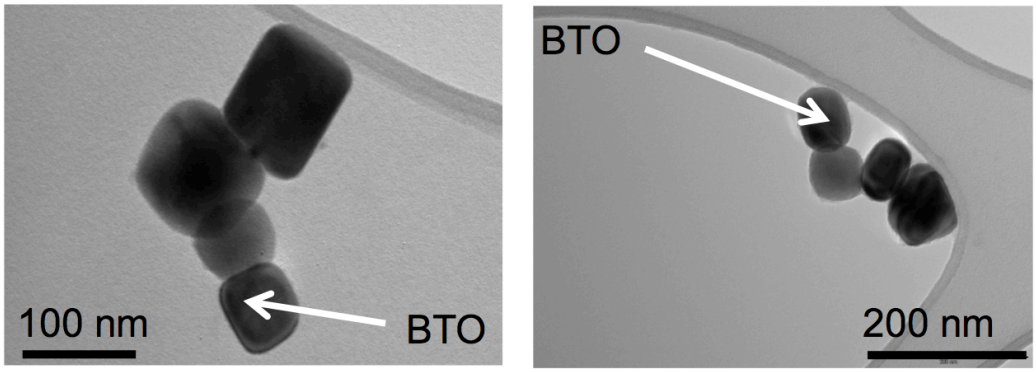

Figure 23. Transmission electron microscopy images of the $BaTiO_3$-$CoFe_2O_4$ **Ia** electrostatic assemblies in H_2O.

The nanoparticle assemblies are made more chemically robust in route **II** (Scheme 6) which involves the addition of the chemical coupling agent N-N' dicyclohexylcarbodiimide (DCCI) to the reaction mixture in THF. DCCI chemically links the carboxylic acid and amine terminated particles via the formation of covalent amide bonds, and was added after overnight stirring of the functionalised particles at RT (this ensured the nanoparticles were adequately dispersed and large same-phase aggregates were broken up). Following DCCI addition, the solution was then heated at 60 °C for 4 hours in order to promote the formation of the amide linkages between the nanoparticles. TEM images of the product from this reaction are shown in Figure 24.

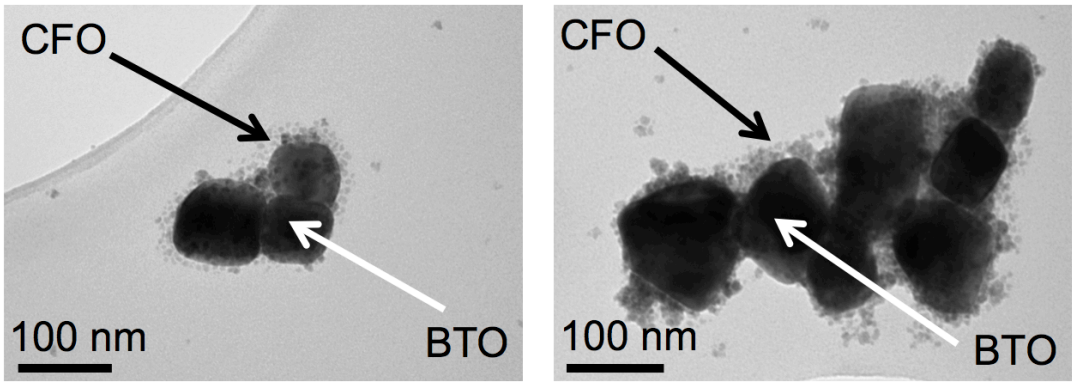

Figure 24. Transmission electron microscopy images of the $BaTiO_3$-$CoFe_2O_4$ DCCI coupled **IIa** assemblies in tetrahydrofuran.

HRTEM combined with fast Fourier transform (FFT) diffraction patterns (Figure 25), and high spatial resolution energy-dispersive X-ray analysis on a STEM (Figure 26), were used to confirm the identities of the particles within the assemblies obtained by route **II**.

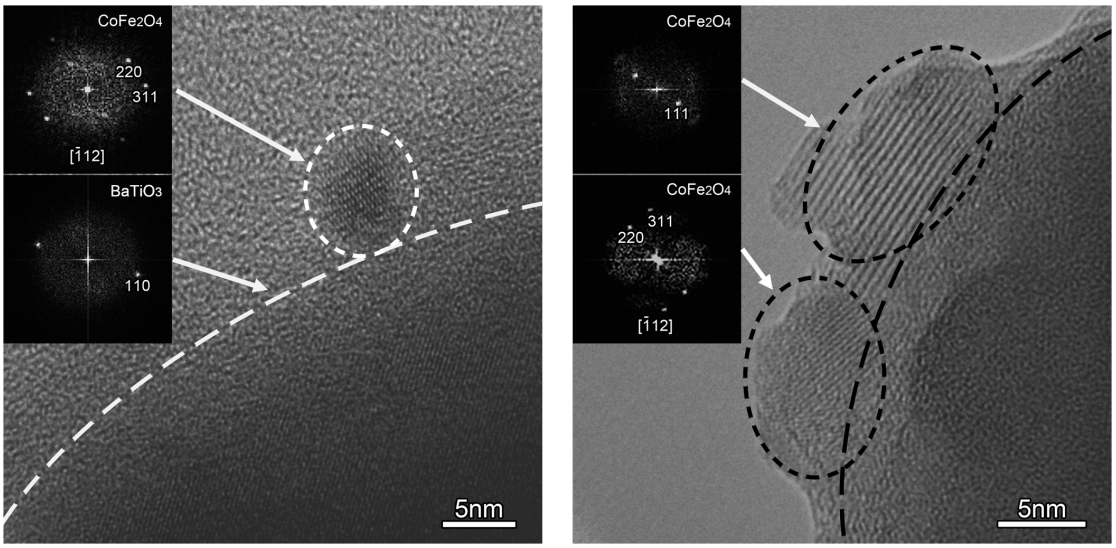

Figure 25. High resolution transmission electron microscopy and fast fourier transformations of two regions of the covalently-assembled **IIa** sample depicted in Figure 24. The image on the left shows a $CoFe_2O_4$ particle on the surface of a larger $BaTiO_3$ particle and the associated fast fourier transform diffraction patterns. The

image on the right shows the fast fourier transform diffraction patterns of two $CoFe_2O_4$ particles on the surface of a larger $BaTiO_3$ particle. Both images were taken from a sample prepared from particles suspended in tetrahydrofuran with a 1:1 molar ratio of $BaTiO_3$ to $CoFe_2O_4$.

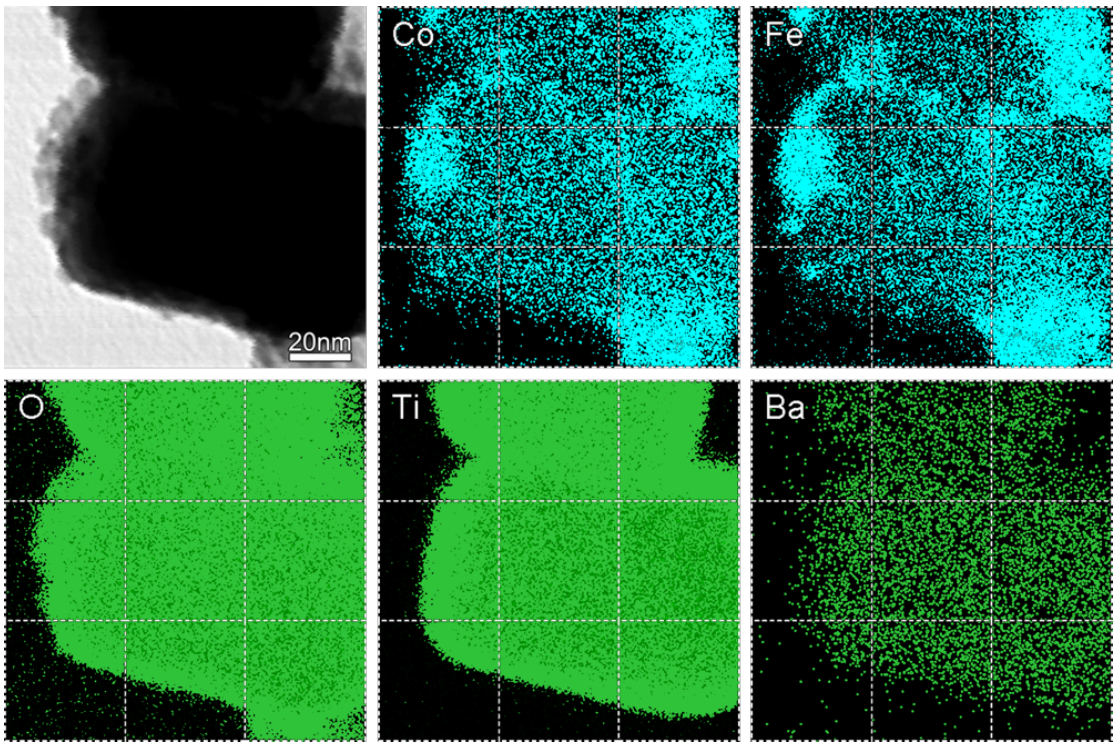

Figure 26. Scanning transmission electron microscopy energy dispersive X-ray spectroscopy mapping of the un-sintered as-prepared amide-bonded **IIa** composite depicted in Figure 24 prepared at a 1:1 molar ratio of $BaTiO_3$ to $CoFe_2O_4$, showing covalent attachment of the $CoFe_2O_4$ particles to the $BaTiO_3$ surface. The sample was taken from the nanoparticles suspended in tetrahydrofuran.

FTIR spectroscopy (Figure 27) confirmed the chemical coupling with the appearance of a peak at 1624 cm^{-1}, which is typical for C=O stretching in amide bonds. The distinct physical behaviour of the **II** aggregates also confirmed chemical coupling as they remained intimately dispersed (by TEM) in the more polar solvent H_2O, in

contrast to the **I** electrostatic assemblies where aggregation is lost upon transfer to H_2O (Figure 28).

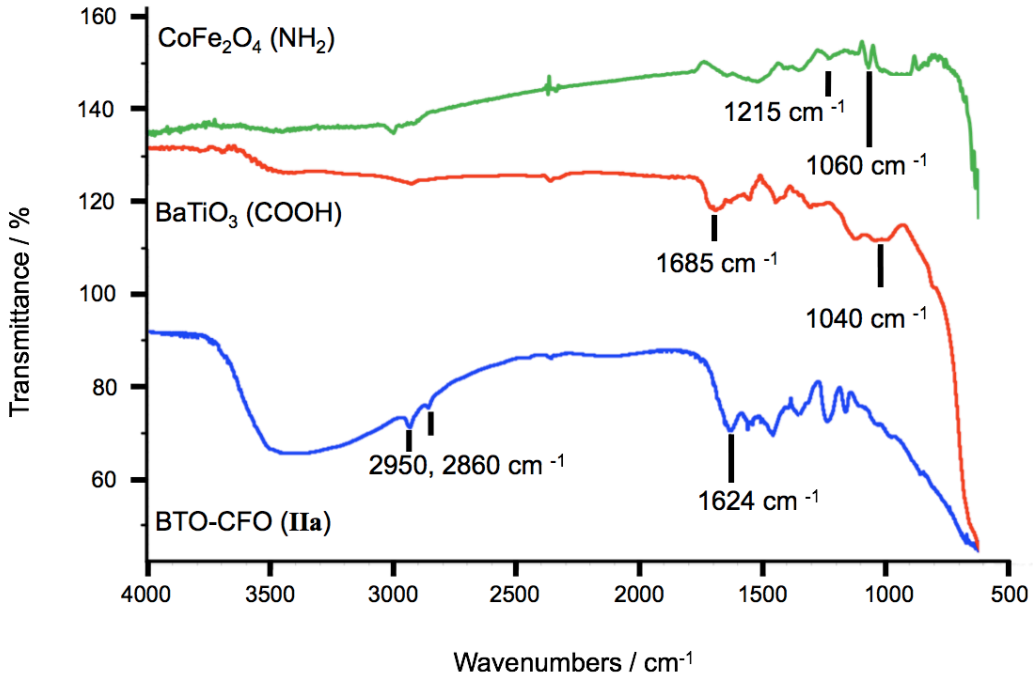

Figure 27. FTIR spectra of the DCCI coupled 50 nm $BaTiO_3$, 10 nm $CoFe_2O_4$ **IIa** composite with functionalised $BaTiO_3$ and $CoFe_2O_4$ nanoparticles shown for comparison.

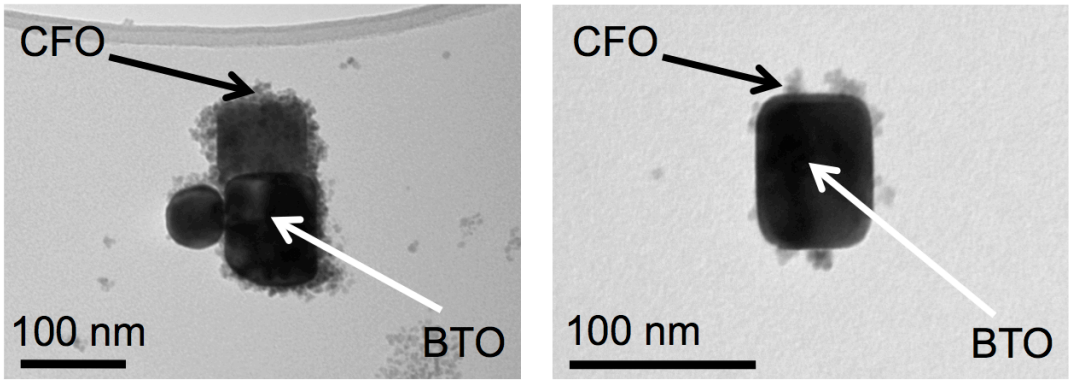

Figure 28. TEM of the $BaTiO_3$-$CoFe_2O_4$ DCCI coupled assemblies prepared *via* route **IIa** in H_2O.

Importantly, control reactions on unfunctionalised particles of BTO and CFO (route **III**, Scheme 6) showed the intimately mixed BTO-CFO aggregates were not formed in THF or H_2O without this prior functionalisation (Figure 29).

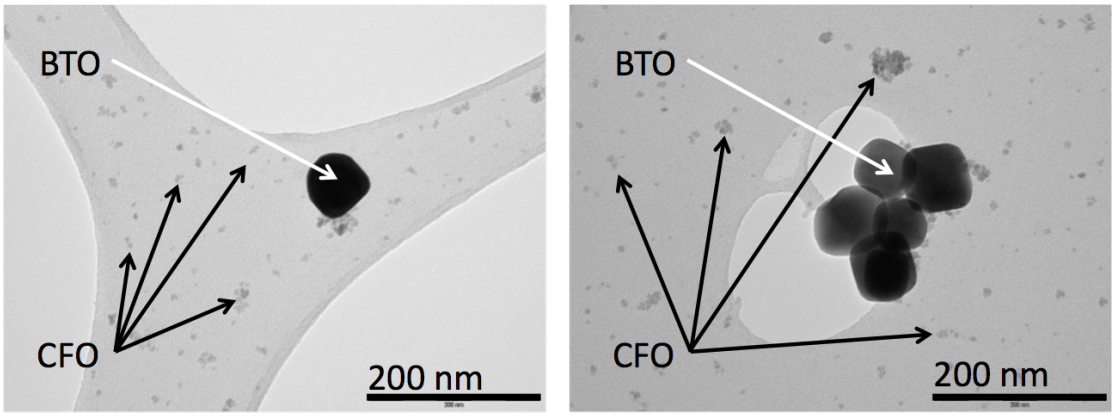

Figure 29. Transmission electron microscopy images of **IIIa** prepared by combining unfunctionalised $BaTiO_3$ and unfunctionalised $CoFe_2O_4$ nanoparticles in tetrahydrofuran, at a 1:1 molar ratio of $BaTiO_3$ to $CoFe_2O_4$.

The size contrast between the 50 nm BTO and 10 nm CFO used in the proof-of-principle step is necessary to clearly demonstrate the assembly of robust arrays *via* **II**, but the resulting processed **IIa** ceramics do not show room temperature magnetoelectric response. Whilst this work is dealt with in detail in Chapter 5, it was thought that this was due to the low piezeoelectric constant (d_{33}) of the 50 nm BTO particles. Measurement of the piezoelectric constant (d_{33}) of 200 nm BTO nanoparticles suggested these would be better candidates for the synthesis of a magnetoelectrically active composite of assembled nanoparticles.

4.3.8 Functionalisation of 200 nm BTO Particles

BTO nanoparticles with an SEM-size of 200 nm were used as received from Inframat Advanced Materials LLC. An XRD pattern of these particles can be seen in Figure 30 and TEM images can be seen in Figure 31.

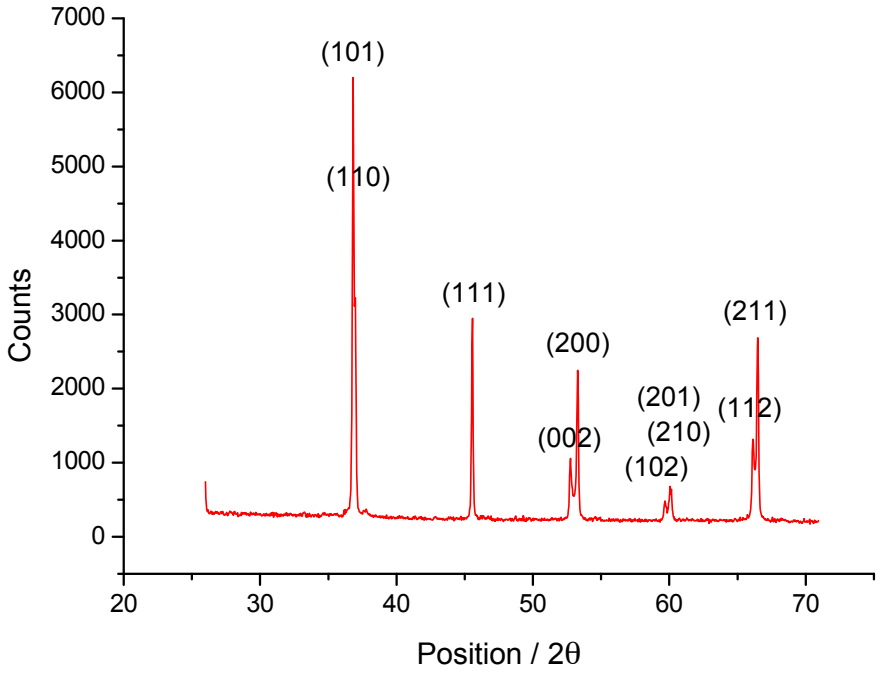

Figure 30. X-ray diffraction pattern of 200 nm (SEM-size) $BaTiO_3$ nanoparticles.

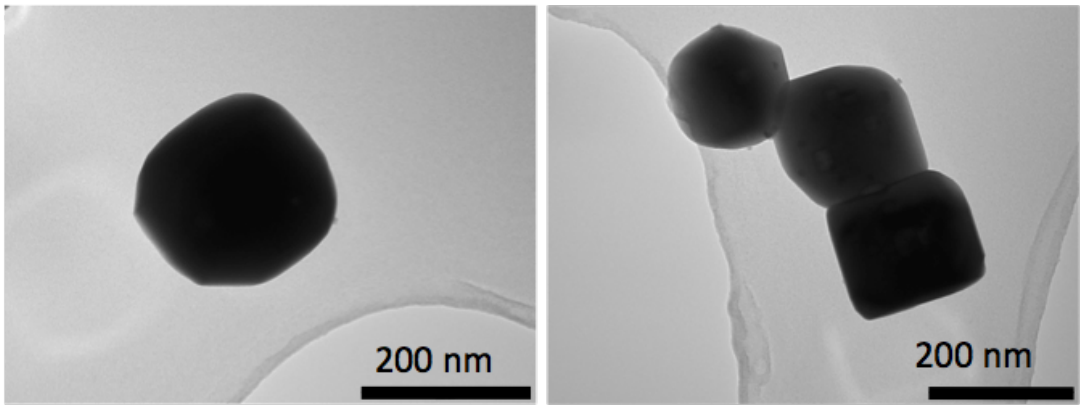

Figure 31. Transmission electron microscopy images of 200 nm (SEM-size) $BaTiO_3$ nanoparticles.

The XRD pattern suggested the particles were phase pure with an XRD particle size of 77 nm, whilst the TEM provided a particle size of 210 ± 73 nm, which was in closer agreement with the 200 nm SEM size provided by the supplier. A histogram of the TEM particle size distribution can be seen in Figure 32. The difference between the XRD and microscopy derived particle sizes is likely due to the 200 nm particles each consisting of multiple domains.

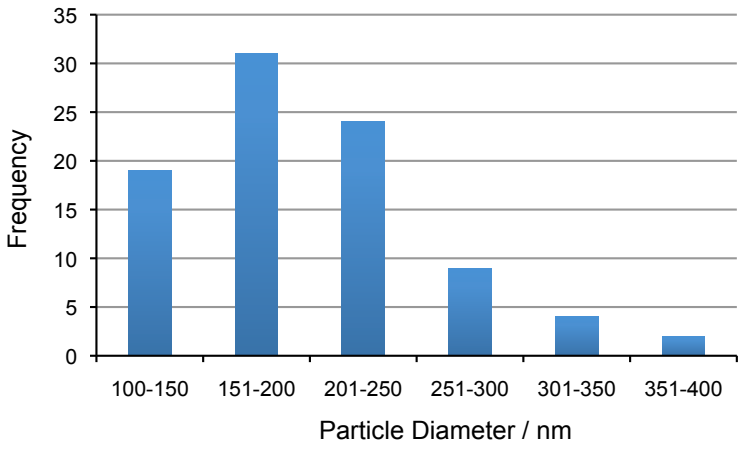

Figure 32. Histogram of the transmission electron microscopy particle size distribution for 210 ± 73 nm TEM-size $BaTiO_3$ nanoparticles.

As for the 50 nm BTO particles, the 200 nm particles were functionalised with 3-phosphonopropionic acid in order to engender them with a terminal carboxylic acid functionality. CHN microanalysis was carried out, though it was not possible to determine a loading of the phosphonic acid on the BTO particle surface in this case. This is likely due to the overall lower organic content and the detection limits of the instrument. For instance, the theoretical BET surface area of the 200 nm particles is 5.14 m^2g^{-1}, whilst it is 20.51 m^2g^{-1} for the 50 nm BTO cubic particles.

The FTIR data in Figure 33 shows a weak absorption at 1680 cm^{-1}, which is a typical C=O stretching frequency for a carboxylic acid. The peak at 3100 cm^{-1} is assigned to O-H stretching of the carboxylic acid along with surface O-H. Again, the peaks are weak due to the low organic content relative to the amount of BTO. The unfunctionalised 200 nm BTO particles also have several absorptions between 1100 and 1700 cm^{-1}, such as the peaks at 1130 and 1190 cm^{-1}. This further makes assignment of bands due to surface anchored species difficult for this sample, as the P=O and P-O bands observed for the 50 nm sample (Figure 20) typically occur between 1040-1100 cm^{-1} and are thus not observed here.

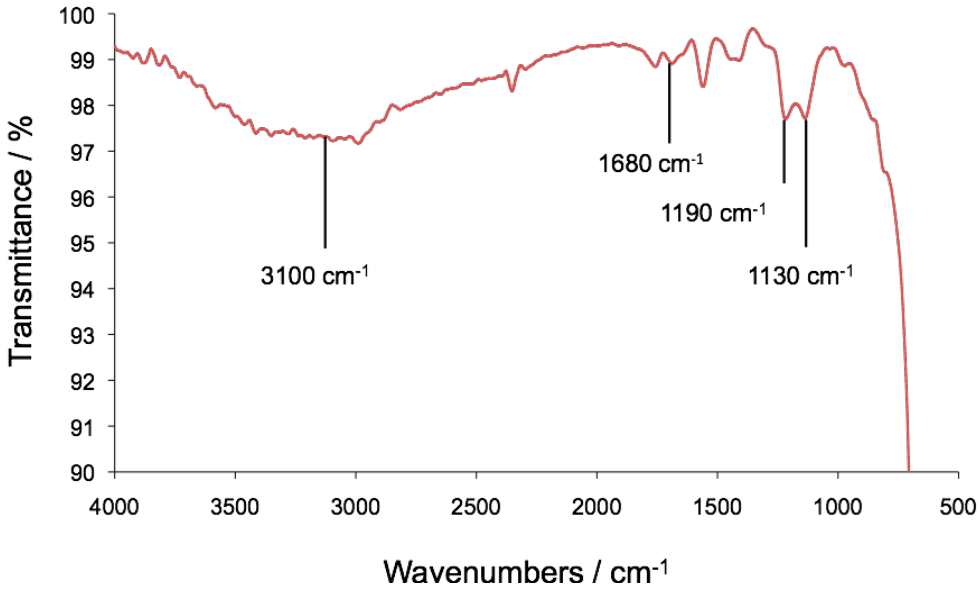

Figure 33. FTIR spectrum of 3-phosphonopropionic acid functionalised 200 nm $BaTiO_3$ nanoparticles.

Fluorescent molecule tagging and fluorescence microscopy imaging provided a qualitative proof of the anchoring of the phosphonic acid molecules to the 200 nm BTO surface. The fluorescent molecule lucifer yellow was bound to the carboxylic

acid terminated BTO nanoparticles *via* an EDC coupling reaction that was performed by overnight stirring at room temperature (Scheme 7).

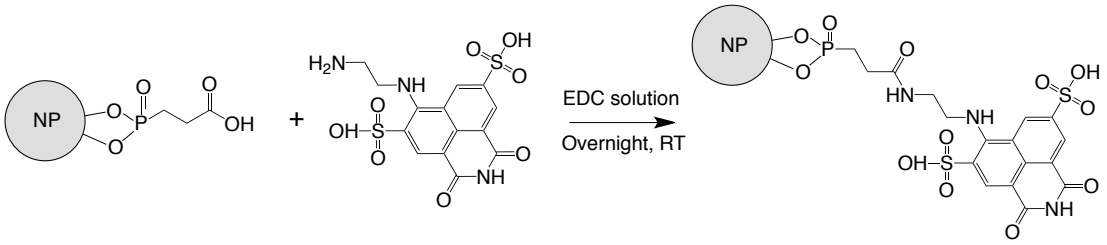

Scheme 7. Illustration of the binding of the fluorescent marker lucifer yellow to the surface of carboxylic acid terminated 200 nm $BaTiO_3$ nanoparticles.

The product of this reaction was imaged under the fluorescence microscope and the images can be seen in Figure 34. It can be clearly seen that there is green emission for the functionalised particles and no emission for the unfunctionalised particles (Figure 35). Lucifer yellow is known to emit at around 532 nm, the green part of the visible light spectrum and this data leads to the conclusion that the 200 nm BTO particles had been successfully functionalised with the phosphonic acid, as was the case for the 50 nm BTO.

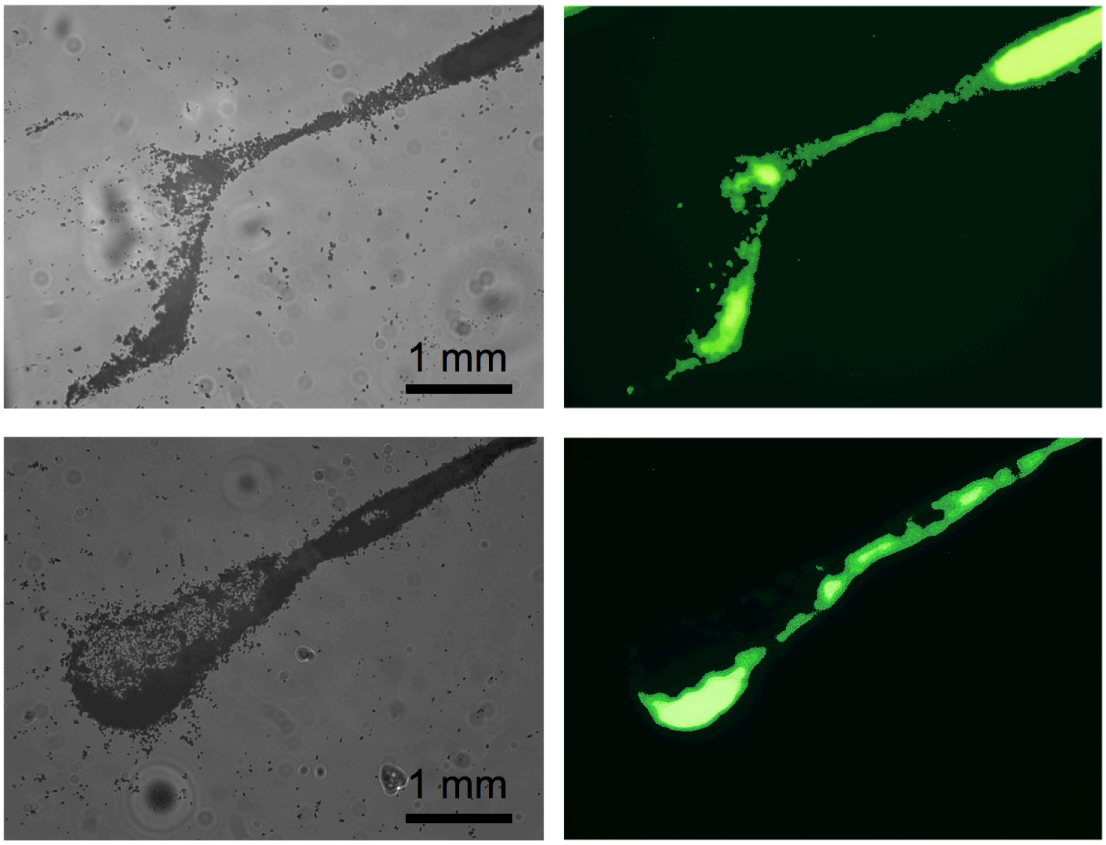

Figure 34. Optical microscope images (left) and fluorescence microscope image (right) of the phosphonic acid modified 200 nm $BaTiO_3$ particles after reaction with lucifer yellow. Note that the brightness of the green coloured fluorescence has been increased through image processing in order to enhance clarity.

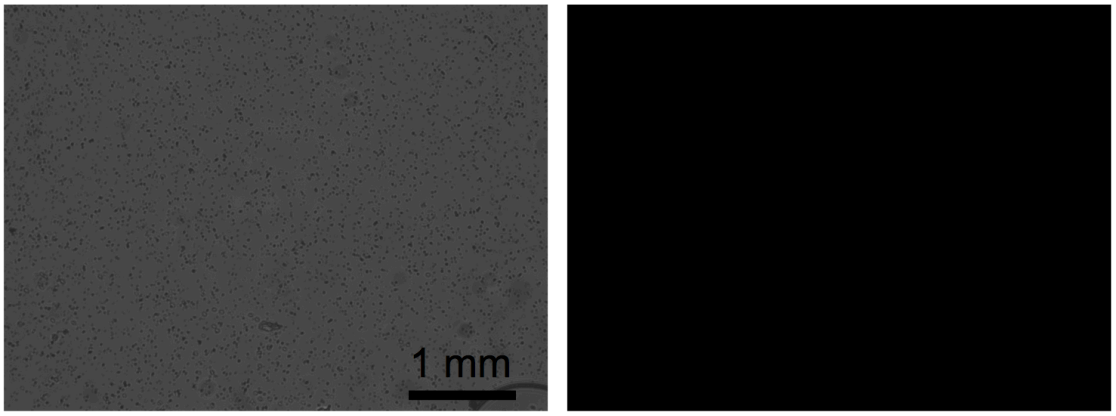

Figure 35. Optical microscope image (left) and fluorescence microscope image (right) of 200 nm $BaTiO_3$ unfunctionalised particles and lucifer yellow control reaction. $BaTiO_3$ particles can be seen in the optical microscope image and no fluorescence can be observed in the fluorescence microscope image.

*4.3.9 Preparation of BTO (200 nm) – CFO (12.5 nm) "**b**" Assemblies*

The coprecipitated 12.5 nm CFO nanoparticles that were discussed in section 4.3.3 were used as the second constituent of the **b** assemblies, with the goal of preparing a magnetoelectrically active composite. Whilst both the starting sets of 200 nm BTO and 12.5 nm CFO particles have larger particle size distributions and show greater aggregation in the characterising TEM data than the 50 nm BTO and 10 nm CFO, it is important to emphasize that the goal here was to prepare magnetoelectrically active composites that utilise the nanoparticle functionalisation and assembly procedure, rather than to prepare assemblies with smaller size distributions to aid TEM imaging, which has already been demonstrated above to show the alternating particle assembly in section 4.3.7. The lack of capping groups on the nanoparticles (50, 200 nm BTO and 12.5 nm CFO) means that the functional organic molecules can be readily anchored to their surfaces, however this inevitably also means there is

a larger particle size distribution and more inter-particle aggregation than if surface capped and stabilised particles were used.

The particles were coupled *via* the covalent assembly route **II** to afford composite aggregates **IIb** (Figure 36). This series of composites is referred to as **b**, denoting assemblies of 200 nm BTO and 12.5 nm CFO, to distinguish from **a** above, with 50 nm BTO and 10 nm CFO. A molar ratio of 5.5:1 BTO to CFO was chosen by considering the available surface area of the 200 nm BTO particles (5.1 m^2g^{-1}), which is approximately equal to the surface area of the imprint of the CFO particles at this composition (28.29 m^2g^{-1}, taking the imprint of each CFO particle to be a circle with an area of $\pi \times r^2$). Therefore it would be theoretically possible to get complete coverage of CFO onto BTO at this composition, provided the coupling reaction went to completion and in the absence of CFO aggregation and CFO particles linking to multiple BTO particles.

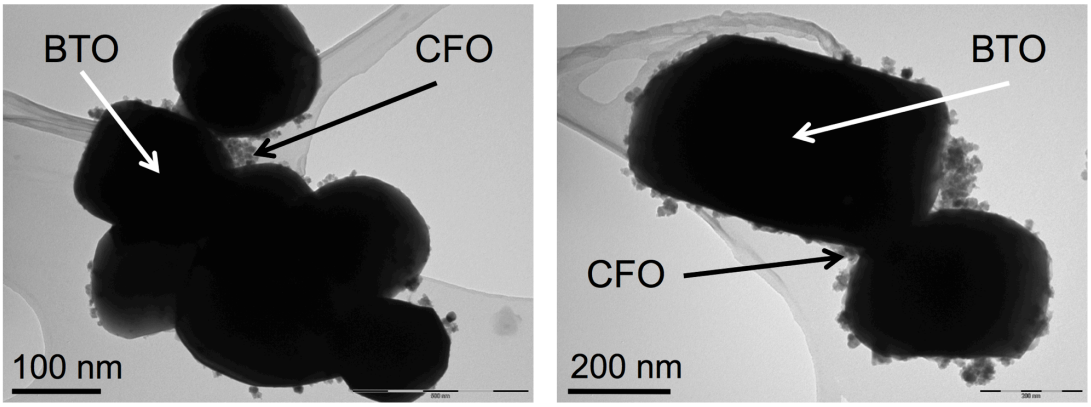

Figure 36. Transmission electron microscopy images of the as-prepared DCCI coupled $BaTiO_3$ (200 nm) - $CoFe_2O_4$ (12.5 nm) **IIb** composite prepared a 5.5:1 of $BaTiO_3$ to $CoFe_2O_4$ in tetrahydrofuran.

The TEM images in Figure 36 demonstrate the incomplete coverage of CFO on BTO that was observed at this 5.5:1 composition, likely due to CFO particle aggregation and the CFO particles bridging across multiple BTO particles. Figure 37 shows a **IIb** composite prepared with a higher CFO content, a 2.75:1 molar ratio of BTO/CFO. This represents an excess of CFO, though at this composition the TEM images do show near complete coverage of the BTO particle surface by the CFO nanoparticles.

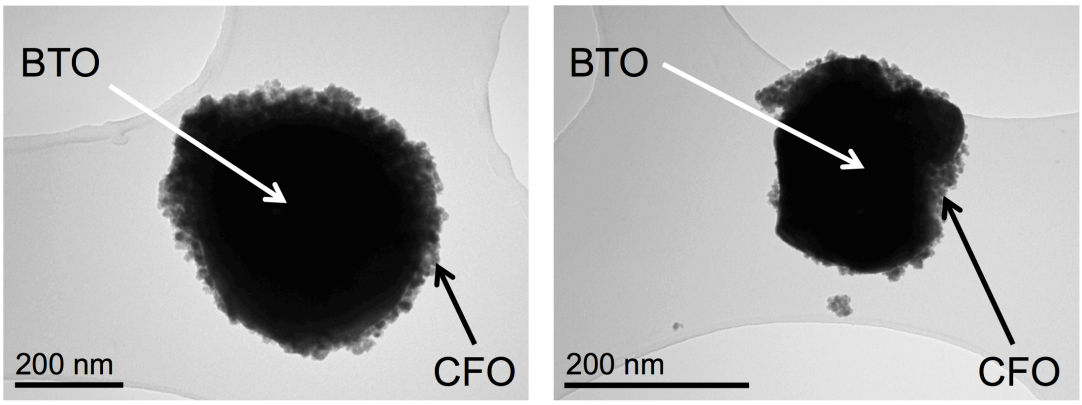

Figure 37. Transmission electron microscopy images of an as-prepared DCCI coupled $BaTiO_3$ (200 nm) - $CoFe_2O_4$ (12.5 nm) **IIb** composite prepared at a $BaTiO_3$ to $CoFe_2O_4$ 2.75:1 molar ratio in THF. The images show the larger $BaTiO_3$ particles decorated by the smaller $CoFe_2O_4$ particles, as was observed in the **IIa** $BaTiO_3$ (50 nm) - $CoFe_2O_4$ (10 nm) system (Figure 24).

4.3.10 Further Control Reactions

In addition to the **IIIa** control reaction performed using unfunctionalised particles (Figure 29), a number of other control reactions were performed using the 50 nm BTO and 10 nm CFO nanoparticles. These were as follows: 1) BTO (NH_2) and CFO (NH_2) in THF 2) BTO (NH_2) and CFO (NH_2) in H_2O and 3) BTO (NH_3^+) and CFO (NH_3^+) in H_2O.

TEM images of the product from reaction 1) can be seen in Figure 38a. Here it can be seen that the BTO and CFO nanoparticles assemble as observed for the BTO (COOH) and CFO (NH_2) system. It was thought that this assembly was due to hydrogen bonding between the terminal primary amine groups on the nanoparticles; the hydrogen bonds between amine groups are weak and this would explain why the coverage of the CFO nanoparticles on the BTO nanoparticle surface is lower than for the amine and carboxylic acid assembly. The theory that hydrogen bonding was responsible for these assemblies was supported by the TEM images taken of the same sample after transfer to the more polar H_2O. A TEM image of this sample is shown in Figure 38b and it shows that the BTO and CFO nanoparticles were not assembled as observed in THF, likely due to the terminal amine groups of the nanoparticles forming stronger hydrogen bonds with the water molecules rather than with each other.

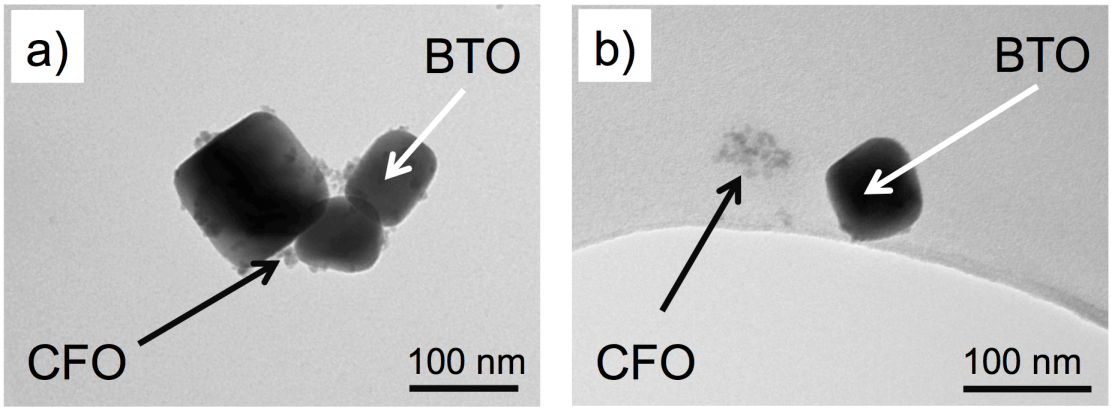

Figure 38. TEM images of $BaTiO_3$ (NH_2) – $CoFe_2O_4$ (NH_2) control reaction in a) tetrahydrofuran and b) H_2O.

A control reaction was also carried by suspending the amine-terminated nanoparticles in an aqueous solution of acetic acid at pH 4. The TEM images shown

in Figure 39 demonstrate how the BTO-CFO nanoparticle assembly is not observed in this sample, and the nanoparticles appeared more disperse than before protonation, likely due to electrostatic repulsion between the same-charged nanoparticles.

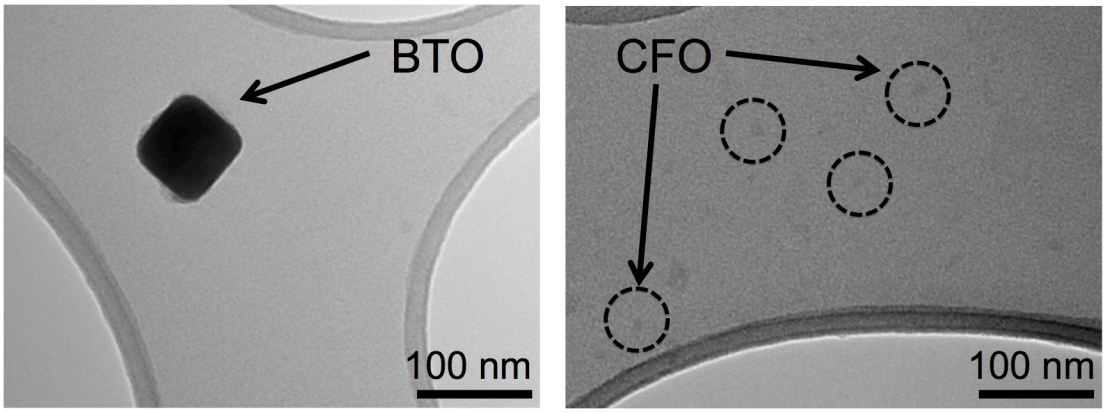

Figure 39. TEM images of $BaTiO_3$ (NH_3^+) – $CoFe_2O_4$ (NH_3^+) particles in H_2O. The nanoparticles were functionalised as described previously, and suspended in an aqueous solution of acetic acid at pH 4.

4.3.11 Assemblies using Bio-molecules

Further to the assembly using aminosilane and phosphonic acid molecules, assembly using adenosine monophosphate (AMP) and thymine-1-acetic acid (TAA) was attempted, with the goal of producing assemblies *via* the highly-specific hydrogen bonding that adenine and thymine undergo with one another (Scheme 8).

50 nm BTO nanoparticles were directly functionalised with AMP using the same approach that was developed for the functionalisation with 3-phosphonopropionic acid, while an EDC/NHS coupling reaction was used to bind the TAA to the amine-terminated 10 nm CFO nanoparticles *via* amide bonds. Assembly reactions were performed as for the electrostatic **Ia, b** assemblies and TEM images of the assembled nanoparticles can be seen in Figure 40. From the TEM images it appears the

assembly of BTO and CFO nanoparticles is taking place, though further work would be needed to characterise the functionalised particles, in order to rule out assembly *via* hydrogen bonding interactions between terminal amine groups

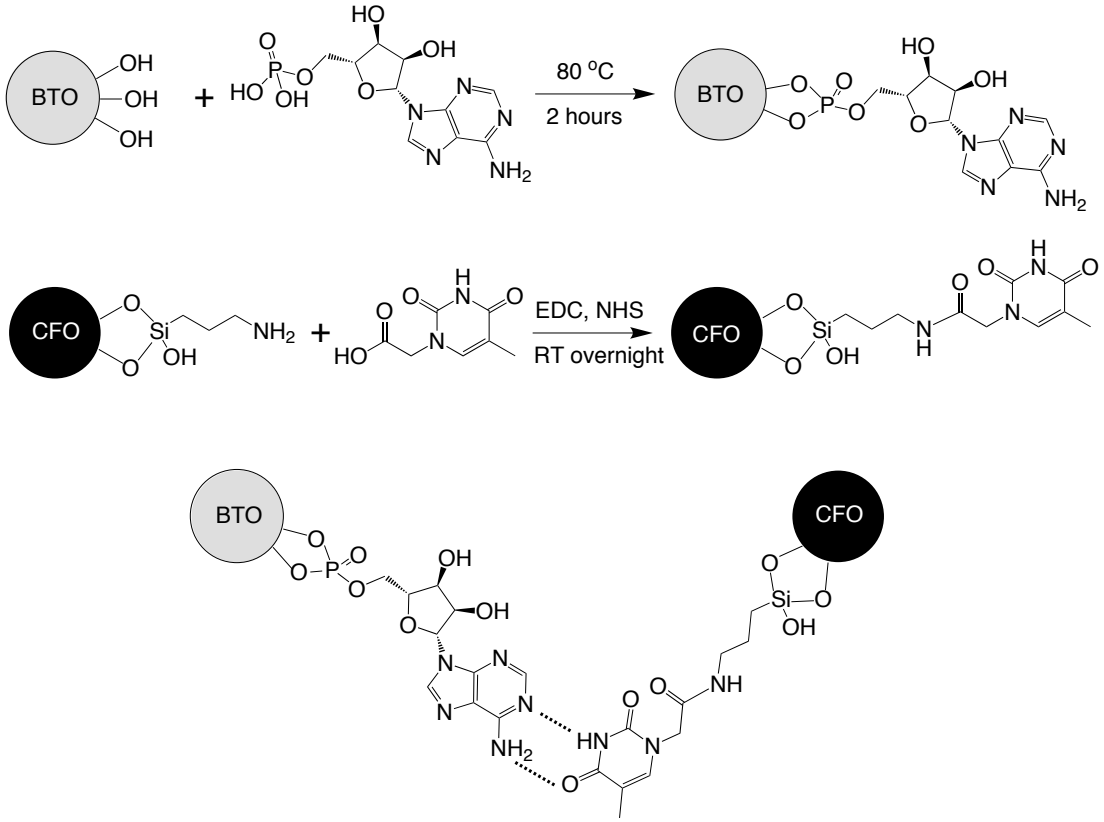

Scheme 8. An illustration of the functionalisation of $BaTiO_3$ and $CoFe_2O_4$ nanoparticles with adenosine 5'-monophosphate and thymine-1-acetic acid, and their assembly *via* hydrogen bonding interactions.

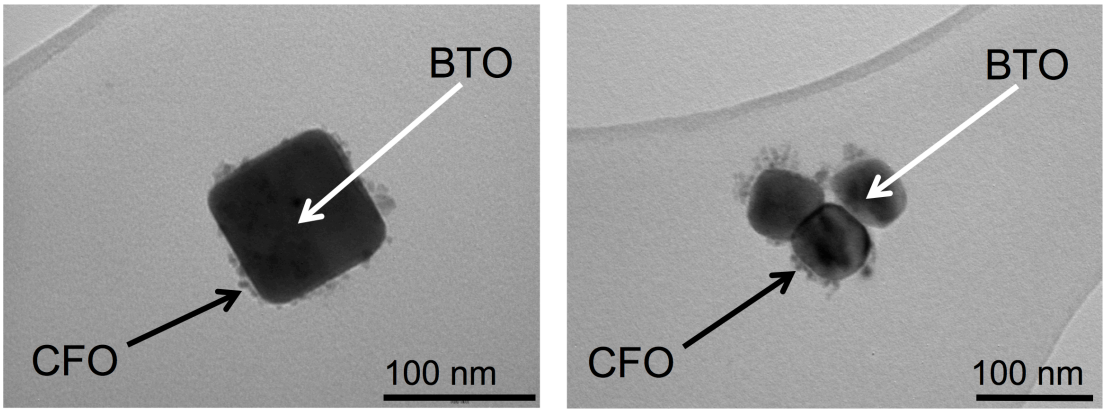

Figure 40. TEM images of $BaTiO_3$ and $CoFe_2O_4$ nanoparticles assembled using surface thymine and adenine groups.

4.3.12 Assembly of BTO Nanowires and CFO Nanoparticles

In order to establish whether the functionalisation and assembly strategy was extendable to other morphologies of nanomaterials, experiments were carried out to functionalise and assemble BTO nanowires and CFO nanoparticles. This system is also of interest for the development of more efficient magnetoelectric devices, an area dealt with in detail in Chapter 5.

BTO nanowires were synthesised *via* a $K_2Ti_4O_9$ precursor as detailed by Kang et al.[20] Following treatment with acetic acid, the nanowires were found to be phase pure by XRD (Figure 41), while SEM and TEM images (Figures 42 and 43) show nanowires were predominantly obtained, with a good degree of dispersity and a TEM length of 3.8 ± 2 μm and width of 90 ± 30 nm. Histograms of the TEM length and width of the nanowires can be seen in Figure 44. The sample was primarily the nanowire morphology, though approximately 2.5% of the sample was the cross-shaped particles of approximately 1 μm in diameter, as observed in Figure 43.

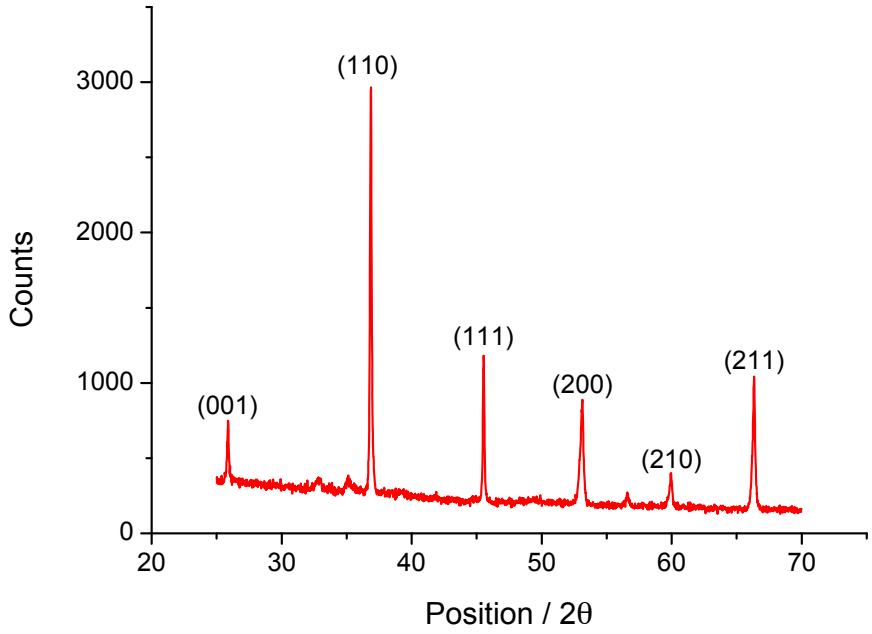

Figure 41. X-ray diffraction pattern of $BaTiO_3$ nanowires. Additional unlabelled peaks were identified as unreacted $K_2Ti_4O_9$.

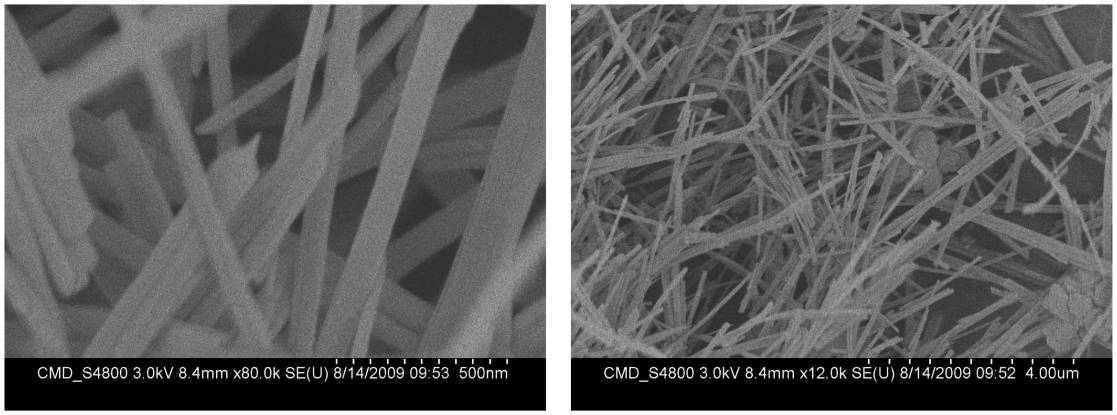

Figure 42. Scanning electron microscopy images of $BaTiO_3$ nanowires prepared *via* a $K_2Ti_4O_9$ precursor.

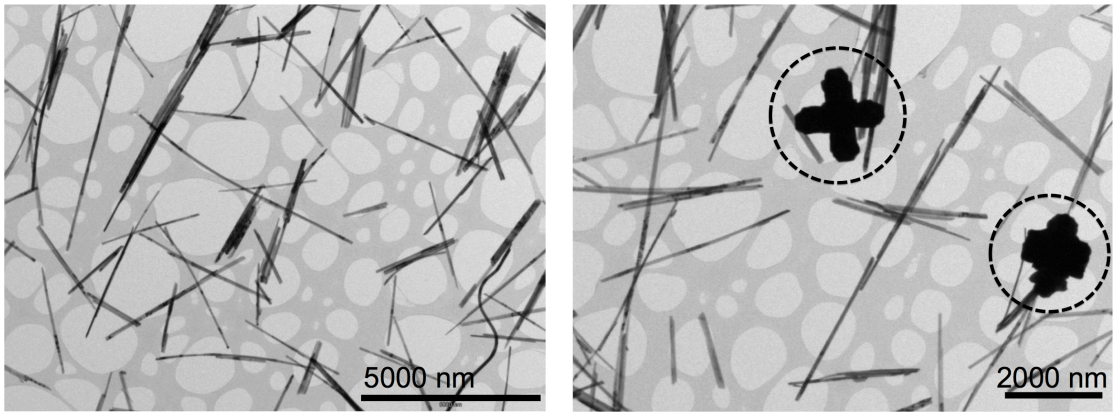

Figure 43. Transmission electron microscopy images of $BaTiO_3$ nanowires in H_2O. The cross-shaped $BaTiO_3$ particles, a minor phase in the sample, is circled in the image on the right.

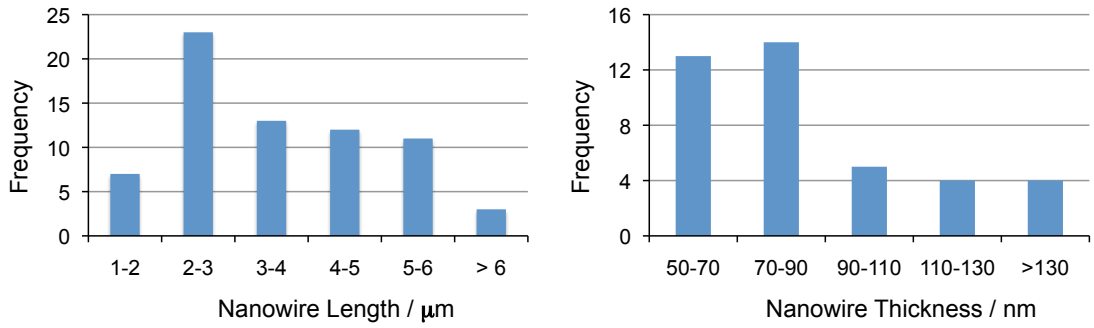

Figure 44. Histograms of the transmission electron microscopy size distribution for the $BaTiO_3$ nanowires length (left) and width (right).

Functionalisation experiments were performed as described for the 50 nm BTO particles, though owing to the low theoretical surface area of the BTO nanowires (7.69 m^2g^{-1} compared to 20.51 m^2g^{-1} for 50 nm BTO), it was not possible to determine a surface coverage using CHN microanalysis or study the vibrational absorption bands using FTIR.

DCCI coupling reactions were carried out with 12.5 nm coprecipitated CFO nanoparticles at a molar ratio of 2.75:1 BTO to CFO, and TEM images of the

assemblies can be seen in Figure 45. The images show the assembly of the CFO particles on the surface of the BTO nanowire surface, as observed for the **IIa,b** assemblies discussed previously. Similarly, the DCCI assemblies were stable in H_2O.

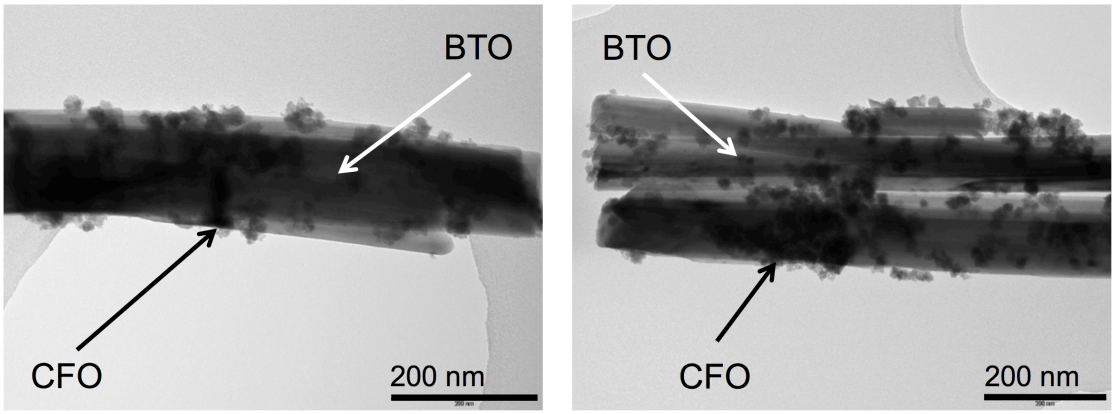

Figure 45. Transmission electron microscopy images of the DCCI coupled $BaTiO_3$ nanowires and 12.5 nm $CoFe_2O_4$ nanoparticles in THF, prepared at a molar ratio of 2.75:1 $BaTiO_3/CoFe_2O_4$.

4.4 Conclusions

Barium titanate and cobalt ferrite nanoparticles have been assembled by the chemical bond-controlled aggregation of oxide nanoparticles carrying complementary functional groups to ensure alternation of the FE and FM phases. 50 nm $BaTiO_3$ nanoparticles were engendered with terminal carboxylic acid functionalities *via* the anchoring of phosphonic acid molecules to the nanoparticle surfaces, while the cobalt ferrite nanoparticles were given terminal amine functionalities *via* the oleic acid to aminosilane ligand exchange reaction. The nanoparticles were assembled *via* electrostatic interactions, and though coupling of the amine and carboxylic acid groups using DCCI, with the two types of aggregates showing distinctly different behaviour in solvents of different polarities. The assembly strategy was extendable to

particles of different sizes, with assemblies of 200 nm barium titanate and 12.5 nm cobalt ferrite also formed. Furthermore, the strategy was not limited by particle morphology with nanowires and nanoparticles also being assembled *via* the same route. This synthetic methodology is widely applicable to the construction of other types of multifunctional hybrid oxide nanoparticle composites with property combinations of interest, for example, in light harvesting and catalysis, as well as biomedicine. It offers spatially directed assembly of controlled interfaces through chemical bonds formed under mild conditions, and, while necessarily less specific than DNA-based methods, is scalable and cheap.

References

1. J. E. Millstone, W. Wei, M. R. Jones, Y. Yoo, C. A. Mirkin, *Nano Lett*. **2008**, 8, 2526.
2. M. Ghosh, K. Biswas, A. Sundaresan, C. N. R. Rao, *J. Mater. Chem*. **2005**, 16, 106.
3. K. Page, C. S. Schade, J. Zhang, P. J. Chupas, K. W. Chapman, T. Proffen, A. K. Cheetham, R. Seshadri, *Mater. Res. Bull*. **2007**, 42, 1969.
4. F. Bonell, A. Sanchot, E. Dujardin, R. P´echou, C. Girard, M. Li, S. Mann, *J. Chem. Phys.* **2009**, 130, 034702.
5. S. A. Corr, M. Grossman, J. D. Furman, B. C. Melot, A. K. Cheetham, R. Seshadri, *Chem. Mater*. **2008**, 20, 6396.
6. X. Xu, N. L. Rosi, Y. Wang, F. Hou, C. A. Mirkin, *J. Am. Chem. Soc*. **2006**, 128, 9286.
7. T. H. Aglow, A. K. Boal, V. M. Rotello, *Adv. Mater*. **2000**, 12, 576.
8. M. Li, S. Mann, *J. Mater. Chem*. **2004**, 14, 2260.

9. S. Mornet, C. Elissalde, O. Bidault, F. Weill, E. Sellier, O. Nguyen, M. Maglione, *Chem. Mater*. **2007**, 19, 987.
10. D. V. Talapin, *ACS Nano* **2008**, 2, 1097.
11. E. V. Shevchenko, D. V. Talapin, C. B. Murray, S. O'Brien, *J. Am. Chem. Soc*. **2006**, 128, 3620.
12. I. E. Sendroiu, D. J. Schiffrin, J. M. Abad, *J. Phys. Chem. C*. **2008**, 112, 10100.
13. D. G. Thompson, R. J. Stokes, R. W. Martin, P. J. Lundahl, K. Faulds, D. Graham, *Small* **2008**, 4, 1054.
14. M. Niederberger, G. Garnweitner, *Chem. Eur. J*. **2006**, 12, 7282.
15. M. Winter, R. J. Brodd, *Chem. Rev*. **2004**, 104, 4245.
16. J. L. G. Fierro, L. L. G. Fierro, *Metal Oxides: Chemistry and Applications, CRC Taylor & Francis, Boca Raton* **2006**.
17. A. Verma, V. M. Rotello, *Chem. Commun*. **2005**, 3, 303.
18. Y. V. Kolen'ko, K. A. Kovnir, I. S. Neira, T. Taniguchi, T. Ishigaki, T. Watanabe, N. Sakamoto, M. Yoshimura, *J. Phys. Chem. C*. **2007**, 111, 7306.
19. B. Hou, Z. J. Li, Y. Xu, D. Wu, Y. H. Sun, *Chem. Lett*. **2005**, 34, 1040.
20. S-O. Kang, B. H. Park, Y-I Kim, *Cryst. Growth. Des*. **2008**, 8, 3180.
21. J. Xie, S. Peng, N. Brower, *N. Pourmand*, S. X. Wang, S. H. Sun, Pure Appl. Chem. **2006**, 78, 1003.
22. P. Kim, S. C. Jones, P. J. Hotchkiss, J. N. Haddock, B. Kippelen, S. R. Marder, J. W. Perry, *Adv. Mater*. **2007**, 19, 1001.
23. R. De Palma, S. Peeters, M. J. Van Bael, H. Van den Rul, K. Bonroy, W. Laureyn, J. Mullens, G. Borghs, G. Maes, *Chem. Mater*. **2007**, 19, 1821.
24. P. H. Mutin, G. Guerrero, A. Vioux, *J. Mater. Chem*. **2005**, 13, 3761.
25. M. Mikhaylova, D. K. Kim, C. C. Berry, A. Zagorodni, M. Toprak, A. S. G.

Curtis, M. Muhammed, *Chem. Mater*. **2004**, 16, 2344.

26. C. Zhang, B. Wängler, B. Morgenstern, H. Zentgraf, M. Eisenhut, H. Untenecker, R. Krüger, R. Huss, C. Seliger, W. Semmler, F. Kiessling, *Langmuir* **2007**, 23, 1427.
27. I. Alkorta, J. Elguero, A. Fruchier, D. J. Macquarrie, A. Virgili, *J. Organomet. Chem*. **2001**, 625, 148.
28. B. L. Cushing, V. L. Kolesnichenko and C. J. O'Connor, *Chem. Rev*. **2004**, 104, 3893-3946.
29. S. Mohapatra, P. Pramanik, *Colloids Surf. A*. **2009**, 339, 35.
30. J. Pawsey, K. Yach, L. Reven, *Langmuir*, **2002**, 18, 5205.
31. S. Onclin, B. J. Ravoo, D. N. Reinhoudt, *Anew, Chem. Int. Ed*. **2005**, 44, 6282.

Chapter 5

Chapter 5

5 Chemical Bond Assembled Multifunctional Oxide Nanocomposites

5.1 Introduction

Magnetoelectric (ME) composites are materials that become electrically polarised upon the application of an external magnetic field. The ME effect is described as a 'product property' and it arises from the coupling of the magnetostrictive and piezoelectric components. ME materials provide opportunities for the development of new multifunctional devices such as magnetic-electric transducers, sensors, actuators and memory devices.[1,2] ME composites of ferroelectric (FE) and ferromagnetic (FM) components can exhibit a ME response above room temperature (RT) and examples include bulk ceramic composites of piezoelectrics and ferrites, two-phase composites of magnetic alloys and piezoelectrics and nanostructured thin films.[3–5] One of the problems associated with current particulate ME composites (materials comprised of FE and FM particles) lies in their preparation route; they are normally prepared by grinding the FE and FM particles together and then sintering a pressed pellet at high temperature in order to increase its density. It should be noted that dense pellets are required in order to observe a ME effect, as the effect requires efficient transmission of the magnetostrictive force to the piezoelectric phase, which produces a charge when compressed. Consequently, the extent of the interaction

between the FE and FM phases is limited by how well dispersed these phases are within one another, which is usually poor in composites prepared by the traditional grinding and firing method.[6]

Thus, one of the big challenges in developing the next generation of particulate ME composites comes in achieving a high degree of dispersity between the FE and FM components, in order to maximise the extent of the mechanical coupling between the phases, and therefore increase the magnitude of the ME effect.[6]

The chemical functionalisation and assembly procedure that was demonstrated in Chapter 4 involves the predictable assembly of FE ($BaTiO_3$) and FM ($CoFe_2O_4$) particles into solution-based assembles and this is, therefore, an attractive pathway for the preparation of ME materials, provided the solution based assemblies can be processed into dense composites that retain the intimate mixing of the two phases. Electrostatic assembly of silica-coated $BaTiO_3$ /PZT-γFe_2O_3 composites has been reported by Mornet et al.[7] The authors used aminosilane functionalised $BaTiO_3$@SiO_2 or PZT@SiO_2 nanoparticles and assembled them with γ-Fe_2O_3 *via* electrostatic interactions. The sintered composites did not exhibit magnetoelectric properties, thought to be because of leakage due to the silica coating on the nanoparticles, and the low magnetostriction of γ-Fe_2O_3.

However, by directly attaching complementary functional groups to the FE and FM oxide surfaces, we were able to covalently bind an alternating array of intimately dispersed piezoelectric $BaTiO_3$ (BTO) and magnetostrictive $CoFe_2O_4$ (CFO) particles, without the need for a silica coating. In this chapter the processing of these assembled nanoparticles into dense ceramics is presented, along with characterisation of their properties and measurements of the ME effect. In addition, comparisons are drawn between the assembled ceramic composites and those prepared *via* the

traditional grinding and firing method. A more detailed discussion on the background to magnetoelectric materials is given in Chapter 1.

5.2 Experimental

5.2.1 Preparation of BTO/CFO Ceramics

The BTO/CFO composite (250 mg for the **A** composite, 500mg for all others) was pressed in a 10 mm die at a pressure of 5 tons, and further pressed in a cold isostatic press at a pressure of 30,000 psi.

5.2.2 Processing of BTO/CFO Ceramics

The pellets were sintered at 850 °C for 12 h (5 and 10 °C min^{-1} heating and cooling rates, respectively) and further sintered at the desired temperature (1050-1200 °C) for 30 min (5 and 10 °C min^{-1} heating and cooling rates, respectively). Contacts were painted onto the samples using an Ag-based paint. The samples were poled in a silicone oil bath for a period of 1 h by applying a potential across the sample and cooling to RT through the BTO cubic to tetragonal transition temperature, starting at 160 °C.

5.2.3 Reaction of 200 nm BTO with H_2O_2

300 mg of 200 nm BTO particles were refluxed in 106 mL of 30 wt% hydrogen peroxide solution at 100 °C for 4 hours. The particles were retrieved by centrifugation, washed 3 times with H_2O and then dried at 80 °C overnight. The nanoparticles were then functionalised with 3-phosphonopropionic acid and assembled with 12.5 nm CFO as was described for the **IIb** assemblies in Chapter 4. The nanoparticles were then treated with H_2O_2 with a view to increasing the number

of reactive surface hydroxyl groups, as described by Chang et al.[8]

5.2.4 Synthesis of 50 nm CFO Nanoparticles

5.869 g (2.10 mmol) $FeSO_4.7H_2O$ and 2.511 g (1.05 mmol) $CoCl_2.6H_2O$ were dissolved in 120 mL H_2O and heated to 90 °C. A second solution of 1.4093 g (1.40 mmol) KNO_3 and 2.114 g (5.29 mmol) NaOH in 40 mL H_2O was also prepared and heated to 90 °C. The Co, Fe salt solution was then added to the KNO_3, NaOH solution under stirring at 240 rpm. The mixture was left stirring for 3 hours at 90 °C, and then the liquid was decanted, with the nanoparticles collected by the use of a magnet. The particles were washed 3 times with H_2O and dried overnight at 80 °C in air. This route is as detailed by Ollson et al.[9]

5.2.5 Characterisation

5.2.5.1 X-ray Diffraction

X-ray diffraction data were collected on a PAN'alytical X-Pert diffractometer with an X-Celerator detector and Co $K_{\alpha 1}$ radiation and using variable divergence slits with an illuminated length of 15mm.

5.2.5.2 TEM Imaging

The lower resolution TEM images were recorded using a FEI Tecnai G2 Spirit BioTWIN instrument with a W filament, operating at 100 kV. HRTEM were taken on a Jeol 300 kV JEM3010 instrument with a LaB_6 filament and EDS maps were collected using a VG HB601 UX STEM operating at 100 kV equipped with an Oxford Instruments INCA TEM 300 EDS system. All TEM samples were prepared by sonicating the powder (of as-prepared samples or pre-grinded ceramics) in the

appropriate solvent (THF or H_2O), and then dropping the suspended powder onto a holey copper grid covered with holey carbon film. Dr Zhongling Xu at the University of Liverpool performed the TEM imaging.

5.2.5.3 SEM Imaging

SEM images were recorded using a Hitachi S4800 Type II cold field emission scanning electron microscope. The samples were sputter coated with Au prior to analysis using an Emitech K550X automated sputter coater and were held in place using a M3 aluminium 15 mm sample holder. For ceramic cross-sections the samples were cooled in liquid N_2 and broken into half using a hammer and chisel (this technique is known as freeze-fracturing), with the samples held into place using a M3 aluminium 15 mm cross-section sample holder. All samples were observed using a mix of upper and lower secondary electron detectors operating at acceleration voltages of 3 or 25 kV, with working distances of 8.0 or 15 mm, respectively. The exact operation conditions are noted on each SEM image. EDX analysis using the SEM was performed with an Oxford Instruments 7200 EDX detector with 25 kV operating acceleration voltage and 15 mm working distance.

5.2.5.4 Piezoelectric Constant Measurements

Piezoelectric constant measurements (d_{33}) were performed on a Piezotest Piezometer System PM300 at a frequency of 110 Hz with a dynamic force of 0.25 N. The samples were turned after each measurement to ensure the positive and negative readings were consistent with one another.

5.2.5.5 Measurement of the Magnetoelectric Coefficient (α_E)

The ME coefficient α_E was measured employing the lock-in technique in which a small AC magnetic field (0.25 Oe, calculated from the driving current that was measured using a Mapin Precision Gold M-5010 EC multimeter) produced by a Helmholtz coil of 28 turns each with 50 mm diameter and powered by a function generator (Wavetek) and an amplifier (Prosound 1600), is superimposed onto the DC bias field (up to 10 kOe) which is generated by an electromagnet (LakeShore, Model EM4-HVA) and a programmable DC power source (LakeShore Model 642 Electromagnet Power Supply). The ME response was measured using a lock-in amplifier (Signal Recovery, Model 5210). The samples were placed perpendicular to the field and thus the ME coefficient measured is a longitudinal one. All measurements were carried out at RT. Data acquisition was performed by altering the current produced by the DC power source between 0 A and 60 A at 5 A intervals, noting the ME signal and phase at each point.

5.2.5.6 Fourier transform infrared spectroscopy (FTIR)

FTIR spectra were recorded on a Jasco FTIR-4200 spectrometer equipped with an ATR attachment. The spectra were acquired over the range 4000-500 cm^{-1} at a resolution of 4 cm^{-1}.

5.2.5.7 Elemental Analysis

Microanalysis was performed on a Thermo Flash EA 1112 Series C, H, N and S analyzer.

5.2.5.8 Thermogravimetric Analysis (TGA)

TGA was performed using a Seiko SII-TG/DTA 6300 thermal analyser under a flow of air. The samples were heated at a rate of 5 °C min^{-1}, held for 30 minutes at the target temperature and cooled at 10 °C min^{-1}.

5.2.5.9 Raman Spectroscopy

The Raman spectra were recorded on JY LabRam-HR Spectrometer operated in backscattering geometry by using 514.5 nm radiation and a sample area of 500 μm diameter, with a typical acquisition of 20 × 7 seconds. The calibration was performed by referencing the spectrometer to the 520.07 cm^{-1} line of silicon.

5.2.5.10 SQUID

Magnetic properties of the studied samples were investigated using a Quantum Design MPMS SQUID magnetometer at 300 K and a field up to 1 T. These measurements were performed by Dr. Giap van Duong at the University of Liverpool.

5.3 Results and Discussion

*Note: The ceramic composites discussed on this chapter are given the descriptors '***A***' to '***F***'. All of the ceramics, unless otherwise specified, were prepared via route* ***II****, detailed in Chapter 4, which involved the DCCI-coupling assembly of BTO (COOH terminated) and CFO (NH_2 terminated) particles.*

5.3.1 Preparation of BTO (50 nm) /CFO (10 nm) '**A**' *Ceramic Composites*

The initial experiment involved the synthesis of a ceramic from the DCCI-coupled

BTO (50 nm) /CFO (10 nm) **IIa** composite that was discussed in Chapter 4. 250 mg of the assembled **IIa** composite was dried at 100 °C overnight. The dried powder was pressed at 5 tons in a 10 mm die, and further pressed at 30,000 psi in a cold isostatic press (CIP). Pressing in the CIP increased the pellet density and helped produce more uniform pellets. While the densities were not measured before pressing in the CIP due to their fragility, they were dense enough to be handled after pressing. Sintering was then carried out at 850 °C for 12 hours, with the aim of increasing the sample density in order to enable the efficient transmission of the magnetostrictive force generated by CFO to the piezoelectric BTO.

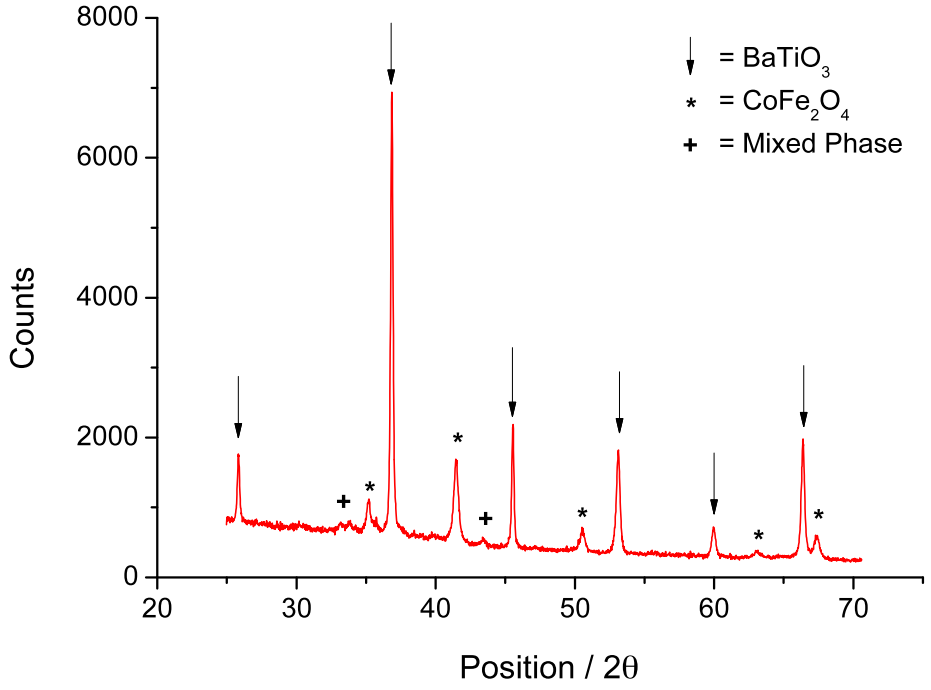

Figure 1. X-ray diffraction pattern of the $BaTiO_3$ (50 nm)/$CoFe_2O_4$ (10 nm) **A** ceramic prepared at a molar ratio of 1:1 $BaTiO_3$ /$CoFe_2O_4$ and sintered at 850 °C for 12 hours.

Post-sintering, measurement of the sample dimensions and mass showed it had reached 64% of the theoretical maximum density for a BTO/CFO 1:1 molar ratio composite, with the a small amount of $BaFe_{12-x}Co_xTi_xO_{19}$ magnetoplumbite-related impurity present, labelled as 'mixed phase' in the XRD in Figure 1.

The formation of these mixed phase impurities is an expected consequence of the sintering process; the CFO grains coalesce with one another and react with the surface of the larger BTO particles during sintering, which leads to pores in the sample being filled and the sample density increasing.[11, 12]

The sample was then electrically poled. This process involves applying a strong direct-current (DC) electric field across the ceramic so that the dipoles within the individual crystallites are reoriented to align preferentially toward the direction of the applied electric field.[13] The results in the material possessing net piezoelectricity, and the process was performed by heating the ceramic to 160 °C – above the Curie temperature of BTO where the ferroelectric to paraelectric phase transition occurs (132 °C, though this varies with particle size)[14] – and then cooling it to RT under an electric field of 1800 V cm^{1} over 1 h (this was the highest voltage that could be sustained across the sample). Poling was deemed successful following the measurement of a piezoelectric constant d_{33} for the poled sample, where d_{33} is the induced charge per unit force applied in the same direction.

The longitudinal ME coefficient, α_E, was then measured by the dynamic method,[10] with α_E defined as follows:

$$\alpha_E = \frac{V}{H_{ac} \times d} \tag{5.1}$$

Where V is the voltage across the sample in mV, d is the sample thickness in cm and

H_{ac} is the amplitude of the AC field (in this case 0.25 Oe).

No ME effect was measured for this BTO (50 nm) /CFO (10 nm) **A** sample, which was initially thought to be due to the sample density (63% of the theoretical maximum) being too low for the density-dependent ME effect to be observed.[15, 16] Further sintering was performed at 900, 950, 1000 and 1050 °C for 30 minutes, with the ME effect measured after each step. 30 minutes was chosen as the preparation of ME ceramics composites of nanomaterials often benefits from employing short sintering steps. This can help maximise the sample density, while minimising the amount of impurity formed when the reactive nanoparticles coalesce with one another under high temperatures.[6, 11, 12] The relationship between the sample density and sintering temperature for this sample is shown in Figure 2.

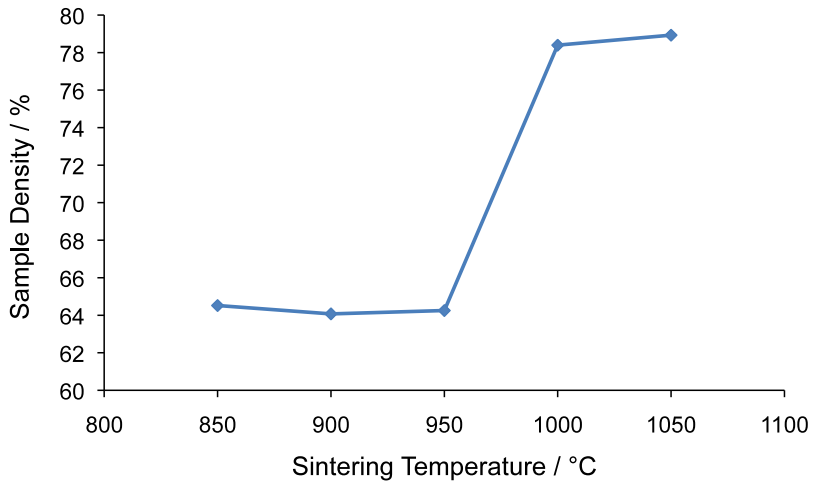

Figure 2. A graph of sample density versus sintering temperature for the $BaTiO_3$ (50 nm) /$CoFe_2O_4$ (10 nm) **A** ceramic.

These results showed that between 950 and 1000 °C the sample density increased by 14%, while no increase in density was observed between 850 and 950 °C. This

indicated that a sintering temperature greater than 1000 °C was required to make dense BTO/CFO nanoparticle ceramics, and only short sintering times of around 30 minutes were necessary. The XRD pattern of the sample after sintering at 1050 °C for 30 minutes is shown in Figure 3. The data shows more $BaFe_{12-x}Co_xTi_xO_{19}$ magnetoplumbite-related impurity was present after sintering at this higher temperature, though BTO and CFO were still clearly the major phases.

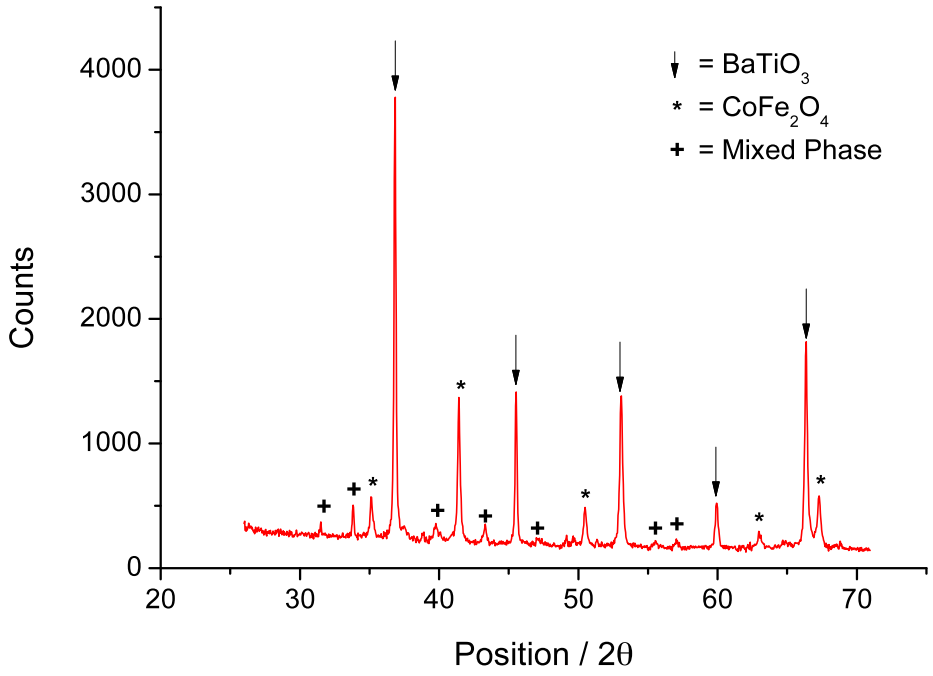

Figure 3. X-ray diffraction pattern of the $BaTiO_3$ (50 nm) /$CoFe_2O_4$ (10 nm) **A** ceramic sintered at 1050 °C for 30 minutes.

Irrespective of sample sintering temperature and density, no ME effect was observed in this BTO (50 nm) /CFO (10 nm) **A** ceramic. This was thought to be due to the small d_{33} for both a pure 50 nm BTO pellet sintered at 850 °C, which was 5.5 pC N^{-1}, and for the 850 °C sintered BTO (50 nm) /CFO (10 nm) ceramic, which was 0.57 pC N^{-1}. While the latter showed the composite ceramic was piezoelectric, the presence

of CFO was clearly reducing the magnitude of the d_{33}. This was both due to less BTO being present in the composite ceramic than in the pure BTO pellet, and also because of the higher conductivity of the CFO nanoparticles, which reduced the efficiency of the poling of the piezoelectric phase, and which also causes the leakage of the stored charge.[12, 17, 18]

5.3.2 The Piezoelectric Properties of 8, 50 and 200 nm BTO

The lack of magnetoelectricity in the BTO (50 nm)/CFO (10 nm) **A** composites lead to a consideration of the piezoelectric properties of differently sized BTO particles in order to help identify a set of BTO nanoparticles for the preparation of magnetoelectrically active composites.

The magnitude of piezoelectric constant is dependent on a number of factors including the number of surface defects (e.g. the abundance of lattice hydroxyl (OH^-) and carbonate (CO_3^{2-}) groups), which tend to increase with diminishing particle size,[19] and which also depend on the nanoparticle morphology and synthesis route. Consequently, smaller particles generally tend to have smaller piezoelectric constants.[14, 20]

For BTO, the magnitude of the piezoelectric constant d_{33} of a sample is also influenced by the particle size-dependent ratio of the paraelectric cubic phase to that of the FE tetragonal phase. Generally, the amount of tetragonal phase BTO increases with particle size; though the precise relationship between cubic to tetragonal ratio and particle size remains unclear. For instance, it is not certain whether the ferroelectricity of BTO can be reduced to zero simply a through reduction in particle size, and microscopic first-principle calculations have shown that 5 nm quantum dots can possess large ferroelectric off-centre displacements.[21]

As the cubic and tetragonal phases of BTO often coexist in the same sample, it can be challenging to determine the presence of the minor phase by XRD analysis. One reason is that the peak positions from both phases overlap, and so the major phase will mask the appearance of the minor phase in the XRD. This, coupled with the inherent broadness of the reflections for nanomaterials means that peak splitting, which is indicative of tetragonal BTO, can be difficult to observe for small particles.[22] This problem has been tacked by a number of authors. Buscaglia et al.[23] performed XRD analysis on 50 nm BTO and the lack of peak splitting in the XRD pattern obtained at room temperature suggested these particles were cubic phase BTO. However, the authors found a significant variation in the full width half maxiumum (FWHM) of the (002)/(200) reflection between RT and 225 °C, i.e. over a temperature range that includes that of the tetragonal to cubic phase transition for BTO. No variation in the FWHM was observed for the (111) peak that does not undergo peak splitting during the tetragonal to cubic transition. The variation in the FWHM over the recorded temperature range led the authors to conclude that there was some distortion of the perovskite structure from the ideal cubic lattice, though they were unable to determine the relative proportions of the cubic and tetragonal phases. They estimated the 50 nm particles had a c/a ≈ 1.003 (where c and a are the lattice parameters) in comparison to bulk samples which have a c/a ≈ 1.01. Powder XRD analysis generally produces data consistent with an increasingly cubic structure at smaller particle sizes, though it does not distinguish between average and local structure.[22, 24, 25] It should also be noted that the tetragonal to cubic transition observed for these 50 nm particles was significantly broader than that observed for bulk phase BTO. This broadening of the transition temperature is typical behaviour for BTO particles as the size decreases.

Raman spectroscopy is a useful tool for performing a comparative assessment of the abundance of each phase in different samples, and has supported the existence of tetragonal symmetry at small dimensions, even though it was not discernable by XRD.[26] This is due to polar tetragonal phase BTO being Raman active, while BTO with perfect cubic symmetry is inactive, according to selection rules.[27] It should be noted however, that in spite of the large number of studies, the allocation of the vibration modes in BTO is still a matter of debate.[28, 29]

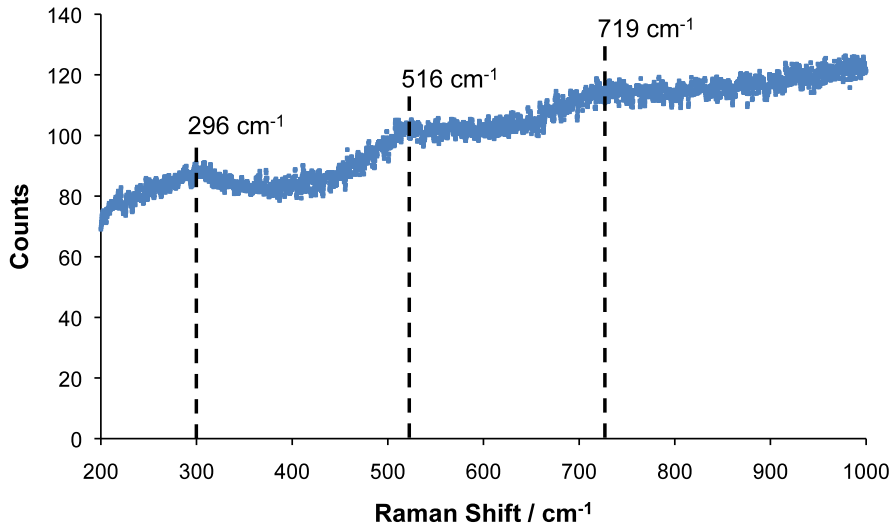

Figure 4. Raman spectrum 8 nm $BaTiO_3$ nanoparticles.

Figure 4 shows the Raman spectrum for the 8 nm solvothermally prepared BTO nanoparticles, which were used in Chapter 4. The peaks at 296, 516 and 719 cm^{-1}, can be assigned to the [B_1, E(TO + LO)], [A_1, E(TO)] and [A_1, E(LO)] phonon modes of tetragonal BTO, as according to a previous report.[30] The peaks are weak and broad, indicating the sample consists of locally distorted cubic phase BTO.[30, 31] However, while symmetry demands that cubic $BaTiO_3$ should be completely Raman-

inactive, broad peaks centered at 260 and 530 cm^{-1} have been observed by some authors above the tetragonal to cubic phase-transition temperature.[26] These have generally been attributed to disorder of titanium in the nominally cubic phase[30] and it may be that these peaks are contributing to the broad peaks observed for these 8 nm BTO particles. Raman spectroscopy above the Curie temperature would help determine whether that was the case.

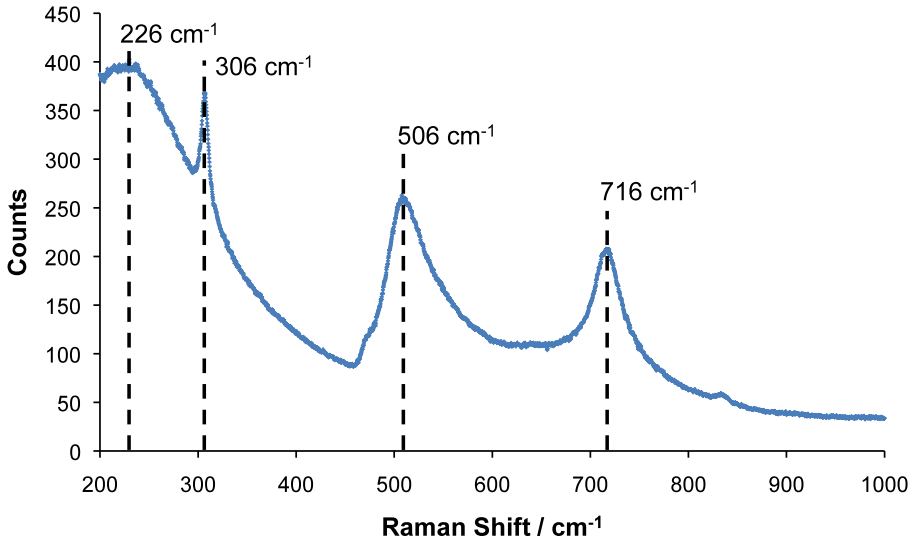

Figure 5. Raman spectrum of the 50 nm $BaTiO_3$ cube-like nanoparticles.

The Raman spectrum of 50 nm BTO, which was used for the preparation of the BTO (50 nm) /CFO (10 nm) **A** ceramics discussed previously is shown in Figure 5. Peaks are observed at 226, 306, 506 and 716 cm^{-1} and can be assigned to [A_1(TO)], [B_1, E(TO + LO)], [A_1, E(TO)] and [A_1, E(LO)] phonon modes of tetragonal BTO respectively, as according to a previous report.[30] The sharpness of the peak at 306 cm^{-1}, the additional broad peak at 226 cm^{-1}, and the overall increased intensity and sharpness of all peaks compared to those in Figure 4 indicates that more tetragonal

phase BTO is present in the 50 nm sample than the 8 nm.[30, 32] This is in agreement with the Raman data presented by Smith et al. for 25, 46 and 70 nm BTO, they observed smaller particles showing broader and less intense peaks than larger particles, and this was attributed to the higher degree of tetragonallity in the larger particles. The authors also observed a marked reduction in peak intensity and an increase in linewidth as they approached the curie transition temperature in their temperature-dependent Raman study. They found the temperature dependent broadening of the Raman peaks was less dramatic for smaller particles, owing to the more diffuse tetragonal to cubic transition discussed earlier.

Bearing in mind the lack of a ME effect in the initial samples was likely due to the small d_{33} of the 50 nm BTO, and considering the size dependence of the piezoelectric constant; 200 nm BTO particles were identified as candidates for the synthesis of ME-active composites, with the idea that they would have superior piezoelectric properties owing to the larger particle size.[23] The solution-based assembly of these particles with 12.5 nm CFO was dealt with in Chapter 4 (termed **IIb** composites). The d_{33} of these the pure-200 nm particles was found to be 134 pC N^{-1} (for a pellet prepared by sintering at 850 °C for 12 hours), which is over 24 times larger than the 5.5 pC N^{-1} recorded for the 50 nm particles.

Raman spectra were collected in order to establish whether the larger d_{33} for the 200 nm particles was due, in part, to a greater proportion of tetragonal phase BTO. The Raman spectrum of 200 nm BTO in shown in Figure 6. The peaks at 254, 305, 515 and 713 cm^{-1} are assigned to the [A_1(TO)], [B_1, E(TO + LO)], [A_1, E(TO)] and [A_1, E(LO)] phonon modes of tetragonal BTO respectively, matching those reported previously.[30] The bands of the 200 nm particles are more intense than those of 50 nm particles shown in Figure 5. For instance, the peak at 515 cm^{-1} for the 200 nm

particles in Figure 6 has an intensity of approximately 400 counts, while the same peak at 506 cm^{-1} in Figure 5 for the 50 nm particles has an intensity of only 150 counts. From this, one can draw the conclusion that these 200 nm particles are more tetragonal than the 50 nm set, inline with observations in the literature.[22] The Raman spectrum in Figure 6 also closely resembles that of bulk tetragonal phase BTO reported in the literature.[21] The increased tetragonallity of the 200 nm versus the 50 nm particles explains the larger d_{33} that was measured for these particles.

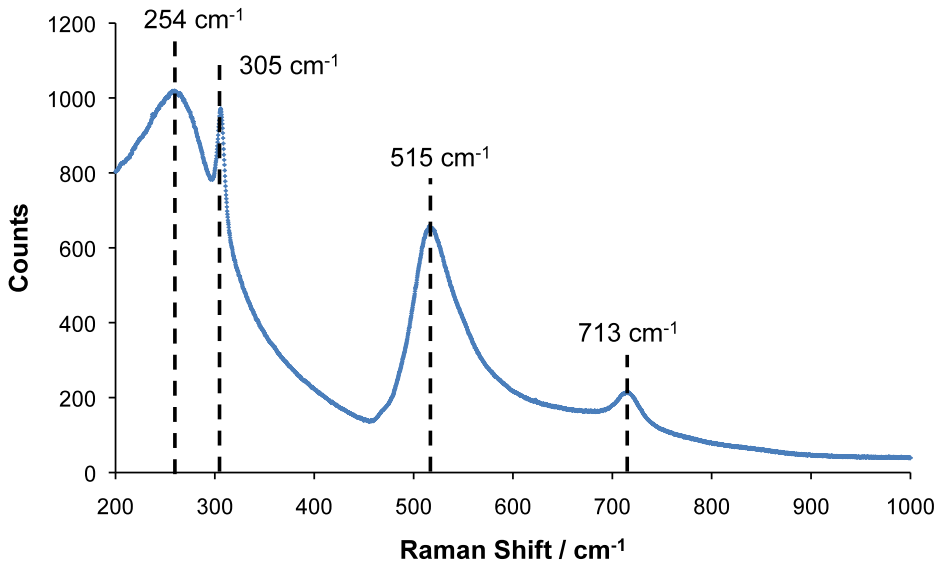

Figure 6. Raman spectrum of the 200 nm SEM-size $BaTiO_3$ particles.

The XRD (Figure 7) shows the splitting of the (200) and (210) peaks is also more pronounced for the 200 nm particles than for the 50 nm particles.

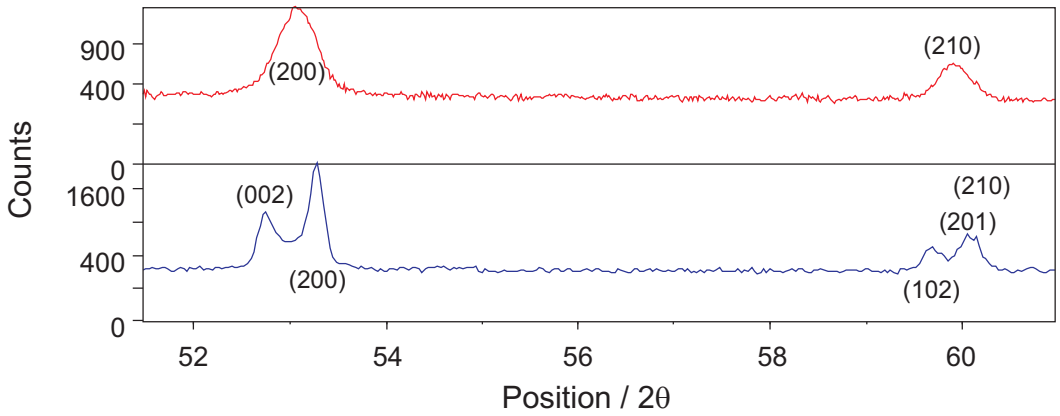

Figure 7. A selected area of the X-ray diffraction patterns of: 50 nm $BaTiO_3$ (red) and 200 nm (blue). This data demonstrates the difference in peak splitting between the two sizes of particles.

In summary, the measurement of the large d_{33} for the 200 nm BTO particles lead to them being chosen for the production of the second generation of the DCCI-coupled BTO/CFO ceramic composites. The larger d_{33} was thought to arise due to the greater proportion of the tetragonal, ferroelectric phase BTO in the 200 nm particles, which was indicated by the Raman spectroscopy and XRD. The larger particle size of the 200 nm particles also likely meant fewer surface defects, such as lattice hydroxyl OH^- and CO_3^{2-} groups, further enhancing the piezoelectric properties.

5.3.3 Preparation and Characterisation of BTO (200 nm) /CFO (12.5 nm) '**B**' Ceramic C*omposites*

Note: what follows is a description of BTO (200 nm) /CFO (12.5 nm) **B** *ceramics prepared using the DCCI-coupling route (termed* **IIb B***), using electrostatically assembled particles (termed* **Ib B***) and unfunctionalised particles (termed* **IIIb B***).*

IIb B Ceramic composites of BTO (200 nm) /CFO (12.5 nm) were prepared following the same steps that were outlined for the synthesis of the BTO (50 nm) /CFO (10 nm) **A** ceramics. 500 mg of the BTO (200 nm) /CFO (12.5 nm) **IIb** assembled composite was used to prepare the pellets, as opposed to 250 mg for the BTO (50 nm) /CFO (10 nm) **IIa** composite. 12.5 nm CFO was used due to the coprecipitation and direct-functionalisation route yielding a much larger amount of functionalised 12.5 nm CFO nanoparticles than the ligand exchange route afforded 10 nm functionalised CFO. Using larger pellets was beneficial as they were less prone to breaking during processing. The ME coefficient, α_E, is normalised with respect to sample thickness.

The first pellet was prepared at a molar ratio of 5.5:1 BTO/CFO because, at the 5.5:1 ratio, each BTO particle would be completely covered with CFO provided perfect amide-driven particle alternation was achieved. A further four pellets were prepared at compositions of 4.135:1 2.75:1, 1.875:1 and 1:1, with the CFO content being incrementally increased moving from 5.5:1 to 1:1. This was done because near this 1:1 composition the ME effect should, theoretically, be highest.[6, 33] As for the BTO (50 nm) /CFO (10 nm) **A** ceramic discussed earlier, these BTO (200 nm) /CFO (12.5 nm) **IIb B** ceramics were initially sintered at 850 °C for 12 hours.

Post-sintering, the XRD showed the samples were phase pure, with only BTO and CFO present. The XRD CFO particle size was observed to slightly increase after sintering, from 12.5 nm to 20 nm for the 2.75:1 BTO/CFO **IIb B** sample shown in Figure 8. The 200 nm BTO retained its 77 nm XRD-size post-sintering, with the ceramics at different compositions showing the same trend of a stable BTO size and a small increase in CFO size.

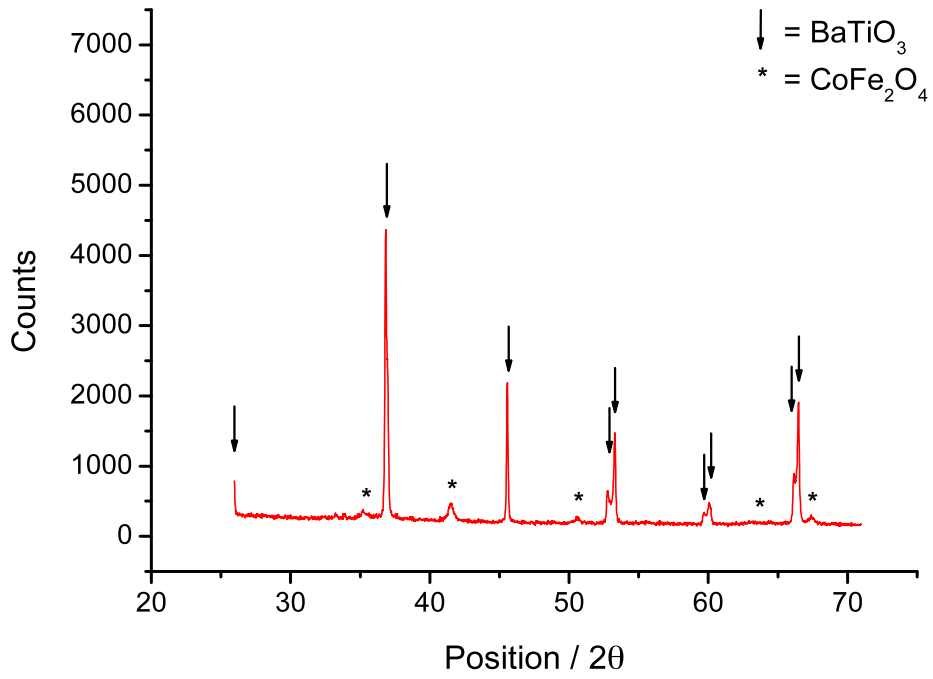

Figure 8. X-ray diffraction pattern of the $BaTiO_3$ (200 nm) /$CoFe_2O_4$ (12.5 nm) **IIb B** ceramic composite prepared at a $BaTiO_3$ to $CoFe_2O_4$ 2.75:1 molar ratio. The sample was sintered at 850 °C for 12 hours.

After sintering at this temperature, each of the five samples were approximately 70% of the theoretical maximum density, with STEM analysis on a ground pellet (Figure 9) showing the BTO/CFO assemblies produced in the solution phase had been retained after these initial processing steps.

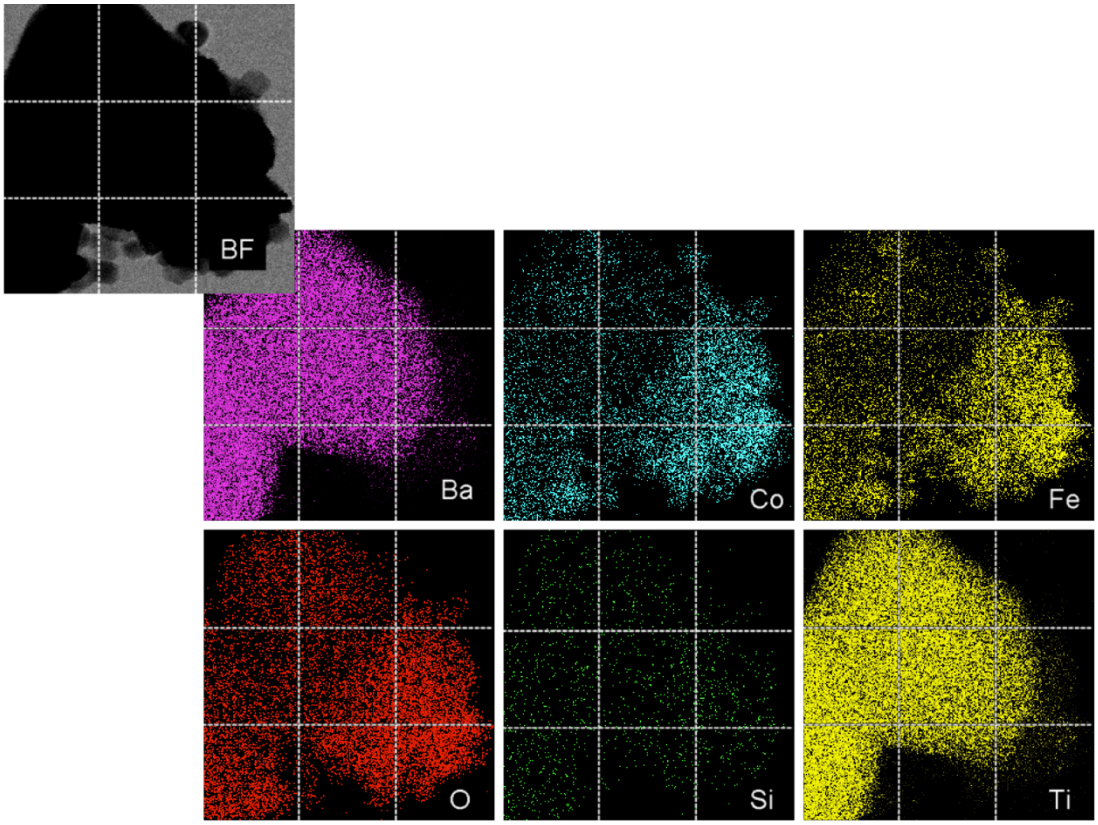

Figure 9. Scanning transmission electron microscopy element maps of the $BaTiO_3$ (200 nm) /$CoFe_2O_4$ (12.5 nm) **IIb B** ceramic prepared at a 2.75:1 molar ratio of $BaTiO_3$ /$CoFe_2O_4$ and sintered at 850 °C for 12 hours. 'BF' indicates the TEM image is a bright field image.

Further sintering at 1050 °C for 30 minutes was then performed in order to increase the sample density. The samples were sintered at 1050 °C, as it was at this temperature that a significant increase in density was observed for the BTO (50 nm) /CFO (10 nm) **A** ceramics discussed earlier. Post-sintering, the samples were poled at 4000 V cm^{-1}, though the 1:1 BTO/CFO **IIb B** composite was poled at its highest sustainable voltage, which was 1840 V cm^{-1}. For the 1:1 BTO/CFO **IIb B** ceramic which had the highest CFO content of these BTO (200 nm) /CFO (12.5 nm) **IIb B** samples, the conductivity was high enough for current to flow though the sample at high potentials, meaning the 4000 V cm^{-1} poling potential used for the other samples

could not be sustained.

The longitudinal magnetoelectric (ME) coefficient, α_E, was determined for these samples by the dynamic method and the results are shown in Figure 10.

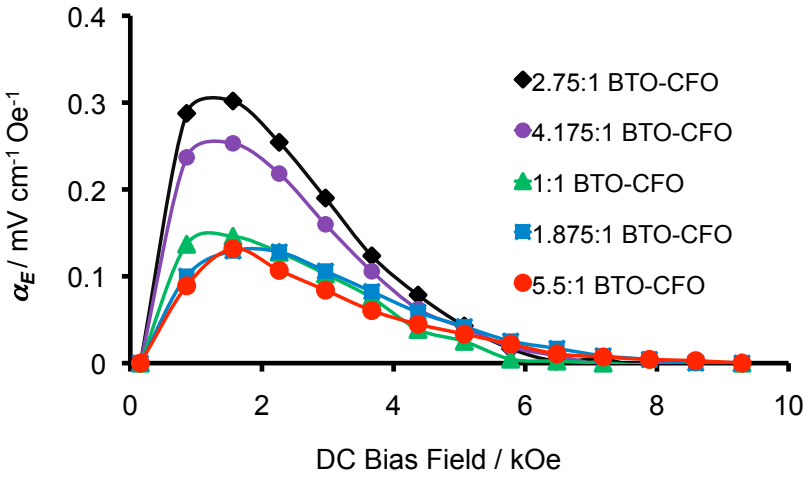

Figure 10. A graph showing the variation of the longitudinal ME coefficient, α_E, with DC bias field for covalently bonded $BaTiO_3$ (200 nm) /$CoFe_2O_4$ (12.5 nm) **IIb B** ceramic composites prepared at a range of compositions and sintered at 1050 °C for 30 min.

α_E tends to increase with DC bias field for all samples, up to the point where the magnetostriction of CFO is saturated, after which a reduction in α_E is observed. The observed relationship between the DC bias field and α_E is typical for ME composites of this type.[6, 34, 35] This figure is discussed further later. The relationship between the maximum magnetoelectric coefficient for each sample, α_E *max*, and sample composition is shown in Figure 11.

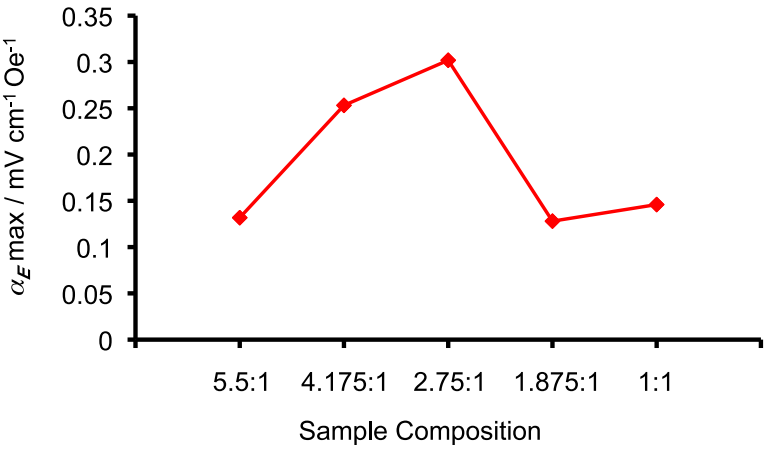

Figure 11. A graph showing α_E *max* versus sample composition for the $BaTiO_3$ (200 nm) /$CoFe_2O_4$ (12.5 nm) **IIb B** composites sintered at 1050 °C for 30 minutes.

The data in Figure 11 shows α_E *max* increasing with increasing ferrite content from a BTO/CFO molar ratio of 5.5:1 to 2.75:1. This correlates with the increased coverage of CFO on BTO observed *via* TEM imaging as the CFO molar ratio increases (Chapter 4, Figures 36 and 37 respectively). This can be understood because, as the coverage of CFO on the surface of BTO increases, then mechanical strain per unit of magnetic field that can be exerted on the BTO particles will also increase.[6, 15, 16] This, in turn, will lead to a greater potential being generated by the larger compressive force of the CFO particles on BTO. However, increasing the ferrite content beyond BTO/CFO 2.75:1 reduces α_E *max*, which is assigned to leakage of the piezoelectrically generated charge and the conductivity of CFO preventing effective poling.[6, 11] At a certain point, in this case beyond the BTO/CFO 2.75:1 composition, it is no longer possible to sustain a large enough field across the sample to effectively pole it due to current flow through the sample. Table 1 shows the d_{33} constants and densities for this range of samples.

Sample	d_{33} / pC N^{-1}	α_E max / mV cm^{-1} Oe^{-1}	Sample Density / %
BTO-CFO 5.5:1	21.3	0.13	80
BTO-CFO 4.175:1	15.6	0.25	80
BTO-CFO 2.75:1	4.9	0.31	79
BTO-CFO 1.875:1	3.3	0.13	76
BTO-CFO 1:1	2.8	0.15	81

Table 1. A table of the d_{33} piezoelectric constants and sample densities of the $BaTiO_3$ (200 nm) /$CoFe_2O_4$ (12.5 nm) **IIb B** ceramics prepared at molar ratios from 5.5:1 to 1:1 $BaTiO_3$ /$CoFe_2O_4$ and sintered at 1050 °C for 30 minutes.

As expected, the d_{33} is reduced with decreasing BTO content, with the d_{33} falling from 21.3 pC N^{-1} in the 5.5:1 BTO/CFO **IIb B** sample to 2.8 pC N^{-1} in the 1:1 BTO/CFO **IIb B** sample. A corresponding increase in the dielectric loss *tan* δ was also observed, increasing from 0.0913 to 0.3829 as the CFO content increased from 5.5:1 to 1:1 BTO/CFO. A *tan* δ value of 0.0194 was recorded for the pure 200 nm BTO pellet, smaller than for any composite sample containing CFO. The decrease of the d_{33} is not directly proportional to the decrease in the amount of BTO in each sample, due to the leakage of the stored charge discussed earlier. The smaller α_E *max* for the 1.875:1 sample can be attributed to the slightly lower sample density (76% versus a 79-81% for the previous samples), as the ME effect is known to be density dependent.[6, 15, 16]

XRD (Figure 12) showed the BTO and CFO phases were intact in this series of samples, with a larger amount of $BaFe_{12-x}Co_xTi_xO_{19}$ magnetoplumbite-related phases (marked with a '+') present than after the initial 850 °C for 12 hours sintering step.

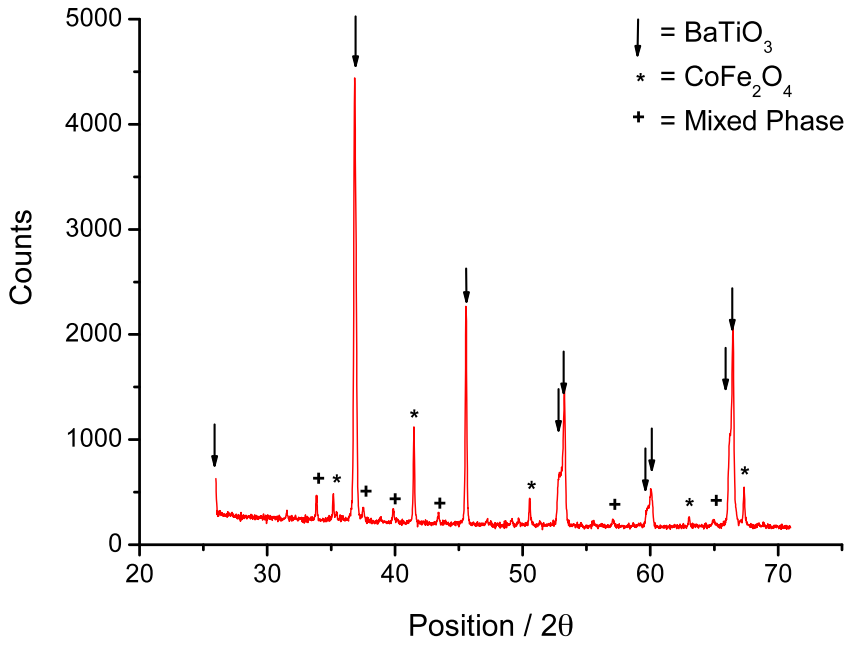

Figure 12. X-ray diffraction pattern of the $BaTiO_3$ (200 nm) /$CoFe_2O_4$ (12.5 nm) **IIb B** composite prepared at a 2.75:1 molar ratio of $BaTiO_3$ /$CoFe_2O_4$ and sintered at 1050 °C for 30 minutes.

Increasing the sintering temperature for these **IIb B** ceramics from 1050 to 1200 °C for 30 minutes, at the optimal BTO/CFO 2.75:1 composition, raised α_E to 0.61mV cm^{-1} Oe^{-1} (Figures 13, 14).

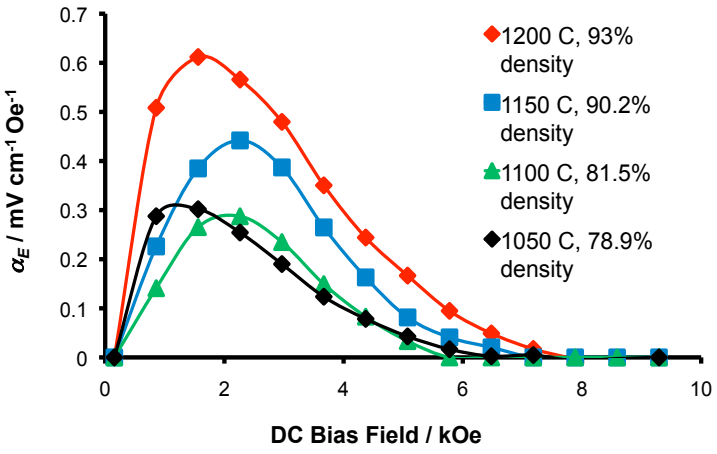

Figure 13. A graph of the variation of the longitudinal ME coefficient, α_E, with DC bias field for covalently bonded $BaTiO_3$ (200 nm) /$CoFe_2O_4$ (12.5 nm) **IIb B** ceramic

composites prepared at a 2.75:1 $BaTiO_3/CoFe_2O_4$ molar ratio, at range of sintering temperatures.

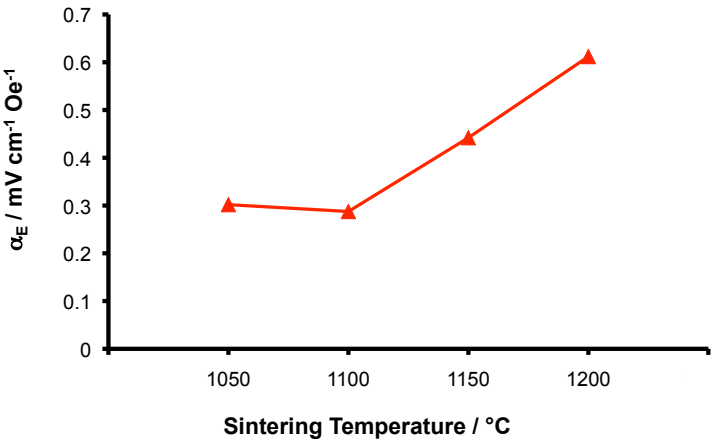

Figure 14. A graph of α_E *max* versus sample density for the $BaTiO_3$ (200 nm) /$CoFe_2O_4$ (12.5 nm) **IIb B** composites prepared at a 2.75:1 $BaTiO_3/CoFe_2O_4$ molar ratio.

The increase in α_E *max* is assigned to the increasing composite density (93% of the theoretical maximum for the 1200 °C sample). The mechanical coupling between the FE and FM phases becomes more efficient as the sample density increases, explaining this result.[6, 15, 16]

What follows is the characterising data for the best sample; the 2.75:1 BTO (200 nm) /CFO (12.5 nm) **IIb B** ceramic sintered at 1200 °C for 30 minutes, which had an α_E of 0.61mV cm^{-1} Oe^{-1}. The XRD (Figure 15) shows the CFO and BTO phases are still present in these more dense BTO/CFO 2.75:1 **IIb B** samples, though due to the increased sintering temperature more $BaFe_{12-x}Co_xTi_xO_{19}$ magnetoplumbite-related phases are formed, the peaks for which are labelled as 'mixed phase'. $BaFe_8Co_2Ti_2O_{19}$ provided the best match in the XRD, fitting to the peaks at 35.35, 37.48, 39.83, 43.36, 47.14, 49.65 and 64.88°.

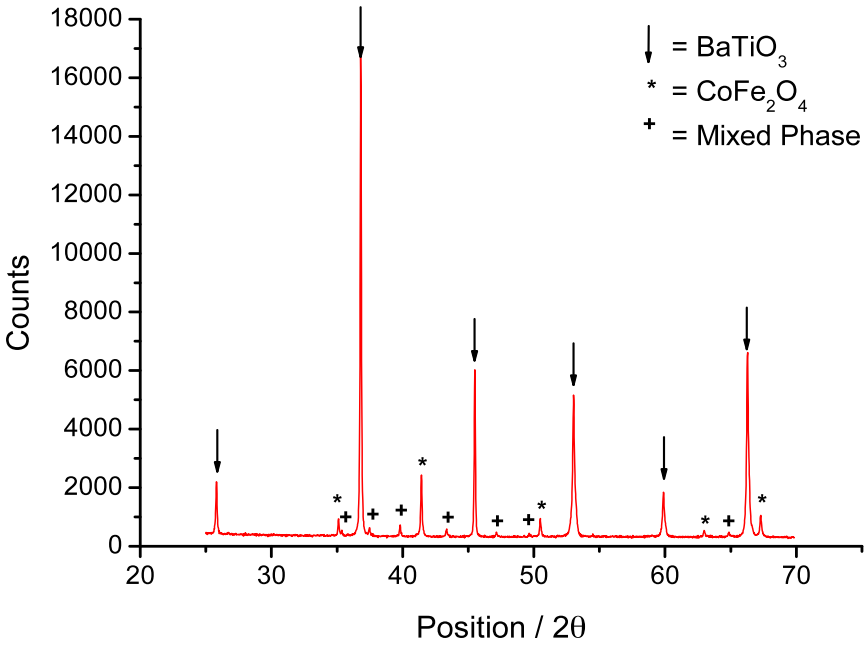

Figure 15. XRD pattern of the $BaTiO_3$ (200 nm) /$CoFe_2O_4$ (12.5 nm) **IIb B** ceramic prepared at a molar ratio of BTO/CFO 2.75:1 and sintered at 1200 °C for 30 minutes.

TEM images of the ground ceramic composite sintered at 1200 °C for 30 minutes are shown in Figure 16 below.

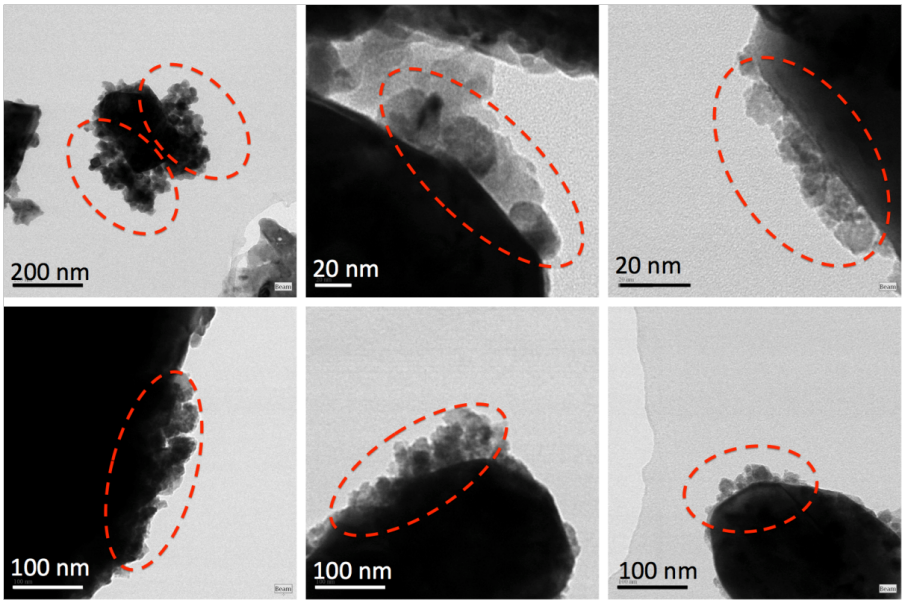

Figure 16. TEM of the BTO (200 nm) /CFO (12.5 nm) **IIb B** ceramic prepared a 2.75:1 molar ratio of BTO to CFO and sintered at 1200 °C for 30 minutes.

These images show how the CFO particle size increases with sintering temperature (compare with the images in Chapter 4, Figure 37), with the boundaries between the CFO particles, and the boundaries between the BTO and CFO particles becoming less clear due to diffusion. This is supported by the observed increase in particle size by XRD. For example, for the sample shown in Figure 15, an increase from 12.5 nm to 70 nm in the 1200 °C sintered sample was observed.

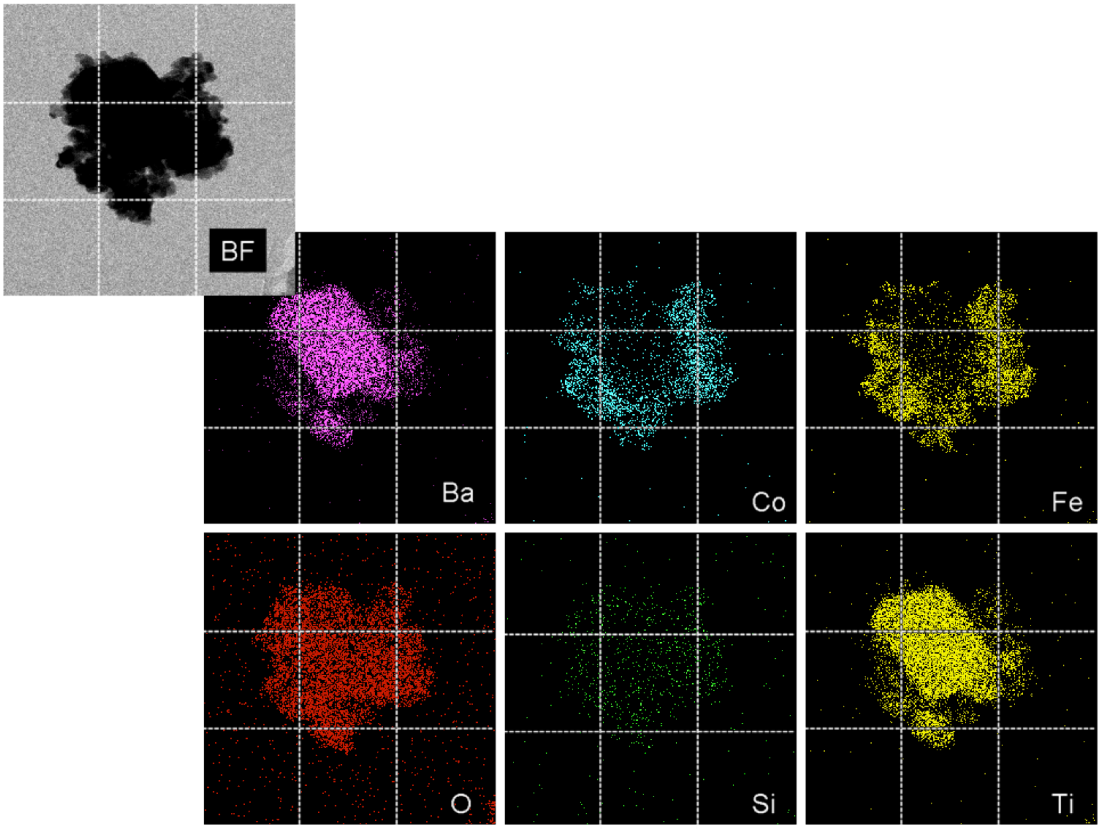

Figure 17. Scanning transmission electron microscopy element maps of the **IIb B** ceramic prepared at a 2.75:1 molar ratio of $BaTiO_3$ /$CoFe_2O_4$ and sintered at 1200 °C for 30 minutes. The letters 'BF' indicate the images are bright field TEM images.

STEM analysis (see Figure 17) on the ground 1200 °C sintered **IIb B** ceramic showed that the intimate dispersion of BTO and CFO in the solution-based assemblies is successfully transferred into dense ceramic, which was one of the

initial major goals behind this work. The Co and Fe remain distributed on the surface of the BTO particles post sintering, indicating that the mixed nanoparticle aggregates synthesised at RT translate into a high degree of contact between the BTO and CFO phases in the ceramic.

The uniform BTO and CFO distribution in the composite pellets is demonstrated in the EDX element mapping in Figure 18. The data shows a homogeneous distribution of BTO and CFO across the mapped area, and this provides further evidence that the BTO/CFO solution-based assemblies are successfully transferred into a composite with a high degree of homogeneity between the FE and FM phases, which is considered a key property for the development of new, more functional magnetoelectrics.[6, 34]

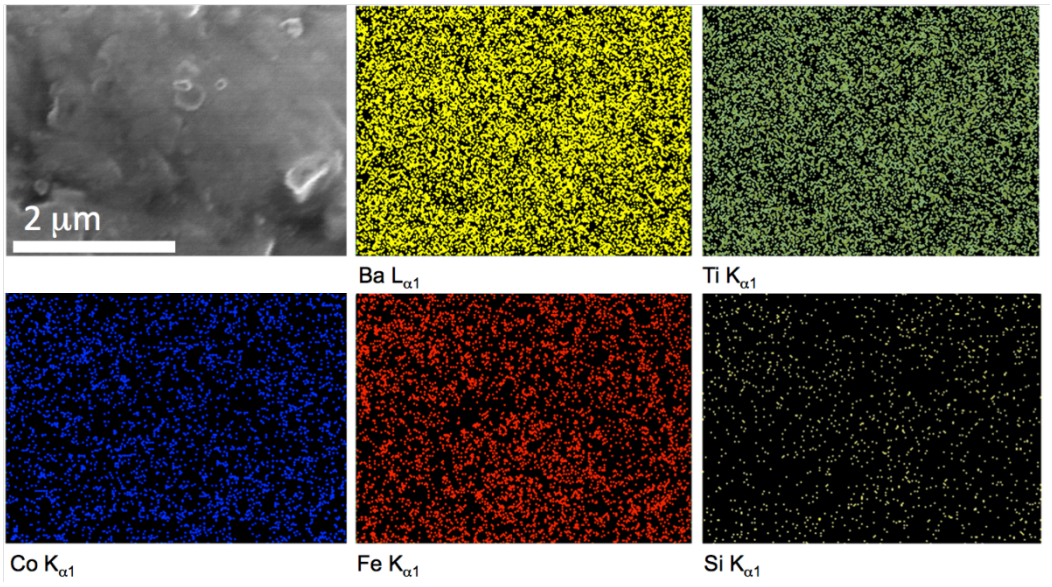

Figure 18. Scanning electron microscopy energy dispersive X-ray spectroscopy element maps of a cross-section of the $BaTiO_3$ (200nm) /$CoFe_2O_4$ (12.5nm) **IIb B** ceramic prepared at a molar ratio of 2.75:1 and sintered at 1200 °C for 30 minutes.

Quantitative EDX analysis (Table 2) of the area mapped in Figure 18 gives a BTO/CFO composition of 2.48:1, close to the expected 2.75:1 with 1.86% Si recorded, likely from SiO_2 resulting from the oxidation of the aminosilane molecules during sintering. The presence of this assembly-derived silica in the sintered samples will reduce the mechanical coupling between FE and FM components.[7] This suggests that surface functionalisation with volatile reagents that do not form inert solids on ceramic processing could be a key future goal.

Within the limits of error, the ratios of Co to Fe and Ba to Ti are what are expected for CFO and BTO respectively. The weight percentage of Si is somewhat higher than the 0.56% that would be expected calculating from the microanalysis results for aminosilane functionalised CFO particles. This may be due to a localised variation in the level of loading of the aminosilane on the CFO particles, in addition to experimental uncertainty in quantification that arises from EDX analysis on elements with a low abundance and performed on non-flat and non-polished samples.

Element and X-ray line	Weight %	Sigma weight %	Atomic / %
O $K_{\alpha1}$	23.67	0.55	59.88
Si $K_{\alpha1}$	1.29	0.12	1.86
Fe $K_{\alpha1}$	13.46	0.24	9.76
Co $K_{\alpha1}$	7.04	0.18	4.84
Ba $L_{\alpha1}$	40.74	0.44	12.01
Ti $K_{\alpha1}$	13.8	0.24	11.66
Total	100		100

Table 2. Quantitative energy dispersive X-ray spectroscopy analysis data from the area mapped in Figure 18, for a $BaTiO_3$ /$CoFe_2O_4$ 2.75:1 **IIb B** ceramic sintered at 1200 °C for 30 minutes.

SEM of the ceramic (Figure 19) shows the BTO particles within the composite. These particles were not observed to increase in particle size by XRD (Figure 15), likely due to the bound CFO particles providing a 'protective coating' during sintering, as the smaller CFO particles aggregate and coalesce with one another on an individual BTO particle surface, and with the BTO surface, thus preventing the BTO particles agglomerating and reacting with one another.

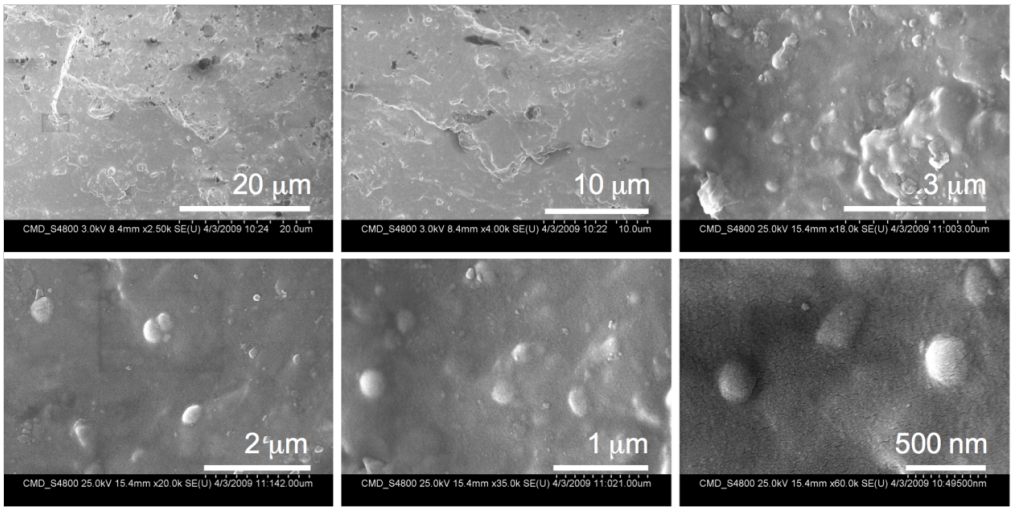

Figure 19. Scanning electron microscopy cross-section images of the $BaTiO_3$ (200 nm) /$CoFe_2O_4$ (12.5 nm) **IIb B** ceramic prepared at a 2.75:1 molar ratio of $BaTiO_3$ to $CoFe_2O_4$ and sintered at 1200 °C for 30 minutes.

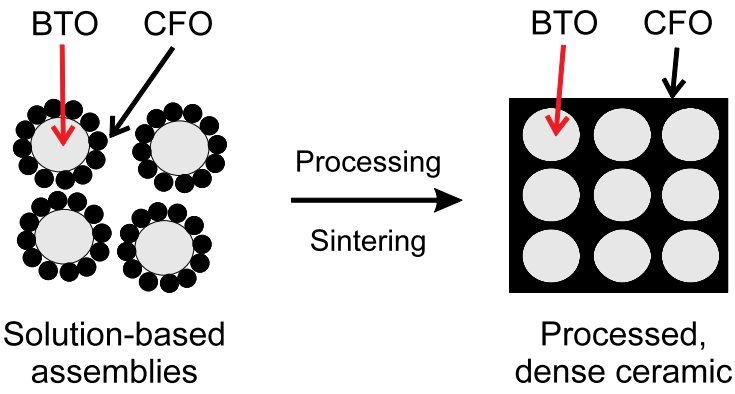

Figure 20. An illustration of the effect of the sintering process on the structure of the

$BaTiO_3$ /$CoFe_2O_4$ assemblies, with a 2D 'slice' through the processed ceramic depicted on the right.

The sintering process and the proposed microstructure of the ceramic is illustrated in Figure 20. α_E is larger in the BTO (200 nm) /CFO (12.5 nm) **IIb B** sample prepared from the DCCI-coupled **IIb** assemblies (0.61 mV cm^{-1} Oe^{-1}) than in a **B** composite prepared using the same ceramic processing conditions and composition, but without functionalised particles (0.21 mV cm^{-1} Oe^{-1}, Figure 21), this ceramic is termed **IIIb B** to indicate it was prepared using route **IIIb** detailed in Chapter 4. This is assigned to the larger FE–FM interface produced by the BTO/CFO particle alternation enforced by the DCCI coupling, and is supported by the EDX element mapping in Figure 22, which shows the distribution of BTO and CFO is much less homogeneous in the **IIIb B** sample prepared with unfunctionalised particles, than in the sample where the **IIb B** assemblies were used (Figure 18).

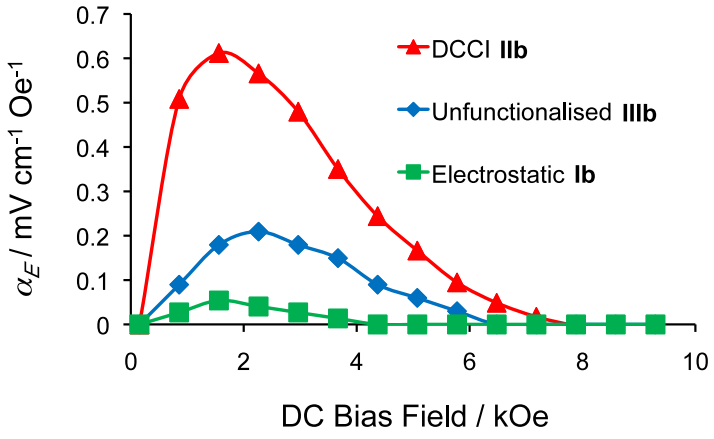

Figure 21. Longitudinal magnetoelectric coefficients, α_E, for **B** ceramics prepared using electrostatically assembled **Ib,** DCCI-coupled **IIb** and unfunctionalised **IIIb** $BaTiO_3$ (200 nm) /$CoFe_2O_4$ (12.5 nm) particles. Pellets were prepared at a 2.75:1 molar ratio of $BaTiO_3$ to $CoFe_2O_4$ and sintered at 1200 °C for 30 minutes.

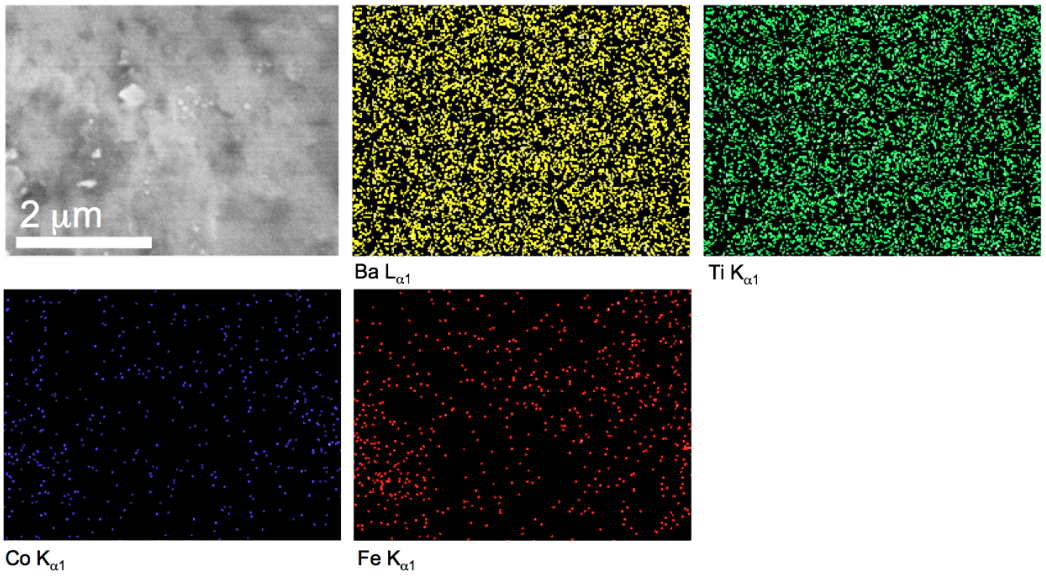

Figure 22. Scanning electron microscopy energy dispersive X-ray spectroscopy element maps the **IIIb B** composite prepared using unfunctionalised particles at a molar ratio of 2.75:1 $BaTiO_3$ /$CoFe_2O_4$ and sintered at 1200 °C for 30 minutes.

Quantitative analysis of the area mapped in Figure 22 gives a BTO/CFO composition of 6.6:1 (Table 3), further demonstrating the lower degree of homogeneity in ceramic prepared with unfunctionalised particles.

Element and X-ray line	Weight %	Sigma weight %	Atomic / %
O $K_{\alpha1}$	15.18	1.29	49.18
Fe $K_{\alpha1}$	6.45	0.40	5.99
Co $K_{\alpha1}$	3.58	0.38	3.15
Ba $L_{\alpha1}$	55.65	1.14	21.00
Ti $K_{\alpha1}$	19.13	0.68	20.69
Total	100		100

Table 3. Quantitative EDX analysis data from the area mapped in Figure 22, a BTO /CFO **IIIb B** ceramic prepared with unfunctionalised particles, at a BTO to CFO 2.75:1 molar ratio and sintered at 1200 °C for 30 minutes.

XRD (Figure 23) shows this composite has retained the BTO and CFO phases post-sintering and has the same $BaFe_{12-x}Co_xTi_xO_{19}$ magnetoplumbite-related impurity that was present in the DCCI-coupled **IIb B** ceramic composites.

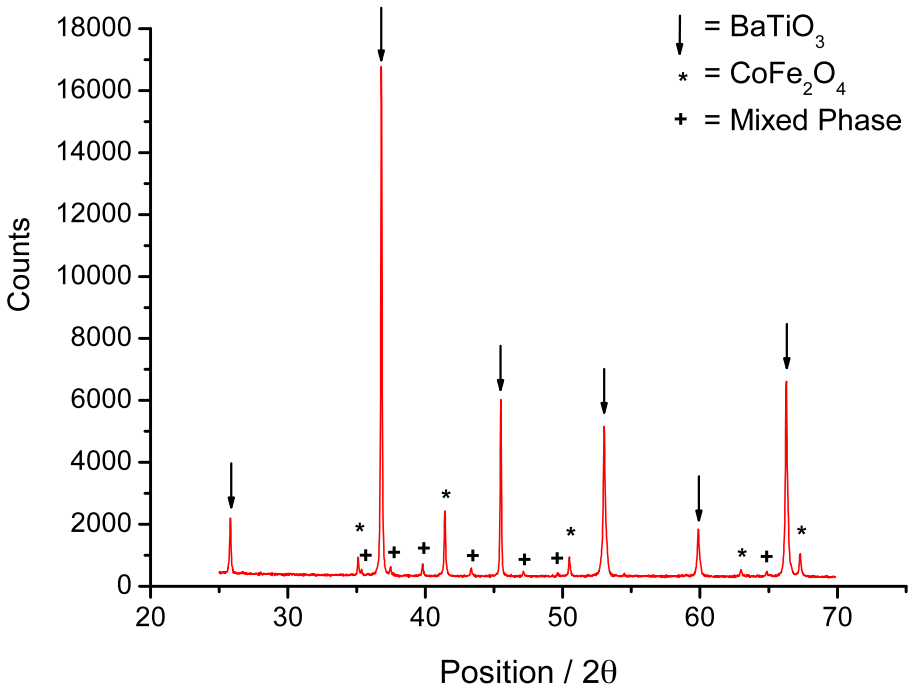

Figure 23. X-ray diffraction pattern of the **IIIb B** ceramic prepared at a 2.75:1 molar ratio of $BaTiO_3$ to $CoFe_2O_4$ and fired at 1200 °C for 30 minutes.

The XRD also shows the CFO particle size increasing from 12.5 nm to 78.5 nm post-sintering for the **IIIb B** sample (12.5 nm to 70 nm was observed for the DCCI-coupled **IIb B** sample prepared under the same conditions), with the BTO particle size increasing from 77 nm to 100 nm post-sintering. This suggests the CFO particles are not providing the same 'coating' of the BTO particle surface that prevents coalescence of the BTO particles with one another, as was observed for the DCCI-coupled **IIb B** composite (Figure 15), and it further illustrates the difference in microstructure between these composites.

A **B** composite assembled with electrostatic attraction between functionalised BTO and CFO particles but without covalent DCCI coupling (termed **Ib B**) had an α_E of 0.05 mV cm^{-1} Oe^{-1} (Figure 21). This suggests the increased robustness of the particle alternation provided by the covalent amide linkage in the **IIb B** composites is beneficial to α_E, whilst also demonstrating that the surface functionalities (which lead to silica interlayers between the active particles) are detrimental to the magnitude of α_E, as the **Ib B** electrostatic case had an α_E lower than the **IIIb B** sample prepared without functionalisation. The densities of the ceramics were comparable, measured at 94%, 93% and 96% for the **Ib B**, **IIb B** and **IIIb B** pellets respectively.

Finally, experiments carried out to test the measurement system using pure BTO, CFO and blank samples showed the measurement has a background much lower than the values measured for the **IIb B** samples, with the magnetoelectric coefficient not tracking the same curve as with respect to DC bias field as was observed for the magnetoelectrically active samples (Figure 24).

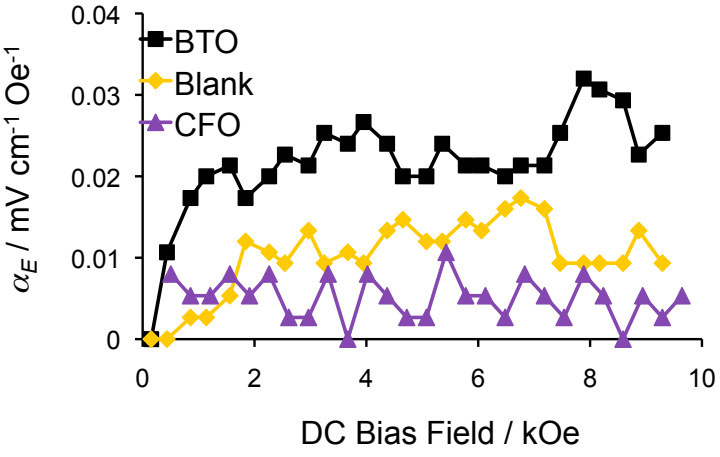

Figure 24. Longitudinal magnetoelectric coefficients, α_E, for pure $BaTiO_3$ (200 nm) and pure $CoFe_2O_4$ (12.5 nm) pellets sintered at 1200 °C for 30 minutes, and for a blank sample, where the field was swept with no sample inserted.

Figures 10 and 13 show that α_E of the **IIb B** composites have a sample-dependent maximum with DC bias field (noted as H_{max} where α_E reaches a maximum), in the range of 1–2 kOe. H_{max} is larger than the coercive field H_c; for instance, after correcting for the demagnetization field, H_{max} is 1.25 kOe for the sample sintered at 1200 °C (H_c = 0.335 kOe) and 1.91 kOe for the sample sintered at 1100 °C (H_c = 0.580 kOe) (Figure 25). The values of H_{max} in these composites are comparable to the fields at which the coupling coefficient $k = \lambda\, d\lambda/dH$ is maximized (1.57 kOe – here λ is the magnetostriction of the ferrite component).[15] Variation from this value can be attributed to microstructure control of domain wall motion – the higher H_c in the smaller CFO particle size composite is due to more numerous pinning sites, which therefore require a higher field to saturate the magnetostriction. The control of α_E by the coupling coefficient k suggests that the ME effect in these chemically assembled composites arises from mechanical coupling between CFO and BTO *via* the interface of the connected particles.

Figure 25 shows the magnetisation of the CFO particles increases from 41.5 emu g^{-1} in the initial CFO nanoparticles to 45.6 emu g^{-1} after sintering (in a **IIb B** composite) at 1100 °C for 30 min and to 51.9 emu g^{-1} after sintering (in a **IIb B** composite) at 1200 °C for 30 min. This can be understood as the CFO particle size increases post-sintering, according to XRD and TEM, and thus the spin canting is reduced (XRD size increases from 12.5nm before sintering to 44 nm after sintering at 1100 °C for 30 min and to 70 nm after sintering at 1200 °C for 30 min). The magnetisations of the sintered CFO particles in the **IIb B** BTO/CFO composites are lower than that of 40 nm CFO prepared *via* the citrate gel method (75 emu g^{-1}), likely due to spin canting occurring at the interfaces with the non-magnetic BTO particles in the composites.

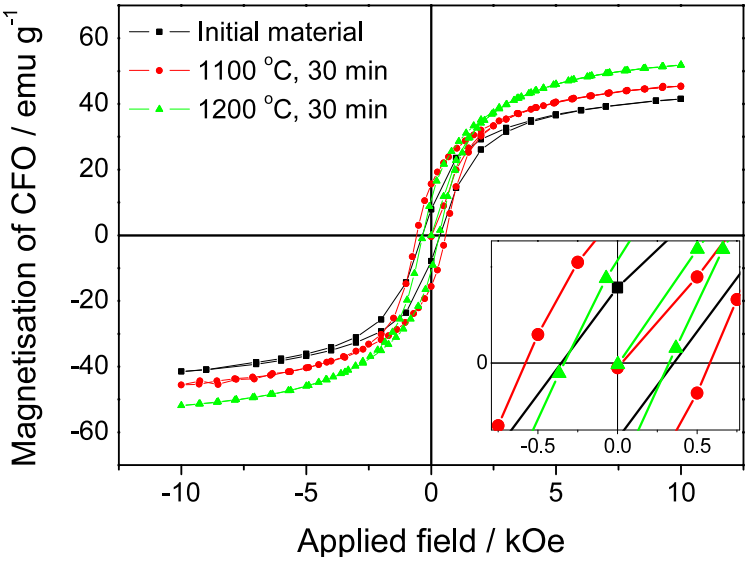

Figure 25. Hysteresis loop of the $CoFe_2O_4$ component in **IIb B** composites at a 2.75:1 $BaTiO_3$ /$CoFe_2O_4$ ratio sintered at 1100 and 1200 °C for 30 minutes, and for the 12.5 nm $CoFe_2O_4$ particles. The samples were measured at 300 K. At 1 T the magnetisation of the $CoFe_2O_4$ particles is 45.6 and 51.9 emu g^{-1} for the 1100 and 1200 °C samples, respectively, and 41.5 emu g^{-1} for the initial $CoFe_2O_4$ particles. H_c is 580 and 335 Oe for the 1100 and 1200 °C, respectively, and 375 Oe for the initial material.

In ME composites, materials with connectivity denoted as 3–1 (or 1–3) have amongst the largest values for α_E.[36] The connectivity of the composites prepared here lies between 0–3 (which describes a system in which particles of one phase are embedded in a matrix of the other) and 0–0 (where there is continuous, regular alternation between the two phases). However neither connectivity scheme completely describes the present composites. Firstly, the BTO and CFO particles are intimately mixed and the CFO phase is comprised of sintered nanoparticles that are not in a sufficiently large excess to be considered a matrix material (as in the 0–3

system). Secondly, there is not perfect BTO–CFO alternation with identically sized particles (as is required in a 0–0 system).

The presence of the interparticle SiO_2 layer should be borne in mind when comparing the ME coefficients of these assemblies with literature results. The amplitude of the ME coefficient for the best sample (**IIb B**, 0.61 mV cm^{-1} Oe^{-1}) is comparable to those reported for a CFO/BTO core–shell composite (3.87 mV cm^{-1} Oe^{-1})[15] and a BTO/CFO particulate composite (0.19 mV cm^{-1} Oe^{-1}),[37] though smaller than that of multilayer eutectic composites with alternate layers prepared by the unidirectional solidification method.[38] However, these samples show a control of microstructure that may benefit further development, such as for the low temperature assembly of multi-component films and thin layers. Furthermore, there is considerable scope for the enhancement of the ME properties through optimisation of the composition, sintering conditions, surface functionalisation and the starting particle sizes, shapes and compositional ratio, and, in particular, by modification of the chemistry to remove the interparticle silica layer necessarily present between the active particles in these initial systems where the chemical assembly of ME composites is demonstrated.

5.3.4 Other systems

A number of parameters dictate whether an ME effect is present, as well as its magnitude. Amongst these are the magnetostriction (λ) of the magnetic component and the piezoelectric constant d_{33} (the induced charge per unit force applied in the same direction) of the ferroelectric component. The effectiveness of the mechanical coupling between the phases[15, 16] is also crucial (i.e., the composite density, so that the deformation due to magnetostriction in the FM phase can be transferred to the FE

phase), as is the size of the interface between the FE and FM components, which can be thought of as the degree of component particle dispersity in particulate composites. The composition (the relative amounts of FE and FM phases)[6, 33] and the connectivity[35] of the composite are also important.

What follows is a discussion of the results where attempts were made to increase the magnitude of α_E by:

1) Increasing the d_{33} of the FE phase by using larger BTO particles
2) Reducing the leakage of the composites by lowering the molar ratio of CFO, while retaining the near-complete CFO on BTO coverage
3) Using larger CFO particles with a higher magnetisation and magnetostriction
4) Altering the connectivity by using a different morphology of BTO

5.3.5 Synthesis and Characterisation of a BTO (400 nm) /CFO (12.5 nm) '**C**' *Ceramic Composite*

Considering the substantial increase in d_{33} that was observed when moving from using the 50 nm BTO to the 200 nm BTO, experiments were carried out with 400 nm SEM-size BTO particles, to assess whether the ME coefficient could be increased further.

A ceramic composite was prepared, as for the **B** ceramics discussed earlier, using DCCI-coupled BTO (400 nm) /CFO (12.5 nm), at a composition whereby the theoretical surface area of the BTO particles (2.6 m^2g^{-1}) matched to the area of the imprint of the 12.5 nm CFO (28.29 m^2g^{-1}), this was at the 11:1 BTO/CFO composition. TEM imaging (Figure 26) showed the BTO/CFO assemblies were formed, as for the **IIb** system, with ceramic processing carried out under the same conditions as for the 5.5:1 BTO (200 nm) /CFO (12.5 nm) **B** composites described

earlier.

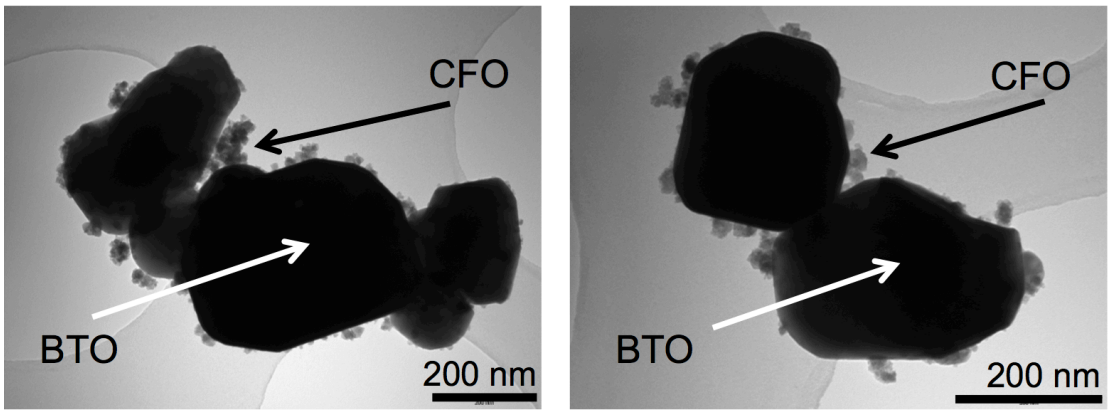

Figure 26. Transmission electron microscopy images of the as-prepared DCCI coupled $BaTiO_3$ (400 nm) /$CoFe_2O_4$ (12.5 nm) composite prepared at a molar ratio of 11:1 of $BaTiO_3$ to $CoFe_2O_4$ in THF.

Measurement of α_E showed this sample was less active than its 200 nm BTO counterpart, despite using the larger particle size BTO (Figure 27). The sample densities were 80% and 78% for the 200 nm and 400 nm BTO pellets respectively.

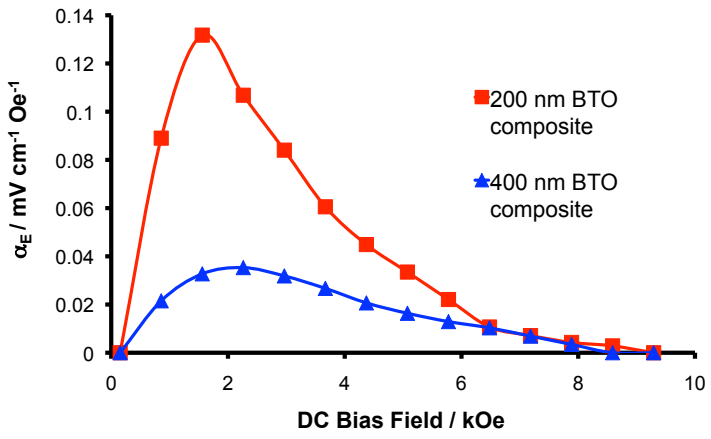

Figure 27. Longitudinal magnetoelectric coefficients, α_E, measured for the **B** and **C** ceramic composites using 200 nm and 400 nm $BaTiO_3$ respectively, with 12.5 nm

$CoFe_2O_4$ and assembled using the DCCI-coupling route. The pellets prepared at molar ratios of $BaTiO_3$ /$CoFe_2O_4$ 5.5:1 (200 nm) and 11:1 (400 nm), and sintered at 1050 °C for 30 minutes.

d_{33} measurements made on the 400 nm BTO particles showed that whilst the size dependent relationship of the d_{33} held for these 400 nm particles (the d_{33} was 157 pC N^{-1} compared to 134 pC N^{-1} for 200 nm BTO), the d_{33} was not substantially larger than for 200 nm BTO. The magnetoelectric data can be understood by considering the extent of the FE-FM interface in this larger BTO-size composite, which will be smaller than for the BTO (200 nm) /CFO (12.5 nm) **B** composites as the 400 nm BTO particles have a smaller surface area than the 200 nm particles.

5.3.6 Hydroxylated BTO (200 nm) /CFO (12.5 nm) '**D**' *Ceramic Composites*

Chang et al.[8] recently demonstrated a method to enhance the reactivity of the BTO nanoparticle surface using H_2O_2. The nanoparticle surface is hydroxylated, with M-O-M bonds broken, resulting in an increase in the number of reactive surface hydroxyl species. This was applied to the 200 nm particles used in the most-active **IIb B** composites, with the idea of increasing the degree of surface functionalisation. Though it was not possible to derive a coverage of the 3-phosphonopropionic acid molecules on the 200 nm particles used in the **IIb** assemblies due to their low surface area, they were found to have reactive terminal COOH functionalities by fluorescence microscopy (Chapter 4, Figure 34). However, the literature shows that commercially acquired particles often have poorly reactive surfaces[8] and, therefore, by enhancing the reactivity using H_2O_2, it may have been possible to get complete coverage of CFO on BTO (which was observed at the 2.75:1 BTO/CFO composition

and above for the **IIb** assemblies) at a lower loading of CFO, which would be beneficial as CFO causes leakage of the charge stored on the FE phase, and this leakage effect increases with increasing CFO content. The nanoparticles were treated with H_2O_2, and then reacted with 3-phosphonopropionic acid as described in Chapter 4.vFTIR (Figure 28) confirmed binding with the peak at 1681 cm^{-1} characteristic of C=O stretching and the peaks at 1050 and 1130 cm^{-1} indicating P=O stretching vibrations.[39]

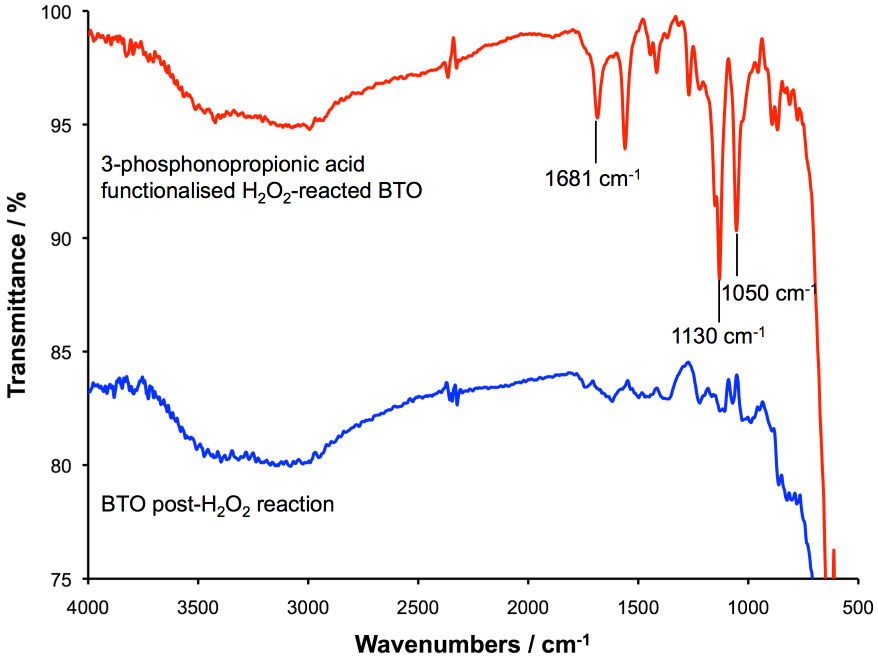

Figure 28. FTIR spectra of 3-phosphonopropionic acid functionalised 200 nm $BaTiO_3$ nanoparticles after treatment with H_2O_2 (red), and unfunctionalised 200 nm $BaTiO_3$ nanoparticles after treatment with H_2O_2 (blue).

TGA (Figure 29) was used to assess the coverage of the 3-phosphonopropionic acid on the BTO particle surface.

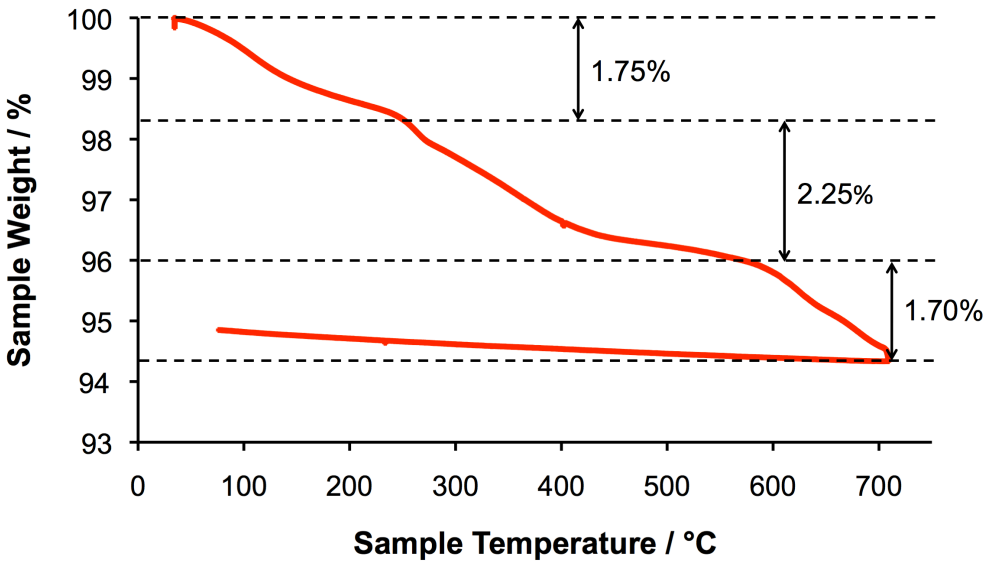

Figure 29. Thermogravimetric analysis of 200 nm $BaTiO_3$ nanoparticles functionalised with 3-phosphonopropionic acid after pre-treatment with H_2O_2.

Using the equation detailed by de Palma et al[40] a coverage of 5.45 phosphonic acid molecules per surface ion was calculated, suggesting multilayers of organic functionalities were present on the BTO surface. The TEM provided some insight into the reason for the high organic content. The images in Figure 30 show how the 'roughness' of the BTO surface has been increased during the H_2O_2 reaction, and the BET surface area was found to have increased from 3.7 to 12 m^2g^{-1}. Considering the larger surface area of the H_2O_2-reacted particles, the coverage can be recalculated to be 1.68 phosphonic acid molecules per surface ion, which indicates some multilayer adsorption of the organic molecules on the particle surface.

Assembly reactions were performed as described for the BTO (200 nm) /CFO (12.5 nm) **IIb** systems described in Chapter 4, with TEM images shown in Figure 31 suggesting these reactions were successful.

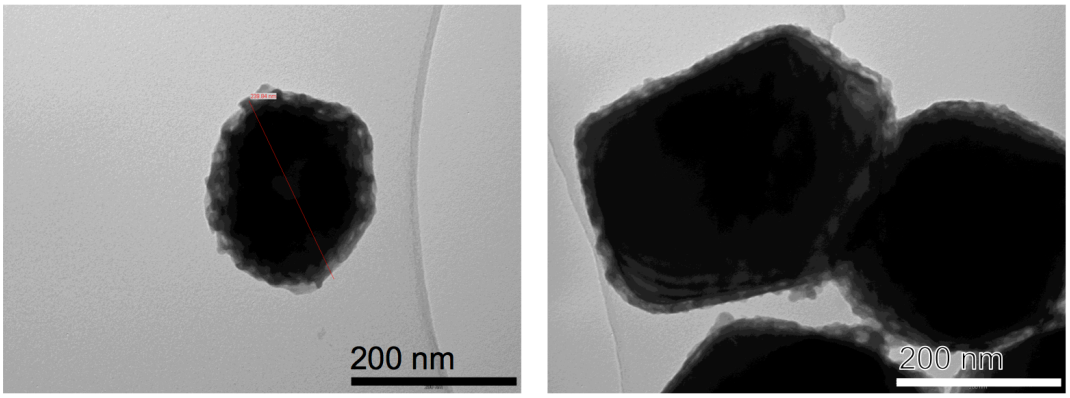

Figure 30. Transmission electron microscopy images of 200 nm $BaTiO_3$ particles after treatment with H_2O_2.

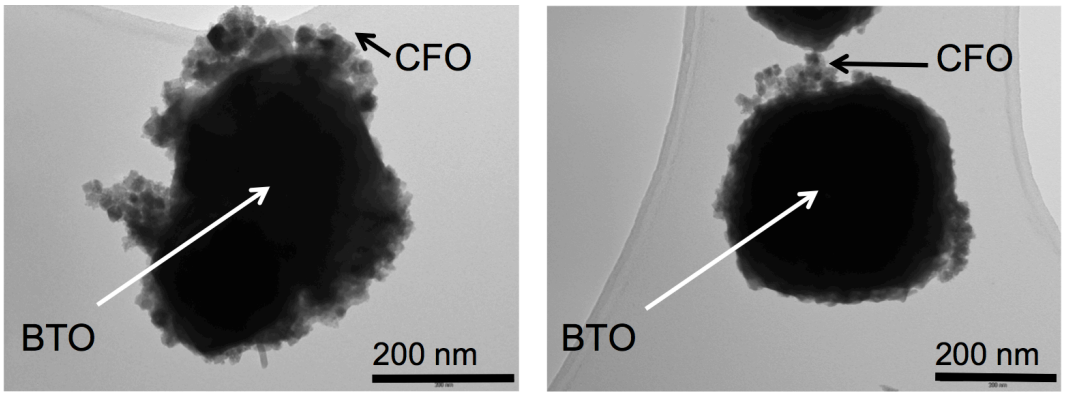

Figure 31. Transmission electron microscopy images of the assemblies formed between H_2O_2 treated, functionalised 200 nm $BaTiO_3$ and 12.5 nm $CoFe_2O_4$ in tetrahydrofuran, at a 2.75:1 molar ratio of $BaTiO_3$ /$CoFe_2O_4$.

Magnetoelectric composites were prepared as described previously for the BTO (200 nm) /CFO (12.5 nm) **B IIb** system, though no α_E was measurable for these samples. The d_{33} provided an explanation for this, with the piezoelectric constant of the H_2O_2-treated BTO determined to be 17 pC N^{-1}, lower than that measured for the 200 nm BTO particles before reaction with H_2O_2 (134 pC N^{-1}). This is likely due to the H_2O_2 etching the nanoparticle surface and increasing the surface area while reducing the d_{33} though the production of surface defects.

5.3.7 BTO (200 nm) /CFO (50 nm) '**E**' *Ceramic Composites*

Pellets were also prepared using 50 nm CFO nanoparticles instead of the coprecipitated 12.5 nm. The aim was to increase α_E using larger FM nanoparticles which have a higher magnetisation[41, 42] and magnetostriction,[43] and so increase the magnetostrictive force applied to the FE particles.

Reactions were carried out using amine terminated CFO, for which microanalysis showed C = 0.41%, H = 0.22% and N = 0%, increased from C = 0%, H = 0.17% and N = 0% in the unfunctionalised sample. The nitrogen content is likely below the detection threshold of the microanalysis instrument, and a coverage of 0.66 APTMS molecules per surface ion was estimated from this microanalysis data based on the carbon content.

DCCI-coupling assembly to 200 nm functionalised BTO was performed, as described in Chapter 4 for the **IIb** assemblies, with STEM (Figure 32) used to assess the success of the reaction. The STEM images suggested the reactions had not been successful, with no BTO/CFO assemblies found as in the **IIb** system. This is likely due to ferromagnetic attraction of the larger CFO nanoparticles, which reduces their dispersability and consequently makes attachment to the BTO surface more difficult.

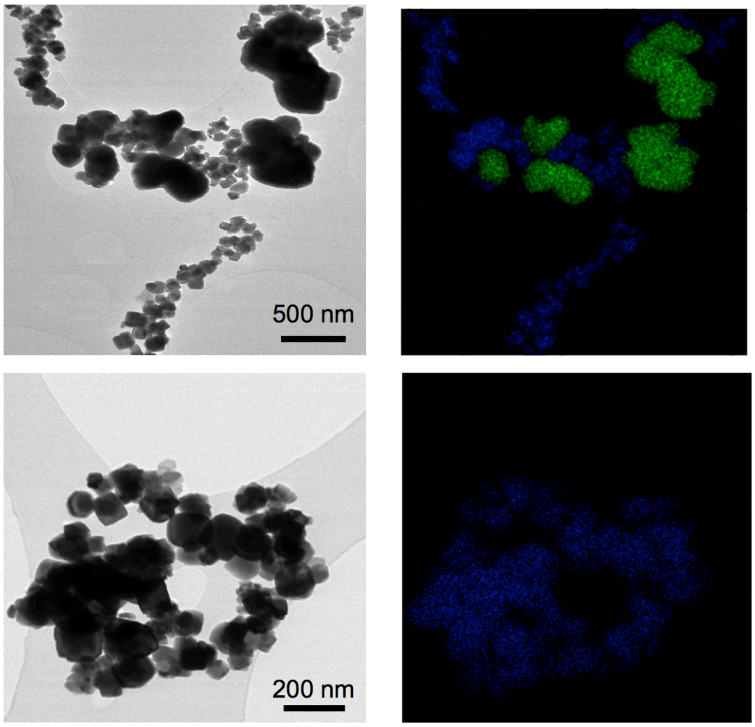

Figure 32. Scanning transmission electron microscopy images and energy dispersive X-ray spectroscopy of two areas in the $BaTiO_3$ (200 nm) /$CoFe_2O_4$ (50 nm) composite. STEM images are shown on the left, with the STEM maps on the right. The blue colour represents Co, while the green color represents Ba.

A BTO (200 nm) /CFO (50 nm) **E** pellet was prepared at molar ratio of 2.75:1 BTO/CFO (i.e. the 'optimal' ratio for the **B** ceramics discussed earlier), in order to assess whether the α_E was larger than the **B** ceramics, despite not possessing the intimate mixing of the BTO and CFO phases. The data for the longitudinal magnetoelectric coefficient, α_E, with respect to DC bias field for a 2.75:1 BTO (200 nm) /CFO (50 nm) **E** pellet sintered at 1200 °C for 30 minutes is shown in Figure 33.

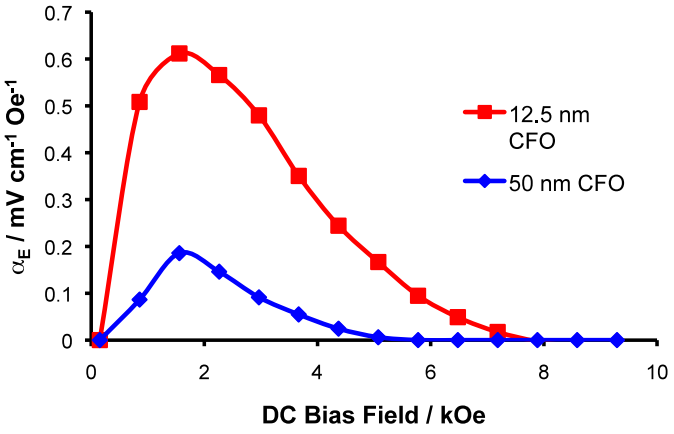

Figure 33. Longitudinal magnetoelectric coefficients, α_E, measured for $BaTiO_3$ (200 nm) /$CoFe_2O_4$ (12.5 nm) **B** and $BaTiO_3$ (200 nm) /$CoFe_2O_4$ (50 nm) **E** pellets prepared at a molar ratio of $BaTiO_3$ /$CoFe_2O_4$ 2.75:1 and sintered at 1200 °C for 30 minutes.

The results show the α_E is significantly lower for these samples, and this demonstrates the influence of the BTO/CFO assembly chemistry. The value for α_E (0.19 mV cm^{-1} Oe^{-1}) is close to the 0.21 mV cm^{-1} Oe^{-1} measured for the unfunctionalised **IIIb B** ceramic discussed earlier, despite the presence of silica, which it is thought reduces α_E. This suggests the use of larger particle size CFO could increase the magnitude of α_E if it were possible to successfully adapt the assembly chemistry to work with this larger CFO particle size. The densities of the samples were 93% for the **B** ceramic and 90% for the **E** ceramic.

5.3.8 BTO (nanowire) /CFO (12.5 nm) '**F**' Ceramic C*omposites*

Finally, ceramics of BTO (nanowires) /CFO (12.5 nm) were prepared. 3–1 (or 1–3) have amongst the largest values for α_E[35] with these systems typically consisting of FE/FM rods aligned in a matrix of FM/FE material. The idea was to produce a pellet with a microstructure similar to that in the 3-1 connectivity systems, which may then

lead to composites with a higher α_E. The assembly of the BTO nanowires with CFO nanoparticles was demonstrated in Chapter 4, and uses the same functionalisation and assembly chemistry developed for the **IIa, b** samples, that is, DCCI-coupling of amine terminated CFO, and carboxylic acid terminated BTO. Pellets were prepared using the same procedure as for the **B** ceramics discussed previously, with sintering at 1200 °C carried out in order to increase the sample density.

No ME effect was observed in these samples, despite the sample density being 88% of the theoretical maximum. This was comparable to the 93% density recorded for the best sample, for which an α_E of 0.61 mV cm^{-1} Oe^{-1} was measured. This was attributed to the piezoelectric constant, which was 0.42 pC N^{-1} compared to 134 pC N^{-1} for the 200 nm BTO particles, for pure-BTO pellets sintered at 850 °C for 12 hours. This can be explained by the absence of peak splitting in the XRD (Figure 41, Chapter 4), which suggests the sample is primarily the paraelectric cubic-phase of BTO. Despite the nanowire length of 3.8 ± 2 μm, it appears that the width of 90 ± 30 nm controls which BTO phase is present in these nanowires. The smaller d_{33} for the nanowires also demonstrates the influence of particle shape and synthesis on the piezoelectric properties, with the recorded value less than the 5.5 pC N^{-1} that was measured for the 50 nm BTO cube-like particles discussed earlier.

5.4 Conclusions

Magnetoelectric composites were prepared from BTO and CFO nanoparticle assemblies. The approach differs from that described by Mornet et al.[7] as direct functionalisation of the nanoparticle surface was performed with complementary functional groups, rather than indirect assembly using silica-coated nanoparticles. This meant the processed ceramics were magnetoelectric with an α_E of 0.6 mV cm^{-1}

Oe^{-1} measured for the best sample, that prepared at a BTO/CFO molar ratio of 2.75:1 and sintered at 1200 °C for 30 minutes. The magnetoelectric properties of the processed ceramics were strongly dependent on both the composite composition and sintering temperature. The optimal composition was that which struck the best balance between having a large enough CFO content to promote the strain-induced magnetoelectric effect, and a small enough CFO content to minimise conductivity and leakage of the piezoelectrically stored that is promoted by CFO.[17, 18] There was also a clear relationship between the sintering temperature, composite density and the magnitude of the magnetoelectric effect. At higher densities the mechanical coupling effect becomes more efficient, leading to larger values of α_E, though XRD suggested phase purity is compromised at higher temperatures due to interdiffusion of the BTO and CFO phases. The magnetoelectric effect was strongly linked to the particle size of the FE phase; when 50 nm BTO particles were used no magnetoelectric effect was observed, but the use of BTO with 200, 300 and 400 nm particles produced the desired magnetoelectric composites. This was explained by the d_{33} measurements, which showed a critical size dependence of the piezoelectric constant, thus below a certain size the poled FE phase produces an insufficient charge for a magnetoelectric coefficient to be measureable. This size dependence was due to the relative amounts of the ferroelectric, tetragonal phase and paraelectric, cubic phase BTO in the samples, with Raman spectroscopy showing the larger particle size BTO samples were much more tetragonal than the 50 nm particles. The magnetoelectric coefficient of the best sample (0.6 mV cm^{-1} Oe^{-1}) is comparable to that in similar nanoparticle-based systems, and larger than that of a composite prepared *via* the traditional grinding and firing approach using the same sized particles. This was attributed to the sample microstructure, with the alternating BTO-CFO arrangement resulting in a

ceramic composite with a high degree of homogeneity between the FE and FM phases, as was observed in SEM EDX and STEM analysis. Thus, it appeared the solution based BTO-CFO assemblies were translated into dense ceramics possessing an intimate mixture of FE and FM particles. The developed magnetoelectrics show a control of microstructure that may be useful for the low temperature assembly of multi-component films and thin layers; in these systems leakage effects are removed due to the lack of a conducting path through the sample and so larger values for α_E can likely be obtained. There is also considerable scope for the enhancement of the magnetoelectric properties through optimisation starting particle size, shape and optimisation of the ceramic composition and sintering conditions. Modification of the chemistry to remove the interparticle silica layer, necessarily present in these initial systems, could further improve the magnetoelectric properties.

References

1. A. Spaldin, M. Fiebig, *Science* **2005**, 309, 391.
2. M. Fiebig, J. Phys D **2005**, 38, R123.
3. G. V. Duong, R. Groessinger, R. S. Turtelli, *IEEE Trans. Magn*. **2006**, 42, 3611.
4. J. Ryu, A. V. Carazo, K. Uchino, H. E. Kim, *Jpn. J. Appl. Phys*. **2001**, 40, 4948.
5. H. Zheng, J. Wang, S. E. Lofland, Z. Ma, L. Mohaddes-Ardabili, T. Zhao, Salamanca-Riba, S. R. Shinde, S. B. Ogale, F. Bai, D. Viehland, Y. Jia, D. G. Schlom, M. Wuttig, A. Roytburd, R. Ramesh, *Science* **2004**, 303, 661.
6. W. Nan, M. I. Bichurin, S. X. Dong, D. Viehland, G. Srinivasan, *J. Appl. Phys*. **2008**, 103, 031101.

7. S. Mornet, C. Elissalde, O. Bidault, F. Weill, E. Sellier, O. Nguyen, M. Maglione, *Chem. Mater*. **2007**, 19, 987.

8. S-J. Chang, W-S Liao, C-J. Ciou, J-T. Lee, C-C Li, *J. Coll. Int. Sci.* **2009**, 329, 300.

9. R. T. Olsson, G. Salazar-Alvarez, M. S. Hedenqvist, U. W. Gedde, F. Lindberg, S. J. Savage, *Chem. Mater.* **2005**, 17, 5109.

10. G. V. Duong, R. Groessinger, M. Schoenhart, D Bueno-Basques, *J. Magn. Magn. Mater.* **2007**, 316, 390.

11. Q. H. Jiang, Z. J. Shen, J. P. Zhou, Z. Shi, C. W. Nan, *J. Eur. Ceram. Soc.* **2007**, 279.

12. Z. Shen, M. Nygren, *Chem. Rec.* **2005**, 5, 173.

13. C. W. Nan, D. R. Clarke, *J. Am. Ceram. Soc.* **1996**, 79, 2563.

14. M. Yashima, T. Hoshina, D. Ishimura, S. Kobayashi, W. Nakamura, T. Tsurumi, S. Wada, *J. Appl. Phys.* **2005**, 98, 014313.

15. G. V. Duong, R. Groessinger, *J. Magn. Magn. Mater*. **2007**, 316, E624.

16. J. Ryu, A. V. Carazo, K. Uchino, H-E Kim, *J. Electroceram.* **2001**, 7, 17.

17. S. Y. Tan, S. R. Shannigrahi, S. H. Tan, F. E. H. Tay, *J. Appl. Phys.* **2008**, 103, 094105.

18. Y. Wu, J. Wan, C. Huang, Y. Weng, S. Zhao, J. Liu, G. Wang, *J. Appl. Phys.* **2008**, 93, 192915.

19. B. D. Begg, E. R. Vance, J. Nowotny, *J. Am. Ceram. Soc.* **1994**, 77, 3186.

20. S. Wada, S. Kondo, C. Moriyoshi, Y. Kuroiwa, *Jpn. J. Appl. Phys.* **2008**, 47, 7612.

21. H. Fu, L. Bellaiche, *Phys. Rev. Lett.* **2003**, 91, 257601.

22. M. B. Smith, K. Page, T. Siegrist, P. L. Redmond, E. C. Walter, R. Seshadri, L.

E. Brus, M. L. Steigerwald, *J. Am. Chem. Soc.* **2008**, 130, 6955.

23. V. Buscaglia, M. T. Buscaglia, M. Viviani, L. Mitoseriu, P. Nanni, V. Trefiletti, P. Piaggio, I. Gregora, T. Ostapchuk, J. Pokorný, J. Petzelt, *J. Eur. Ceram. Soc.* **2006**, 26, 2889.
24. M. H. Frey, D. A. Payne, *Phys. Rev B* **1996**, 54, 3158.
25. S. Wada, T. Tsurumi, H. Chikamori, T. Noma, *Jpn. J. Appl. Phys.* **1998**, 37, 5385.
26. M. El Marssi, F. Le Marrec, I. A. Lukyanchuk, M. G. Karkut, *J. Appl. Phys.* **2003**, 94, 3307.
27. J. D. Freire, R. S. Katiyar, *Phys. Rev. B* **1988**, 37, 2074.
28. C. H. Perry, D. B. Hall, *Phys. Rev. Lett.* **1965**, 15, 700.
29. M. DiDomenico, S. H. Wemple, S. P. S. Porto, *Phys. Rev.* **1968**, 174, 522.
30. U. D. Venkateswaran, V. M. Naik, R. Naik, *Phys. Rev. B* **1998**, 58, 14256.
31. M. P. Fontana, M. Lambert, *Solid State Commun.* **1972**, 10, 1.
32. Y. V. Kole'nko, K. A. Kovnir, I. S. Neira, T. Taniguchi, T. Ishigaki, T. Watanabe, N. Sakamoto, M. Yoshimura, *J. Phys. Chem. C* **2007**, 111, 7306.
33. C. W. Nan, *Phys. Rev. B* **1994**, 50, 6082.
34. G. Srinivasan, E. T. Rasmussen, B. J. Levin, R. Hayes, *Phys. Rev. B* **2002**, 65, 134402.
35. C. W. Nan, M. Li, J. H. Huang, *Phys. Rev. B* **2001**, 63, 144415.
36. J. Wan, Y. Weng, Y. Wu, Z. Li, J. Liu, G. Wang, *Nanotechnology* **2007**, 18, 465708.
37. R. P. Mahajan, K. K. Patankar, M. B. Kothale, S. C. Chaudhari, V. L. Mathe, S. A. Patil, *Pramana – J Phys.* **2002**, 58, 1115.
38. J. V. Suchetelene, *Phillips Res. Rep.* **1972**, 27, 28.

39. J. Pawsey, K. Yach, L. Reven, *Langmuir*, **2002**, 18, 5205.

40. R. De Palma, S. Peeters, M. J. Van Bael, H. Van den Rul, K. Bonroy, W. Laureyn, J. Mullens, G. Borghs, G. Maes, *Chem. Mater*. **2007**, 19, 1821.

41. C. Liu, A. J. Rondinone, Z. J. Zhang, *Pure Appl. Chem.* **2000**, 72, 37.

42. K. Mazz, A. Mumtaz, S. K. Hasanain, A. Ceylan, *J. Magn. Magn. Mater.* **2007**, 308, 289.

43. T. A. Duenas, G. P. Carman *J. Appl. Phys.* **2001**, 90, 2433.

Chapter 6

Chapter 6

6 Final Conclusions and Future Work

6.1 Final Conclusions

The $CoFe_2O_4$ nanoparticles reported in Chapter 3 provided a showed a significantly higher CO oxidation activity than those reported by Pirogova et al.[1] with the best sample displaying a T_{50} of 123 °C, compared to 160 °C reported by the afore mentioned authors. The studies showed the nanoparticles were thermally stable, able to withstand the temperatures they were subjected to for 100% conversion (360 °C for the least active sample) without an increase in XRD particle size, or loss of CO oxidation activity on subsequent test runs. The particles appeared resistant to the flow of CO, retaining a high degree of activity when held at a particular test temperature for a period of 120 minutes, and any loss in activity observed during these isothermal tests was recovered on the next test cycle. The size-activity relationship was determined over the range 5.8 to 30 nm, enabling determination of the CO oxidation activity of $CoFe_2O_4$ nanoparticles within this size range based only on XRD particle size. This is advantageous as the XRD particle size can be determined quickly and easily, whereas direct catalyst testing can take a number of hours. Plotting of the size-activity relationship also enables comparisons to be made between the activities of $CoFe_2O_4$ and another catalysts of a known particle size, as was demonstrated in the $NiFe_2O_4$ nanoparticle example presented in Chapter 3. The use of oxalic acid, ethylenediamine and triethanolamine as capping groups enabled

the synthesis of controlled size nanoparticles, and this combination of capping groups has not previously been used to prepare oxide nanoparticles to our knowledge. These small, volatile organic capping groups also meant a high temperature activation step was not necessary, with particle size stabilising groups removed *in-situ* during testing. The XRD particle size could also be modified by adjustment of the ratios of these capping groups, while this is traditionally done by modification of parameters such as temperature, reaction time and stirring rate. While the prepared catalysts can not match supported Au nanoparticles for activity (these can carry out 100% conversion at room temperature), they are active over a larger range of particle sizes in the unsupported state, and could have higher temperature applications, such as for the removal of CO in H_2 rich gas feeds used for fuel cells.[2, 3]

The work presented in Chapter 4 dealt with the surface modification and assembly of $BaTiO_3$ and $CoFe_2O_4$ nanoparticles. The protocols developed and discussed in this chapter add to the range of methods available for the assembly of oxide nanoparticles. Initial work using 8 nm $BaTiO_3$ and 12.5 nm $CoFe_2O_4$ lead to products that were difficult to characterise using TEM due to the similar sizes and particle size distributions present in both sets of nanoparticles. This was overcome by using larger $BaTiO_3$ nanoparticles that had a distinctly different particle size and shape to the $CoFe_2O_4$ nanoparticles. Characterising data suggested the functional groups that were anchored to the nanoparticle surfaces were reactive and they were used to form electrostatic assemblies of $BaTiO_3$ and $CoFe_2O_4$. A simple chemical coupling step using DCCI then enabled the electrostatic assemblies to be transformed into chemically linked assemblies, which were not sensitive to solvent polarity. Techniques including HRTEM and STEM were used to characterise these

assemblies, and this functionalisation and assembly protocol was extendable to the assembly of nanostructures with different particle sizes, illustrated by the assembly of 200 nm $BaTiO_3$ and 12.5 nm $CoFe_2O_4$ and to different morphologies, demonstrated by the assembly of $BaTiO_3$ nanowires and $CoFe_2O_4$ nanoparticles.

Chapter 5 dealt with the preparation of magnetoelectric materials from the nanoparticle assemblies discussed in Chapter 4. Initial measurements of the magnetoelectric coefficient, α_E, using the 50 nm $BaTiO_3$ and 10 nm $CoFe_2O_4$ composites showed no magnetoelectric effect, due to the low tetragonallity and small piezoelectric constant of the $BaTiO_3$ nanoparticles. This was addressed by using a larger particle size $BaTiO_3$, with composites incorporating 200 nm $BaTiO_3$ nanoparticles possessing the desired magnetoelectric properties. Optimisation of the magnetoelectric coefficient was performed by tuning both the composite composition and sintering temperature. The former required a balance between the amount of $CoFe_2O_4$, which theoretically leads to larger magnetoelectric coefficients up to a fraction of 0.5 relative to $BaTiO_3$, but which also leads to increased sample conductivity and leakage of the piezoelectrically stored charge.[4, 5] The latter involved increasing the sample sintering temperature, and therefore the density, in order to reach a balance between density; which improves the efficiency of the transfer of strain between the ferromagnetic and ferroelectric phases, and phase purity; which decreases with increasing sample density due to interdiffusion of the $BaTiO_3$ and $CoFe_2O_4$ phases.[4-6] The system incorporating 200 nm $BaTiO_3$ and 12.5 nm $CoFe_2O_4$ gave the largest magnetoelectric coefficient, 0.61 mV cm^{-1} Oe^{-1}, when composites were prepared at a molar ratio of 2.75:1 $BaTiO_3/CoFe_2O_4$ using a sintering temperature of 1200 °C for 30 minutes. This magnetoelectric coefficient was larger the 0.21 mV cm^{-1} Oe^{-1} measured for a sample prepared under the same conditions

but using unfunctionalised nanoparticles, and it indicated that the nanoparticle assembly enforced by DCCI coupling was increasing the magnitude of the magnetoelectric coefficient. SEM EDX supported the theory that this was due to a more intimate dispersion of the $BaTiO_3$ and $CoFe_2O_4$ phases with one another. While the magnitude of the magnetoelectric coefficient of the best sample prepared in this work cannot match that measured, for example, for the $CoFe_2O_4/BaTiO_3$ sample prepared by unidirectional solidification where a value of 130 mV cm^{-1} Oe^{-1} was measured,[4] this proof of principle work show does how the nanostructuring and controlled assembly of magnetoelectric composites can lead to materials with desirable microstructural properties which manifest into larger magnetoelectric coefficients when considered next to comparable systems.

6.2 Future Work

Further work related to the $CoFe_2O_4$ CO oxidation catalysts could aim to increase the activity *via* a reduction in particle size. It may be possible to achieve this though further modification of the capping group ratios, or by adjustment of the synthesis conditions, including the reaction temperature and time. Preparing smaller nanoparticles of $CoFe_2O_4$ would also enable investigation of the size-activity relationship at particle sizes beyond what were measured in this thesis. This may help determine the critical size at which mass transfer limits the CO oxidation activity. Dispersing the nanoparticles on a suitable high surface area support would also likely increase the activity of these samples. The synthesis of $Cu_{0.5}Co_{0.5}Fe_2O_4$ or $CuFe_2O_4$ nanoparticles using the same synthetic methodologies could also lead to a reduction in T_{50}, as these were the most active ferrites in the samples prepared and

tested by Pirogova et al,[1] though our initial attempts to prepare them as nanoparticles using the same synthetic methodologies employed for $CoFe_2O_4$ were unsuccessful. As the CO oxidation activity of these catalysts suggests they could be useful catalysts in fuel cells, it would also be important to study the preferential oxidation of CO by these catalysts in the presence of H_2, it is under these conditions that any fuel cell catalyst needs to operate.

Further work regarding the work detailed in Chapter 4 could focus on the preparation of $BaTiO_3/CoFe_2O_4$ composites without the use of aminosilanes, which result in the formation of silica interlayers between the nanoparticles in the processed ceramics, reducing the magnitude of the magnetoelectric coefficient due to leakage.[7] One way this could be achieved is through the use of amine terminated phosphonic acid molecules, or dopamine-type molecules. Some work was done in our group on such materials, though further optimisation was needed. The assembly chemistry could be extended to other systems, including the formation of magnetic-luminescent hybrid nanostructures that have biological applications. Initial experiments on the assembly of ferromagnetic and ferroelectric nanoparticles with thymine and adenine equivalents proved promising, though further characterisation would be required to fully understand the interactions between the nanoparticles and functional molecules, and between the functionalised nanoparticles in these systems.

Chapter 5 dealt with the preparation of magnetoelectric ceramics from assembled nanoparticles. Optimisation of these systems could come from further tuning of the composition of $BaTiO_3/CoFe_2O_4$, though it is unlikely to produce substantially larger magnetoelectric coefficients by itself. Optimisation of the sample sintering temperature could also help, as could the deployment of techniques such as spark plasma sintering for the preparation of dense ceramics with minimal loss of the

active $BaTiO_3$ and $CoFe_2O_4$ phases. Increasing the magnetisation of the $CoFe_2O_4$ nanoparticles either through an increase in particle size or other mechanisms could be of huge benefit, but while some attempts were made at forming nanoparticle assemblies using 50 nm $CoFe_2O_4$ nanoparticles, it appeared ferromagnetic attraction of $CoFe_2O_4$ nanoparticles hindered their dispersability and assembly with $BaTiO_3$. It may also be interesting to develop a system where the $BaTiO_3$ nanoparticles are smaller than the $CoFe_2O_4$ nanoparticles, in order to eliminate the conducting path that is likely present in the assemblies discussed in this thesis. This would reduce leakage of the piezoelectrically stored charge, reduce conductivity and enable more efficient poling. This could prove challenging however, due to the afore mentioned difficulties encountered in the assembly of larger $CoFe_2O_4$ nanoparticles with $BaTiO_3$. Another way to address the conductivity problem could be to prepare a magnetoelectric composite of the assembled nanoparticles with a different connectivity between the ferroelectric and ferromagnetic phases. Robust, alternating layers of DCCI-coupled $BaTiO_3$ and $CoFe_2O_4$ could be prepared, for example, by dip-coating a substrate into functionalised $BaTiO_3$ and $CoFe_2O_4$ nanoparticle suspensions. The assembled film could then be sintered, as for the nanoparticle assemblies, and there would not be a conducting path through the sample in this 2-2-type connectivity film.[8, 9]

References

1. G. N. Pirogova, N. M. Panich, R. I. Korosteleva, Y. V. Voronin, G. E. Kalinina, *Russ. Chem. Bull.* **1996**, 45, 42.

2. A. Wang, Y-P. Hsieh, Y-F. Chen, C-Y. Mou, *J. Catal.* **2006**, 237, 197.

3. A. Manasilp, E. Gulari, *Appl. Catal. B* **2002**, 37, 17.

4. C-W. Nan, M. I. Bichurin, S. Dong, D. Viehland, G. Srinivasan, *J. Appl. Phys.* **2008**, 103, 031101.

5. J. Ryu, A. V. Carazo, K. Uchino, H. E. Kim, *J. Electroceram*, **2001**, 7, 17.

6. G. V. Duong, R. Groessinger, *J. Magn. Magn. Mater*. **2007**, 316, E624.

7. S. Mornet, C. Elissalde, O. Bidault, F. Weill, E. Sellier, O. Nguyen, M. Maglione, *Chem. Mater*. **2007**, 19, 987.

8. G. Srinivasan, E. T. Rasmussen, J. Gallegos, R. Srinivasan, Y. I. Bokhan, V. M. Laletin, *Phys. Rev. B* **2001**, 64, 214408.

9. G. Srinivasan, E. T. Rasmussen, B. J. Levin, R. Hayes, *Phys. Rev. B* **2002**, 65, 134402.